Multi-fluid modelling of idealized convection

Daniel Shipley

Department of Meteorology

University of Reading

A thesis presented for the degree of

Doctor of Philosophy

September 2021

Version number: 1.20

For Jean, Don, Joe, and Pam.

Declaration

I confirm that this is my own work, and that the use of all material from other sources has been properly and fully acknowledged.

Daniel Shipley

Acknowledgements

This thesis is the culmination of four years of hard work: there were times that I doubted whether I'd ever finish, moments of hair-pulling frustration (and abject horror[1]), and long periods of anxiety that I'd never get the damn thing written down. However, there were also myriad moments of joy; elation at understanding something new, at discovering something — however small — that nobody has ever seen before; and a continually deepening love affair with fluid dynamics. While it may have been a turbulent time, the ups were at least as strong as the downs. I am convinced that my four-years-younger self would be proud of both the work I've done, and the researcher I've become.

Of course, a huge number of people helped ensure I got to this point. First and foremost, thanks must go to my supervisors, Hilary Weller and Peter Clark. It is often said that a PhD is an "apprenticeship in research", and their wisdom and support has been instrumental in guiding me towards independence as a researcher. Thank you for treating me like a colleague; it has been an absolute pleasure working on these fascinating problems with you. Thanks also to Tom Webb, who was on my supervisory team for the first two years, and helped immensely with my writing.

Being part of the vibrant research community of the ParaCon project was hugely helpful. Thank you for all of your feedback, useful and interesting discussions on all things convection, in particular to Will McIntyre, John Thuburn, and Georgios Efstathiou. I hope I get to work with you more closely in the future!

My monitoring committee had something of a revolving cast: Bob Plant steered the ship admirably, and Giles Harrison, Clare Watt, and Remi Tailleux crewed it with him. Thanks in particular to Giles for his wisdom and understanding during the difficult early part of my PhD, without which I may not have continued. To Clare for her enthusiasm, wit, and the fresh outside perspective she brought. To Remi for stepping in at short notice for the last MC, and reassuring me I was on the right track! And to Bob, thanks for being immensely supportive throughout my PhD, for providing balance, and for indulging my nattering — I have always enjoyed speaking to you about my work and about convection more generally.

[1] Ask me about the time I accidentally executed `sudo rm -rf /*` instead of `rm -rf */` on the drive containing *all* of my simulation data...

Thanks again to Bob, and also to Tapio Schneider, for examining my thesis. I thoroughly enjoyed the viva: it was a huge honour to speak to you both in depth about my work, and your insights and the discussion they generated both broadened my perspective and sharpened this final version of my thesis. Thank you both for also actually bothering to check all of the maths!

And now to the less tangible, but no less important, influences. The Reading University Meteorology department is an incredibly friendly place to work; I have really missed impromptu coffee room chats since the start of the pandemic. To the denizens of 2U08: thank you for putting up with all my shenanigans, especially my paper plane obsession (sorry Sally!). And to the Shenanigans themselves, Beth & Dom: thanks for making music with me, and sharing some of the happiest and most ridiculous moments of the last few years. I promise to never sleep on a roof again.

Outside of the Met department, I have been incredibly lucky to have a great many close friends and family who have kept me sane throughout the PhD. Firstly, my deep gratitude to Jonathan, whose Monday night calls have been a highlight every week these last couple of years. (For me, at least; my apologies for being "unfailingly long-form".) Tom Babb, too, has been the greatest of friends. Thank you for indulging my mathematical whimsies; but more than that, for being there to pick up the pieces when I needed you. I can't thank you enough.

Thanks to my family, who have been supportive of my decision to stay at university for so bloody long, despite my failure to be able explain to them what I do. In particular, thank you to my extended set of parents, Mam, Dad, Geoff, and Gill; to my sister Kate (for keeping me grounded) and step-siblings Jade and Daniel; to my wonderful mad aunties, Sam and Lynn, thank you for all of your generous advice; and to my Grandma Jean for her kindness and unfailing optimism (sorry I haven't been on the telly yet). To my other grandparents, sadly no longer with us: I hope you're proud. And to Don in particular: thank you for always testing the bounds of my knowledge, pushing me to learn more. Your relentless enthusiasm for learning was infectious, and continues to inspire me.

Lastly, and most importantly, my thanks to Kaja — moim ulubionym człowiekiem — who has been an unwavering source of joy, laughter, wisdom, silliness, and support.

[incomprehensible dinosaur noises]

I love you. Thank you for everything.

Abstract

Atmospheric convection is hugely important for weather and climate prediction, but parametrizations of the process in weather and climate models often behave poorly. Traditional parametrization assumptions break down at resolutions comparable to the dominant energy-containing structures. Lack of understanding of this convective "grey zone" is one of the biggest barriers to improving our representation of convection.

The grey zone is a concept that applies to any turbulent flow — dry or moist. Therefore this thesis focuses on the simplest convection problem: Rayleigh-Bénard convection (RBC). It is shown that RBC possesses remarkably similar grey zone behaviour to that observed in numerical weather prediction models.

In convection, large portions of the turbulent fluxes are carried by coherent structures. This motivates the split into "convection" and "environment" underlying traditional mass flux schemes, which can be generalized via conditional filtering. Introducing explicit discontinuous fluid relabelling terms leads to a multi-fluid equation set that is more complete than those currently published. New expressions for resolved relabelling terms are derived, and an argument is presented linking pressure differences between fluids to an isotropic stress introduced by relabelling.

To show the validity of the multi-fluid approach, a 1D, time-dependent model of RBC is developed. The model has one rising and one falling fluid, and assumes that this split captures all subfilter variability. A scaling argument for the pressure differences between fluids reduces the free parameters to two $\mathcal{O}(1)$ constants. After determining these constants, correct scalings of the domain-averaged heat and momentum fluxes are predicted over six decades of buoyancy forcing. Thus even a simple two-fluid model can capture the essentials of convection.

In 2D, the same model formulation improves initiation of convection across the grey zone, and reduces sensitivity of heat and momentum fluxes to grid spacing, compared to a single-fluid model with constant viscosity. It is shown that the closures successful in a single column do not provide sufficient constraint to maintain the correct sign of vertical velocity in the grey zone. The need for better understanding of the relabelling terms and their resolution-dependence emerges as the key barrier to progress.

List of Figures

List of Tables

A Note on Notation

The turbulence modelling community already suffers from an abundance of sub- and superscripts; multi-fluid modelling only adds to the cacophony. As well as the proliferation of indices, there is a direct conflict between uses of the Latin subscript notation ($(\dots)_i$): in most of physics, including turbulence theory, φ_i is shorthand for the spatial component of the vector φ in the direction of the ith basis vector; while in multi-fluid (or multi-phase) modelling, φ_i customarily denotes the value of φ in the ith fluid partition. Although my preferred notation uses Greek subscripts (from the beginning of the alphabet) to denote fluid partitions, keeping the Latin subscripts free for spatial components, it made no sense to make this departure from the literature when very few expressions in the thesis required spatial index notation. I therefore follow the multi-fluid literature in labelling fluid partitions by Latin subscripts, beginning with i. Where possible, tensor expressions are presented in Gibbs vector notation to avoid the need for more subscripts. However, when index notation is required for clarity, I use Greek letters from the middle of the alphabet (i.e. beginning μ) and employ the Einstein summation convention.

There will still be lots of subscripts and superscripts; probably too many, but I haven't come up with a nicer way to do it yet.

Note in particular the use of $\sim, \approx, \simeq, =$ to denote different strengths of equality. This usage largely follows that of Tennekes and Lumley (1972).

Unfamiliar to non-mathematicians may also be the use of $:=$ and $=:$ for definitions; I find this clearer than the alternative triple-equality $\equiv$ (more commonly used in physics textbooks).

Notation	Description
φ	A generic flow variable, assumed $\varphi(\mathbf{x}, t)$
$\langle\varphi\rangle_g$	Spatial filter of variable φ with respect to the kernel g
φ^{r}	Resolved part of variable φ
φ^{s}	Subfilter part of variable φ
I_i	Indicator function of partition i
φ_i^{r}	Resolved part of variable φ in partition i
φ_i^{s}	Subfilter part of variable φ in partition i
$s(a, b)$	Generalized centred second moment of variables a, b
$s_i(a, b)$	Generalized partitioned centred second moment of variables a, b in partition i
a	A scalar
$\mathbf{a}$	A vector (components a_μ)
$\mathbf{a}$	A tensor (components $a_{\mu\nu}$)
$\mathbf{I}_d$	d-dimensional identity tensor
$\mathbb{R}$	The real numbers
$\in$	Set inclusion, i.e. $a \in S$ means "a is a member of the set S"
$\mathcal{O}$	"Big Oh" asymptotic order notation.
$\sim$	Used for approximate numerical values that are correct to within an order-1 constant (i.e. equality within a factor $\gtrsim \frac{1}{5}$ but $\lesssim 5$)
$\approx$	Used for approximate numerical values that are stated to a precision of approximately 30% **or** to mark any approximations made in an equation where the order of approximation is not stated.
$\simeq$	Used for approximate numerical values that are correct to at least the stated precision.

Contents

The purpose of models is not to fit the data but to sharpen the questions.

Samuel Karlin

Chapter 1

Background

Atmospheric convection is one of the most important components of the global atmospheric circulation, providing significant contributions to global energy, momentum, and moisture transport, as well as strongly coupling to larger scale features such as monsoons and the Madden-Julian Oscillation. Deep convection is responsible for some of the highest-impact weather events both in mid-latitudes and the tropics. However, convection is consistently one of the weakest aspects of numerical weather prediction (e.g. Holloway et al. 2013; Stein et al. 2015) and climate (e.g. Stephens et al. 2010; Stevens and Bony 2013; Sherwood et al. 2014) models, in spite of great efforts to improve its representation (Yano et al. 2018).

Modelling of convection tends to rely on dynamical or thermodynamical balances which only (approximately) apply on large spatiotemporal scales (Plant and Yano 2016a, chapter 4). For example, the mass flux paradigm of Arakawa and Schubert (1974), which conceptually underlies most closures employed in operational numerical weather prediction (NWP) and climate models, relies on a horizontally homogeneous quasi-equilibrium between convection and large-scale forcing. Balances of this type assume that the resolution[1], Δ_r, is much coarser than the largest dynamical scales of the convection, ℓ_L, perhaps ~ 1 km for shallow cumulus, and at least ~ 10 km for deep. This is known in the turbulence community as the "Reynolds averaging" or RANS ("Reynolds-averaged Navier-Stokes") regime. Since current and near-future NWP resolutions are ~ 1 km, these scale separation assumptions clearly cannot be expected to be valid.

However, the smallest dynamically relevant scales of (coherent) convection are $\ell_\mathrm{S} \sim$ 10–100 m. Thus, in order to have a truly "convection-resolving" model, the spatial resolution must be $\sim$ 10–100 m; this is the large eddy simulation (LES) regime, often used for "truth" datasets in atmospheric modelling. In this regime the

[1]By "resolution", we mean "the smallest distance over which we can identify separate objects"; anyone who has taken a course in optics knows that this notion is surprisingly difficult to define rigorously. However, we may note that strictly $\Delta_\mathrm{r} \geq \Delta_\mathrm{f}$ (the filter scale) for a continuous model, and $\Delta_\mathrm{r} > 2\Delta x$ (the grid spacing) for a discrete one.

largest, energy-containing structures of the turbulent flow are explicitly resolved, so resolution is not wasted on the *relatively* unimportant smaller-scale flow. However, these unresolved scales cannot be entirely neglected: they must provide the correct fluxes of energy, enstrophy, and tracers (generally dissipative, but backscatter is also usually important for the most accurate modelling). In order for usual LES closures to apply, the filter scale Δ_f must lie within the inertial subrange of the energy spectrum of the flow (Mason 1994) — again requiring a separation of scales between the filter and the dominant energy-containing length scales. In practice, this means that the resolved part of the flow must still be a fully-developed turbulent flow, i.e. $\mathrm{Re} \gtrsim 10^3$, implying a minimum resolution of ≈ 10 m for shallow cumulus (via the relation $\eta/L \sim \mathrm{Re}^{3/4}$; see section 1.2.1). This is far beyond the reach of weather and climate models for the foreseeable future. Running without a convective parametrization at so-called "convection-permitting" resolutions often produces better results than with a convective parametrization, but results do not clearly converge with increasing resolution (Stein et al. 2015), and there are still significant problems — for instance convection developing at incorrect scales, and with unrealistically intense pockets of highly-localized precipitation (Honnert et al. 2011; Lean et al. 2008; Stein et al. 2015).

We have stumbled upon the "grey-zone" problem: we are forced to consider convection on scales that are too small for traditional convective closure assumptions to work ($\Delta_\mathrm{r} < \ell_\mathrm{L}$), but are yet too large for traditional LES approaches to be valid ($\Delta_\mathrm{r} > \ell_\mathrm{S}$). Any attempt to understand or model convection at these intermediate scales must move beyond these assumptions. Part of the problem is the unhelpful distinction between "convection" and "turbulence" in the atmospheric science community; "turbulence" appears to be used to refer to small-scale, largely homogeneous and isotropic turbulence, often characterised simply by increased mixing. Strongly inhomogeneous, anisotropic features (convective plumes, thermals, clouds) are excluded by this view. But there is no good reason for this exclusion: the coherent structures of convection *are turbulence*. Moreover, even at LES scales, closures must take into account the effects of buoyancy forcing — and what is convection if not the buoyancy-forced part of a fluid flow?

One way of relaxing the traditional convective closure assumptions, yet retaining the useful conceptual partitioning of a fluid flow into "updraft" and "environment" parts from the mass flux approach, is to return to the Navier-Stokes equations and apply a conditional filter to them (see Thuburn et al. 2018, for the method applied to the compressible Euler equations). This results in a fully 3D and prognostic equation set for each fluid partition, where the partitions are coupled by exchanges of mass, momentum, energy etc., as well as by the pressure field. Closures for these exchanges are the analogue of parametrizing entrainment and detrainment in

a traditional convection scheme[2]. Thus, within this framework the convection is fundamentally a part of the dynamics: there is no separate "convection scheme" which is called by the dynamical core. This approach is similar to those used in the modelling of multi-phase engineering flows (e.g. Brennen 2005; Städtke 2007), and has historically been investigated for application to intermittent turbulent flows (Dopazo 1977).

The overarching framework provided by Thuburn et al. (2018) is agnostic as to how to best partition the fluids to represent turbulent convection, but the conceptual idea is to use the partitioning to directly represent the dominant coherent overturning structures. This contrasts with the traditional turbulence approach of representing variability via centred moments of the flow variables — i.e. the mean of each flow variable, then the covariances between all pairs of flow variables, then the third central moment which defines the skewness of the distribution, and so on. We will use the term "multi-moment" to describe this traditional approach, to complement the term "multi-fluid". The most common closures used in atmospheric modelling are first-order (e.g. downgradient eddy diffusion closures) but some second-order statistics — particularly the turbulent kinetic energy (TKE) — are also often used. With a finite number of degrees of freedom available to represent the flow, it is possible that the multi-fluid representation may present a better low-order description of flows where strongly anisotropic coherent structures are a key part of the flow, particularly where third- and higher-order statistics are important. The overturning structures of convection are coherent and strongly anisotropic, and distributions of variables — particularly vertical velocity — exhibit high skewness, suggesting that a multi-fluid representation could be useful.

This thesis aims to investigate the usefulness of a multi-fluid model for parametrizing atmospheric convection by considering its application to the simplest convective system: dry Rayleigh-Bénard convection (RBC). First studied experimentally by Henri Bénard at the turn of the 20th century (Bénard 1900, 1901), the problem was given a theoretical treatment by Lord Rayleigh in 1916 (Lord Rayleigh 1916) and has been well-studied in the applied mathematics and engineering turbulence communities in the century since, providing a rich library of experimental, numerical, and theoretical results to draw upon (see Ahlers et al. 2009; Chillà and Schumacher 2012 for reviews). Most of the challenges of atmospheric grey zones are present within RBC, but the problem is simpler and more symmetric, providing greater constraints on possible parametrizations and hopefully clarifying the underlying physics. Although used by B. Zhou et al. (2014) as a qualitative analogy for the grey zone of the dry convective boundary layer (CBL), the grey zone of RBC has not previously

[2]Closures are also required for subfilter fluxes, analogous to those which arise in any spatially filtered equation set.

been quantitatively explored.

This introductory chapter aims to provide the relevant background for understanding the problem of parametrizing atmospheric convection, as well as its importance. Section 1.1 briefly overviews the fundamentals of convection, venturing definitions of convection and buoyancy and introducing some of the notation and conventions for the rest of the thesis. The section concludes with an exploration of the instabilities which give rise to convection. Section 1.2 presents a view of convection from the vantage point of turbulence theory, discussing the degrees of freedom required to simulate a turbulent flow accurately, as well as the turbulence closure problem and both statistical and LES frameworks for turbulence modelling. Framing the discussion in this way shows that the problem of the "grey zone(s)" arises naturally for any turbulent process. This is followed by a critical overview of traditional convection parametrizations, showing where and why they break down; the grey zone emerges as the fundamental barrier to progress. Some current attempts to improve convection representation are discussed. The final section sketches the approach this thesis takes taken to tackling this problem; however, detailed introductions to (and critiques of) the relevant techniques and literature will be given in their relevant chapters.

1.1 Convection overture

1.1.1 What is convection?

There are at least three common uses for the word "convection" within fluid dynamics; the most general sense is as a synonym for "advection", which is the transport of properties within a fluid by the motion of the fluid itself. This usage is common within the engineering and applied mathematics communities of fluid dynamicists. The second sense is for any fluid motion caused by the effects of body forces on inhomogeneous material properties of the fluid. When the body force is gravity, and the material property is density, we call the force the "buoyancy force". This includes the third, more restrictive, definition seen in meteorology, which we adopt in this thesis (see §1.1 of Emanuel 1994):

Definition 1 (Convection)**.** Convection is motion of a fluid directly caused by instability due to gravity acting on variations of density. The "vertical" direction, which will customarily be denoted $\hat{\mathbf{z}}$ or $\mathbf{k}$, is defined by the direction of the gravitational vector, $\mathbf{g}$: $\hat{\mathbf{z}} \coloneqq -\frac{\mathbf{g}}{|\mathbf{g}|}$.

Convection in this narrow sense[3] still encompasses a fantastically broad array of

[3]Note that this third, most restrictive sense, is historically how the term was first defined

phenomena, from smoke plumes and cumulus clouds in the Earth's atmosphere, to the convection cells in the mantle driving plate tectonics, to convection in the outer core of the Earth (and in outer layers of stars) driving magnetic fields. Convection driven by salt concentrations (as well as temperature) is one of the major driving forces behind the ocean circulation. In the words of the late Charlie Doering, "on length scales bigger than us, the buoyancy force is probably the most important force in nature: it is the way that nature chooses to move stuff around" (Doering 2021). The focus of this thesis is squarely on atmospheric convection, but it is worth noting the incredible wealth of phenomena convection encompasses — and therefore that a better understanding of atmospheric convection may lead to insights applicable much more widely.

1.1.2 Buoyancy

In this section we will define buoyancy mathematically, before looking at some of its general effects on fluids. The discussion is similar to that in Section 1.2 of Emanuel (1994). The compressible Navier-Stokes equation for a Newtonian fluid forced by gravity is (Batchelor 1967, p.164; Landau and Lifshitz 1987, p.45):

$$\frac{\partial \rho \mathbf{u}}{\partial t} + \boldsymbol{\nabla} \cdot (\rho \mathbf{u} \otimes \mathbf{u}) = -\boldsymbol{\nabla} p - \rho \mathbf{g} + \boldsymbol{\nabla} \cdot \left(2\mu \mathbf{e} + \left(\zeta - \frac{2\mu}{d} \right) (\boldsymbol{\nabla} \cdot \mathbf{u}) \, \mathbf{I}_d \right) \tag{1.1}$$

$$\iff \rho \frac{\mathrm{D}\mathbf{u}}{\mathrm{D}t} = -\boldsymbol{\nabla} p - \rho \mathbf{g} + \boldsymbol{\nabla} \cdot \left(2\mu \mathbf{e} + \left(\zeta - \frac{2\mu}{d} \right) (\boldsymbol{\nabla} \cdot \mathbf{u}) \, \mathbf{I}_d \right). \tag{1.2}$$

Here ρ is the fluid's density, $\mathbf{u}$ its velocity, p its thermodynamic pressure, $\mathbf{e} \coloneqq \boldsymbol{\nabla}\mathbf{u} + (\boldsymbol{\nabla}\mathbf{u})^{\mathsf{T}}$ its rate-of-strain tensor, μ its shear viscosity, and ζ its volume viscosity[4]. All of these are assumed functions of d spatial dimensions and time. $\mathbf{I}_d$ is the d–dimensional identity tensor. The momentum equations arising in atmospheric fluid dynamics are all versions of this equation, subject to various approximations, changes of reference frame, and potentially the additions of other body forces besides gravity.

Gravity introduces a preferred direction, meaning that it makes sense to split motion into its components parallel and perpendicular to the gravitational field. If the fluid is at rest, the vertical component of the momentum equation reduces to:

$$\frac{\partial p_{\mathrm{r}}}{\partial z} = -\rho_{\mathrm{r}} g \qquad (g \coloneqq |\mathbf{g}|), \tag{1.3}$$

(pp.77-78; 81 of Prout 1834), though the author also uses the less restrictive second sense later in the book when discussing the origin of the global atmospheric circulation (p.276), and the Latin etymology of the term — "*convectio*, a carrying or conveying" (p.78) — lends itself well to the first, most general interpretation.

[4]The volume viscosity (also called the bulk viscosity, and less frequently the second coefficient of viscosity) quantifies the fluid's irreversible resistance to isotropic compression or expansion.

defining reference "hydrostatic" density and pressure profiles, which are functions of z only. Subtracting these reference hydrostatic contributions from the full pressure gradient and gravitational accelerations gives:

$$\frac{\partial p - p_\mathrm{r}}{\partial z} = -\left(\rho - \rho_\mathrm{r}\right) g. \tag{1.4}$$

Dividing through by density shows that once this reference state has been subtracted, the gravity only affects the flow via the *buoyancy*, defined by:

$$b \coloneqq -g\frac{(\rho - \rho_\mathrm{r})}{\rho}. \tag{1.5}$$

i.e. the relative gravitational acceleration experienced by a parcel of fluid with density different to the hydrostatic reference. This leads us to extend the idea of a hydrostatic reference state: in general, any reference state obeying equation (1.3) may be subtracted from the full flow to give a representation in terms of the perturbation pressure, and the buoyancy.

If the perturbations from the reference state are small, it is helpful to write

$$p = p_\mathrm{r} + \varepsilon p', \qquad \rho = \rho_\mathrm{r} + \varepsilon\rho', \tag{1.6}$$

with dimensionless constant $\varepsilon \in \mathbb{R}_{>0}$ chosen such that ρ_r/ρ' and p_r/p' are $\mathcal{O}(1)$.

The vertical pressure gradient and gravity terms of (1.2) can then be written as (dividing through by the density):

$$\begin{aligned}
\frac{1}{\rho}\frac{\partial p_\mathrm{r} + \varepsilon p'}{\partial z} + g &= \frac{1}{\rho_\mathrm{r}\left(1 + \varepsilon\frac{\rho'}{\rho_\mathrm{r}}\right)}\frac{\partial p_\mathrm{r} + \varepsilon p'}{\partial z} + g \\
&= \frac{1}{\rho_\mathrm{r}}\left(1 - \varepsilon\frac{\rho'}{\rho_\mathrm{r}} + \mathcal{O}\left(\varepsilon^2\right)\right)\left(\frac{\partial p_\mathrm{r}}{\partial z} + \varepsilon\frac{\partial p'}{\partial z}\right) + g \qquad \left(\text{for } \left|\frac{\varepsilon\rho'}{\rho_\mathrm{r}}\right| < 1\right) \\
&= \frac{1}{\rho_\mathrm{r}}\frac{\partial p_\mathrm{r}}{\partial z} + g - \epsilon\left(\frac{\rho'}{\rho_\mathrm{r}}\frac{1}{\rho_\mathrm{r}}\frac{\partial p_\mathrm{r}}{\partial z} - \frac{1}{\rho_\mathrm{r}}\frac{\partial p'}{\partial z}\right) + \mathcal{O}(\varepsilon^2).
\end{aligned} \tag{1.7}$$

Using equation (1.3) to replace $(1/\rho_\mathrm{r})\,\partial p_\mathrm{r}/\partial z$ by $-g$, we see that the $\mathcal{O}(1)$ term cancels. Thus the leading approximation to the pressure gradient and gravitational terms is $\mathcal{O}(\varepsilon)$, which will be a good approximation so long as $\varepsilon \ll 1$:

$$-\frac{1}{\rho}\frac{\partial p_\mathrm{r} + \varepsilon p'}{\partial z} - g = -g\frac{\varepsilon\rho'}{\rho_\mathrm{r}} - \frac{1}{\rho_\mathrm{r}}\frac{\partial\varepsilon p'}{\partial z}. \tag{1.8}$$

This leads us to a more useful expression for the buoyancy:

$$b = -g\frac{(\rho - \rho_\mathrm{r})}{\rho_\mathrm{r}}, \tag{1.9}$$

i.e. the reference state may be used in the denominator. Note that this expression is inherently a linearization: for larger density perturbations the higher-order terms must be retained, and for very large density perturbations $\varepsilon\rho'/\rho_\mathrm{r} \geq 1$ the Taylor expansion of $(1+\varepsilon\rho'/\rho_\mathrm{r})^{-1}$ diverges. Within this approximation, which is *very* good within the lower atmosphere, the buoyancy force defined with the reference state in the denominator captures all of the gravitational influence on the momentum equation.

1.1.3 Instability

Convection as defined in Def. 1 requires instability, so we need to ask "what density differences will cause instability?" before we can ask "what sort of motion will result?". Assuming an inviscid fluid (i.e both $\mu = 0$ and $\zeta = 0$) we can derive necessary conditions for instability based on a linear stability analysis for a parcel isentropically displaced from some reference height. This is what is usually termed "static stability" in meteorology. Consider the infinitesimal, isentropic displacement of an initially resting fluid parcel from a height z, with density $\rho(z) = \rho_\mathrm{r}(z)$, to a height $z+\delta z$. Neglecting viscous forces and the perturbation pressure gradient term (i.e. assuming the perturbation pressure gradient is approximately constant with height), the vertical component of the momentum equation for the parcel is:

$$\frac{\mathrm{D}}{\mathrm{D}t}\left(\frac{\mathrm{D}\delta z}{\mathrm{D}t}\right) = \frac{-g}{\rho_\mathrm{r}}\left[\rho(z+\delta z) - \rho_\mathrm{r}(z+\delta z)\right]. \tag{1.10}$$

The density of the parcel is not necessarily conserved in the isentropic perturbation; however, by definition, the potential density is (being the density the fluid parcel would have if isentropically brought to a reference pressure). Let ρ_θ denote the potential density. Following Vallis (2017, §2.9.2), we let the reference pressure be the pressure at $z+\delta z$, giving $\rho(z+\delta z) = \rho_\theta(z+\delta z)$, and $\rho_\mathrm{r}(z+\delta z) = \rho_{\theta,\mathrm{r}}(z+\delta z)$[5]. Since the potential density of the parcel is conserved, $\rho_\theta(z+\delta z) = \rho_\theta(z)$; and since the parcel's density was initially equal to the environmental reference density, $\rho_\theta(z) = \rho_{\theta,\mathrm{r}}(z)$. Therefore $\rho(z+\delta z) = \rho_{\theta,\mathrm{r}}(z)$, and the vertical momentum equation becomes:

$$\frac{\mathrm{D}}{\mathrm{D}t}\left(\frac{\mathrm{D}\delta z}{\mathrm{D}t}\right) = \frac{-g}{\rho_\mathrm{r}}\left[\rho_{\theta,\mathrm{r}}(z) - \rho_{\theta,\mathrm{r}}(z+\delta z)\right] \tag{1.11}$$

$$\implies \frac{\mathrm{d}^2\delta z}{\mathrm{d}t^2} \approx -\left[-\frac{g}{\rho_{\theta,\mathrm{r}}}\left(\frac{\partial\rho_{\theta,\mathrm{r}}}{\partial z}\right)\right]\delta z. \tag{1.12}$$

[5]This is not just for convenience; in general, for a multi-component fluid (e.g. the salty ocean, or the moist atmosphere), ρ_θ is a nonlinear, multi-valued function of the other thermodynamic variables. Therefore it must be referenced *locally* for the linear stability analysis to hold.

This is a harmonic oscillator equation with frequency $N = \sqrt{-(g/\rho_{\theta,\mathrm{r}})\,\partial\rho_{\theta,\mathrm{r}}/\partial z}$, usually called the "buoyancy frequency" or "Brunt-Väisälä frequency". Clearly if $N^2 > 0$ the solutions for the displacement δz are oscillatory, while if $N^2 < 0$ the solutions are exponentially increasing or decaying. Therefore, neglecting perturbation pressure gradient forces and viscosity, a sufficient condition for static instability is $N^2 < 0$, or, equivalently, $\partial\rho_{\theta,\mathrm{r}}/\partial z > 0$. Similar arguments can be found in many texts on geophysical fluid dynamics (for instance Salmon 1998, §§15-16; Vallis 2017, §§2.9.1-2.9.2).

Casting the discussion in terms of isentropic perturbations allows the final expression above to be applied, with the correct approximations, to both dry and moist atmospheric convection (Emanuel 1994; as well as to the ocean, Vallis 2017). For dry air (approximated as an ideal gas), note that the equation of state relating the potential density, the potential temperature, and the reference pressure, is simply the ideal gas law evaluated at the reference pressure, $p_R = \rho_\theta R\theta$, giving $N^2 = (g/\theta_\mathrm{h})\,\partial\theta_\mathrm{h}/\partial z$. For unsaturated moist air, θ may be replaced by the virtual potential temperature. In more complex fluids (such as moist *saturated* air), there will often be multiple competing effects governing the static stability. This can be seen by writing the potential density as a function of the other thermodynamic variables; here we shall choose entropy η, pressure p, and C, a variable representing composition:

$$\mathrm{d}\rho_\theta = \left(\frac{\partial\rho_\theta}{\partial\eta}\right)_{p,C}\mathrm{d}\eta + \left(\frac{\partial\rho_\theta}{\partial p}\right)_{\eta,C}\mathrm{d}p + \left(\frac{\partial\rho_\theta}{\partial C}\right)_{\eta,p}\mathrm{d}C. \tag{1.13}$$

Even neglecting pressure perturbations (consistent with the linear stability analysis), there must be contributions to the potential density gradient from both changes in the environmental entropy profile, *and* changes in the environmental concentration profile. These details are explicitly worked out for moist saturated air in, for instance, Emanuel (1994, §6.2).

In a real fluid, the pressure gradient force does vary with height, and viscosity is not necessarily negligible. This complicates the linear stability analysis, to the extent that it is not necessarily solvable for arbitrary boundary conditions. However we may generally see that the effect of viscosity is to suppress the convective instability, since the viscous term dissipates kinetic energy. Therefore in a viscous fluid the sufficient condition for instability is generally stronger than for an inviscid fluid. For the simple case of Rayleigh-Bénard convection of a Boussinesq fluid confined between two flat horizontal plates, each held at fixed buoyancy (which will be reviewed extensively in Chapter 2), this can be seen explicitly: the background buoyancy profile must be steeper than a (calculable) critical buoyancy profile, $\partial b_\mathrm{ref}/\partial z > (\partial b_\mathrm{ref}/\partial z)_\mathrm{c}$. This critical background buoyancy profile is a function of the distance between the plates,

and the viscosity and thermal diffusivity of the fluid. Because the Reynolds number in atmospheric flows tends to be very large, this correction to the stability criterion matters little unless one is directly considering the effects of enhanced turbulent mixing on stability with respect to a *turbulent* reference state (e.g. Thuburn et al. 2019).

Since fluid dynamics is *nonlinear*, we also need to seek the *necessary* conditions for convection to occur. Linear stability analysis is fit to tell us sufficient conditions for instability, and, since the unstable solutions to the linearized perturbation equations grow exponentially, *necessary* conditions for stability. To find necessary conditions for *in*stability, we need to find sufficient conditions for stability, i.e. we need to find the requirements for any finite-amplitude perturbation to decay. In the nonlinear analysis, there is no restriction on the size of these perturbations (i.e. they need not be small). This process can be quite involved; one successful method for establishing nonlinear stability is known as the "method of energy" (Doering and Gibbon 1995; Straughan 2004), where one finds sufficient conditions such that the kinetic energy of the perturbations will eventually decay to zero.

In general, the linear and nonlinear stability criteria will not match, meaning that we must also consider finite-amplitude instabilities. This is well-known to atmospheric scientists and meteorologists under the name of "conditional instability" (Emanuel 1994, §6.3): a parcel of air may be stable to an infinitesimal displacement ("statically stable"), but unstable to a sufficiently large one. Conditional instability is due to the presence of water in the atmosphere[6], which undergoes first-order phase transitions between its vapour, liquid, and solid phases. Such phase changes are associated with a discontinuous change in entropy at constant temperature (Blundell and Blundell 2009, chapter 28; Callen 1985, §9.2) — or "latent heat" — introducing an extra source of buoyancy. This complicates the convection problem: while basic results of linear and nonlinear stability are well-established for dry Rayleigh-Bénard convection, neither are established for any of the various extensions to moist convection (Bretherton 1987, 1988; Pauluis and Schumacher 2010; Schumacher and Pauluis 2010; Weidauer et al. 2010; Weidauer and Schumacher 2012; Vallis et al. 2019).

Conditional instability is immensely important for atmospheric moist convection: deep convection almost always occurs due to conditional instability in a statically-stable environment. There are various methods for estimating conditional instability in the atmosphere, which generally estimate the potential energy available to convective instability by following the ascent of some idealized fluid parcel. However, the general nonlinear stability criteria for moist atmospheric convection are not known.

[6]Of course, water is not special: methane plays this role on Jupiter's moon Titan (Hayes et al. 2018).

1.2 Turbulence and the Parametrization Problem

Convection in geophysical contexts is invariably *turbulent*. In the atmospheric context this follows obviously from noting that a typical Reynolds number for convection is very large: in the dry CBL, for instance, typical updraft velocities are ~ 1 m s^{-1}, the boundary layer depth is $\sim 10^3$ m, and the viscosity of air $\sim 10^{-5}$ m^2 s^{-1}, giving Re $\sim 10^8$. Heuristically, a fluid flow will be turbulent if its Reynolds number is sufficiently large ($\gtrsim 10^3$), so by this practical definition, atmospheric convection must be a turbulent flow. But mentioning turbulence within the context of atmospheric convection can cause controversy and misunderstanding, so for the avoidance of doubt we will discuss and define the term now.

Turbulence does not have a broadly-accepted mathematical or even verbal definition (Tennekes and Lumley 1972, §1.1; Doering and Gibbon 1995, §3.1; Salmon 1998, p.207; Lesieur 2008, §1.1; Vallis 2017, p.413). Authors tend to describe the characteristics of a turbulent flow, rather than venturing a definition; as Vallis notes, "it is hard to disentangle a definition from a property". All of the above authors agree that a turbulent flow must possess some of the following properties[7]:

1. Unpredictability (also "randomness", "irregularity", "lack of bounded sensitivity");
2. Nonlinearity: these flows are dominated by the nonlinear term in the Navier-Stokes equation, giving rise to interactions between, and generation of, multiple scales;
3. A large range of spatial and temporal scales (a consequence of strong nonlinearity, implying a large Reynolds number);
4. Enhanced mixing (globally): turbulent flows mix tracers and active fluid properties far more efficiently than molecular processes alone, though there *can* be local regions of up-gradient transport;
5. Inherently vortical (irrotational flows cannot be turbulent).

Atmospheric convection exhibits *all* of these characteristics: atmospheric convection *is* a turbulent flow, and consequently when we try to understand, model, or parametrize atmospheric convection, we are wrestling directly with turbulence. The distinction between "convection" and "turbulence" is therefore artificial, and we will not make it in this thesis: we take the view that atmospheric convection is atmospheric turbulence generated by unstable distributions of buoyancy.

[7]Some authors (e.g. Tennekes and Lumley 1972) add the stipulation that turbulence *must* be three-dimensional; in our view this is unhelpful, as certain two-dimensional flows can exhibit all of the other characteristics of turbulence (though the nature of the propagation of energy through scale space is admittedly fundamentally different).

In particular, for the remainder of the thesis, the word turbulence will be taken to mean the following:

Definition 2 (Turbulence)**.** A **turbulent flow** is a fluid flow which exhibits (a) spatial and temporal unpredictability, and (b) a wide range of spatial and temporal scales. **Turbulence** describes such a flow.

Turbulent flows often exhibit what are called "coherent structures" within the otherwise random, uncorrelated three-dimensional vorticity fluctuations; that is, emergent structures within the flow which are coherent over length scales large compared to the dissipation length scale of the flow (Hussain 1986). The overturning circulations of convection, both dry and moist, are striking examples of these phenomena.

Viewing convection through the lens of turbulence is a powerful tool for unpicking many of the issues which arise when trying to understand and model it; that is the goal of the remainder of this section. We note that there are (at least) two main strands of research in turbulent flow; one could broadly be described as the "understanding" of the flow, and the other is the "simulation" of the flow. Of course, the two strands overlap.

1.2.1 Length scales; direct numerical simulation; requirement for parametrization

One way in which turbulent flows differ from laminar flows is the presence of a wide range of length and time scales within the flow, all of which are relevant to the dynamics. How many scales? Following Kolmogorov (1941) (hereafter "K41"; reviewed beautifully with emphasis on symmetry principles in Frisch 1995, chapters 6-7), we assume that a turbulent flow possesses a scale, ℓ_0, which is the characteristic scale of energy input (usually set by the initial or boundary conditions). Despite the dominance of the nonlinear term on large scales $\sim \ell_0$, the viscous term term will become important on small enough scales; therefore we introduce the second length scale η, called the "Kolmogorov length" or "dissipation length", defined as the scale for which inertial and viscous accelerations become equally important. In the region of scale-space between these two scales, direct interaction with ℓ_0 will be negligible sufficiently far from ℓ_0, and so direct energy input is negligible. Further, on scales sufficiently larger than η, direct energy dissipation by viscosity will be negligible. This region of scale space, where $\ell_0 \gg \ell \gg \eta$, is termed the "inertial subrange" (ISR) (because the viscous terms, and external forcing terms, are negligible, and so the dynamics are dominated by the remaining, inertial, terms).

Under the assumption of a statistically stationary state, the rate of energy input at the large scale ℓ_0 must be equal to the rate of dissipation by viscosity at the small

scale η. The rate of energy input from scale ℓ_0 to smaller scales is $\sim u_0^2/t_0$, where u_0 is the characteristic velocity of fluctuations with length scale $\sim \ell_0$, and t_0 is the characteristic time scale of such fluctuations, known as the "eddy turnover time" — that is, fluctuations at the integral scale ℓ_0 disperse their kinetic energy to smaller scales in a characteristic time t_0. The eddy turnover time itself may be related to the characteristic velocity and length scales of an eddy of size ℓ by $t_\ell \sim \ell/u_\ell$, giving an energy flux at the energy input scale ℓ_0 of u_0^3/ℓ_0. This must be equal to the rate of dissipation by viscosity at the scale η:

$$\varepsilon \sim \frac{u_0^3}{\ell_0}. \tag{1.14}$$

Note that this only assumes statistical stationarity (and, implicitly, finite dissipation rate as $\nu \to 0$, and local isotropy and homogeneity; see Frisch 1995, p.103), and not (yet) the localness of interactions in scale space. This is effectively just a restatement of the requirement that, in a statistically stationary state, the production of energy must be balanced by its dissipation, plus a very simple and widely applicable scaling argument for the dependence of the flux of energy at the outer length scale ℓ_0 (which is equal to the rate of production of energy) on the outer velocity and length scales — since for an incompressible fluid with negligible viscosity at scale ℓ_0, these are the only parameters on which the flow can depend.

At some scale η, the viscous terms become equally as important as the nonlinear terms. This means that the Reynolds number at a scale η must be $\mathcal{O}(1)$:

$$1 \sim \mathrm{Re}(\eta) = \frac{u_\eta \eta}{\nu}. \tag{1.15}$$

To estimate the velocity, we need to assume that equation (1.14) is valid for all of the intermediate scales $\ell_0 > \ell > \eta$ in the inertial range; this is equivalent to assuming that the velocity field is scale-invariant (or "self-similar") for scales $\ell \ll \ell_0$ (see Frisch 1995 §§6.1, 6.3.2, 7.3). Replacing $\ell_0 \to \eta, u_0 \to u_\eta$ in equation (1.14) then gives $u_\eta \sim \varepsilon^{1/3}\eta^{1/3}$; substituting this in the expression for $\mathrm{Re}(\eta)$:

$$\frac{\varepsilon^{1/3}\eta^{4/3} \cdot \eta}{\nu} \sim 1 \qquad \implies \eta \sim \left(\frac{\nu^3}{\varepsilon}\right)^{1/4}. \tag{1.16}$$

Rearranging equation (1.14) for the outer length scale ℓ_0 allows us to relate the largest and smallest length scales in the flow:

$$\frac{\ell_0}{\eta} \sim \left(\frac{\ell_0 u_0}{\nu}\right)^{3/4} = \mathrm{Re}(\ell_0)^{3/4}. \tag{1.17}$$

This states that the ratio between the largest and smallest dynamically relevant

length scales in the flow scales strongly with the Reynolds number. Using the estimates of $u_0 \sim 1$ m s^{-1}, $\ell_0 \sim 10^3$ m, and $\nu \sim 10^{-5}$ m^2 s^{-1} from the CBL example at the beginning of Section 1.2, the smallest dynamically relevant scale for the CBL is ~ 1 mm (the same estimate is given in Cullen and Brown 2009). Resolutions this fine are unlikely to ever be possible.

Seen another way: to accurately numerically simulate all of these scales on a uniform grid, there must be $\sim \mathrm{Re}^{3/4}$ grid points in each dimension for each integral length scale. To simulate accurately in time, the time-step must also be approximately proportional to the grid spacing (because the flow is inertially-dominated until the very smallest scale), and we must simulate for at least one eddy turnover time. This means that the computational power required to simulate a turbulent flow accurately for a fixed length of time grows very strongly with the Reynolds number: in d spatial dimensions, the total number of operations, N, scales as $N \sim \mathrm{Re}^{3(d+1)/4} = \mathrm{Re}^3$ if $d = 3$, or $\mathrm{Re}^{9/4}$ if $d = 2$ (Frisch 1995; Moin and Mahesh 1998; Davidson 2009; Wyngaard 2010). This is what we must do if we wish to simulate all of the scales of a turbulent flow accurately, with no approximation; such a simulation is called a "direct numerical simulation" (DNS; an excellent review is provided by Moin and Mahesh 1998, while a wonderful non-technical overview is given by Patterson and Orszag 1973).

Direct simulations are simply not possible for geophysical flows in general, nor for atmospheric convection in particular: for the dry CBL flow discussed at the beginning of this section, $\mathrm{Re} \geq 10^8$, implying at least $N \sim 10^{24}$ operations would be required to simulate a single eddy turnover time (on the order of $10 - 15$ minutes). The world's fastest supercomputers can currently perform $\sim 10^{18}$ operations per second[8], meaning that even the fastest supercomputer would need $\gtrsim 10^6$ s ≈ 11 days to directly simulate a single large eddy scale for a single eddy turnover time.

This must be a lower bound, as we have assumed only one operation per grid point per time-step, which is clearly an underestimate since the Navier-Stokes equations are a coupled system of partial differential equations, requiring $\sim$ 10–100 operations per grid point per time step. Therefore the lower bound is quite loose, and would in reality be larger by at least a factor of 10. Since many eddy turnover times and, preferably, many eddy turnover scales are required for even idealized studies, this is clearly not yet viable even as a research tool, let alone for real-time

[8] A ranking of the world's fastest computers has been compiled in June and November of each year since 1993 by the TOP500 Project. The fastest computer on the latest (November 2022) list is "Frontier", hosted at the Oak Ridge Leadership Computing Facility in the USA, which performed 1.1×10^{18} floating-point operations per second in the project's standard benchmark (The TOP500 Project 2022). Several supercomputers operated by meteorological agencies are in the top 100, including one of the UK Met Office's HPE machines (ranked 82$^{\text{nd}}$ at 7×10^{15} operations per second).

forecasting of the weather!

To be able to be used to forecast the weather, such a simulation must run faster than real time; as an upper bound, this would require the simulation wall clock time for a single turnover time to be equal to the turnover time: $T_{\text{sim}} = t_0$. For $u_0 \sim 1\text{ m s}^{-1}, \ell_0 \sim 10^3\text{ m}, t_0 \sim 1000\text{ s}$. We would also require simulation over a much larger area than a single large eddy scale; assuming we would like a regional forecast only over a $1000\times1000\times10$ km cuboid over the British Isles gives us a volume of $V \sim 10^7\ell_0^3$. (In choosing the British Isles as our example, we have effectively described the problem faced by the operational forecasters at the UK Met Office.) Assuming $N \sim 10^{18}$ operations per second, the largest Reynolds number that can be simulated in real time is then given by $(V/\ell_0^3)\,\text{Re}_{\text{max}}^3 \lesssim N \times T_{\text{sim}} \implies \text{Re}_{\text{max}} \lesssim 10^{14/3} \approx 50,000 \ll 10^8$. Again, this upper bound is quite loose: accounting for more than one operation per grid point per time-step, communication time between different computational nodes, data input and output, post-processing, and data assimilation, would all lower the bound. These slow-downs are inherent to simulation of the Navier-Stokes equations for forecasting purposes, and will never fully disappear.

So, the possibility of *directly* numerically simulating the weather in real time is a fantasy, and will be for a very long time. This problem is even greater if we wish to directly simulate the entire atmosphere, and greater still if we wish to directly simulate the climate — DNS on these scales is unlikely to ever be possible. We are forced to somehow reduce the number of degrees of freedom in order to make a simulation possible (the resulting system will be called a "reduced order" or "low order" *model* of the underlying flow). It is also desirable to reduce the number of degrees of freedom, or at least analyse them separately, in order to build an understanding of how the different scales in a turbulent flow interact with each other. The most common way to do this is by applying some sort of averaging or filtering operation to the governing equations:

Definition 3 (Linear filtering operation)**.** Given flow variables φ, ψ, and constant $\alpha \in \mathbb{R}$, we define a **linear filtering operation**, denoted by angle brackets, $\langle \ldots \rangle$, as a formal operation which satisfies the following properties (Germano 1992):

$$\left\langle \frac{\partial \varphi}{\partial \mathbf{x}} \right\rangle = \frac{\partial \langle \varphi \rangle}{\partial \mathbf{x}}, \qquad \left\langle \frac{\partial \varphi}{\partial t} \right\rangle = \frac{\partial \langle \varphi \rangle}{\partial t} \qquad \text{(commutation with partial derivatives)} \tag{1.18}$$

$$\langle \alpha\varphi + \psi \rangle = \alpha \langle \varphi \rangle + \langle \psi \rangle \qquad \text{(linearity)}. \tag{1.19}$$

Any flow variable can then be decomposed into its filtered (or "resolved") and residual (or "subfilter") parts:

Definition 4 ("Resolved" and "subfilter" variables: incompressible case)**.** For a variable φ, and filtering operation $\langle \dots \rangle$, we define the ***resolved part of*** φ by:

$$\varphi^{\mathrm{r}} \coloneqq \langle \varphi \rangle \,. \tag{1.20}$$

Similarly, we define the ***subfilter part of*** φ by:

$$\varphi^{\mathrm{s}} \coloneqq \varphi - \varphi^{\mathrm{r}}. \tag{1.21}$$

Clearly then $\varphi = \varphi^{\mathrm{r}} + \varphi^{\mathrm{s}}$. For now we will not worry about the exact nature of the filter; we merely note that it is generally the goal of turbulence study (theoretical, numerical, observational, and experimental) to understand and/or predict the effects of the subfilter flow on the resolved flow.

As a first step, we will simply apply a linear filter to the governing Navier-Stokes equation (assumed, for simplicity, to be incompressible, with homogeneous reference density ρ_{r}, and homogeneous kinematic viscosity ν):

$$\frac{\partial \langle \mathbf{u} \rangle}{\partial t} + \boldsymbol{\nabla} \cdot (\langle \mathbf{u} \otimes \mathbf{u} \rangle) = -\boldsymbol{\nabla} \left\langle \frac{p}{\rho_{\mathrm{r}}} \right\rangle + \left\langle b \hat{\mathbf{k}} \right\rangle + \nu \boldsymbol{\nabla}^2 \langle \mathbf{u} \rangle.$$

Defining the pressure potential by $P \coloneqq p/\rho_{\mathrm{r}}$, and assuming the gravitational vector to be constant and therefore commute with the filtering, this becomes:

$$\frac{\partial \langle \mathbf{u} \rangle}{\partial t} + \boldsymbol{\nabla} \cdot \langle \mathbf{u} \rangle \otimes \langle \mathbf{u} \rangle = -\boldsymbol{\nabla} \langle P \rangle + \langle b \rangle \hat{\mathbf{k}} + \nu \boldsymbol{\nabla}^2 \langle \mathbf{u} \rangle - \boldsymbol{\nabla} \cdot (\langle \mathbf{u} \otimes \mathbf{u} \rangle - \langle \mathbf{u} \rangle \otimes \langle \mathbf{u} \rangle) \,. \tag{1.22}$$

This is the momentum equation for the *filtered* velocity field, which looks exactly like the unfiltered momentum equation except for the presence of the extra term $\langle \mathbf{u} \otimes \mathbf{u} \rangle - \langle \mathbf{u} \rangle \otimes \langle \mathbf{u} \rangle$. This term is usually called the "subfilter momentum flux" or "subfilter stress". To tidy up the appearance of later equations, we will follow Germano (1992) and define the "subfilter flux" operator:

Definition 5 (Generalized second centred moment/"subfilter flux")**.** For any two flow variables φ, ψ, and a linear filtering operation, $\langle \dots \rangle$, we define the **generalized second centred moment** $s(\varphi, \psi)$ by:

$$s(\varphi, \psi) \coloneqq \langle \varphi \psi \rangle - \langle \varphi \rangle \langle \psi \rangle \,. \tag{1.23}$$

Note that this operator, s, is linear in both of its arguments: $s(a_1 + a_2, b_1 + b_2) = s(a_1, b_1) + s(a_1, b_2) + s(a_2, b_1) + s(a_2, b_2)$ (Germano 1992). It is the extension of the covariance (or, second centered moment about the mean) to a general linear filtering operation. Where one of the variables is the fluid velocity, $s(\mathbf{u}, \psi)$ then represents

the subfilter flux of the quantity ψ; hence we may sometimes refer to this operator as the "subfilter flux" operator.

With this definition, the filtered Navier-Stokes equation becomes:

$$\frac{\partial \langle \mathbf{u} \rangle}{\partial t} + \boldsymbol{\nabla} \cdot \langle \mathbf{u} \rangle \otimes \langle \mathbf{u} \rangle = -\boldsymbol{\nabla} \langle P \rangle + \langle b \rangle \hat{\mathbf{k}} + \nu \boldsymbol{\nabla}^2 \langle \mathbf{u} \rangle - \boldsymbol{\nabla} \cdot s(\mathbf{u}, \mathbf{u}). \tag{1.24}$$

Immediately we are presented with the "turbulence closure problem": filtering introduces terms of the form $s(\mathbf{u}, \mathbf{u})$, so there are now more unknowns than equations. We can derive an evolution equation for $s(\mathbf{u}, \mathbf{u})$, but this will involve terms like $\langle \mathbf{u} \otimes \mathbf{u} \otimes \mathbf{u} \rangle$, which are also not known. Systems of equations with more (independent) unknowns than (independent) equations are said to be "unclosed"; thus additional equations, or relations between the known variables and the new variables introduced by filtering, must be added in order to "close" the equation set. The task of finding/guessing/deriving these relations is known as the turbulence closure problem. Note that the problematic term would not have arisen if the Navier-Stokes equation were linear: nonlinearity is the cause of the closure problem. Therefore nonlinearity both causes turbulence, forcing us to need to reduce the number of degrees of freedom in order to make sense of the flow, *and* causes the closure problem, which makes that reduction nontrivial.

Terms like $s(\mathbf{u}, \mathbf{u})$ capture the effects of the nonlinear interactions in the unfiltered flow on the filtered flow. This can be seen more clearly by splitting the velocity field into its filtered (or "resolved") and residual (or "subfilter") parts:

$$\mathbf{u} = \langle \mathbf{u} \rangle + (\mathbf{u} - \langle \mathbf{u} \rangle) = \mathbf{u}^{\mathrm{r}} + \mathbf{u}^{\mathrm{s}} \tag{1.25}$$

$$\implies s(\mathbf{u}, \mathbf{u}) = (\mathbf{u}^{\mathrm{r}} \otimes \mathbf{u}^{\mathrm{r}})^{\mathrm{r}} - \mathbf{u}^{\mathrm{r}} \otimes \mathbf{u}^{\mathrm{r}} + (\mathbf{u}^{\mathrm{r}} \otimes \mathbf{u}^{\mathrm{s}} + \mathbf{u}^{\mathrm{s}} \otimes \mathbf{u}^{\mathrm{r}})^{\mathrm{r}} + (\mathbf{u}^{\mathrm{s}} \otimes \mathbf{u}^{\mathrm{s}})^{\mathrm{r}} \tag{1.26}$$

$$= s(\mathbf{u}^{\mathrm{r}}, \mathbf{u}^{\mathrm{r}}) + [s(\mathbf{u}^{\mathrm{r}}, \mathbf{u}^{\mathrm{s}}) + s(\mathbf{u}^{\mathrm{s}}, \mathbf{u}^{\mathrm{r}})] + s(\mathbf{u}^{\mathrm{s}}, \mathbf{u}^{\mathrm{s}}). \tag{1.27}$$

The first term (called the Leonard term; Leonard 1974) represents purely filtered stresses, while the middle two terms (the cross, or Clark, terms) capture nonlinear interactions between the filtered and subfilter momenta, and the final term (named the Reynolds term after Reynolds 1895) represents the purely subfilter stresses.

So, how do we close the equation set? Well, the unknown terms (generally $s(\varphi, \psi)$ for flow variables φ, ψ) must be replaced by a representation in terms of only filtered variables: $s(\varphi, \psi) \to f(\{\chi_\alpha^{\mathrm{r}}\})$, where $\{\chi_\alpha^{\mathrm{r}}\}$ denotes the set of all filtered variables. To do this we need to decide what the filter is representing, and therefore what assumptions and deductions we can make about the unknown terms.

1.2.2 The statistical (or RANS) approach

The traditional way of thinking about turbulence modelling is the "Reynolds averaging" approach, introduced by Reynolds (1895). A Reynolds averaging operator is a linear filtering operator[9], $\langle \ldots \rangle_{\mathrm{R}}$, which satisfies also the following "Reynolds condition":

$$\langle \varphi \langle \psi \rangle_{\mathrm{R}} \rangle_{\mathrm{R}} = \langle \varphi \rangle_{\mathrm{R}} \langle \psi \rangle_{\mathrm{R}} \tag{1.28}$$

$$\implies \langle \langle \varphi \rangle_{\mathrm{R}} \rangle_{\mathrm{R}} = \langle \varphi \rangle_{\mathrm{R}}, \quad \langle \langle \varphi \rangle_{\mathrm{R}} - \varphi \rangle_{\mathrm{R}} = 0, \tag{1.29}$$

that is, the Reynolds averaging operator projects the flow onto a sub-space of the solution phase space which is invariant under whatever group action the operator is averaging along. As a specific example, if the average is a time average, the corresponding Reynolds operator projects onto a time-invariant — or "stationary" — sub-space (and so, Reynolds average flows constructed based on time averages *cannot* have time dependence — see e.g. Tennekes and Lumley 1972, p.28). Similar must be true if the average is a spatial average: the corresponding Reynolds operator then projects onto a spatially-invariant — or "homogeneous" — sub-space, meaning that the spatially Reynolds-averaged flow cannot have any spatial dependence. An important corollary of this definition is that the Leonard term and Clark terms of Equation 1.27 are identically zero — i.e. only the Reynolds term is nonzero.

Reynolds used both spatial and temporal averages in his original paper (Reynolds 1895, respectively equation (4) and the first non-numbered equation after (8A)), but explicitly assumed the Reynolds conditions above, which are not generally true for such averages. Therefore in a modern theoretical context a statistical *ensemble* average is usually understood: that is, an average over a large number of independent realizations of the flow. For ensemble averages, the Reynolds properties are automatically satisfied. In practice, ensemble averages which actually converge are rarely used; numerical simulations of turbulence are too computationally expensive to run enough for the ensemble average to converge, and the use of ensembles of independent flows with identical initial conditions is clearly impossible for atmospheric observations. Instead time- and/or spatial averages are used, which tend towards the ensemble average given suitably large times/length scales (and assumptions of ergodicity; see Wyngaard 2010, § 2.3)[10].

[9] Note that the operator need not *necessarily* commute with space and time translations, and therefore space/time partial derivatives, though Reynolds operators in fluid dynamics are usually assumed to commute with either Eulerian or Lagrangian translations.

[10] Note that an ensemble average does not, in general, mean a smooth parametrized flow when applied in a spatially *in*homogeneous framework — for instance an urban area. The RANS flow may well have discontinuities, so further spatial filtering may be necessary, leading to dispersive fluxes.

Clearly the Reynolds averaging (often abbreviated to RANS: "Reynolds-averaged Navier-Stokes") approach cannot apply literally to modelling of the atmosphere: the problem is neither homogeneous, nor stationary, and we have only one Earth. However, under assumptions of approximate stationarity or homogeneity over large enough length and time scales for the problem at hand, approximate RANS methods can be applied. Such arguments are central to our understanding of the atmospheric boundary layer, and are very often used in its parametrization (Garratt 1994; Stull 1988, Wyngaard 2010, Part II). However, RANS arguments can only be applied on large enough space and time scales — for smaller scales, those on which we humans live day-to-day, for which we would like to predict the weather, they cannot even approximately be applied without leading to errors.

1.2.3 The LES approach

An alternative approach to the modelling of turbulence is that of "large eddy simulation", which does what the name suggests: LES aims to explicitly represent the large, energy-containing scales of a turbulent flow, and focus computational (and/or analytical) efforts on these, while modelling the effects of the smaller-scale motions which contain less energy. This partition of the flow into large-scale and small-scale parts is performed by a spatial filtering operation:

Definition 6 (Spatial filter)**.** For a flow variable $\varphi(\mathbf{x}, t)$ we define the operation of **spatial filtering** by:

$$\langle\varphi\rangle_g \coloneqq \int_{\mathbb{R}^d} g(\mathbf{x}-\mathbf{x}';\boldsymbol{\delta})\varphi(\mathbf{x}',t)\,\mathrm{d}^d\mathbf{x}', \tag{1.30}$$

where $g(\mathbf{x}-\mathbf{x}';\boldsymbol{\delta})$ is a **filter kernel** satisfying the normalization condition:

$$\int_{\mathbb{R}^d} g(\mathbf{x}-\mathbf{x}';\boldsymbol{\delta})\,\mathrm{d}^d\mathbf{x}' = 1. \tag{1.31}$$

$\langle\ldots\rangle_g$ is read as "filtering with respect to the kernel g". We also require that the filter kernel guarantees the following properties (Berselli et al. 2006):

$$\lim_{|\boldsymbol{\delta}|\to 0}\langle\varphi\rangle = \varphi, \tag{1.32}$$

$$\|\langle\varphi\rangle\| \le C\|\varphi\| \quad \text{(uniformly in } |\boldsymbol{\delta}|), \tag{1.33}$$

which can be interpreted simply as requiring that it is "well-behaved".

All such filters are linear by the definition in equation (1.19); in the absence of boundaries, and for filter widths $\boldsymbol{\delta}$ which do not depend on space or time, such

filters also commute with space and time derivatives, equation (1.18). So long as the filter kernel has a strong decay in wavenumber space above some wavenumber k_c — which is true for the commonly-used spectral cutoff and Gaussian filter kernels[11] — this filtering can be seen to split the flow into "large scale" variations with $k \lesssim k_c$, represented by φ^{r}, and "small scale" variations with $k \gtrsim k_c$, represented by φ^{s}.

Within the cascade picture provided by Richardson (qualitatively; see Richardson 1922, p. 66) and Kolmogorov (quantitatively; see Kolmogorov 1941), so long as the filter scale is smaller than the scale(s) of energy injection, the closure problem translates to trying to model the effects of the less-energetic small scales on the much more energetic large scales, which seems hopeful even if not necessarily mathematically well-posed.

This also bears a direct relevance to the situation in atmospheric modelling: we use the smallest grid spacing that the available computational resources allow, in order to resolve as much of the flow as possible. However, the real flow still varies *considerably* on length scales comparable to a model grid box (Δx); as such, it must be filtered in order to produce a field which varies smoothly and slowly on scales $\sim \Delta x$. We are then tasked with coming up with a good representation of the interactions between the large- and small-scale flows, such that the final model well approximates reality. In its simplest form, this is done all the time in atmospheric models: artificial diffusion is added to stabilize the numerical integration, acting effectively as a crude subfilter model. From this point of view, effectively all numerical atmospheric modelling can be viewed as LES: Cullen and Brown (2009) argue that all numerical models of the atmosphere, from high resolution research models through to long-term climate projections, are effectively large eddy simulations of some form or other. This may be true in the sense that Reynolds averaging never strictly applies on any scale of the atmosphere, but it clearly is not true if we understand LES in the narrower sense that the filter scale must be in the inertial subrange *of the process you are modelling the subfilter-scale effects of.*

It is in this narrower sense that LES is usually understood (Mason 1994), because in practice the assumptions used to build subfilter models for LES tend to rely on results valid only in the inertial subrange of the flow. This allows the various well-established[12] results of K41 to be used to interpret terms in the budgets

[11] As the name implies, the spectral cutoff filter sharply splits the flow into a part with wavenumbers strictly$> k_c$ and a part with wavenumbers strictly $< k_c$; for other filters there is some overlap. For example, for the Gaussian filter (which is its own Fourier transform, and can therefore be considered an eigenfunction of the Fourier transform operator), the overlap region in frequency space, though technically infinite, is mostly confined to a region $\sim 1/|\boldsymbol{\delta}|$.

[12] Decades of both experimental and numerical results support the basic validity of K41 (i.e. universality of the energy spectrum, with $E(k) \propto k^{-5/3}$) for 3D flows, far enough removed from boundaries, at high enough Reynolds number; see for instance Figure 2.4 of McComb (1990). In addition, the standard K41 results have now been derived asymptotically in the limit of infinite

for subfilter quantities, and in some cases even to perform explicit calculations. For instance, many (most?) LES closures assume that, for a filter scale situated well within the inertial subrange of the flow, the main effect of the subfilter motions is dissipative — allowing their effects to be modelled by an eddy viscosity, i.e. $s(\mathbf{u},\mathbf{u}) \to \nu_t \left(\boldsymbol{\nabla}\mathbf{u}^{\mathrm{r}} + (\boldsymbol{\nabla}\mathbf{u}^{\mathrm{r}})^{\mathsf{T}}\right)$. Lilly (1962) derived a closure by assuming that transport terms (i.e. terms which can be written inside a divergence) in the evolution equation for the subfilter stress $s(\mathbf{u},\mathbf{u})$ are *locally* negligible, that the production terms due to tilting — i.e. reorientation of the stress tensor — are also negligible, and that the destruction of the subfilter stress by pressure is simply proportional to the stress itself divided by some timescale. Then the subfilter stress is proportional to the resolved strain, with proportionality factor ("eddy viscosity") given by a characteristic turbulent velocity scale (the square root of the turbulent kinetic energy) and a characteristic mixing length. Lilly (1966) used Smagorinsky (1963)'s formulation to close the eddy viscosity, and then calculated the remaining dimensionless constant by requiring that the filter scale be within an inertial subrange obeying the K41 theory.

Smagorinsky-Lilly subfilter schemes have been very widely used in LES, particularly in the atmospheric sciences (potentially with extensions to better account for buoyancy; Mason and Brown 1999). Significantly more complex models do exist, for instance based on assumed probability distributions (e.g. the eddy-damped quasi-normal Markovian model; Mason 1994), wave number asymptotics (e.g. the "Rational LES" model; Berselli et al. 2006, chapter 7), or on some assumptions of scale similarity (e.g. the dynamic LES first proposed by Germano et al. 1991 in the Smagorinsky-Lilly context; see Berselli et al. 2006, chapter 8 for an overview of more recent attempts). In practice, it has been found that, if the LES is well-converged (i.e. if the filter scale really is well-within the inertial subrange), there is little sensitivity to the specific subfilter model used (e.g. Mason and Brown 1994) — but this cannot be expected for larger filter scales where self-similarity does not apply. This is because all of these attempts either explicitly or implicitly work only when the filter scale is greatly separated from the energy-injection scale: $\Delta_{\mathrm{f}} \ll \ell_0$. This is emphatically not the case in current weather and climate modelling, and hence traditional LES approaches cannot be expected to work at these scales. In particular, we would expect to see greater importance of the Leonard and cross terms at intermediate scales — the localness of interactions in scale space cannot be assumed outside of the inertial subrange.

Reynolds number directly from the Navier-Stokes equations, assuming only the finiteness of the kinetic dissipation as $\nu \to 0$ (Lundgren 2003).

1.2.4 The grey zone; why traditional approaches do not work here

In the preceding two subsections we have outlined two broad approaches to the modelling of turbulent flow: the Reynolds-averaging approach, and the large-eddy simulation approach. Within the context of spatial filtering, for a RANS approach to be valid, we require the filter scale $\Delta_\mathrm{f} \gg \ell_\mathrm{L}$, the largest length scale in the flow; while in the LES limit, we require instead $\Delta_\mathrm{f} \ll \ell_0$, the smallest energy injection scale in the flow. In between these two limits there is a range of scales for which we have not yet developed adequate parametrization techniques: scales on which neither the assumptions underlying statistical equilibrium approaches, nor the assumptions underlying LES, are valid. This vast gulf is called the "grey zone" or "terra incognita" (Wyngaard 2004) in the convection and boundary layer parametrization literatures.

In section 3 of Cullen and Brown (2009), the authors present convection as a specific example of a process that is currently completely statistically parametrized (i.e. using RANS-like arguments) in climate models, but would require grid lengths $\mathcal{O}(1\text{ m})$ in order to be fully resolved. Thus new parametrization techniques which are different from both statistical closures and traditional LES techniques must be developed.

Based on the arguments in the preceding sections, what sort of problems do we expect to encounter in the grey zone with inadequate parametrizations? Firstly, there is the possibility of double-counting: a RANS-based parametrization assumes all vertical fluxes are subfilter, but now some of these will be resolved. A standard LES closure might be too dissipative, since the Leonard and cross terms, and processes nonlocal in both scale and physical space are likely to be more important in the grey zone.

Another problem in the grey zone relates directly to the length scales of convection. B. Zhou et al. (2014) argued (based on Rayleigh-Bénard convection) that if a grid is too coarse to resolve the critical wavelength of a convection problem, structure will instead form at the grid scale if the subfilter feedback is not correctly accounted for. Beare (2014) noted a related problem, in that if the dissipation length scale of the flow (a multiple of the grid spacing) becomes similar to the dominant energy containing length scale, structures tend to develop on scales which are too large.

There are two more fundamental barriers to progress in the grey zone, however. Firstly, traditional atmospheric (RANS-based) parametrizations of atmospheric processes rely on assumptions of horizontal homogeneity, statistical stationarity, or (more often) both. This makes the parametrizations intrinsically 1D and time-independent. Clearly both assumptions must be relaxed in the grey zone, but that

fundamentally changes the nature of the parametrizations — atmospheric RANS-based schemes carry no information about the horizontal fluxes or memory terms which are required to relax the assumptions. A second fundamental problem is that grey zone schemes must in principle be stochastic; this will be discussed further in Section 1.3.2.

In the next section we will examine the formulation of traditional convection parametrizations, showing them to rely fundamentally on assumptions which are not valid at grey zone resolutions. We will then look at what actually goes wrong in convection parametrizations run at grey zone resolutions.

1.3 Parametrization of atmospheric convection

The general problem of convection parametrization is to estimate the contribution to the subfilter flux $s(\mathbf{u}, \varphi)$ from convection in the evolution equation for a flow variable φ:

$$\frac{\partial \langle \varphi \rangle}{\partial t} + \boldsymbol{\nabla} \cdot (\langle \mathbf{u} \rangle \langle \varphi \rangle) = -\boldsymbol{\nabla} \cdot s(\mathbf{u}, \varphi) + \langle S_\varphi \rangle \,, \tag{1.34}$$

where S_φ denotes sources and sinks of φ. For simplicity and conceptual clarity, we again consider the flow to be incompressible, such that we need not worry about the density. This foreshadows the introduction of the Boussinesq approximation in Chapter 2, which is the framework we shall work within for the remainder of the thesis.

1.3.1 Traditional parametrizations

The original reason convection schemes were required was in order to stabilize numerical models (Manabe et al. 1965). Unstable profiles of potential temperature close to the surface of the Earth led to convection occurring at the grid scale, which is unrealistic and caused numerical instabilities. (The simplest "parametrization" of any subfilter flux is simply to assume it can be neglected; clearly this was not the case for those early global models.) Therefore some sort of representation of subfilter convective processes was required. The simplest thing to do is to notice that convection acts to remove instability; therefore (Manabe et al. 1965) parametrized the effect of moist convection on the resolved motions as a relaxation of temperature and humidity variables to ensure a neutrally buoyant, saturated profile.Other early ideas to tame the convective instability were put forward by tropical cyclone modellers, using large-scale moisture convergence to parametrize cumulus heating (e.g. Charney and Eliassen 1964; Kuo 1965). A few years later, Ooyama (1971) and

Arakawa and Schubert (1974) introduced the mass flux approach which remains the basis for most operational convection schemes, as well as framing much of the conceptual thinking around convection parametrization.

From a suitably general perspective, all three classes of traditional schemes — adjustment, moisture convergence, and mass flux — can be seen as one type of closure, as they rely on similar assumptions. In particular, all three approaches rely fundamentally on an approximate equilibrium between large-scale forcing and small-scale convection, an idea which came to be known as "convective quasi-equilibrium". Therefore in this section we will investigate the mass flux–type formulation in detail, since this is the most widely used; at the end of the explanation, we will sketch how the other two types of scheme fit within the same framework.

Structure of traditional mass flux schemes

Mass flux-type parametrizations begin with a partitioning of the flow into convection and its environment; indeed, many researchers strongly associate the term "mass flux" with this conceptual partition. To do so, variables are decomposed into their values within convective elements, denoted by a subscript c, and within the environment, denoted by a subscript e. Filtering a variable φ then returns $\langle\varphi\rangle = \sigma_\mathrm{c} \langle\varphi\rangle_\mathrm{c} + \sigma_\mathrm{e} \langle\varphi\rangle_\mathrm{e}$, where σ_c and σ_e are the fraction of the filter volume occupied respectively by convection and environment[13]. Traditionally the filter is an area average, and so σ_c is the convective area fraction. Applying this decomposition to the subfilter flux $s(\mathbf{u}, \varphi)$, we find:

$$\begin{aligned} s(\mathbf{u},\varphi) &\coloneqq \langle\mathbf{u}\varphi\rangle - \langle\mathbf{u}\rangle\langle\varphi\rangle \\ &= \sigma_\mathrm{c}\langle\mathbf{u}\varphi\rangle_\mathrm{c} + \sigma_\mathrm{e}\langle\mathbf{u}\varphi\rangle_\mathrm{e} - (\sigma_\mathrm{c}\langle\mathbf{u}\rangle_\mathrm{c} + \sigma_\mathrm{e}\langle\mathbf{u}\rangle_\mathrm{e})(\sigma_\mathrm{c}\langle\varphi\rangle_\mathrm{c} + \sigma_\mathrm{e}\langle\varphi\rangle_\mathrm{e}) \\ &= \sigma_\mathrm{c}\langle\mathbf{u}\varphi\rangle_\mathrm{c} - \sigma_\mathrm{c}^2\langle\mathbf{u}\rangle_\mathrm{c}\langle\varphi\rangle_\mathrm{c} + \sigma_\mathrm{e}\langle\mathbf{u}\varphi\rangle_\mathrm{e} - \sigma_\mathrm{e}^2\langle\mathbf{u}\rangle_\mathrm{e}\langle\varphi\rangle_\mathrm{e} \\ &\qquad - \sigma_\mathrm{c}\sigma_\mathrm{e}(\langle\mathbf{u}\rangle_\mathrm{c}\langle\varphi\rangle_\mathrm{e} + \langle\mathbf{u}\rangle_\mathrm{e}\langle\varphi\rangle_\mathrm{c}). \end{aligned}$$

The first four terms on the right hand side *almost* look like subfilter fluxes within the convection and environment partitions; such a term would look like $s_\mathrm{c}(\mathbf{u},\varphi) \coloneqq \langle\mathbf{u}\varphi\rangle_\mathrm{c} - \langle\mathbf{u}\rangle_\mathrm{c}\langle\varphi\rangle_\mathrm{c}$ for the subfilter flux of φ within the convective elements. Inspired by this, we can use that $\sigma_\mathrm{c} = 1 - \sigma_\mathrm{e}$ (and vice versa) to rewrite the second and

[13]The convective part of this is sometimes further split into contributions from lots of different convective elements, $\sigma_\mathrm{c}\langle\chi\rangle_\mathrm{c} = \sum_i \sigma_{\mathrm{c},i}\langle\chi\rangle_{\mathrm{c},i}$; this introduces only minor differences to the present derivation. If decomposed in this way, the resulting scheme is usually called "spectral" after Arakawa and Schubert (1974).

fourth terms on the right hand side in a more useful way:

$$\begin{aligned} s(\mathbf{u},\varphi) &= \sigma_\mathrm{c}\left\langle \mathbf{u}\varphi\right\rangle_\mathrm{c} - \sigma_\mathrm{c}\left\langle \mathbf{u}\right\rangle_\mathrm{c}\left\langle \varphi\right\rangle_\mathrm{c} + \sigma_\mathrm{e}\left\langle \mathbf{u}\varphi\right\rangle_\mathrm{e} - \sigma_\mathrm{e}\left\langle \mathbf{u}\right\rangle_\mathrm{e}\left\langle \varphi\right\rangle_\mathrm{e} \\ &\qquad + \sigma_\mathrm{c}\sigma_\mathrm{e}\left(\left\langle \mathbf{u}\right\rangle_\mathrm{c}\left\langle \varphi\right\rangle_\mathrm{c} + \left\langle \mathbf{u}\right\rangle_\mathrm{e}\left\langle \varphi\right\rangle_\mathrm{e} - \left\langle \mathbf{u}\right\rangle_\mathrm{c}\left\langle \varphi\right\rangle_\mathrm{e} - \left\langle \mathbf{u}\right\rangle_\mathrm{e}\left\langle \varphi\right\rangle_\mathrm{c}\right) \\ &= s_\mathrm{c}(\mathbf{u},\varphi) + s_\mathrm{e}(\mathbf{u},\varphi) + \sigma_\mathrm{c}\sigma_\mathrm{e}\left(\left\langle \mathbf{u}\right\rangle_\mathrm{c} - \left\langle \mathbf{u}\right\rangle_\mathrm{e}\right)\left(\left\langle \varphi\right\rangle_\mathrm{c} - \left\langle \varphi\right\rangle_\mathrm{e}\right). \end{aligned} \tag{1.35}$$

This exact relation states that the subfilter flux of φ may be decomposed into contributions from the subfilter flux within the convective elements (the first term), the subfilter flux within their environment (the second term), and the *resolved* flux due to the difference between the filtered flow variables within the convection and the environment (the third term). The form suggests the identification of the final term with *coherent structures*, and the first two terms with *internal variability*. To our knowledge, this relation first appeared in Siebesma and Cuijpers (1995, their Equation 4.1) to define convective coherent structures ("organized turbulence") and their environment[14].

We take the view that this decomposition of the subfilter flux is the fundamental starting point for mass flux-type convection parametrizations. This is true both for the original pioneering formulations, as well as more modern developments. We shall now take the time to examine the traditional formulations in some detail.

The original mass flux formulations introduced by Arakawa and Schubert (1974) and Ooyama (1971) make use of a few fundamental assumptions about how convection operates:

1. Convection is assumed to be in a horizontally homogeneous quasi-equilibrium with the large-scale forcing (called the "convective quasi-equilibrium" [CQE] assumption). The equilibrium can be interpreted as thermodynamical or dynamical; see Yano and Plant (2012) for a discussion. Horizontal homogeneity is required such that area averages tend to ensemble averages for very large area; thus we are firmly in the Reynolds-averaging regime. Note that this means that closures based on this assumption (or similar RANS-regime assumptions) are *fundamentally one-dimensional*.

2. It is assumed that the subfilter variability within the convective components, and within the environment, is negligible. This is known to most as the "top hat" assumption, but has also been termed the "segmentally constant approximation" by Yano (2014), where convective elements and the environment are

[14] Siebesma and Cuijpers (1995) present the result for a Reynolds operator acting in the horizontal direction only. Our result is a straightforward generalization to an arbitrary linear filtering operator; it is intriguing that it takes precisely the same form, which appears to be an extension of Germano (1992)'s "averaging invariance". See Appendix B.3 for a proof of the general case of n partitions.

denoted "segments".

3. It is assumed that the area taken up by convection, σ_c, is very small compared to the area *not* taken up by convection, σ_e (called the "small/vanishing area fraction" assumption).

Before discussing the validity of these assumptions, let us see where they take us.

From horizontal homogeneity, only the vertical part of $\boldsymbol{\nabla}\cdot s(\mathbf{u},\varphi) = \partial s(w,\varphi)/\partial z$ is nonzero, so we need only consider $s(w,\varphi)$ in the following. Using (1.35), the vertical part of the subfilter flux of variable φ is:

$$s(w,\varphi) = s_c(w,\varphi) + s_e(w,\varphi) + \sigma_c\sigma_e\left(\langle w\rangle_c - \langle w\rangle_e\right)\left(\langle\varphi\rangle_c - \langle\varphi\rangle_e\right) \tag{1.36}$$

Using Assumption 2, we neglect the internal variability, dropping the first two terms on the right hand side. Additionally, horizontal homogeneity means that the total filtered vertical velocity must be zero (a consequence of the continuity equation and the no-normal flow condition at the surface): $\langle w\rangle = \sigma_c\langle w\rangle_c + \sigma_e\langle w\rangle_e = 0$. Therefore the environmental vertical velocity may everywhere be replaced by $\langle w\rangle_e = -\frac{\sigma_c}{(1-\sigma_c)}\langle w\rangle_c = -(\sigma_c + \mathcal{O}(\sigma_c^2))\langle w\rangle_c$:

$$s(w,\varphi) \approx \sigma_c\langle w\rangle_c\left(\langle\varphi\rangle_c - \langle\varphi\rangle\right) + \mathcal{O}(\sigma_c^2), \tag{1.37}$$

so long as $|\langle\varphi\rangle_c - \langle\varphi\rangle|/|\langle\varphi\rangle| > \mathcal{O}(\sigma_c)$ (i.e. we expect there to be appreciable differences between the average value of a variable, and its average value within convective elements). Invoking Assumption 3 ($\sigma_c \ll 1$) now allows the $\mathcal{O}(\sigma_c^2)$ terms to be neglected.

Defining the convective "mass flux" through unit area by $M_c \coloneqq \sigma_c\langle w\rangle_c$ (standard formulations include the density, but this is not necessary within our Boussinesq context; this means that our "mass flux" is actually the "mass flux through unit area *per unit mass*"), the final expression for the convective contribution to the subfilter flux becomes:

$$s(w,\varphi) \approx M_c\left(\langle\varphi\rangle_c - \langle\varphi\rangle\right), \tag{1.38}$$

correct to order σ_c given our assumptions of horizontal homogeneity and negligible variability within either the convection or environment. This reduces the evolution equation for $\langle\varphi\rangle$ to:

$$\frac{\partial\langle\varphi\rangle}{\partial t} + \boldsymbol{\nabla}\cdot\left(\langle\mathbf{u}\rangle\langle\varphi\rangle\right) = -\frac{\partial}{\partial z}\left(M_c(\langle\varphi\rangle_c - \langle\varphi\rangle)\right) + \langle S_\varphi\rangle\,. \tag{1.39}$$

Therefore, within the (traditional) mass flux approximation, the closures required are a) finding the form of $M_c(z)$, and b) finding the values of variables within the clouds, $\langle\varphi\rangle_c$. The former is usually done by first considering the evolution equation for the volume fraction of convection, σ_c[15]:

$$\frac{\partial\sigma_c}{\partial t} + \frac{\partial M_c}{\partial z} = E - D, \tag{1.40}$$

where E denotes sources of area fraction, and is called "entrainment"; while D denotes sinks of area fraction, and is called "detrainment". The use of these terms hints at the historical development of cumulus parametrization by analogy with entraining plumes, a frequent topic of study in early- to mid-20$^{\text{th}}$ century fluid dynamics (reviewed in, for instance, Emanuel 1994, chapter 2; Kaye 2008).

Environmental variables can be recovered from:

$$\langle\varphi\rangle = \sigma_c \langle\varphi\rangle_c + \sigma_e \langle\varphi\rangle_e \tag{1.41}$$

$$\implies \langle\varphi\rangle_e = \frac{(\langle\varphi\rangle - \sigma_c \langle\varphi\rangle_c)}{(1-\sigma_c)} \tag{1.42}$$

$$= \langle\varphi\rangle + \mathcal{O}(\sigma_c), \tag{1.43}$$

so we may replace $\langle\varphi\rangle_c \to \langle\varphi\rangle$ to leading order. This allows the corresponding budget equation for variable φ within the convecting area to be written as:

$$\frac{\partial\sigma_c \langle\varphi\rangle_c}{\partial t} + \frac{\partial M_c \langle\varphi\rangle_c}{\partial z} = E\langle\varphi\rangle - D\langle\varphi\rangle_c + \sigma_c \langle S_\varphi\rangle_c, \tag{1.44}$$

where $\langle\varphi\rangle_e$ has been replaced by $\langle\varphi\rangle$ in the entrainment term. The relatively simple form of the entrainment and detrainment terms on the right hand side is a direct consequence of Assumption 2, that there is negligible variability *within* either convecting or environmental areas. The non-conservative source term is written as $\sigma_c \langle S_\varphi\rangle_c$ so that $\langle S_\varphi\rangle = \sigma_c \langle S_\varphi\rangle_c + \sigma_e \langle S_\varphi\rangle_e$.

The time derivative of the area fraction of convection may be neglected due to the quasi-equilibrium assumption. This can be seen by scaling the two terms on the left hand side: $\partial M_c/\partial z \sim \sigma W/H$, where σ is a characteristic convective area fraction, W is a characteristic convective velocity scale, and H is the characteristic height of a cloud; $\partial\sigma_c/\partial t \sim \sigma/T$. Since the convection is assumed to be in quasi-equilibrium with the large scale forcing, the convective timescale must be much less than the time-scale of change in the forcing: $T_W = H/W \ll T$. This means there must be a separation of time scales between the convection and the large-scale forcing in

[15]Similar equations are effectively plucked out of thin air in Arakawa and Schubert (1974) (their eqs. 10 and 43-50), though they may be derived by considerations of indicator functions for the various flow partitions, as will be shown extensively in Chapter 3.

order for quasi-equilibrium to hold. Assuming this is true, we now have a diagnostic equation for the mass flux:

$$\frac{\partial M_c}{\partial z} = E - D \tag{1.45}$$

$$\frac{1}{M_c}\frac{\partial M_c}{\partial z} = \varepsilon - \delta, \tag{1.46}$$

where in the second line we have divided through by M_c to give the commonly-used formulation in terms of *fractional* entrainment and detrainment rates, respectively $\varepsilon \coloneqq E/M_c, \delta \coloneqq D/M_c$.

At this point a separation of variables is usually performed[16], writing

$$M_c = M_{c,0}(t)m(z). \tag{1.47}$$

Here $M_{c,0}(t)$ depends entirely on the large-scale forcing and sets the amplitude of convection, while the dimensionless function $m(z)$ specifies the shape of the mass flux profile. Equation (1.46) may thus be used to determine the shape of the mass flux profile by specifying the fractional entrainment and detrainment rates. A separate closure must be provided for $M_{c,0}(t)$ (which is often termed "*the* closure" in mass flux convection parametrization). Traditionally $M_{c,0}(t)$ is chosen to be the mass flux at cloud base, and is therefore usually called the "cloud-base mass flux". Note that it is only in providing the magnitude of the mass flux that the time-dependence of the large-scale forcing can enter directly.

Assuming $\langle S_\varphi \rangle$ may be neglected — which occurs either when φ is genuinely conserved (this is a good reason to formulate the model in terms of cloud-conserved variables), or when the non-conservative term acts on much slower timescales than the convection — then equation (1.44) reduces to:

$$\frac{\partial M_\mathrm{c} \langle \varphi \rangle_\mathrm{c}}{\partial z} = E \langle \varphi \rangle - D \langle \varphi \rangle_\mathrm{c} . \tag{1.48}$$

E and D are known from parametrizing equation (1.46), which also specifies M_c, while $\langle \varphi \rangle$ is one of the primitive filter-scale variables and therefore known. Thus in the absence of convective-scale forcing, parametrizing the mass flux equation (1.46) entirely determines all of the unknowns. This shows the power of the mass flux approach (assuming the validity of its underlying assumptions): once it is parametrized, all of the other unknowns can be determined.

Using the diagnostic relations for M_c and $\langle \varphi \rangle_\mathrm{c}$, we can simplify the equation for

[16]It is worth noting that this separation is not always valid (Yano 2014, §7.7); it is a form of the so-called "entrainment hypothesis" introduced by Ooyama (1971), and effectively assumes that the entrainment and detrainment rates are not directly dependent on the slowly-varying large-scale forcing.

$\langle\varphi\rangle$:

$$\begin{aligned}\frac{\partial\langle\varphi\rangle}{\partial t}+\boldsymbol{\nabla}\cdot(\langle\mathbf{u}\rangle\langle\varphi\rangle) &= -\frac{\partial M_{\mathrm{c}}\langle\varphi\rangle_{\mathrm{c}}}{\partial z}+M_{\mathrm{c}}\frac{\partial\langle\varphi\rangle}{\partial z}+\langle\varphi\rangle\frac{\partial M_{\mathrm{c}}}{\partial z}+\langle S_\varphi\rangle \\ &= D\langle\varphi\rangle_{\mathrm{c}}-E\langle\varphi\rangle-\sigma_{\mathrm{c}}\langle S_\varphi\rangle_{\mathrm{c}}+M_{\mathrm{c}}\frac{\partial\langle\varphi\rangle}{\partial z}+\langle\varphi\rangle(E-D)+\langle S_\varphi\rangle \\ &= D(\langle\varphi\rangle_{\mathrm{c}}-\langle\varphi\rangle)+M_{\mathrm{c}}\frac{\partial\langle\varphi\rangle}{\partial z}+\langle S_\varphi\rangle-\sigma_{\mathrm{c}}\langle S_\varphi\rangle_{\mathrm{c}}\,. \qquad (1.49)\end{aligned}$$

Assuming $\langle S_\varphi\rangle$ and $\langle S_\varphi\rangle_{\mathrm{c}}$ are the same order, the dependence on the non-conservative source within the cloud is negligible, and the equation set is now closed.

Convection parametrization within the traditional mass flux framework thus consists of the following three steps:

1. Determine whether convection is likely. If it is likely, then the convective part of the subfilter flux must be accounted for (this is called "triggering" of the convection scheme, but is really just a diagnosis of convective instability).
2. Provide the shape of the vertical profile of the mass flux, $m(z)$. This is usually done indirectly by specifying the entrainment and detrainment. The vertical profile is often called the "cloud model".
3. Provide the magnitude of the mass flux, $M_{c,0}(t)$, usually at the cloud base (dependent on the large-scale forcing). This is often called the "closure".

Examples of traditional schemes

Before giving a brief overview of some traditional mass flux schemes, let us remark that both closures and triggering mechanisms are very often based on some form of the potential energy available to convection, which is some measure of the nonlinear instability (c.f. Section 1.1.3). This includes the "cloud work function" introduced by Arakawa and Schubert (1974), as well as various forms of estimated convective available potential energy (CAPE), which is usually easier to calculate.

- The Gregory and Rowntree scheme (Gregory and Rowntree 1990) is a bulk mass flux scheme. It is used (in modified form) in the regional and global NWP and climate configurations of the Met Office Unified Model (MetUM). Entrainment and detrainment closures considered are for an ensemble of entraining plume models, summed over to give a bulk scheme. The mass flux closure is *local*: "the initial convective mass flux [is] proportional to the parcel's initial buoyancy on ascent". The authors say "This approach is different from the assumption that a quasi-equilibrium exists" (p.1489); while this is true of the closure for the cloud-base mass flux, quasi-equilibrium is still required to derive the stationary, homogeneous mass flux equations in the first

place, so the scheme still implicitly depends on CQE. Originally, function was also local and buoyancy-based: is a parcel at some vertical level with excess buoyancy greater than a critical threshold, still excessively buoyant by more than a second (lower) critical threshold at the next vertical level? However, the currently operational MetUM scheme uses a trigger function based on CAPE estimated via parcel ascent.

- The Kain and Fritsch scheme (Fritsch and Chappell 1980; Kain and Fritsch 1990, 1993) is a mass flux scheme which includes heating from cloud, a "*two-way* exchange of mass between clouds and their environment". Entrainment and detrainment closures are provided by a plume model based on "buoyancy sorting" (detrainment of air parcels which become negatively buoyant due to the mixing of convecting and environmental air). The trigger function is a step function on the(grid-scale) vertical velocity above some threshold vertical velocitycalculated via a parcel ascent. The cloud base mass flux is closed via an estimated CAPE.This parametrization is available (in modified form) in the Weather Research and Forecasting model (WRF) developed by the United States National Center for Atmospheric Research (NCAR) and National Oceangraphic and Atmospheric Administration (NOAA). A very similar trigger function is used in the European Centre for Medium Range Weather Forecasts' (ECMWF) operational Integrated Forecast System (IFS); however the cloud model and closure in the IFS are based on Tiedtke (1989) with subsequent modifications ("IFS Documentation CY47R3 - Part IV Physical processes" 2021, Chapter 6).
- In the Kuo scheme (Kuo 1965), a "moisture convergence" scheme, convective heating is assumed to be proportional to large scale moisture convergence. Entrainment and detrainment are not considered; moisture convergence is used as the "closure", and a profile of the heating which is the equivalent of the "mass flux profile" $m(z)$. This scheme is often criticized for assuming that convection consumes moisture rather than potential energy; it can lead to unrealistic feedbacks because of this (Emanuel 1994).
- The Betts and Miller scheme (Betts 1986; Betts and Miller 1986) is a convective adjustment scheme. The trigger function is based on the instability of a parcel ascent in the current atmospheric profile. If so, profiles of temperature and moisture are adjusted to reference profiles over some timescale which must be specified.These reference profiles perform a conceptually similar role to the heating profile in a moisture convergence scheme, and to the mass flux profile in a mass flux scheme. The adjustment timescale then provides the "closure" for the scheme. A modified version of the Betts-Miller scheme is still in use as

part of NOAA's North American Mesoscale model (based on WRF).

Thus adjustment, moisture convergence, and mass flux closures can all be regarded as versions of the same idea: assume convection is in horizontally-homogeneous quasi-equilibrium with a large-scale forcing. (Conceptual differences between the three families of schemes arise in the nature of the assumed quasi-equilibrium.) Then follow the same three steps as for a mass flux scheme, but modify steps 2 and 3 to: "provide the vertical profile of heating/moistening/mass flux", and "provide the closure (cloud-base mass flux, convection/relaxation time scale, large-scale moisture convergence etc.)".

Validity of mass flux assumptions

Having presented a sketch of the derivation of the traditional (bulk) mass flux formulation, we are in a position to see why it has been so widely used, and also why it has been so hard to move beyond. First and foremost, the entire edifice of mass flux relies on the assumptions of horizontally-homogeneous quasi-equilibrium (requiring a temporal scale-separation between the forcing and the convection). These are what allow such a simple formulation to drop out, a formulation where all that matters is the mass flux profile. But this explicitly prohibits horizontal and temporal variation of the convective response on scales smaller/faster than that dictated by variation of the large-scale forcing. This means that convective memory, horizontal transport of convection, and net vertical mass flux, are all directly prohibited in a traditional mass flux formulation, by the overarching quasi-equilibrium assumption.

On large spatial and temporal scales, quasi-equilibrium is approximately maintained in the tropics (Emanuel 1994; Vallis 2017) (though this is not accepted by all researchers: there are some who entirely question the validity of CQE, see § 5 of Yano and Plant 2012). On much smaller scales, commensurate with the grid spacings of current climate ($\sim$ 25 km) and weather ($\sim$ 1 km) models, there is no doubt that convective quasi-equilibrium does not hold, no matter how it is interpreted. Further, on these scales the convective area fraction is not vanishingly small — given that a single deep convective cloud can be kilometres across. Therefore the two most powerful assumptions underlying the mass flux framework must be relaxed.

The third assumption, the so-called "top hat" or "segmentally-constant" approximation, is also not generally a good assumption (Young 1988; Siebesma and Cuijpers 1995; Wang and Stevens 2000; Gu et al. 2020). These studies mostly focus on the use of the "top hat" assumption within bulk mass flux schemes for estimating traditional turbulence statistics (i.e. momentum and scalar variances and covariances), finding that bulk "top hat" representations tend to under-estimate

fluxes, variances and covariances. In particular, "all the variance and covariances are dominated by the environmental subplume variability terms" (Wang and Stevens 2000), and "[t]he bulk mass flux approximation based on traditional cloud sampling significantly underestimates the vertical fluxes" (Gu et al. 2020).

To some extent, the second and third assumptions may be relaxed while retaining most of the structure of the mass flux formulation. However, losing the assumption of a horizontally-homogeneous quasi-equilibrium breaks most of the derivation presented in this section, and means the mass flux loses its primacy: the convective area fraction, and the convective and environmental values of flow variables, must now be retained. This is a much harder problem: there are far more terms to parametrize, and the equations become prognostic (and, in general, three-dimensional), increasing their analytical and computational complexity. In addition, the separation of convective scale variables into a time-dependent part governed by the large-scale forcing (the "closure"), and a height-dependent part governed by fractional entrainment and detrainment (the "cloud model"), is no longer possible. This means that many of the traditional tools of convection parametrization are not easily applicable.

Splitting the flow into convecting and non-convecting parts is not itself reliant on these assumptions, though, and is effectively just a recognition that turbulent convection produces coherent structures (the plumes/thermals/clouds) which behave qualitatively differently to the relatively well-mixed, incoherent environment. Considering the coherent structures directly, rather than implicitly via their impact on the distributional moments of the flow variables, may provide a better low-order description of the convective flow. This approach to coherent structures in turbulence was advocated by Hussain (1983), who constructed "phase averages" to describe separately the coherent, incoherent, and non-turbulent parts of a fluid flow in a RANS context. The conceptual similarity to the mass flux convection-environment decomposition is striking. Fully prognostic and three-dimensional equation sets for arbitrarily many partitions have been derived (Yano 2014; Thuburn et al. 2018), which are the basis for the multi-fluid approach to convection modelling to be explored in this thesis.

1.3.2 Beyond bulk mass flux

Problems with traditional schemes at grey zone resolutions

Various problems occur when running traditional schemes at grey zone resolutions, but a statement which applies to all observed problems is that in the grey zone, the convection produced by the model directly depends on the grid spacing of the model. A (non-exhaustive) summary of observed problems is:

- Convection occurs at the wrong length scales, i.e. inter-cloud spacing and cloud size can be too large (e.g. Lean et al. 2008).
- "Grid point storms" can form, where single model grid cells produce unrealistically intense convection and thus precipitation, surrounded by clear sky (e.g. Deng and Stauffer 2006).
- The timing of the onset of convection in the diurnal cycle is incorrect (multi-day studies), and initiation of convection is delayed in single-day and idealized studies (e.g. Petch et al. 2002).
- The convective response is highly intermittent between model time-steps (e.g. Whitall 2017).
- The convection scheme couples poorly to the large-scale circulation, with effects such as producing incorrect tropical wavemodes, and an unrealistic Madden-Julian oscillation (MJO). See, for instance, Holloway et al. (2013), who found that a realistic MJO was observed in the MetUM only when the mass flux convection scheme was turned off, *and* the boundary layer scheme was replaced. See also Chapter 15 of Plant and Yano (2016b) for a discussion of the required modifications to the ECMWF mass flux convection scheme in order to generate the correct tropical wavemodes and a realistic MJO.

Note that the term "convection-permitting" is sometimes used instead of "grey zone" to describe the resolution of models which partially resolve convection (e.g. Plant and Yano 2016b). We prefer the term "grey zone" as this both suggests that there is not a sharp distinction between grey zone resolutions and resolutions at which traditional LES or RANS arguments apply, and is not specific to convection. The latter is important since grey zones should be found in all turbulent systems.

"Explicit" convection

Due to these problems with traditional schemes, enormous computational power is spent on achieving resolutions $\sim$ 1 km at which convection is "resolved" (Satoh et al. 2019). The limited area numerical weather prediction models now commonly run at such resolutions are often described as having "no convection scheme" or "explicit convection". In practice what this means is that the models are run with no mass flux–like RANS-based convective closure, but there is always still a subfilter turbulence model, often based on the Smagorinsky-Lilly eddy viscosity model previously described. These models contain corrections due to buoyancy, so in our wider view of atmospheric convection as "atmospheric turbulence generated by unstable distributions of buoyancy", these eddy diffusivity schemes are still parametrizing convection.

Although simulations at grey zone resolutions tend to produce better results when run with so-called "explicit convection" than with a traditional mass flux-type scheme, numerous systematic errors remain (Lean et al. 2008, Clark et al. 2016). Further, results do not necessarily improve with increasing resolution: Stein et al. (2015) found that the Met Office Unified Model, run with so-called explicit convection, did not converge as the horizontal grid spacing was decreased from 1.5 km to 100 m. This is because as the grid spacing decreases, more modes of turbulence can be excited at the grid scale, so the overall representation does not necessarily improve, unless the modelling of subfilter variability also changes with resolution to account for the differences in the realizable flow.

Therefore high-resolution schemes need to be modified for the grey zone. For instance, Hanley et al. (2019) found improvements due to implementation of parametrizations of the Leonard term in the MetUM. This is linked to the importance of tilting terms in the grey zone, as local gradients cannot be assumed small anymore. There are thus two broad approaches to the grey zone parametrization problem: modifications to LES-type closures to make them applicable for larger filter scales, and modifications to RANS-type closures to make them applicable to smaller filter scales. In order for the two approaches to have any hope of meeting in the middle they should be placed within one unifying framework.

In addition to the problems with modifying LES-like parametrizations for suitability in the grey zone, there are several other issues with the idea that "convection-permitting" models make convection parametrization obsolete. Firstly, these ~ 1 km resolutions are not yet suitable for long-term climate projection, for which even deep convective parametrization is still required. Secondly, given the inherent limits to the predictability of turbulent flow, it may be more prescient to spend computational power on better parametrizations (and more ensemble members) rather than just resolution, in order to better represent both mean behaviour and variability. Finally, even when the motions are resolved, there are still fundamental questions which remain unanswered. Tropical cyclones have been resolved by models for decades, yet understanding their genesis and intensification is still an active area of research. Likewise, direct numerical simulations of highly turbulent Rayleigh-Bénard convection are now routinely performed, yet many fundamental processes remain only partially understood (such as the mechanism(s) of formation of large-scale structure).

Extensions to mass flux

Since mass flux is by far the dominant approach to parametrizing convection, a wealth of different extensions and generalizations to mass flux have been proposed in

response to the problems noted in the previous section. A non-exhaustive list follows below, sorted by the ways in which the traditional approach has been modified.

- *Non-vanishing convective area fraction*
  Arakawa and Wu (2013) proposed a so-called "unified parametrization" intended to work across a wide range of filter scales, where the convective area fraction is not assumed to be small. All of the other standard mass flux assumptions are retained. Within this generalization, they showed that the dependence of the vertical turbulent fluxes on the convective area fraction is quadratic (as, indeed, we did in the previous Section). Additionally assuming an adjustment-based closure (of either CAPE or cloud work function), they derived a cubic equation for the convective area fraction. The quadratic dependence of the vertical fluxes on the convective area fraction has been included in some operational schemes (such as the US National Centres for Environmental Prediction's Global Forecast System, Han et al. 2017). However, as far as we are aware, the cubic determination of the area fraction has not been used operationally; Han et al. (2017) note that it produces unrealistically small convective area fraction at high resolutions. This could be due to inconsistent relaxation of assumptions; in particular, it is not at all obvious that it is consistent to retain the CQE and "top hat" assumptions at very high resolutions, which are what lead to the cubic closure for the area fraction.

- *Time-dependence of convective response*
  Pan and Randall (1998) proposed a mass flux scheme with a cloud-base mass flux closure based on a prognostic cloud work function. This avoids some problems associated with triggering, such as extreme temporal intermittency. However, the parametrization still assumes horizontal homogeneity over very large areas, so is not suitable for grey zone.

  Gerard and Geleyn (2005), on the other hand, explicitly attempt to extend mass flux deep convection parametrization to the grey zone. They generalize the traditional framework by relaxing both the assumptions of CQE and small area fraction, presenting a bulk mass flux scheme with prognostic updraft vertical velocity and convective area fraction. The prognostic updraft vertical velocity equation is similar to expressions appearing in models of entraining plumes (e.g. Simpson and Wiggert 1969), while the prognostic area fraction equation is justified based on moisture convergence arguments. Horizontal transports, though vitally important in the grey zone, are not considered.

- *Net mass transport*
  Malardel and Bechtold (2019) relax what they describe as the assumption "that all of the compensating environmental flow occurs in the grid column,

i.e. the convective and environmental mass fluxes cancel each other in term of mass transport". This is achieved by essentially re-defining the vertical velocity in the dynamical core (of the ECMWF IFS) to not include the convective part, allowing net mass transport by convection (in principle) both horizontally and vertically. They find these changes make little difference in reforecasts at moderately high horizontal resolutions up to 5 km. This is perhaps unsurprising since the coupling of the convection with the continuity equation is minimal, as the convection parametrization itself remains a diagnostic bulk mass flux scheme with no representation of horizontal transports.

We would argue that "all of the compensating environmental flow occurs in the grid column" is *not* actually an assumption of the traditional mass flux formulation; instead, the impossibility of net mass transport is a consequence of the assumption of horizontal homogeneity of both the large scale forcing and the convective response. Therefore it is potentially inconsistent to relax the assumption of horizontal homogeneity in one place (i.e. the continuity equation, to allow net mass transport) while retaining it elsewhere (i.e. still neglecting horizontal convective fluxes in the mass flux parametrization).

- *Eddy diffusivity-mass flux (EDMF)*
  In an attempt to unify modelling of the convective boundary layer with parametrization of deep convection, Teixeira and Siebesma (2000) proposed modifying the traditional mass flux formulation by modelling internal variability within the environment via a downgradient closure, consistent with assuming that turbulence in the environment is largely homogeneous and dissipative. This approach is similar to standard CBL parametrizations that split the total contribution to the turbulent flux into a local, downgradient contribution, and a nonlocal, counter-gradient contribution (first proposed by Deardorff 1966). Since the downgradient diffusion is a representation of variability within the environment, EDMF may be seen as one way of relaxing the "top-hat" assumption.

  Subsequent work by Soares et al. (2004) and Siebesma et al. (2007) presented and evaluated an EDMF scheme suitable for the dry CBL, which was shown to compare favourably to traditional direct parametrization of the nonlocal flux, particularly for entrainment at the top of the boundary layer. A modified version of EDMF is used to parametrize the unstable boundary layer in the operational ECMWF IFS ("IFS Documentation CY47R3 - Part IV Physical processes" 2021).

  Despite these successes, standard EDMF is a RANS-based scheme suffering from the same problems as noted for traditional mass flux schemes in the grey

zone.

- *Assumed distribution closures*
  A common approach in turbulence theory and modelling has been to assume (joint) PDFs and calculate the consequences for the observable quantities of interest, i.e. variances, covariances, and fluxes. This has been extended (Lappen and Randall 2001) to cumulus parametrization by partitioning the flow into convective and non-convective parts (inspired by the mass flux paradigm), assuming distributions for each partition, and then calculating the consequences of this for the fluxes and (generally prognostic) budgets of various second- and third-order moments by integrating over the assumed distributions. Assuming a PDF ensures that all of the calculated moments are consistent with each other.

  The specification of distributions may generally be used to relax the "top hat" assumption: the "top hat" assumption is equivalent to assuming that the PDFs of variables in each partition are all Dirac delta distributions. While the original "ADHOC" parametrization of Lappen and Randall (2001) did assume Dirac delta distributions, later approaches have used more complicated PDFs, such as Larson et al. (2012) who assume a multi-variate Gaussian for the convective partition, and a multi-variate Gaussian for the environmental partition. Larson et al. (2012) found improved results over conventional mass flux parametrizations, including better scaling with resolution; however the approach is very computationally expensive, and suffers from the need to determine many free parameters.

- *Extended EDMF and multi-fluid modelling*
  With the exception of assumed distribution closures, the above approaches have all attempted to generalize the traditional mass flux formulation in at most one or two ways. In recent years, the extended EDMF (Cohen et al. 2020; J. He et al. 2020; Tan et al. 2018) and multi-fluid modelling (Thuburn et al. 2018; Thuburn and Vallis 2018; Thuburn et al. 2019; Weller and McIntyre 2019; McIntyre et al. 2020; Weller et al. 2020; Shipley et al. 2022) communities have presented more significant generalizations of the mass flux framework, capable in principle of simulation of multiple convective components at all length scales from planetary down to LES. The most general equation set currently published was derived by Thuburn et al. (2018), though the Yano (2014) equation set is similar. This is a unified framework for convection across all scales, and is the approach that this thesis will take to tackling the grey zone of convection. We will therefore discuss these extensions at length in the introduction to Chapter 3.

Traditional turbulence approach

One approach which really is completely removed from the mass flux paradigm is that taken by Alan Grant (Grant 2006a,b; Grant and Lock 2004). In this series of papers (reviewed by Grant in chapter 24 of Plant and Yano 2016b) a similarity theory for (shallow) cumulus convection is developed based on analysis of budgets of turbulent kinetic energy. This similarity theory provides answers to some long-standing questions in moist convection parametrization, including candidate explanations for why updraughts occupy only a small area fraction, and what determines the updraught vertical velocity.

In Grant (2006a,b), the similarity theory and LES data are used to develop scalings for the closures required in mass flux parametrizations[17], such as the entrainment rate and cloud base mass flux. He also presents an alternative closure, derived under different assumptions, closer to nonlocal parametrizations used for the dry convective boundary layer. Both first-order closures are shown to give reasonable diagnostic agreement with the LES. Grant (2006a) also shows how the mass flux approximation may be used to suggest closures for the terms appearing in the budgets of turbulent kinetic energy and turbulent scalar transport. In addition, entrainment and detrainment closures can be derived from the turbulent flux budgets without detailed consideration of entraining plume models. This latter flux-gradient relationship illustrates that alternatives to the mass flux paradigm are perfectly possible, and that the (shallow) cumulus parametrization problem can be directly linked to the parametrization of dry convection. Further, situating the analysis within one overarching theory — in this case, that of Reynolds-averaged turbulence — allows the assumptions underlying different results to be made clear, as well as the relationships between those different results. Finally, the turbulence approach allowed answers to be found to questions which had long eluded the mass flux parametrization community.

The similarity approach, and the homogeneity and stationarity assumed when analysing the TKE budget, are not directly applicable *locally* to grey zone parametrizations. However, the approach does give some constraints on what grey-zone budgets should look like when averaged over a larger area, and therefore could be helpful for constraining parametrizations. Moreover, the idea to use turbulence theory to illuminate and provide closures for mass flux theory can be extended to the grey zone. That is, extensions of the mass flux approach which rely on fewer assumptions (such as the multi-fluid approach which will be the focus of this thesis) could be related to budgets for variances, covariances etc. in traditional turbulence theory,

[17]Note that an environmental eddy diffusivity was required to be introduced for consistency of the mass flux approximation with the scalar flux budget diagnosed from LES, making the scheme technically an EDMF scheme rather than pure mass flux.

in order to suggest possible closures. Both traditional RANS analyses, giving global budgets, and local LES and scale-space budgets, could and should be used. There is no reason why the powerful tools of the turbulence community should not be brought to bear on convection.

Stochastic parametrization

Within the spatial filtering framework we should in general expect a stochastic component to all parametrizations: though a single turbulent flow gives rise to a given set of resolved-scale fields at a given time, $\{{\varphi_\alpha}^{\mathrm{r}}\}$, that set of resolved-scale fields is compatible with multiple subfilter flow realizations. Therefore the modelling of the subfilter-scale flow, and its impacts on the resolved scales, should draw from a distribution of possible subfilter-scale realizations. In the limit of infinite separation of scales (also sometimes termed a "spectral gap") between the dominant resolved-scale and subfilter-scale processes, the distribution collapses to a delta function, admitting a deterministic parametrization of the subfilter-scale effects. As emphasized earlier, assumptions of scale separation are implicit in, for instance, deterministic quasi-equilibrium mass flux convection parametrizations, or LES closures based on a local inertial subrange equilibrium between production and dissipation of TKE. In the absence of a well-defined scale separation — i.e. in the grey zone — the distribution of subfilter-scale realizations must be taken into account; in general this accounting should be stochastic. See, for instance, Section 6 of Lucarini et al. (2014) for this perspective applied generally to the parametrization problem in climate dynamics.

However, one cannot simply introduce an arbitrary stochastic component to a physical model and expect improved results, particularly if the model is hoped to be physically realistic and/or scale-aware. In this vein, Berner et al. (2017) argues that stochastic parametrizations should be introduced more carefully, and preferably more rigorously. As one example, white noise is often added to give a crude random element to a simulation; however, the stochastic backscatter only becomes white noise in the limit of infinite scale separation between the large and small scales. Additionally, Berner et al. (2017) note that "the merit of stochastic parameterization goes far beyond providing uncertainty estimations for weather and climate predictions but may be also needed for better representing the mean state".

Within the mass flux paradigm, some success has been found by incorporating these ideas of stochastic fluctuations around equilibrium into parametrizations. The prototypical example is given by the stochastic deep convection parametrization of Plant and Craig (2008), who assumed that CQE is valid on large scales, but that the actual model resolution may be somewhat smaller, such that fluctuations about this equilibrium are observed in the filter-scale variables. For instance, one might

envisage a large ensemble of $\sim 10^3$ clouds in quasi-equilibrium with a large scale forcing; however, a typical filter volume may contain only ~ 10 of those clouds. Their scheme thus computes the equilibrium statistics of the convective ensemble over a large area (potentially many filter volumes), then draws randomly from this distribution to determine the mass flux and (via the Kain 2004 plume model) other convective-scale properties within each filter volume. The scheme was extended to shallow convection by Sakradzija et al. (2015), which required the inclusion of memory effects. Both schemes are successful in producing a scale-aware response across a wide variety of model resolutions.

However, both schemes rely on the assumption of a macroscopic convective equilibrium for their closure, meaning that they cannot account for non-equilibrium stochastic effects, as required for simulating, for example, the correct initiation of convection in the diurnal cycle. In addition, both schemes use models for the individual convective elements that are not themselves scale-aware. For example, the plume model of the Kain (2004) mass flux parametrization suffers from all of the usual objections to RANS-type schemes, especially as the filter scale approaches the size of the plumes themselves.

Other approaches

Arakawa et al. (2011) introduce two possible routes to building successful grey zone parametrizations. Their "route 1" is what this thesis would term a "scale-aware" grey zone parametrization, while their "route 2", the so-called "multiscale modelling framework", consists of embedding high-resolution (though usually 2D) models within the grid boxes of a coarser resolution model. Also known as superparametrization (Randall 2013), this has the potential to improve model performance by explicitly representing some of the small-scale motions. However, the ability of this approach to actually shed light on the fundamental physics of convection is limited, in our view, and therefore the approach will not be discussed further. Convolutional neural networks have also been used in recent years to directly parametrize convection (Gentine et al. 2018; Rasp et al. 2018); again, this is something of a black box approach, so it will not be discussed.

Machine learning methods are a possibly very useful extra addition to the theorist/modeller's toolkit, however: nonlinear Bayesian regression techniques can be used to do systematically what we already try to do by eye, in finding relationships between unknown terms diagnosed from data, and resolved variables. As an explicit example, an alternative to convolutional neural networks, which would allow for finding closed-form parametrizations of unknown terms, is the relevance vector machine (RVM) approach (Tipping 2001). Given a data set of the desired subfilter

term diagnosed from a high-resolution simulation, and a library of resolved variables upon which the specified subfilter term is conjectured to depend, a sparse Bayesian regression is used to discover which combination of resolved variables best reproduces the subfilter term. This results in a directly interpretable parametrization which can then be analysed for physical consistency.

The RVM method has been used to "discover" the Navier-Stokes and Burgers equations from noisy simulation data (Rudy et al. 2017; Zhang and Lin 2018). Sparse Bayesian regression methods have also recently been used to suggest closed-form equations for eddy Reynolds stresses and buoyancy fluxes in ocean mesoscale eddy parametrization (Zanna and Bolton 2020), and to suggest closures for Reynolds stresses in two-phase Reynolds-averaged modelling of disperse multi-phase flow, including partitioning of TKE between the phases (Beetham et al. 2021). Due to the complexity of the flow, the wealth of high-resolution simulation data, and the difference of the unknown terms compared to those traditionally considered either in turbulence modelling or convection closure, grey zone convection parametrization is an interesting candidate for "data-driven" closure discovery. Sound physical reasoning is still required by the modeller in order to select reasonable basis functions, and to interpret and validate the resulting closures. Data-driven methods could thus be a useful supplement to the analytical and heuristic methods already used to suggest possible closures.

1.4 Summary and outlook

In this chapter we have presented an introduction to the atmospheric convection parametrization problem, stressing the need for parametrizations for the foreseeable future. In addition, there are still fundamental physical questions which require answers: what governs the length scales of moist convection, i.e. cloud size and inter-cloud spacings? Even in the context of dry convection, the mechanisms governing the organization of the large-scale circulation (and therefore setting the inter-plume spacing) in fully developed turbulent convection are not known. We have stressed the point of view of convection as a turbulent flow, and of convection modelling as needing to be understood in a spatial filtering context; but also the strong anisotropies and important large-scale circulation make convection very different to traditional turbulence problems. This perspective leads to the grey zone parametrization problem as a natural and inevitable consequence, and a fundamental barrier to progress until it is better understood.

Since moist convection is such a difficult problem, with feedbacks to many processes, both smaller and larger in scale, it makes sense to isolate the grey zone

problem for further understanding. That is the approach we will take in this thesis. The simplest fluid dynamical convection problem is that of Rayleigh-Bénard convection (RBC), which will be the arena of study for the rest of the thesis. Chapter 2 will introduce Rayleigh-Bénard convection in detail, presenting a suite of direct numerical simulations and motivating RBC as an ideal testbed for developing ideas about convection parametrization: it is fully nonlinear and turbulent, with similar boundary conditions and phenomenology to the (dry) convective boundary layer. It is also simpler, more constrained by symmetry, and has been studied quantitatively for longer, providing a wealth of experimental, numerical, and theoretical results to draw from and compare to when constructing parametrizations.

The problems of mass flux notwithstanding, the basic idea of partitioning the flow into its coherent structures and well-mixed environment is a good and underdeveloped one. In Chapter 3, we will present an overview of one relatively new convection parametrization approach: the multi-fluid method. After deriving the multi-fluid Boussinesq equations, we will present various new results which should be useful for the development of future multi-fluid parametrizations. We will also investigate the consequences of the new terms arising from conditional filtering as far as possible without introducing a specific set of fluid partition definitions.

In Chapter 4, a two-fluid single-column model of Rayleigh-Bénard convection is developed and tested. We introduce specific fluid definitions based on the sign of vertical velocity. We will show that, even with very simple closures, a two-fluid model can accurately reproduce the horizontally-averaged DNS results over several decades of buoyancy forcing. In Chapter 5, we will evaluate the performance of the single-column model formulation across the grey zone of 2D RBC, suggesting routes to improve the closures for building a scale-aware, grey zone multi-fluid parametrization.

Chapter 2

Rayleigh-Bénard convection at grey-zone resolutions

Note that abridged versions of Sections 2.1 and 2.2 of this Chapter form the basis of Section 2 of Shipley et al. (2022).

In Chapter 1, we showed that the grey zone is a significant barrier to progress in understanding and modelling atmospheric convection. We also argued that the concept of a grey zone of resolutions is common to the dynamics of all turbulent fluids, and is not restricted to moist convection. Therefore to gain a better understanding of the convective grey zone, a good starting point is to explore the grey zone of the simplest relevant convecting system. Thuburn et al. (2019) describe the dry convective boundary layer as "the simplest relevant problem" for atmospheric convection parametrization, yet the same essential dynamics of convection are captured in Rayleigh-Bénard convection (RBC).

RBC is the simplest fluid dynamical model of convection which retains enough complexity to produce buoyancy-driven turbulence. Despite its simplicity, it still generates a buoyancy-driven flow, the nature of which depends on the imposed forcing, and which becomes turbulent for large enough forcings. First (quantitatively) studied experimentally by Bénard (1900, 1901), the problem was given a theoretical treatment by Lord Rayleigh (1916) which has been the basis of over a century of investigation[1]. Lord Rayleigh (1916) studied the motion of a Boussinesq fluid confined between two perfectly conducting horizontal planes of infinite extent, each held at a constant uniform temperature. For mathematical tractability he considered stress-free velocity boundary conditions at the plates; the no-slip case was tackled by Jeffreys (1926, 1928). The canonical text covering stability and the onset of con-

[1]In fact, the effects of surface tension were important in Bénard's original experiments, though they were neglected by Lord Rayleigh's analysis; the stability problem including surface tension was not treated theoretically until Pearson (1958).

vection is Chandrasekhar (1961); recent reviews covering fully turbulent convection are Ahlers et al. (2009) and Chillà and Schumacher (2012).

RBC has a long history as a simple model of atmospheric convection. For example, Lorenz's seminal discovery of deterministic chaos occurred in analysis of a simplified version of RBC (Lorenz 1963), specifically chosen as an analytically-tractable idealization of numerical weather prediction. Emanuel (1994, chapter 3) also explores RBC in depth as an introduction to global convection, noting that "convection in geophysical fluids almost always originates from buoyancy sources distributed over areas that are large compared to the depth of the convecting layer". This is a key distinction, as many other meteorological test cases such as the consideration of plumes and thermals (Emanuel 1994, chapter 2), or the rising bubble of Bryan and Fritsch (2002) are fundamentally local. RBC is certainly no more of a simplification than the dry plumes/thermals/rising bubbles which form the basis of many entrainment and detrainment closures. However, direct crossover between research in the fields of RBC and atmospheric convection has been surprisingly scarce; Vallis et al. (2019) note in their introduction that "progress in the theory of atmospheric convection has, with a few exceptions, proceeded largely independently of [RBC]". Moist extensions of the model have been considered to gain insight into moist convection, though far less work has been performed on moist versions of the problem than on the dry case (Bretherton 1987, 1988; Pauluis and Schumacher 2010; Vallis et al. 2019; Weidauer and Schumacher 2012). Therefore for the remainder of this thesis we shall focus exclusively on dry RBC.

In this chapter our goal is to quantitatively explore the grey zone of Rayleigh-Bénard convection. We begin with an introduction to the theoretical background of the problem, covering nondimensionalization of the governing equations, classical results of linear and nonlinear stability, exact integral results for the kinetic and thermal dissipation rates, and the construction of scaling theories. This is followed by a discussion of the relevance of RBC to atmospheric convection, especially the dry convective boundary layer, with reference to the current state-of-the-art in Rayleigh-Bénard convection, along with current research directions.

We then describe a suite of direct numerical simulations (DNS) of 2D dry RBC across a range of forcings from fully diffusive to fully turbulent, verifying the simulations against known theoretical, experimental, and numerical results in the RBC literature. These simulations form the reference truth for the main investigation of the chapter: we explore the grey zone of RBC by performing simulations at fixed Rayleigh number for a range of horizontal resolutions from DNS through to so coarse that all convection ceases. We compare the grey zone behaviour of RBC to the known grey zone behaviour of atmospheric convective systems, finding RBC to be a very useful analogue.

2.1 Background

2.1.1 Overview of Rayleigh-Bénard convection (RBC)

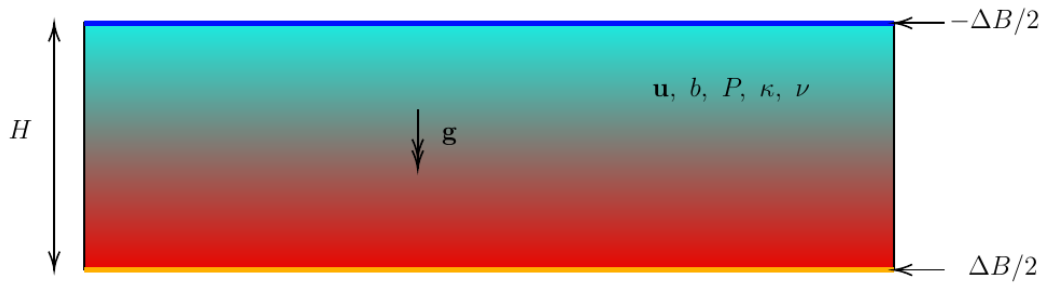

Figure 2.1: Diagram of the Rayleigh-Bénard problem. The boundary conditions imposed at the top and bottom plates are fixed buoyancy and no-slip velocity. Colours are a proxy for buoyancy, with a linear gradient from bottom to top.

Figure 2.1 illustrates the Rayleigh-Bénard problem. A Boussinesq fluid is confined between two smooth, flat, horizontal planes, a fixed distance H apart. Each of these is held at a fixed buoyancy, $\pm\,\Delta B/2$, with no-slip, no-normal flow velocity boundary conditions. For both analytical and numerical simplicity we choose the lateral boundaries to be periodic in all fields φ, with periodicities L_x, L_y. Summarising, the boundary conditions are:

$$b(x,y,t;z=0)=\frac{\Delta B}{2},\qquad b(x,y,t;z=H)=-\frac{\Delta B}{2}, \tag{2.1}$$

$$\mathbf{u}(x,y,t;z=0,H)=\mathbf{0}. \tag{2.2}$$

$$\varphi(y,z,t;x)=\varphi(y,z,t;x+L_x),\qquad \varphi(x,z,t;y)=\varphi(x,z,t;y+L_y). \tag{2.3}$$

The motion of the fluid is described by the following Boussinesq equations of motion:

$$\frac{\mathrm{D}\mathbf{u}}{\mathrm{D}t}=b\mathbf{k}-\boldsymbol{\nabla}P+\nu\boldsymbol{\nabla}^2\mathbf{u}, \tag{2.4}$$

$$\frac{\mathrm{D}b}{\mathrm{D}t}=\kappa\boldsymbol{\nabla}^2 b, \tag{2.5}$$

$$\boldsymbol{\nabla}\cdot\mathbf{u}=0. \tag{2.6}$$

Here $\mathbf{u}$ denotes the velocity field of the fluid; $b \coloneqq g(\rho_{\mathrm{ref}}-\rho)/\rho_{\mathrm{ref}}$ its buoyancy[2]; $P \coloneqq p/\rho_{\mathrm{ref}}$ its pressure potential; ν its kinematic viscosity; κ its buoyancy diffusivity; and $\mathbf{k}$ is a unit vector antiparallel to gravity, defining the vertical (z)

[2]For our desired application to atmospheric convection, $(\rho_{\mathrm{ref}}-\rho)/\rho_{\mathrm{ref}} \approx (\theta-\theta_{\mathrm{ref}})/\theta_{\mathrm{ref}}$, where θ is the potential temperature, though much previous work on Rayleigh-Bénard convection (RBC) is performed in terms of temperature, using the approximation $(\rho_{\mathrm{ref}}-\rho)/\rho_{\mathrm{ref}} \approx (T-T_{\mathrm{ref}})/T_{\mathrm{ref}}$. The equation set retains the same form.

direction. All variables are defined relative to a resting, uniformly constant-density, hydrostatically-balanced pressure reference state. For an asymptotic derivation of the equation set, see for instance pp. 101-103 of Vallis (2017), or Bois (1991) and Klein (2009) for more rigour[3].

Note that the governing equations (2.4)–(2.6) are invariant under the discrete symmetry transformation $b \to -b, \mathrm{d}z \to -\mathrm{d}z$; however the boundary conditions (2.1)–(2.2) fix the constant for the z transformation to $z \to H - z$. This symmetry can be viewed as reflection of the system about the plane $z = H/2$, coupled with reversing the direction of gravity.

The familiar nondimensionalized form of the Boussinesq equations used in modelling RBC is arrived at by performing an isotropic rescaling of the equation set:

$$(\mathbf{x}, t, \mathbf{u}, b, P) \to (X\hat{\mathbf{x}}, T\hat{t}, U\hat{\mathbf{u}}, B\hat{b}, P\hat{P}), \tag{2.7}$$

followed by choosing relationships between the scaling parameters. We are interested in flows where advection is important, so it makes sense to scale the velocity as:

$$U = X/T \quad \text{(equal importance of Eulerian and advective time dependence).} \tag{2.8}$$

The mass continuity equation, Equation (2.6), can tell us nothing about an isotropic scaling. However, looking at the buoyancy equation, Equation (2.5), and requiring both sides to be $\mathcal{O}(1)$ — i.e. diffusion of buoyancy is important — gives the following *diffusive* scaling of time:

$$T_\kappa \coloneqq X^2/\kappa \quad \text{(diffusion of buoyancy is important for T} \sim O(1)). \tag{2.9}$$

Together with Equation (2.8) this implies a diffusive velocity scale $U_\kappa \coloneqq \kappa/x$. It remains only to scale the pressure; we choose:

$$P = \kappa\nu/X^2 \quad \text{(viscous scaling of pressure, P} \sim U\nu/X). \tag{2.10}$$

Nondimensionalizing the Boussinesq equations (2.4)-(2.6) with our chosen scalings shows that two dimensionless parameters[4] govern the flow (the boundary conditions are given for completeness):

$$\frac{\mathrm{D}\hat{\mathbf{u}}}{\mathrm{D}\hat{t}} = \mathrm{Pr}\left(\mathrm{Ra}\,\hat{b}\mathbf{k} - \hat{\boldsymbol{\nabla}}\hat{P} + \hat{\boldsymbol{\nabla}}^2\hat{\mathbf{u}}\right), \tag{2.11}$$

[3]There exists some disagreement over the correct form for the energy equation in a fully formal asymptotic derivation of the Boussinesq equations; see Kiš and Herwig (2010) for an overview.

[4]That there must only be two is a consequence of the Buckingham "Pi theorem" (Vaschy 1892; Buckingham 1914; Curtis et al. 1982), which is really just the rank-nullity theorem of linear algebra applied in the context of dimensional analysis.

$$\frac{\mathrm{D}\hat{b}}{\mathrm{D}\hat{t}} = \widehat{\boldsymbol{\nabla}}^2 \hat{b}, \tag{2.12}$$

$$\widehat{\boldsymbol{\nabla}} \cdot \hat{\mathbf{u}} = 0, \tag{2.13}$$

$$\hat{b}(\hat{z}=0) = \frac{1}{2}, \qquad \hat{b}(\hat{z}=1) = -\frac{1}{2}, \tag{2.14}$$

$$\hat{\mathbf{u}}(\hat{z}=0,1) = \mathbf{0}, \tag{2.15}$$

where we have defined the following dimensionless parameters:

$$\mathrm{Ra} \coloneqq \frac{\Delta B \cdot H^3}{\kappa\, \nu}, \qquad \mathrm{Pr} \coloneqq \frac{\nu}{\kappa}, \tag{2.16}$$

using the boundary conditions to suggest the identifications $\mathrm{X} \equiv H$, $B \equiv \Delta B$.

The Rayleigh number, Ra, is the ratio of buoyancy forcing (ΔB) to viscous diffusion ($\kappa\nu/H^3$); and the Prandtl number, Pr, is the ratio of the diffusion of momentum (ν) to the diffusion of buoyancy (κ). The former can thus be seen as measure of the applied forcing in RBC, whereas the latter is an intrinsic property of the fluid. This nondimensionalization shows that any two RBC systems with the same Ra and Pr support the same solutions, i.e. are dynamically similar[5].

Other possibilities for the scaling of T and P exist, even in the viscous regime; however, unless a limit $\mathrm{Pr} \to 0$ or ∞ is envisaged, the choice is principally an aesthetic one: would factors of Pr be preferred to appear in the momentum, or the buoyancy equation? Note that (2.8) is equivalent to choosing the Strouhal number, $\mathrm{Sr} = 1$ (for flow variables $O(1)$); (2.9) with (2.8) is equivalent to setting the Peclet number, $\mathrm{Pe} = 1$; together these force $\mathrm{Re}^{-1} = \mathrm{Pr} \coloneqq \nu/\kappa$. Thus the nondimensionalization we have chosen is suitable for considerations of instability so long as $\mathrm{Pr} = \mathcal{O}(1)$, which it always is for atmospheric flows.

For consideration of the convective solutions, a nondimensionalization based on the buoyancy forcing is more useful. This "free fall" or "free convective" scaling gives velocity and time scales $U_B \coloneqq \sqrt{\Delta B\ H}, T_B \coloneqq \sqrt{H/\Delta B}$, and is ubiquitous in the CBL literature (where U_B is denoted w^*, see, e.g., Garratt 1994). Such a scaling also gives an a priori estimate for the Reynolds number[6], $\mathrm{Re} \propto \mathrm{Ra}^{1/2}\,\mathrm{Pr}^{-1/2}$. This approximate Re(Ra) scaling is observed for the regimes applicable to this thesis. Nondimensionalizing the governing equations by this free-convective scaling yields

[5] A third parameter, the aspect ratio of the domain, $\Gamma \coloneqq L/H$, enters via the lateral boundary conditions; however, the dependence upon the aspect ratio is generally weak so long as $\Gamma > 1$ — see Ahlers et al. 2009, section 3E; also Johnston and Doering (2009); Bailon-Cuba et al. (2010); Q. Zhou et al. (2012) — and the dependence is weaker for periodic boundaries than for rigid boundaries.

[6] The a priori scaling for the Nusselt number that this predicts, $\mathrm{Nu} \propto \mathrm{Ra}^{1/2}$ — the so-called "ultimate scaling" — is steeper than (unambiguously) observed to date in experimental or numerical dry RBC, because the non-turbulent surface layers next to the boundaries prevent a thermal shortcut.

a qualitatively different equation set, since the choice of scaling specifies a different distinguished limit, but the equations still only depend on Ra and Pr. The equation set with this nondimensionalization, and a dynamic scaling of the pressure $P \sim U_B^2$, still depends only on Ra and Pr (as it must):

$$\frac{\mathrm{D}\hat{\mathbf{u}}}{\mathrm{D}\hat{t}} = \hat{b}\mathbf{k} - \hat{\boldsymbol{\nabla}}\hat{P} + \sqrt{\frac{\mathrm{Pr}}{\mathrm{Ra}}}\hat{\boldsymbol{\nabla}}^2\hat{\mathbf{u}}, \tag{2.17}$$

$$\frac{\mathrm{D}\hat{b}}{\mathrm{D}\hat{t}} = \frac{1}{\sqrt{\mathrm{Ra}\,\mathrm{Pr}}}\hat{\boldsymbol{\nabla}}^2\hat{b}, \tag{2.18}$$

$$\hat{\boldsymbol{\nabla}} \cdot \hat{\mathbf{u}} = 0, \tag{2.19}$$

though clearly the nondimensionalization applies to a different asymptotic limit of the equations. Replacing $\mathrm{Ra}^{1/2}\,\mathrm{Pr}^{-1/2} \to \mathrm{Re}$, the momentum equation becomes the familiar nondimensionalized form of the Navier-Stokes momentum equation suitable for high-Re flow — that is, the form of the equation set useful for considering turbulence.

The equation set (2.11)-(2.15) has a unique stationary zero-flow solution (unique because if $\mathbf{u} = \mathbf{0}$, the equations become a set of two coupled *linear* partial differential equations, for which existence and uniqueness theorems exist and apply), with a linear buoyancy gradient between the plates and a quadratic pressure profile:

$$\mathbf{u} = \mathbf{0}, \qquad b = \frac{1}{2}(1 - 2z), \qquad P = P_0 + \frac{z}{2}(1 - z). \tag{2.20}$$

This solution is both linearly and nonlinearly unstable to perturbations if and only if the Rayleigh number exceeds a critical value, $\mathrm{Ra_c} = \mathcal{O}(10^3)$; importantly, the stability does not depend on the Prandtl number (see, for instance, Chandrasekhar 1961; Joseph 1966; Lindsay and Straughan 1990). Below $\mathrm{Ra_c}$, solutions are purely diffusive; above $\mathrm{Ra_c}$, a circulation develops which increases the heat transport. The circulation that develops can either be steady, periodic, quasi-periodic, or turbulent, depending on the governing parameters $(\mathrm{Ra}, \mathrm{Pr})$, and on the dimensionality of the domain. The precise values of $\mathrm{Ra_c}$ and the wavelength of the most unstable mode, λ_c, depend on the velocity boundary conditions at the top and bottom boundaries, but not on the dimensionality of the domain. Intuitively, $\mathrm{Ra_c}$ must be greater for no-slip boundary conditions than for free-slip or mixed velocity boundary conditions. No-slip is the correct ground boundary condition on the velocity for the real atmosphere; although free-slip at the upper boundary might be closer to the truth, we wished to keep the boundary conditions symmetric for simplicity. For our chosen no-slip conditions, $\mathrm{Ra_c} \simeq 1708$, and the wavelength of the most unstable mode is $\lambda_\mathrm{c} \simeq 2.02H$ (Chandrasekhar 1961, table 3). The most unstable mode is unique (Jeng and Hassard 1999).

The domain- and time-averaged dimensionless buoyancy flux is given by the Nusselt number:

$$\mathrm{Nu} \coloneqq \left\langle \mathbf{k} \cdot \left(\hat{\mathbf{u}}\hat{b} - \hat{\boldsymbol{\nabla}}\hat{b} \right) \right\rangle_{V,t} = \left\langle \hat{w}\hat{b} - \frac{\partial \hat{b}}{\partial \hat{z}} \right\rangle_{A,t}, \tag{2.21}$$

which is the ratio of the actual buoyancy flux to the buoyancy flux of the purely diffusive solution. Averaging the buoyancy equation (2.12) over a horizontal plane and over time (denoted $\langle \dots \rangle_{A,t}$) shows that the Nusselt number is independent of height in a statistically stationary flow.

Exact results for the domain- and time-averaged kinetic and thermal dissipation rates, $\varepsilon_{\mathbf{u}}$ and ε_b, are given by (Chandrasekhar 1961, appendix 1; Shraiman and Siggia 1990; Siggia 1994):

$$\varepsilon_{\mathbf{u}} \coloneqq \langle \boldsymbol{\nabla}\mathbf{u} : \boldsymbol{\nabla}\mathbf{u} \rangle_{V,t} = \mathrm{Ra}(\mathrm{Nu} - 1), \tag{2.22}$$

$$\varepsilon_b \coloneqq \langle \boldsymbol{\nabla} b \cdot \boldsymbol{\nabla} b \rangle_{V,t} = \mathrm{Nu}\,. \tag{2.23}$$

See Appendix A of this thesis for a derivation. Here the "double dot product" denotes the complete contraction of two rank-two tensors, following the convention $\mathbf{A} : \mathbf{B} \coloneqq \sum_{a,b} A_{ab} B^{ab}$. These results use the diffusive nondimensionalization of the governing equations, Equation (2.11)-(2.13); if the free-convective scaling is used instead, Equation (2.17)–Equation (2.19), the result for the dimensionless kinetic dissipation rate, equation (2.22) changes accordingly: $\varepsilon_{\mathbf{u}}(\text{free}) = \varepsilon_{\mathbf{u}}(\text{diffusive})/(\mathrm{Ra} \cdot \mathrm{Pr})$. Thus the vertical buoyancy flux is the only quantity that characterizes the stationary-state global energetic response of the system to the applied forcing $(\mathrm{Ra}, \mathrm{Pr})$[7]. The statistically steady-state Rayleigh-Bénard problem can then be framed as asking the question: if we apply a buoyancy forcing Ra to a Boussinesq fluid characterized by Pr, what is the resulting Nu?

Scaling theories for Nu as a function of Ra and Pr are therefore some of the most sought-after results in RBC. That is, for $\mathrm{Ra} > \mathrm{Ra_c}$, relations of the form

$$\mathrm{Nu} = C_{\mathrm{Nu}}\, \mathrm{Ra}^{\alpha_1}\, \mathrm{Pr}^{\beta_1}, \tag{2.24}$$

are sought. The "classical" scaling argument for RBC is attributed to Malkus (1954)[8]; this was re-interpreted by Howard (1964), who argued that in a turbu-

[7] It is worth noting that these results (2.22)-(2.23) are quite general; in particular they do not rely on the plates being smooth and flat, and they apply equally well also to the cases of stress-free velocity or constant buoyancy flux boundary conditions.

[8] Willem Malkus, rather than Joanne Malkus; the two were married from 1948-1964 (Fleming 2020). Joanne is more well-known to the atmospheric convection community; of particular importance to this thesis is her work on the hot tower/"undiluted chimney" hypothesis which was the precursor to the mass flux paradigm (Riehl and Malkus 1958), as well as — under the sur-

lent state the boundary layers would be marginally stable, leading to $\mathrm{Nu} \propto \mathrm{Ra}^{1/3}$ uniformly in Pr. Malkus discussed in his own work the likelihood that the boundary layers would become turbulent at high enough Ra. Considerations of turbulence in this asymptotically-high Ra regime led Kraichnan (1962) to the scaling law $\mathrm{Nu} \propto \mathrm{Ra}^{1/2}\,\mathrm{Pr}^{-1/4}$ (plus logarithmic corrections) for $0.15 < \mathrm{Pr} \leq 1$; this is known as the "ultimate" scaling. Interestingly, the same scaling law is arrived at if one assumes that the (physical) heat flux is independent of the molecular transport coefficients (Spiegel 1963), as one would expect for an asymptotically high Reynolds number flow. We note that this scaling law really is "ultimate" in the sense that it is the (currently known) upper bound on the high-Ra scaling of the Nusselt number[9]: $\mathrm{Nu} \leq C\,\mathrm{Ra}^{1/2}$. This theorem is initially due to Howard (1963); a wonderful overview of the background field methods used to improve the bounds in more recent decades is provided by Doering and Gibbon (1995). The exponent in the bound is the same for both no-slip and free-slip velocity boundary conditions, and for both constant-value and constant-flux thermal boundary conditions (Fantuzzi 2018).

Experimental and numerical data were broadly consistent with the classical scaling until the late 1980s, when $\mathrm{Nu} \propto \mathrm{Ra}^{2/7}$ began to be observed in experiments (Heslot et al. 1987; Castaing et al. 1989) and later in numerical simulations (Kerr 1996). Castaing et al. (1989) and Shraiman and Siggia (1990) provided partially phenomenological arguments for the newly-observed scaling (sometimes known as the "hard turbulence" scaling), based on the exact relationships for the kinetic and thermal dissipation rates, relaxing the requirement that the thermal boundary layer depth be the only small length scale in the problem (assumed by Malkus and Kraichnan), and making various assumptions about the relationships between the remaining scales in the problem (for instance assuming $\varepsilon_{\mathbf{u}} \propto U^3/H$ is valid within the boundary layers). This "hard turbulence" scaling is commonly observed between $10^4 \lesssim \mathrm{Ra} \lesssim 10^{10}$ for $\mathcal{O}(1)\,\mathrm{Pr}$.

A unifying scaling theory was proposed by Grossmann and Lohse (2000, 2001, 2002, 2003, 2004), attempting to encompass all prior scaling laws within one overarching framework. This scaling theory again begins with the exact results for the kinetic and thermal dissipation rates, but splits each into contributions from the boundary layers/plumes[10] and the bulk. Different scaling regimes follow, depend-

name Simpson — being one of the earliest to apply ideas from the engineering study of entraining plumes/thermals to the representation of atmospheric convection (Simpson and Wiggert 1969). However, perhaps her greatest legacy was pioneering the view that clouds are an active and important dynamical component of the atmosphere, rather than merely a response to the dynamics (Fleming 2020; Houze 2010).

[9] In 2D (with free-slip boundaries), the bound is rigorously known to be lower: $\mathrm{Nu} \leq C\,\mathrm{Ra}^{5/12}$ (Ding and Wen 2020; Whitehead and Doering 2011).

[10] Initially the contribution of plumes was neglected, but experimental results showed their influence to be important and so they were later incorporated (Grossmann and Lohse 2004).

ing on whether each dissipation rate is dominated by contributions from the bulk or plumes, and whether the thermal boundary layer or kinetic boundary layer is thicker (which depends on Pr). The Grossmann-Lohse theory encompasses the earlier "classical" and "ultimate" scaling laws, predicting a transition to the "ultimate" regime around $\mathrm{Ra} \sim 10^{14}$. It is worth noting that the theory never predicts a pure 2/7 power law for the $\mathrm{Nu} - \mathrm{Ra}$ scaling; however the authors show (Grossmann and Lohse 2000) that the combination of 1/4 (predicted for low Ra) and 1/3 (predicted for high, but not asymptotically-high, Ra) power laws with experimentally-determined prefactors mimics a 2/7 power law over up to 10 decades.

There is good agreement between the Grossmann-Lohse theory and numerical and experimental results until at least $\mathrm{Ra} = 10^{11}$ for $\mathrm{Pr} = \mathcal{O}(1)$ (Ahlers et al. 2009; Chillà and Schumacher 2012). Above $\mathrm{Ra} = 10^{12}$ there is uncertainty as to whether the "classical" (1/3) regime continues to hold, or whether it is replaced by the "ultimate" regime; some studies have claimed to find the ultimate scaling (X. He et al. 2012; Zhu et al. 2018) only for their data to later be shown to be consistent with the classical scaling (Doering et al. 2019; Doering 2020). The highest-Ra simulations to date are consistent with the classical scaling up to $\mathrm{Ra} \sim 10^{15}$ (Iyer et al. 2020), although these experiments were conducted in a very small-aspect ratio domain, $\mathrm{AR} = L/H = 1/10$, where the lateral boundaries are likely to have a greater effect on the solution (X. He et al. 2020).

2.1.2 The relevance of RBC to atmospheric flows

While RBC is a valuable test problem in its own right, it is worth considering similarities with and differences from atmospheric flows, in particular the dry atmospheric convective boundary layer (CBL).

Besides the complexities of moisture, the dry RBC problem differs from even dry atmospheric convection in a few important ways. Firstly, the Boussinesq approximation is of questionable validity even on the scale of the atmospheric boundary layer; in practice however, it has long been used in the LES community with excellent results (e.g. Sullivan and Patton 2011). Furthermore, the Boussinesq form has been used to facilitate analysis; experiments using a non-Boussinesq (fully compressible) version of the same code show little qualitative or quantitative differences from their Boussinesq counterparts. We also note that, although NWP models are increasingly moving towards using fully compressible equation sets in their dynamical cores (Davies et al. 2003), numerical studies of deep convection have found that numerical schemes and subgrid models make bigger differences to the solutions than compressibility vs. pseudo-incompressibility (Kurowski et al. 2014).

Secondly, the lower boundary in the CBL is neither smooth, nor uniformly

heated. Recent results show that neither nonuniform heating (Bakhuis et al. 2018) nor rough boundaries (Toppaladoddi et al. 2021; Zhu et al. 2019) drastically change the dynamics of RBC, though the latter does tend to increase the heat flux towards the so-called "ultimate regime", equivalent to the free-convective regime which dominates discussion of scaling in the atmospheric convective boundary layer. Numerical simulations of a CBL-like problem with a smooth lower boundary show scaling laws and profiles of variables consistent those observed in the lower half of RBC (Mellado 2012), suggesting that the primary difference between the two problems is due to smooth boundaries delaying the onset of turbulence in the surface layer of RBC to much higher Rayleigh numbers.

Thirdly, the fixed buoyancy boundary conditions are quite different to CBL conditions, where the lower boundary is closer to (and is often modelled as) a fixed buoyancy flux, and there is no fixed upper boundary for the convection (instead there is a stable atmospheric layer). In practice, solutions of RBC with fixed flux vs. fixed value boundary conditions are similar, especially in 2D (Johnston and Doering 2009; Verzicco and Sreenivasan 2008), as are LES simulations of the CBL. It is thus only the upper boundary that introduces a major difference between RBC and the CBL. Even in that case there has been recent progress on studying modified Rayleigh-Bénard convection with the compensating heat flux provided by radiation in a layer of finite thickness (Doering 2019; Lepot et al. 2018), which the first authors note "spontaneously achieves the 'ultimate' regime of thermal convection".

The above differences in boundary conditions between RBC and the CBL hint at a further difference: the symmetry of the upper and lower boundaries in RBC furnishes the equation set with the discrete symmetry $z \to H - z, b \to -b$. Therefore the time-mean, horizontal-mean solution must be invariant under this discrete transformation. This forces the ratio of vertically-integrated updraft to downdraft fraction to be 1, whereas in the CBL and atmospheric convection more generally, the ratio deviates from 1 due to the lack of symmetry. More importantly, the symmetry means that downdrafts are as strong as updrafts in RBC, and the large-scale circulation is correspondingly stronger. However, despite these differences, quantitative comparison of DNS of a dry CBL-like problem with predictions of RBC theory shows that several important statistics, such as the scaling of the Nusselt number with Rayleigh number, agree between the two systems (Mellado 2012).

We thus consider the classical Rayleigh-Bénard problem to be sufficiently close to atmospheric convection to provide a useful arena for exploring the grey zone, and a testbed for investigating the behaviour of a multi-fluid model of turbulent convection. There remains the question of the applicable parameter regime, to be discussed in the next subsection.

2.1.3 An analogy between constant-viscosity RBC and large-eddy simulation of higher-Ra RBC

The Prandtl number of air in normal atmospheric conditions is virtually constant at around 0.7; taking typical values of the other parameters gives approximate Rayleigh numbers of $\sim 10^{16}$ for the CBL ($U \sim 1$ m s$^{-1}, L \sim 10^3$ m, $\nu \sim 10^{-5}$ m^2 s^{-1}), $\sim 10^{18}$ for shallow cumulus convection ($U \sim 3$m s$^{-1}, L \sim 3 \times 10^3$m), and $\sim 10^{21}$ for deep cumulus convection ($U \sim 10$m s$^{-1}, L \sim 10^4$m). These are *highly* turbulent. By the resolution arguments in Section 1.2.1 of Chapter 1, a DNS of this problem is computationally impossible in 3D with current computing power and would be a challenge even in 2D.

As noted in that earlier section, the atmospheric science community address this problem using large-eddy simulation. Generally the sub-filter contribution to turbulent fluxes is presumed to be predominantly dissipative, and is therefore often represented by an eddy viscosity. We noted that in practice the formulation of eddy viscosity proposed by Smagorinsky (1963) is frequently used in atmospheric modelling, and has been found to give good results provided the filter scale actually is well within the inertial sub-range.

Mason (1994) shows that acceptable results are obtained from a simulation of the CBL in which a constant viscosity is used at each vertical level based upon the horizontal average of the Smagorinsky value. Since eddy length scales are restricted close to the surface and the inversion, we might expect that the height-dependence is largely restricted to these regions[11] — i.e. in the bulk of the flow, a constant value of viscosity should suffice. This is effectively a statement of the Reynolds number independence of the flow: in a well-developed turbulent flow far from boundaries, the flow should not depend directly on the molecular viscosity. Therefore replacing the viscosity with an artificial larger viscosity — implying a larger Kolmogorov microscale, effectively the filter scale associated with the re-normalized viscosity — should not appreciably affect the larger scales, as the TKE dissipation rate remains the same so long as the new η remains in the ISR.

The same argument is what allows experiments with scale models in wind tunnels to be applied to real-world flows. Furthermore, a similar argument is made by Mellado et al. (2018) in a study of stratocumulus convection: they simulate the stratocumulus-capped boundary layer using the anelastic equations with artificially high viscosity, finding the results of their Re $\geq$ 5000 simulations to be in good agreement with the LES ensemble of Stevens et al. (2005). Though they describe

[11] In LES, the collapse in turbulence length scales as boundary layers (or inner layers) are approached is handled via so-called wall functions. A DNS would however not be "direct" if these were applied, and so instead the grid is graded to give greater resolution as the walls are approached — see Section 2.2.

their high viscosity runs as DNS, we would argue that it is more accurate to describe their simulations as a form of LES. Both LES, and using DNS of a higher-viscosity problem to gain insight about a higher-Re flow, rely on the proposed Reynolds number independence of high-Re flows.

We can estimate the value of the eddy viscosity by using the results of Section 1.2.1. Low-pass filtering the flow with a filter of characteristic scale Δ_f and following the arguments of Lilly (1962) (see Section 1.2.3) allows us to replace the molecular viscosity by a turbulent viscosity, $\nu \to \nu_\mathrm{t}$, such that the dissipation rate of TKE remains the same: $\nu\left\|\boldsymbol{\nabla}\mathbf{u} + (\boldsymbol{\nabla}\mathbf{u})^\mathsf{T}\right\|^2 = \nu_\mathrm{t}\left\|\boldsymbol{\nabla}\mathbf{u}^\mathrm{r} + (\boldsymbol{\nabla}\mathbf{u}^\mathrm{r})^\mathsf{T}\right\|^2 = \varepsilon$. For the eddy viscosity hypothesis to be valid, the Reynolds number at the filter scale must be $\mathrm{Re}_\mathrm{f} \sim 1$, giving a scaling for the renormalized viscosity as $\nu_\mathrm{t} \sim U_\mathrm{f}\Delta_\mathrm{f}$, where U_f is the characteristic velocity at the filter scale. Since the filter scale is assumed to be in the inertial subrange of the flow, the dissipation can be scaled as $\varepsilon \sim U_\mathrm{f}^3/\Delta_\mathrm{f} \implies U_\mathrm{f} \sim \varepsilon^{1/3}\Delta_\mathrm{f}^{1/3}$. Therefore a crude estimate of the required eddy viscosity is

$$\nu_\mathrm{t} \sim \varepsilon^{1/3}\Delta_\mathrm{f}^{4/3}. \tag{2.25}$$

To give a simple example, let us return to the example of the CBL. A typical depth is $H \sim 1000$ m, and a typical convective velocity scale is $U_B \sim 1$ m s^{-1}, giving $\Delta B \simeq 4 \times 10^{-3}$ m s^{-2}. Then $\mathrm{Re} = UH/\nu \sim 10^8$ and $\mathrm{Ra} \sim 10^{16}$. The 'outer' mixing length is often taken to be $L \sim 0.1H$, giving $\varepsilon \sim U_B^3/L \sim 10^{-2}$ m^2 s^{-3}. Choosing a filter scale such that the effective dissipation scale is $\eta_\mathrm{f} = 1$ m, the eddy viscosity is $\nu_\mathrm{t} \sim \varepsilon^{1/3}\Delta_\mathrm{f}^{4/3} \sim 0.2$ m^2 s^{-1} and the effective Reynolds number of the resolved flow is reduced to $\mathrm{Re} \approx UH/\nu_\mathrm{t} \sim 5000$ (comparing well with the results of Mellado et al. 2018). We would still expect this flow to be turbulent and approaching the Reynolds number-independent regime (e.g. Davidson 2009; Pope 2000); this hypothesis is supported by the results of Mellado et al. (2018) in the context of convection.

Further support for the Reynolds number similarity comes from LES studies: Sullivan and Patton (2011) show that "the majority of the low-order moment statistics (means, variances, and fluxes) become grid independent when the ratio $z_\mathrm{i}/(C_\mathrm{S}\Delta_\mathrm{g}) > 310$". Their z_i is the depth of the inversion (our H), $C_\mathrm{S} \approx 0.2$ is the Smagorinsky constant, and $\Delta_\mathrm{g} \propto \Delta_\mathrm{f}$ the grid spacing. (C_S can be interpreted as the proportionality constant between the grid spacing and the implied filter width.) For our case, this result implies $\Delta_\mathrm{f} < z_\mathrm{i}/(310C_\mathrm{S}) \approx 16$ m. Hence our notional 1 m resolution should be very well-converged LES.

Therefore we may interpret our relatively low-Ra simulations as reasonable approximations to LES of much higher-Ra flows relevant to the atmosphere, so long

as $\mathrm{Re} \gtrsim 5000 \implies \mathrm{Ra} \gtrsim 10^8$.

Emran and Schumacher (2015) have demonstrated the same principle for weakly-turbulent Rayleigh-Bénard convection in 3D. They performed DNS of turbulent 3D RBC at Ra up to 5×10^5, observing large-scale patterns in the time-averaged temperature and velocity fields. The appearance of these large-scale patterns was explained by computing the effective turbulent diffusivity and viscosity in a manner similar to that outlined above, showing that DNS of a flow at the effective turbulent Ra (much lower than the true Ra) and Pr would produce a flow with the observed large-scale, slowly-varying patterns. This suggests that our analogy between constant-viscosity RBC and LES of higher-Ra RBC may tentatively extend to even lower Rayleigh numbers in 3D.

A slight note of caution may arise from consideration of the boundary conditions, as the turbulence length scale collapses as one approaches the boundary and buoyancy effects on turbulence become more dominant. (The same concerns apply to LES). With a fixed heat-flux boundary condition, the concern is less as the surface exchange serves merely to transport the given surface flux into the fluid where large eddies can start to transport it. In practice, our results are similar for fixed temperature and fixed heat flux boundary conditions, suggesting that, so long as the thermal boundary-layer is adequately resolved the solutions remain applicable to higher Re.

2.2 2D direct numerical simulation of RBC

To provide a reference "truth" for later sections in the thesis, results from two dimensional direct numerical simulations of Rayleigh-Bénard convection over a wide range of Ra are presented. These simulations also serve to illustrate the phenomenology of RBC, and to indirectly validate the numerical methods via comparison with reference results.

While the restriction to two dimensions may seem like too great a simplification, global and large-scale results of Rayleigh-Bénard convection in two and three dimensions are remarkably similar so long as the Prandtl number is not too small. The classical results regarding the critical Rayleigh number, critical wavelength, and onset of convection are unaffected (see Chandrasekhar 1961, chapter 2; though not explicitly stated, the stability analysis does not depend on the dimensionality of the domain). After the onset of convection, for $\mathcal{O}(1)\,\mathrm{Pr}$ and greater, the scalings of global parameters such as the Nusselt and Reynolds numbers, as well as the boundary layer depths, are virtually the same in 2D as in 3D (although the magnitudes differ slightly) — see Schmalzl et al. (2004). van der Poel et al. (2013)

compare 2D results to 3D cylindrical RBC with no-slip sidewalls and small aspect ratio ≈ 1, finding that $\mathrm{Pr} \gtrsim 10$ for good agreement between 2D and 3D results. However, the discrepancies between 2D and 3D results should be smaller for larger aspect ratio domains, for less constraining lateral boundary conditions (free-slip or periodic), and for cuboidal rather than cyclindrical cells, as demonstrated by the results of Schmalzl et al. (2004). Many theoretical analyses of the problem have either included two dimensions as a special case, or actually assumed only two dimensions, the successful Grossmann and Lohse (2000) scaling theory for the Nusselt and Rayleigh numbers being a prime example of the latter. Therefore we choose to perform 2D simulations, given the similarity between 2D and 3D results and the vastly reduced computational requirements for 2D calculations. It is worth noting, however, that for intermediate Rayleigh numbers $10^4 \lesssim \mathrm{Ra} \lesssim 10^7$, the nature of the solution in 2D and 3D is phenomenologically different. For $\mathrm{Pr} \simeq 1$, 3D solutions exhibit a chaotic time-dependence, whereas 2D solutions in the same regime exhibit laminar rolls with at most small periodic time dependence (Deardorff and Willis 1965; DeLuca et al. 1990; Siggia 1994). Therefore in this thesis we restrict our attention to the global properties of the solutions that are less dependent on the dimensionality of the domain.

Our simulation suite runs from fully diffusive ($\mathrm{Ra} \simeq 10^2$) to well into the turbulent regime ($\mathrm{Ra} \simeq 10^{10}$); by the arguments of the previous section, the the flows in the highest two decades of Ra should be approaching Reynolds-number independence. Rayleigh numbers have been chosen such that there is at least one simulation per decade of Ra, with extra simulations run in the vicinity of $\mathrm{Ra_c}$. The Prandtl number is fixed to be $\mathrm{Pr} = 0.707$, the value for dry air at STP ("standard temperature and pressure", i.e. 273.15 K and 10^5 Pa). Reviews of RBC suggest that qualitative results remain similar so long as the asymptotic range of Pr is the same, i.e. $\mathrm{Pr} = \mathcal{O}(1)$ rather than $\mathrm{Pr} \to 0$ or ∞ (Ahlers et al. 2009; Chillà and Schumacher 2012). In particular, the scaling exponent $\mathrm{Nu} \propto \mathrm{Ra}^{\alpha}$ is not strongly Prandtl-number dependent.

Choice of resolution

- By "resolution", Δ_r , we mean the smallest length scale at which it is possible to distinguish features of the flow.
- By "filter scale", Δ_f, we mean the length scale(s) associated with any filter applied to the flow, whether to the solutions or to the governing equations. If a filter is applied to the flow, we will use the terms "filter scale" and "resolution" interchangeably.
- By "grid scale" (alternatively, "grid length" or "grid spacing"), Δ_g, we mean

the actual distance between points (or cell centres) within a discretized model. This grid scale is *always* smaller than the features it can resolve, and therefore the implied filter scale. For instance, a Smagorinsky LES with a Smagorinsky coefficient of $C_\mathrm{S} \approx 0.2$ implies that $\Delta_r \sim \Delta_f \approx 5\Delta_g$ (though the exact proportionality factor is dependent on the numerics; see Mason and Brown 1999 for a detailed discussion).

A direct numerical simulation of a fluid must "resolve" all dynamically relevant scales of the fluid flow in order to justify the assumption that no small-scale processes need to be parametrized. But there are various metrics by which we can test whether a flow is "resolved". To *fully* resolve a turbulent flow, the grid spacing must resolve at least a decade into the viscous subrange (Kerr 1985); this is very computationally expensive. However, to get almost all of the statistics right, the requirements are less extreme: the grid spacing must be of the same order as the Kolmogorov dissipation length, $\eta \coloneqq H(\mathrm{Pr}^2/\varepsilon_\mathbf{u})^{1/4}$ (see, for instance, Davidson 2009, p. 395). Grötzbach (1983) showed that a grid spacing $\lesssim 2\eta$ gives sufficiently accurate turbulence statistics for simulating convection. Within fully-developed turbulence in the bulk of the fluid the exact result for the global kinetic energy dissipation rate, (2.22), may be used to estimate the smallest dynamically relevant scale:

$$\frac{\eta}{H} = \left(\frac{\mathrm{Pr}^2}{(\mathrm{Nu}-1)\,\mathrm{Ra}}\right)^{\frac{1}{4}}. \tag{2.26}$$

For "ultimate" scalings of $\mathrm{Nu} \sim \mathrm{Ra}^{1/2}\,\mathrm{Pr}^{1/2}$ and $\mathrm{Re} \sim \mathrm{Ra}^{1/2}\,\mathrm{Pr}^{-1/2}$, this gives $\eta/H \sim \mathrm{Re}^{-3/4}$, in agreement with the expression given in Chapter 1 for homogeneous isotropic turbulence, equation (1.17).

Towards the boundaries, the kinetic and thermal boundary layers must be resolved — dissipation is typically higher in these regions, reducing the smallest dynamically relevant length scale. Shishkina et al. (2010) estimated local dissipation lengths based on dissipation rates defined within the boundary layers, using these to estimate the minimum number of points N_u, N_b required within each boundary layer (thickness $\delta_\mathbf{u}, \delta_b$) in order to adequately resolve the flow. This estimate is for $10^6 < \mathrm{Ra} < 10^{10}$, so for $\mathrm{Ra} \leq 10^6$ we use the values of N_u, N_b estimated for $\mathrm{Ra} = 10^6$. Note that this extra resolution is only required in the vertical direction.

At any point in the flow the smallest of $\{\eta, \delta_b/N_b, \delta_\mathbf{u}/N_u\}$ must be resolved. Collecting the results of Grötzbach (1983) and Shishkina et al. (2010), the grid spacing is required to satisfy $\Delta x_\eta < 2\eta, \Delta x_b < \delta_b/0.35\,\mathrm{Ra}^{0.15}$, $\Delta x_\mathbf{u} < \delta_\mathbf{u}/0.31\,\mathrm{Ra}^{0.15}$ to be adequate to resolve each respective scale.

To make use of the resolution requirements, the boundary layer thicknesses must be estimated. Since the centre of the domain will be statistically well-mixed (i.e.

we expect $\partial \langle b \rangle_{A,t} \big/ \partial z \approx 0$) after the onset of convection, we must have $\delta_b/H \sim 1/(2\,\mathrm{Nu})$.This result follows from considering the stationary-state horizontally-averaged buoyancy equation in the vicinity of the boundaries; we have

$$\frac{\partial \langle wb \rangle_{A,t}}{\partial z} = \kappa \frac{\partial^2 \langle b \rangle_{A,t}}{\partial z^2}. \tag{2.27}$$

Heuristically, we expect the left hand side to be small close to the wall due to the no normal flow boundary condition. Therefore in the buoyancy boundary layer $\kappa\, \partial^2 \langle b \rangle / \partial z^2 \approx 0$, implying $\partial \langle b \rangle / \partial z \approx$ constant. The boundary conditions are $\langle b \rangle = \pm \Delta B/2$ at $z = 0, H$, and $\langle b \rangle = 0$ at $z = \delta_b, H - \delta_b$. Together with the result $\partial \langle b \rangle / \partial z \,|_{z=0,H} = -\,\mathrm{Nu} \cdot \Delta B/H$, this gives $\delta_b/H = 1/(2\,\mathrm{Nu})$.

For the parameter regimes of this study, $\mathrm{Nu} \sim \mathrm{Ra}^{2/7}$ and so $\delta_b/H \sim \mathrm{Ra}^{-2/7}$ (Ahlers et al. 2009; Castaing et al. 1989; Shraiman and Siggia 1990). Prandtl-Blasius boundary layer theory suggests that the kinetic boundary layer thickness should scale as $\delta_{\mathbf{u}}/H \sim \mathrm{Ra}^{-1/4}$, and $\delta_{\mathbf{u}} < \delta_b$ is expected over the entire Rayleigh number range here considered (Ahlers et al. 2009, figure 3). To estimate the prefactors, an over-resolved simulation with $\Delta x/H = \Delta z/H = 0.01$ was run at $\mathrm{Ra} = 10^5$, finding $\delta_{\mathbf{u}} \simeq 0.56\,\mathrm{Ra}^{-1/4}, \delta_b \simeq 2.8\,\mathrm{Ra}^{-2/7}$; these prefactors do indeed ensure that $\delta_{\mathbf{u}} < \delta_b$ for the Rayleigh number regime of the study.

For each Ra we construct an orthogonal, rectangular grid such that the grid spacing is always smaller than the smallest of the length scales $\{\Delta x_\eta, \Delta x_b, \Delta x_{\mathbf{u}}\}$. This grid consists of, in the z-direction: a uniform grid with spacing $\Delta z^{(0)} = \Delta x_{\mathbf{u}}$ for $0 \leq |z - z_{boundary}| \leq \delta_{\mathbf{u}}$; a uniform grid with spacing $\Delta z^{(1)} : \Delta x_{\mathbf{u}} < \Delta z^{(1)} < \Delta x_b$ for $\delta_{\mathbf{u}} < |z - z_{boundary}| \leq \delta_b$; a nonuniform grid expanding linearly from $\Delta z^{(1)} \to \Delta z^{(2)}$ over the range $\delta_b < |z - z_{boundary}| \leq 2\delta_b$; a uniform grid with spacing $\Delta z^{(2)} = 2\eta$ for $2\delta_b < z < H - 2\delta_b$. In the horizontal direction, grid spacing is uniformly equal to 2η throughout the domain. Time steps are chosen so that restrictions on both the advective and diffusive Courant numbers are satisfied. Details of the grid and time-step for each simulation are given in Table 2.1.

In principle, we could directly check that the resolution is sufficient post-hoc by refining the grid and re-computing all of the statistics; if they do not change as the resolution increases, then the lower resolution "fully resolves" the flow. In practice, for this thesis we note that the grid spacings of our simulations are comparable to those in similar DNS of 2D RBC (e.g. Johnston and Doering 2009).

Numerical method

All simulations referenced in this chapter, unless otherwise specified, were performed with `boussinesqFoam`. The code has been developed as part of AtmosFOAM,

Ra	$T_{\text{tot}}/4T_B$	$\Delta t/4T_B$	$\Delta z_c/H = \Delta x/H$	$\Delta z_w/H$	η/H	$\delta_{\mathbf{u}}/H$
10^2	25	6.393×10^{-5}	0.04	0.04	N/A	N/A
10^3	25	1.599×10^{-3}	0.04	0.04	N/A	N/A
1.6×10^3	51	6.393×10^{-4}	0.02	0.02	N/A	N/A
1.7×10^3	51	6.393×10^{-4}	0.02	0.02	N/A	N/A
1.8×10^3	127	6.393×10^{-4}	0.02	0.02	N/A	N/A
2×10^3	38	7.992×10^{-4}	0.02	0.02	1.410×10^{-1}	8.459×10^{-2}
10^4	25	1.598×10^{-3}	0.02	0.01	7.494×10^{-2}	5.656×10^{-2}
5×10^4	25	1.998×10^{-3}	0.02	0.01	4.240×10^{-2}	3.783×10^{-2}
10^5	38	1.598×10^{-3}	0.02	0.01	3.346×10^{-2}	3.181×10^{-2}
5×10^5	25	9.990×10^{-4}	0.02	7.067×10^{-3}	1.951×10^{-2}	2.127×10^{-2}
10^6	25	9.990×10^{-4}	0.02	5.963×10^{-3}	1.551×10^{-2}	1.789×10^{-2}
5×10^6	38	9.990×10^{-4}	1.797×10^{-2}	2.990×10^{-3}	9.151×10^{-3}	1.196×10^{-2}
10^7	60	5.115×10^{-4}	1.454×10^{-2}	2.515×10^{-3}	7.300×10^{-3}	1.006×10^{-2}
2×10^7	51	3.996×10^{-4}	1.165×10^{-2}	2.114×10^{-3}	5.827×10^{-3}	8.459×10^{-3}
10^8	38	3.197×10^{-4}	6.729×10^{-4}	1.130×10^{-3}	3.459×10^{-3}	5.657×10^{-3}
10^9	22 (45)	1.279×10^{-4}	4.543×10^{-4}	4.544×10^{-4}	1.645×10^{-3}	3.181×10^{-3}
10^{10}	20 (76)	7.992×10^{-5}	1.563×10^{-3}	1.789×10^{-4}	7.832×10^{-4}	1.789×10^{-3}

Table 2.1: Details of 2D DNS of RBC (Section 2.2). The first column gives the Rayleigh number for each simulation. The second column gives the total simulation time, nondimensionalized by the (approximate) eddy turnover time, $T_{\text{e}} \approx 4T_B = 4\sqrt{H/\Delta B}$. The $\text{Ra} = 10^9$ and 10^{10} simulations were spun up on a coarser grid (the $\text{Ra} = 10^8$ grid), then after reaching equilibrium the grid was refined. The simulation time on the finer grid is given, followed by, in parentheses, the total simulation time on both grids for that Rayleigh number. The third column gives the time-step size nondimensionalized by T_{e}. The fourth column gives the vertical grid spacing of the uniform layer in the centre of the domain, which is equal to the uniform horizontal grid spacing. The fifth column gives the vertical grid spacing of the uniform layer adjacent to the upper and lower boundaries. The sixth and seventh columns give the physical length scales used to estimate the required resolution, the (bulk) Kolmogorov dissipation length η/H (equation (2.26)) and the kinetic boundary layer thickness, $\delta_{\mathbf{u}}/H \simeq 0.56\,\text{Ra}^{-1/4}$.

an open-source library for atmospheric computational fluid dynamics, itself based on the OpenFOAM CFD package. AtmosFOAM is freely available on GitHub at github.com/AtmosFOAM/AtmosFOAM as part of the AtmosFOAM project. Version 7 of OpenFOAM was used throughout this thesis (The OpenFOAM Foundation 2019).

In `boussinesqFoam`, the equation set (2.11)-(2.13) is solved in advective form. Advective form was chosen in order for the algorithm to be as close as possible to a single-fluid version of the multi-fluid Boussinesq code described in 4.3. The solver is otherwise similar to the flux-form compressible solver `exnerFoam` described in detail in Weller and Shahrokhi (2014).

Term	Discretization/solution method
advection (b)	Total variation-diminishing with van Leer limiter
advection ($\mathbf{u}$)	2nd-order linear upwind
$\boldsymbol{\nabla}$	2nd order Gauss linear
$\boldsymbol{\nabla}^2$	2nd order Gauss linear
interpolation	2nd order linear (i.e. central differencing)
pressure (P)	GAMG with DIC smoother; rel. tol. 10^{-2}; abs. tol. 10^{-6}
time-stepping	Crank-Nicolson with off-centring coefficient 0.55

Table 2.2: Details of the spatial and temporal discretizations used in the direct numerical simulations, as well as details of the implicit pressure solver.

The spatial discretization uses Arakawa C-grid staggering in the horizontal and Lorenz staggering in the vertical. Temporal discretization is Crank-Nicolson with off-centring coefficient set equal to 0.55; therefore the time-stepping is almost second-order.

Prognostic variables are the buoyancy, b, at cell centres, and the volume flux, $\phi \coloneqq \mathbf{u} \cdot \mathbf{S}_f$, at cell faces, where $\mathbf{S}_f$ is the outward-pointing area vector of face f. Advection of b is total variation-diminishing (with a van Leer limiter) to preserve boundedness, while advection of ϕ is linear upwind. The viscous and diffusive terms are discretized using Gaussian integration with 2nd-order linear interpolation. Thus the spatial discretization is (almost) second-order accurate.

The only diagnostic variable is the pressure, P, at cell centres. A Poisson equation is solved implicitly for P, which maintains a divergence-free velocity field (i.e. it ensures Equation (2.13) is satisfied). The solution is then iterated to convergence. The generalized Geometric-Algebraic MultiGrid (GAMG) method (with diagonal incomplete-Cholesky smoothing) is used for the implicit pressure solves, with a relative tolerance of $\leq 10^{-2}$ and an absolute tolerance of 10^{-6}. An introduction to

algebraic multigrid methods may be found in chapter 13 of Saad (2003), while a description of the OpenFOAM implementation of GAMG is given in Behrens (2009).

Two outer iterations (for the whole of the above method) and two inner iterations (for the implicit pressure solves) are performed per time-step.

Spatial and temporal discretizations of the various terms in Equation (2.11)-(2.13), as well as details of the pressure solver, are summarized in Table 2.2.

Calculation of Nu, Re, δ_b

The Nusselt number, Reynolds number, and boundary layer depths are calculated as follows:

Nu: The most direct way of calculating Nu is to integrate the (dimensionless) heat flux over the entire domain, then take a time average: $\mathrm{Nu} = \langle wb - \partial b/\partial z \rangle_{V,t}$. However, if the flow is statistically stationary, then the time-averaged *horizontally* averaged (dimensionless) heat flux is independent of height, so calculating the time-averaged vertical buoyancy gradient averaged over the top and bottom boundaries gives a second estimate, $\mathrm{Nu_w} \coloneqq \langle - \partial b/\partial z \rangle_{A,t;z=0,H}$. The equivalence of these two expressions for Nu provides an extra check for the statistical steadiness of the numerical solutions. Another check for statistical stationarity is provided via the kinetic and thermal dissipation rates (calculated using equations (2.22)-(2.23)). Thus for a statistically stationary state, convergence of $\mathrm{Nu} = \mathrm{Nu_w} = \varepsilon_b = 1 + \varepsilon_{\mathbf{u}}/\mathrm{Ra}$ is required.

Re: The calculation of a Reynolds number based on the definition $\mathrm{Re} \coloneqq UL/\nu$ requires the choice of a velocity scale and a length scale. For RBC, the only length scale we can reasonably choose for a bulk Reynolds number must be the domain height H, as this is the only external length scale in the problem. However, what is a reasonable representative velocity scale, U? Several possible choices are suggested in Ahlers et al. (2009) and Kerr (1996); we shall consider velocity scales based on the turning points of the velocity variance profile:

$$U_1 \coloneqq \sqrt{\mathrm{mean}(\mathrm{var}(u)_{x,t})}; \quad U_2 \coloneqq \sqrt{\max(\mathrm{var}(u)_{x,t})}; \quad U_3 \coloneqq \sqrt{\max(\mathrm{var}(w)_{x,t})} \tag{2.28}$$

An a priori estimate of Re can be found by assuming free-convective scaling, $U = U_B \coloneqq \sqrt{\Delta B\ H}$, implying $\mathrm{Re} = \sqrt{\Delta B\ H^3/\nu^2} = \mathrm{Ra}^{1/2}\,\mathrm{Pr}^{-1/2}$.

δ_b: If the flow is statistically stationary, the buoyancy will be well-mixed in the interior of the domain, so the time-averaged buoyancy profile must be approximately constant outside of the boundary layers, and approximately linear

within due to the fixed buoyancy boundary conditions. Thus one measure of the thermal boundary layer thickness is

$$\delta_b^{(1)} \coloneqq -\frac{\Delta B}{2\frac{\mathrm{d}\langle b\rangle_{x,t}}{\mathrm{d}z}|_{\mathrm{wall}}}. \tag{2.29}$$

Following Kerr (1996), we also estimate the thermal boundary layer thickness from the locations of the maxima of the buoyancy variance profile:

$$\delta_b^{(2)} \coloneqq |z(\max(\mathrm{var}(b)_{x,t})) - z(\mathrm{wall})|. \tag{2.30}$$

Both the upper and lower boundary layer thicknesses should be the same.

The above time averages are calculated over at least 5 eddy turnover times ($T_\mathrm{e} \approx 4\ T_B$). Time-averages are also calculated over twice and three times this minimum averaging time, and all simulations show convergence between the averages taken over these three different times. The total simulation time for each Rayleigh number is given in Table 2.1.

2.2.1 Phenomenology of RBC

Direct numerical simulations of 2D, dry, Boussinesq Rayleigh-Bénard convection were performed for the range $10^2 \leq \mathrm{Ra} \leq 10^{10}$ for a fluid with Prandtl number 0.707 (the value for dry air at standard temperature and pressure). For each Ra, the fluid was initialized from the hydrostatically-balanced resting state (2.20), with small random perturbations to the buoyancy field $|\delta b_\mathrm{pert}| \leq 0.01\Delta B$ drawn from a uniform distribution. The aspect ratio of the domain was set equal to the critical wavelength: $\Gamma = L_x/L_z = \lambda_c/H \simeq 2.02$. Each simulation was run until a statistically-steady equilibrium was reached, determined by the convergence of the time-mean values of $\mathrm{Nu}, \mathrm{Re}, \delta_b$, and the equivalence of the four methods of estimating Nu. We also ran simulations at a much larger aspect ratio of $\Gamma = 10$ for $10^2 \leq \mathrm{Ra} \leq 10^8$, finding the same results for $\mathrm{Nu}, \mathrm{Ra}, \delta_b$, and no change in the qualitative nature of the solution; therefore all results reported are from the $\Gamma = \lambda_\mathrm{c}$ simulations unless otherwise stated.

Since $\mathrm{Nu} \approx \mathrm{Nu_w} \approx \varepsilon_b \approx 1 + \varepsilon_\mathbf{u}/\mathrm{Ra}$ for all simulations (not shown), verifying statistical steadiness, only Nu is discussed hereafter. All three methods of estimating the Reynolds number also produce very similar results (Figure 2.3b), and the free-convective scaling (with proportionality factor $\simeq 0.4$) gives good agreement with the observed scaling, especially for $\mathrm{Ra} \gtrsim 10^6$.

Figure 2.2 shows single-time snapshots of the 2D buoyancy field in fully developed RBC at various Rayleigh numbers. The solutions show several characteristic

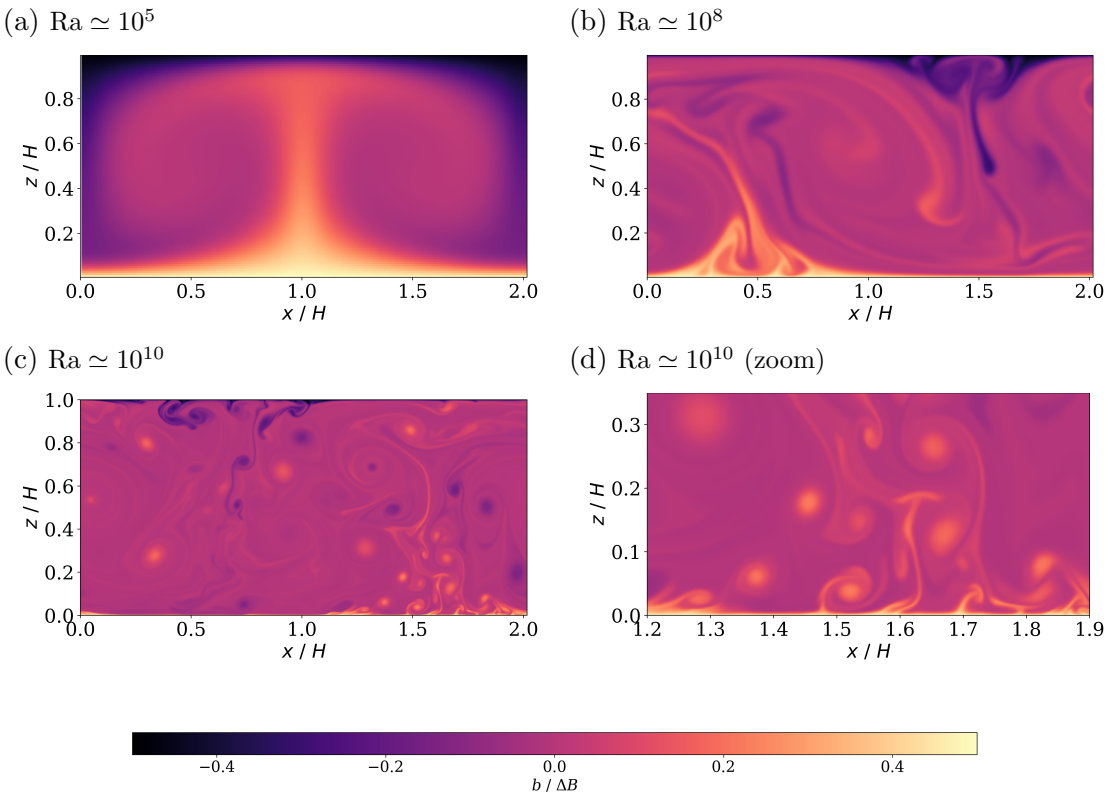

Figure 2.2: Snapshots of buoyancy fields in 2D Rayleigh-Bénard convection at varying Rayleigh number. In (a), the flow is convective but steady; in (b), the flow is turbulent, but only just, with Re $\simeq$ 5000; in (c), the flow is highly turbulent and exhibits many small scale features; (d) is the same flow as (c) but zoomed in to show small-scale features close to the lower boundary layer, and also to demonstrate the resolution.

regimes. For Ra $<$ Ra$_c$, diffusion damps out any motion and the solution is entirely diffusive (not shown). As Ra increases above Ra$_{\text{crit}}$ the solution exhibits first steady convection (a), then transitional turbulence (b), and finally fully-developed convective turbulence (c-d). This broad phenomenology is valid in both 2D and 3D, so for the remainder of the thesis we restrict to 2D. Reproducing this phenomenology serves both to demonstrate the usefulness of RBC as a model of convection, and to validate the chosen numerical method.

The scalings of Nu, Re, and δ_b are shown in Figure 2.3, along with snapshots of buoyancy fields from representative simulations in each phenomenological regime in figure 2.2. A transition from diffusive to convective behaviour is observed in both the Nusselt (figure 2.3a) and Reynolds (figure 2.3b) numbers at Ra $\approx$ 1700, in agreement with the prediction Ra$_c \simeq$ 1708. In addition, this circulation develops with approximately the correct horizontal length scale: the most commonly observed number of convective rolls is 5 in our aspect number 10 domain, implying a critical wavelength $\lambda_c \approx 2$, in good agreement with the theoretical prediction $\lambda_c \simeq 2.02$. A transition to turbulence follows between $10^7 \lesssim$ Ra $\lesssim 10^8$, as expected given that

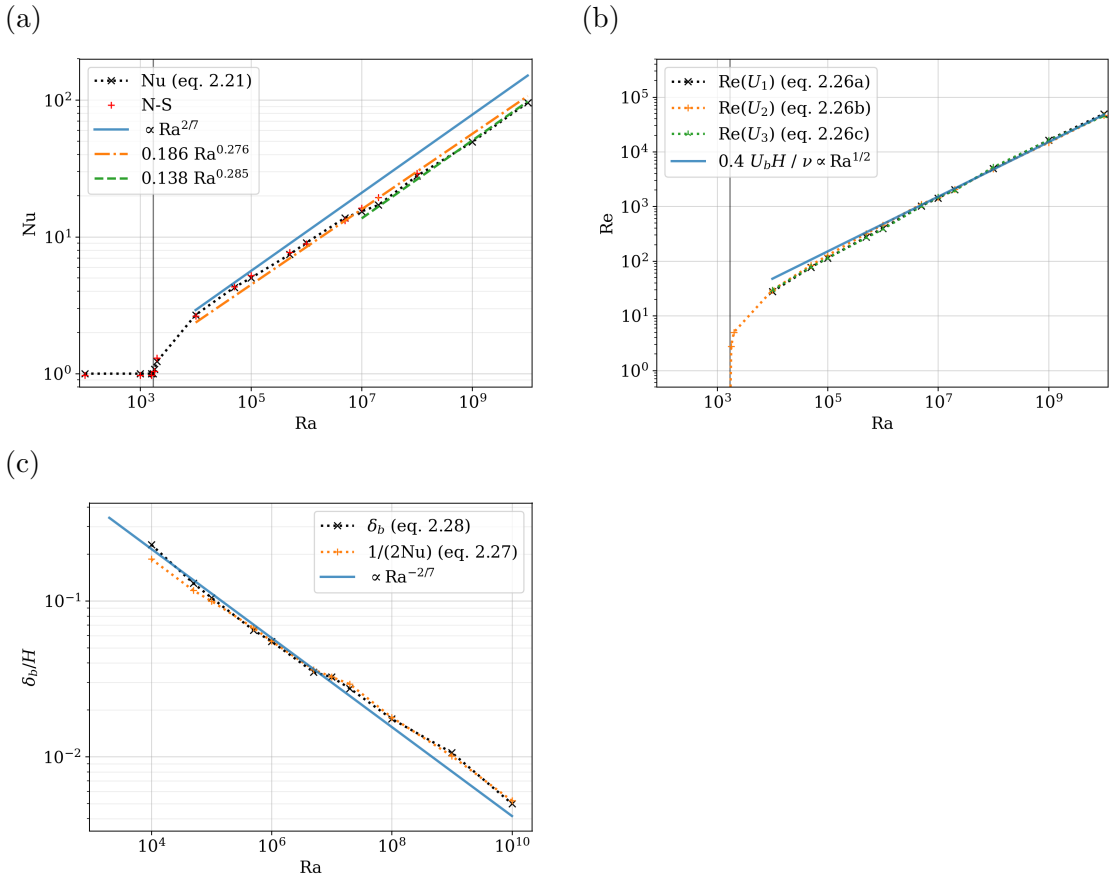

Figure 2.3: Validation of 2D Rayleigh-Bénard direct numerical simulations, showing scaling with applied buoyancy forcing, Ra, of: (a) heat transport (Nu); (b) momentum transport (Re); and (c) thermal boundary layer thickness (δ_b). In (a)-(c), the black crosses joined by a dotted line denote our main results. In (a) and (b), the solid black vertical line marks the theoretical critical Rayleigh number, $\mathrm{Ra_c} \simeq 1708$. In (a) the solid blue line follows the theoretical $\mathrm{Nu} \propto \mathrm{Ra}^{2/7}$ scaling; the orange dash-dotted line follows the best fit line of Kerr (1996), $\mathrm{Nu} = 0.186\,\mathrm{Ra}^{0.276}$ (3D); the green dashed line follows the best fit of Johnston and Doering (2009), $\mathrm{Nu} = 0.138\,\mathrm{Ra}^{0.285}$ (2D), valid above $\mathrm{Ra} \simeq 10^7$. In (a) the red pluses show Nusselt numbers calculated from simulations run with a fully compressible Navier-Stokes solver. In (b) the three dotted lines show Reynolds numbers calculated from the alternative definitions in Equation (2.28); the theoretical scaling, $\mathrm{Re} \propto \mathrm{Ra}^{1/2}$, is shown as a solid blue line. In c), the orange crosses joined by a dashed line show boundary layer thicknesses estimated from $1/2\,\mathrm{Nu}$ (Equation (2.29)); the solid blue line shows the theoretical scaling, $\delta_b \propto \mathrm{Ra}^{-2/7}$.

$\mathrm{Re} \approx 2000$ for $\mathrm{Ra} \approx 2 \times 10^7$. This can be seen in the qualitative nature of the flow: figure 2.2a is steady, representative of all flows with $\mathrm{Ra_c} \lesssim \mathrm{Ra} \lesssim 10^7$; while above $\mathrm{Ra} \gtrsim 2 \times 10^7$ the flow is intermittent and exhibits patterns on multiple scales, characteristic of turbulence, as seen in Figs. 2.2b-d.

The Nusselt number obeys a power law close to $\mathrm{Ra}^{2/7}$, and the Reynolds number a power law close to $\mathrm{Ra}^{1/2}$, from shortly after the onset of convection to the highest Rayleigh number considered. These are the expected exponents within this param-

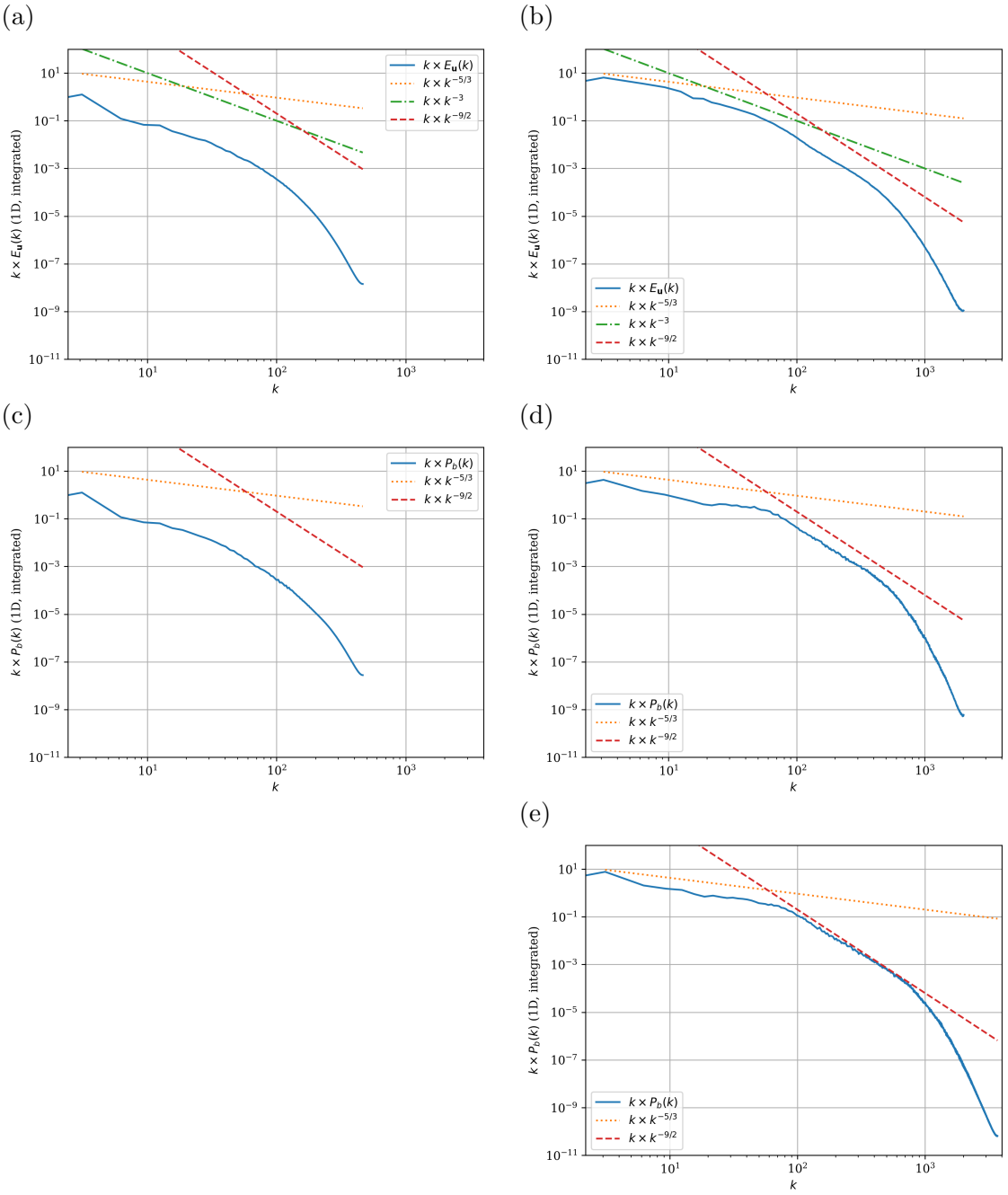

Figure 2.4: Time-averaged, vertically-integrated horizontal spectra of velocity (a,b) and buoyancy (c,d,e) at Ra $= 10^8$ (left column) and Ra $= 10^{10}$ (right column). Solid blue lines plot the spectra; the orange dotted lines are $\propto k^{-5/3}$; the green dot-dashed lines are $\propto k^{-3}$; and the red dashed lines are $\propto k^{-9/2}$. The simulations in (a-d) used a grid spacing in the bulk $\approx 2\eta$, while the simulation in (e) used a grid spacing $\approx \eta$. Spectra are averaged over $\approx 5T_e$, and integrated vertically outside of the boundary layers.

eter regime (Ahlers et al. 2009; Chillà and Schumacher 2012). Both methods of calculating δ_b give similar results for all Ra, and for Ra $\gtrsim 10^5$ the agreement is very close, showing that the interior of the domain is well-mixed outside of the boundary layers for Ra $\gtrsim 10^5$. The three different possibilities for the velocity scale in the

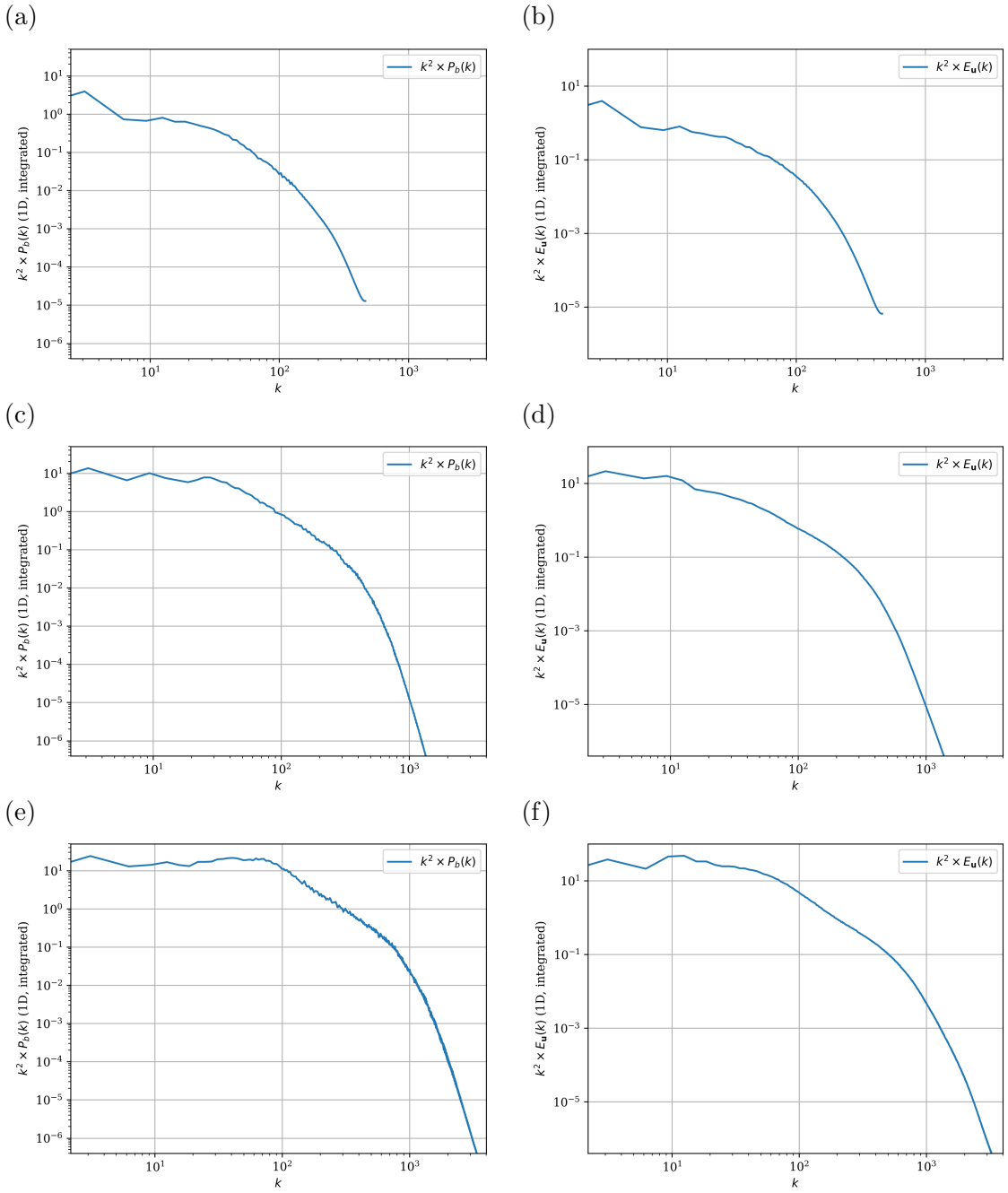

Figure 2.5: Time-averaged, vertically-integrated horizontal spectra of thermal (left column) and kinetic (right column) dissipation rates at Ra = 10^8 (a,b), 10^9 (c,d), and 10^{10} (e,f). Spectra are averaged over $\approx 5T_e$, and integrated vertically outside of the boundary layers.

Reynolds number calculation give similar results. A reduction in the prefactor of the power law for Nu is observed between $10^7 < \mathrm{Ra} < 10^8$, which coincides with the onset of turbulence. A similar transition is seen in the results of Johnston and Doering (2009) for finite-difference DNS of 2D dry RBC with Pr = 1. Above $\mathrm{Ra} \approx 10^7$ they observe a power law relationship between Ra and Nu of $\mathrm{Nu} = 0.138\,\mathrm{Ra}^{0.285}$, which our data are in excellent agreement with. Least-squares best-fits to our data

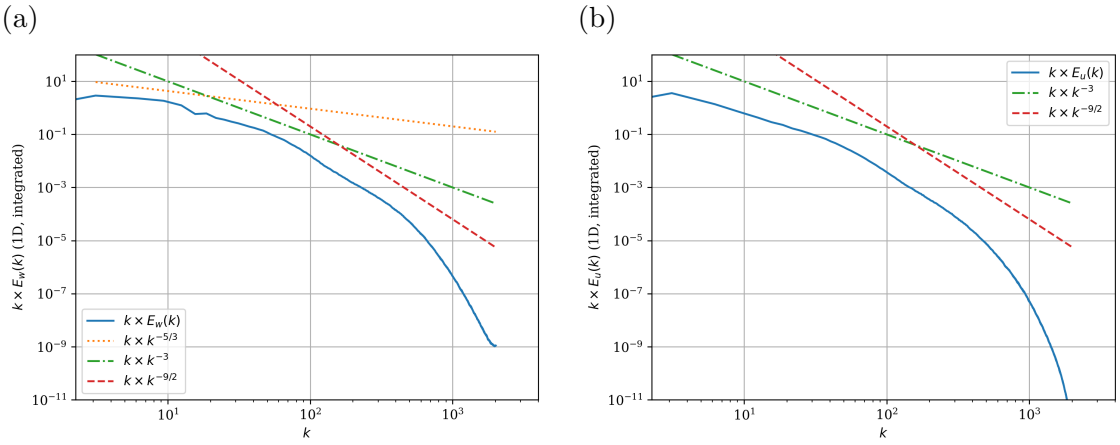

Figure 2.6: Time-averaged, vertically-integrated horizontal spectra of (a) vertical and (b) horizontal turbulent kinetic energy in RBC at Ra $= 10^{10}$. Solid blue lines plot the spectra; the orange dotted lines are $\propto k^{-5/3}$; the green dot-dashed lines are $\propto k^{-3}$; and the red dashed lines are $\propto k^{-9/2}$. Spectra are averaged over $\approx 5T_e$, and integrated vertically outside of the boundary layers.

below Ra $= 2 \times 10^7$ give Nu $= 0.268 Ra^{0.253}$, Re $= 0.238 Ra^{0.536}$, while best-fits above Ra $= 2 \times 10^7$ give Nu $= 0.174\,\mathrm{Ra}^{0.274}$, Re $= 0.473\,\mathrm{Ra}^{0.501}$.

We also ran some simulations with a fully compressible Navier-Stokes solver, with a buoyancy equation in terms of dry potential temperature. We used a reference potential temperature of 300 K and a temperature drop between the planes of 60 K, giving $\Delta\theta/\theta_r = 0.2$, meaning that for these simulations the Oberbeck-Boussinesq approximation is of questionable validity. Nusselt numbers determined from simulations with that solver (subject to the same resolution and convergence requirements as the Boussinesq solver) are shown in Figure 2.3; results are almost identical for Ra $\lesssim 5 \times 10^6$, although for Ra $\gtrsim 10^7$ the Navier-Stokes simulations do not produce the drop in prefactor observed in the Boussinesq simulations. This shows that the Boussinesq equations are more than adequate to simulate RBC.

Figure 2.4 shows time-averaged horizontal spectra of the velocity (a,b) and buoyancy (c,d,e) at Ra $= 10^8$ (left column) and Ra $= 10^{10}$ (right column). The spectra were vertically integrated outside of the boundary layers (i.e. between $2\delta_b$ and $H - 2\delta_b$, and averaged over $\approx 5T_e$. Figs. (a-d) have a resolution $\approx 2\eta$ outside of the boundary layers, while (e) has a grid spacing in the bulk $\approx \eta$. Since the buoyancy spectra (d, e) are identical for wavenumbers greater than the Nyquist wavenumber of the lower-resolution simulation (d), the coarser resolution requirement is clearly adequate; the finer resolution simply serves to resolve further into the dynamically-unimportant dissipation range.

Both Ra $= 10^8$ and Ra $= 10^{10}$ spectra are qualitatively similar, exhibiting power-law scaling with similar exponents. This is clearest in the case of the buoyancy spectra, where scaling approximately $\propto k^{-5/3}$ is clearly visible in Figure 2.4(d, e)

($\mathrm{Ra} = 10^{10}$) for about a decade of wavenumbers, suggesting the presence of fully-developed turbulence. This is followed by a clear drop off around $k \approx 50$ to $\propto k^{-9/2}$ for approximately another decade; this is the viscous subrange. For $\mathrm{Ra} = 10^8$ similar behaviour is observed, although the crossover in scalings is less clear, and occurs at a lower wavenumber ≈ 20, as expected given the relatively low Reynolds number (i.e. the Reynolds number is too small for a well-separated inertial subrange to develop). The similarity of the spectra before the viscous drop-off suggests that the highest Rayleigh numbers considered in our DNS suite are approaching a Reynolds number-independent regime. This can be seen more clearly in Figure 2.5, which shows the time-averaged, vertically-integrated horizontal spectra of the thermal (left column) and kinetic (right column) dissipation rates in fully developed convection at $\mathrm{Ra} = 10^8$ (a,b), 10^9 (c,d), and 10^{10} (e,f). As the Rayleigh number increases, the spectrum remains similar for wavenumbers below the dissipation length. This is especially true for $\mathrm{Ra} = 10^9$ and 10^{10}, whose spectra are very similar for $k \lesssim 30$. Since $k = 2\pi/\lambda$, this suggests that structures larger than $\approx 0.1H$ should be similar between the two flows.

The scaling of the TKE spectra is more ambiguous, appearing to consist of a short Kolmogorov inertial range $\propto k^{-5/3}$ ($\pi \lesssim k \lesssim 10$ in Figure 2.4b), followed by a Kraichnan k^{-3} spectrum ($10 \lesssim k \lesssim 50$ in Figure 2.4b), before the viscous drop off. The scalings are observed in the same range of wavenumbers as the unambiguous $\propto k^{-5/3}$ scaling of the buoyancy power spectral density, i.e. $\pi \lesssim k \lesssim 50$. Figure 2.6 shows the spectra of the vertical (a) and horizontal (b) components of the TKE; the dual scaling is clearest in the spectrum of the vertical TKE, while the horizontal spectrum appears to exhibit only the k^{-3} scaling. Such scalings are expected for 2D turbulence forced at some wavenumber k_F with an inverse energy cascade at low wavenumbers $k < k_F$ and a forward enstrophy cascade at high wavenumbers $k > k_F$ (Kraichnan 1967). However similar scalings have been observed in fully three-dimensional RBC; for instance, Kerr (1996) observed in their TKE spectra (their Figure 5e):

> a low-wavenumber kinetic energy spectrum of $k^{-5/3}$ and a high wavenumber spectrum of k^{-3} are given, very reminiscent of theoretical predictions in two-dimensional turbulence of a backwards energy cascade and a forwards enstrophy cascade, with injection of energy and enstrophy at the transition wavenumber.

Although Kerr noted the buoyant plumes (which are predominantly sheet-like, i.e. quasi-2D, in 3D RBC) as a possible forcing mechanism for this turbulence, no unambiguous peaks were found in the buoyancy flux or kinetic or buoyancy dissipation spectra.

To our knowledge, little further research has been performed on the possibility of an inverse cascade in RBC, forced by the buoyant plumes (although evidence of an inverse cascade has been discovered independently by other researchers, for instance Togni et al. 2015). However, within atmospheric convection the paradigm of "anarchy turbulence" has been advanced (Zilitinkevich 1973; Zilitinkevich et al. 1998, 2021), where buoyancy-driven turbulence is responsible for an inverse cascade *in the vertical*, while mechanical (i.e. shear-driven) turbulence performs a forward cascade. That is, buoyant plumes form at small scales and merge together to form ever-larger scales, generating a circulation on much larger scales than the initial energy injection length scale. This paradigm is clearly qualitatively seen in high-Ra RBC (e.g. Figure 2.2b-d) as well as in LES of the atmospheric boundary layer (for instance, Figure 8 of Bopape et al. 2020). Within RBC, further research is needed to investigate the possible inverse cascade and, if it exists, its length scales of forcing. Clearly the boundary layer depth sets the initial size for plumes, but what sets the length scale once they merge to form a coherent circulation? This meta-plume size appears broadly consistent between our Ra $\sim 10^8$ and 10^{10} simulations, as can be seen qualitatively in the buoyancy fields (respectively Figure 2.2b,c). Assuming the meta-plume size is the energy-injection wavenumber, we can also quantitatively see its consistency between the Ra $= 10^8$ and 10^{10} simulations in the wavenumber of the transition between the $k^{-5/3}$ and k^{-3} scalings in the TKE, which occurs at $k \approx 10$–20 for both (respectively Figs. 2.4a,b), while the buoyancy boundary layer depth decreases by a factor of ≈ 4 (Figure 2.3c).

Regardless of the exact reason for the shape of the spectrum, the fact that the spectra show similar scalings in both two and three dimensions is another reason to consider 2D RBC as a useful testbed for modelling convection, given the reduced computational requirements.

2.2.2 Demonstration of the analogy between constant viscosity RBC and LES of higher-Ra RBC

In Section 2.1.3, we motivated the study of constant-viscosity Rayleigh-Bénard convection at (relatively) low Rayleigh numbers as relevant to the modelling of the real atmosphere because, although the true atmosphere is highly turbulent, an artificially high viscosity is almost always introduced for either numerical stability, or to directly simulate turbulence. We also noted that Mason (1994) found acceptable agreement between simulations using horizontally-averaged values of eddy diffusivities from a Smagorinsky LES, and postulated that removing the vertical dependence may still give reasonable results.

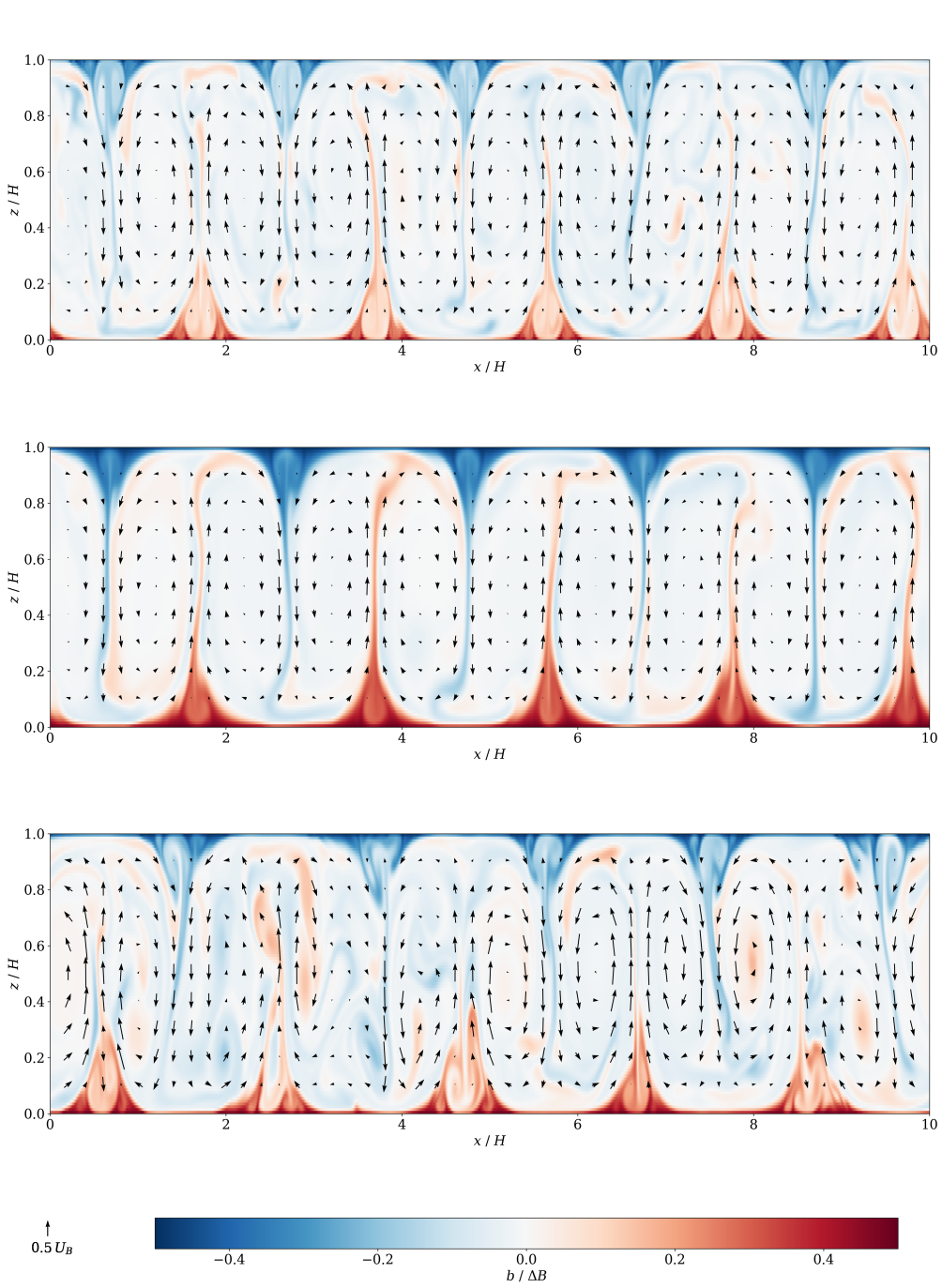

Figure 2.7: Buoyancy (colour) and velocity (arrows) in fully-developed RBC for three different simulations: (a) Smagorinsky LES of RBC with molecular Ra $\simeq 5.6 \times 10^9$, Pr $= 0.707$, using $C_S = 0.2$ and $\mathrm{Pr_t} = 0.86$; (b) constant-viscosity RBC with Ra $\simeq 2.3 \times 10^7$, Pr $= 0.86$, based on the maximum $\nu_t/\nu \simeq 17$ found within the boundary layers in the LES; (c) constant-viscosity RBC with Ra $\simeq 2.2 \times 10^8$, Pr $= 0.86$, based on the maximum $\nu_t/\nu \simeq 5.6$ found outside of the boundary layers in the LES. Both buoyancy and the velocity vectors have the same scale in all three figures.

To demonstrate this correspondence, we performed a simulation of turbulent RBC using a Smagorinsky LES model, and compared the results to simulations with constant viscosity and diffusivity. The LES used the standard OpenFOAM implementation of the Smagorinsky eddy viscosity scheme, with $C_{\mathrm{S}} = 0.2$, and simulated RBC with molecular $\mathrm{Ra} = 5.6 \times 10^9, \mathrm{Pr} = 0.707$ in an aspect ratio 10 domain on a uniform grid with $\Delta x = \Delta y = 0.01H$. By the Grötzbach (1983) criterion of $\Delta x < 2\eta$, this grid should be sufficient to resolve turbulent RBC with an effective $\mathrm{Ra} \approx 3 \times 10^7$ and $\mathrm{Re} \approx 2000$. This resolution criterion only applies in the bulk of the domain; since a grid spacing of $\Delta x = \Delta y = 0.01H$ guarantees that the first cell-centre lies in the log-layer for a simulated $\mathrm{Ra} \gtrsim 2 \times 10^7$ (i.e. $z^+ = z/(\nu/\sqrt{\tau_{\mathrm{wall}}}) > 30$), standard logarithmic wall functions were used to handle the collapsing turbulence length scale towards the boundaries. The turbulent Prandtl number was taken to be constant at $\mathrm{Pr}_{\mathrm{t}} = 0.86$.

After running this large-eddy simulation we diagnosed the maximum values of the turbulent viscosity within the boundary layers, and in the bulk of the domain. The maximum turbulent viscosity observed in the boundary layers was $\nu_{\mathrm{t}}/\nu \simeq 17$, while the maximum observed in the bulk of the domain was $\nu_{\mathrm{t}}/\nu \simeq 5.6$. We then ran two constant viscosity simulations with the same Prandtl number as the LES using the same grid, one with $\nu \to 17\nu$ (corresponding to $\mathrm{Ra} \simeq 2.3 \times 10^7$), and the other with $\nu \to 5.6\nu$ (corresponding to $\mathrm{Ra} \simeq 2.2 \times 10^8$).

Example snapshots of the instantaneous buoyancy fields[12] in fully-developed convection are shown in Figure 2.7. The LES field (a) looks qualitatively similar to the constant-viscosity $\mathrm{Ra} = 10^8$ flow shown in Figure 2.2b: it is turbulent and intermittent, exhibiting structures on multiple scales and recirculation in the regions of plume separation. The constant-viscosity simulations (b,c) are both qualitatively similar to the LES, especially the lower-viscosity simulation (c). In particular, note the similar overturning structures in all three simulations, especially the similar plume widths, and the similar velocity magnitudes across all three simulations: away from the boundaries, the LES is effectively just simulating a lower-Rayleigh number flow. This heuristically demonstrates the correspondence between constant-viscosity simulation, and LES of higher-Reynolds number flow, for 2D RBC.

[12]Note that these simulations were performed with a compressible Navier-Stokes solver, so the buoyancy fields shown in Figure 2.7 are derived from the prognostic dry potential temperature via $b = (g/\theta_{\mathrm{r}})(\theta - \theta_{\mathrm{r}})$, with $g = 9.81$ m s$^{-}2$ and $\theta_{\mathrm{r}} = 300$ K. However the difference in results between constant-viscosity simulations using the compressible Navier-Stokes and Boussinesq equations was shown to be small, even for quite large relative potential temperature differences $\Delta\theta/\theta_{\mathrm{r}} \approx 0.2$ for which the Boussinesq approximation is of questionable validity.

2.3 Exploration of the grey zone of 2D dry RBC

We argued in the Introduction that there is no reasonable hope of ever being able to numerically simulate all dynamically relevant scales of convection, and so we must parametrize some of the inaccessible scales. For filter scales much greater than the length scales of the dominant energy-containing structures of the flow, ℓ_L, Reynolds-averaging ideas apply; this is the regime of applicability of traditional convection and boundary layer parametrization schemes, which are fundamentally one dimensional. For filter scales much less than ℓ_L, the techniques of large-eddy simulation are applicable. However, current model grid spacings imply filter scales in between these two limits; this is the grey zone.

It is not currently well-understood how to parametrize subfilter terms for filter scales in the grey zone. In order to better understand the grey zone, we present an analysis of the grey zone of 2D dry RBC.

To investigate the grey zone of RBC, we performed numerical simulations at $\mathrm{Pr} = 0.707$ and $\mathrm{Ra} = 10^5, 10^8$ over a range of horizontal grid spacings. To ensure that the boundary layers remain adequately resolved, the vertical grid spacing was fixed to be the same as the DNS for all simulations (see Table 2.1). If the boundary layers are not well-resolved, some sort of wall function must be employed to ensure the correct heat and momentum transport at the walls. This is usually employed in LES of the atmosphere, where surface layer similarity theories are used to provide near-wall profiles of flow variables. For our purposes, this would add another layer of complexity, and potentially ambiguity, to the model, and so we chose instead to retain the graded grid close to the walls. Time steps were also kept identical to the DNS.

The horizontal grid spacing was increased sequentially from the DNS grid spacing to $\Delta x = 100H$; see Tables 2.3, 2.4 for details of the grid spacings used at, respectively, $\mathrm{Ra} = 10^5$, 10^8. By definition, at DNS resolution all convection must be resolved. At the coarsest grid spacing, ≈ 50 complete overturning circulations would fit within a single horizontal cell width (and 100–250 in the implied filter volume, $\Delta_\mathrm{f} \sim \Delta_\mathrm{r} > 2\Delta_\mathrm{g}$), meaning convection at this resolution should be fully subfilter. Therefore this range of grid spacings spans the grey zone.

This leads to some cells with very high aspect ratio; motivation for this approach comes from the fact that operational atmospheric models rarely have equal aspect ratio cells, typically having finer grid spacing in the vertical than the horizontal (due to the strongly stratified nature of geophysical flows). For instance, the Met Office UKV operational NWP model has a horizontal grid spacing of 1500 m, but the vertical levels are separated by a spacing of only $\sim$ 10–100 m in the lowest kilometre of the atmosphere, giving a cell aspect ratio of up to ~ 100. Vertical and horizontal

$\Delta x/H$	AR	$T_{\text{tot}}/T_{\text{e}}$	Nu($25T_{\text{e}}$)	Re($25T_{\text{e}}$)	Nu(eqm.)	Re(eqm.)
0.01	10	38	5.01	113	5.01	113
0.02	10	38	5.01	113	5.01	113
0.025	10	38	5.01	114	5.01	114
0.0625	10	38	4.98	115	4.98	115
0.15625	10	38	4.82	118	4.82	118
0.4	10	125	3.83	96.3	4.05	95.5
0.90909	10	100	3.99	89.2	4.11	88.9
1.0	10	250	5.95	110	6.11	111
1.1111	10	100	3.79	83.8	3.86	82.9
0.4	100	100	3.83	96.3	4.08	95.0
0.5	100	125	3.82	87.2	3.83	87.4
0.625	100	100	3.46	81.1	3.74	80.1
0.8	100	100	3.53	81.8	5.17	99.9
0.90909	100	125	3.99	89.2	4.11	89.0
0.97087	100	100	4.93	100	4.92	99.9
1.0	100	250	4.24	89.0	5.26	103
1.0309	100	100	4.85	99.2	4.84	99.0
1.1111	100	125	3.79	83.8	3.86	82.9
1.25	100	125	3.10	66.6	6.12	112
1.5625	100	250	2.80	37.2	4.05	86.4
2.0	100	250	3.41	51.0	6.15	112
2.5	100	250	2.06	25.1	5.45	96.6
3.125	100	250	3.01	51.0	5.48	105
3.5714	100	250	1.54	9.82	6.06	112
4.0	100	250	1.00	2.20×10^{-4}	3.81	75.7
5.0	100	250	1.00	3.44×10^{-6}	5.76	109
5.5556	100	250	1.00	0.356	3.07	43.0
6.25	100	250	1.00	5.39×10^{-3}	5.36	106
4.0	1000	250	1.00	1.60×10^{-3}	6.02	111
5.0	1000	250	1.00	1.74×10^{-4}	5.76	109
5.5556	1000	250	1.00	1.22×10^{-3}	5.98	111
6.25	1000	250	1.00	5.39×10^{-3}	5.37	107

Table 2.3: Details of horizontal grid spacing, domain aspect ratio, and simulation time for single-fluid grey zone simulations at $\text{Ra} = 10^5$. Times are nondimensionalized by the (approximate) eddy turnover time, T_{e}. Except for the highest-resolution simulation, vertical grid spacings are identical to those used in the DNS; see Table 2.1 for details. The highest-resolution simulation has a uniform isotropic grid spacing $\Delta x = \Delta z = 0.01H$; this is the over-resolved simulation which was used to estimate the prefactors for the boundary layer scalings when estimating the DNS resolution requirements in Section 2.2. The final four columns give the Nusselt and Reynolds numbers (averaged over $5T_{\text{e}}$) for the simulations, first at $t = 25T_{\text{e}}$, and secondly at the final equilibrium (or at $t = 250T_{\text{e}}$ if no resolved convective equilibrium was reached by this time). Nusselt numbers are volume-averaged (Equation (2.21)), and the velocity scale for the Reynolds number is taken to be U_3 (Equation 2.28). Continued on next page.

$\Delta x/H$	AR	$T_{\text{tot}}/T_{\text{e}}$	Nu($25T_{\text{e}}$)	Re($25T_{\text{e}}$)	Nu(eqm.)	Re(eqm.)
12.5	1000	250	1.00	0.0123	3.86	55.6
20	1000	250	1.00	2.37×10^{-7}	1.00	3.51×10^{-4}
25	1000	250	1.00	2.14×10^{-9}	1.00	9.42×10^{-5}
40	1000	250	1.00	4.15×10^{-7}	1.00	3.59×10^{-7}
62.5	1000	250	1.00	1.73×10^{-4}	1.00	2.98×10^{-7}
100	1000	250	1.00	4.33×10^{-9}	1.00	2.67×10^{-9}
100	10^4	250	1.00	1.51×10^{-7}	1.00	2.32×10^{-7}

Table 2.3 continued. Details of horizontal grid spacing, domain aspect ratio, and simulation time for single-fluid grey zone simulations at $\text{Ra} = 10^5$. See caption of Table 2.3 for full description.

$\Delta x/H$	AR	$T_{\text{tot}}/T_{\text{e}}$	Nu($25T_{\text{e}}$)	Re($25T_{\text{e}}$)	Nu(eqm.)	Re(eqm.)
6.9156×10^{-3}	10	32	25.1	4760	25.3	4750
0.015625	10	32	24.7	4620	25.3	4590
0.025	10	38	24.5	4530	24.4	4470
0.0625	10	38	24.6	4630	24.1	4800
0.15625	10	51	22.2	3500	22.4	3600
0.4	10	51	21.5	2040	22.6	2330
0.90909	10	125	16.0	1260	17.1	1010
1.0	10	125	16.2	1280	18.9	1340
1.1111	10	125	18.6	1540	19.1	1550
2.0	10^2	125	14.6	1210	25.0	1750
2.5	10^2	125	18.8	1140	21.1	1530
3.125	10^2	125	15.0	1080	18.0	1310
3.5714	10^2	125	12.0	876	15.9	1090
4.0	10^2	125	12.3	809	18.1	1340
5.0	10^2	125	12.4	629	21.7	1420
6.25	10^2	125	14.3	228	21.0	1400
20	10^3	125	1.00	0.127	5.70	194
25	10^3	125	1.00	0.0748	5.60	160
40	10^3	125	1.00	0.0202	1.10	6.40
62.5	10^3	125	1.00	0.0081	1.00	0.0319
100	10^3	125	1.00	0.0016	1.00	0.00113
100	10^4	125	1.00	0.0022	1.00	0.00232

Table 2.4: Details of horizontal grid spacing, domain aspect ratio, and simulation time for single-fluid grey zone simulations at $\text{Ra} = 10^8$. Times are nondimensionalized by the (approximate) eddy turnover time, T_{e}. The final four columns give the Nusselt and Reynolds numbers (averaged over $5T_{\text{e}}$) for the simulations, first at $t = 25T_{\text{e}}$, and secondly at the final equilibrium (or at $t = 125T_{\text{e}}$ if no resolved convective equilibrium was reached by this time). Nusselt numbers are volume-averaged (Equation (2.21)), and the velocity scale for the Reynolds number is taken to be U_3 (Equation 2.28). Vertical grid spacings are identical to those used in the DNS; see Table (2.1) for details.

grid spacings in such models are also often varied independently of each other — in particular, refinements of horizontal grid spacings are often made independently of

refinements in the vertical.

Figure 2.8 shows the Nusselt number (a,b), Reynolds number (c,d), and time to initiation of convection (e,f) as functions of grid spacing. The Nusselt numbers are volume-averaged (Equation 2.21), while the Reynolds numbers use the velocity scale U_3 (Equation 2.28); both are time-averaged over $5T_\mathrm{e}$. Time to initiation of convection is defined as the first time at which the instantaneous value of $\mathrm{Nu} > 1.1$.

At both $\mathrm{Ra} = 10^5$ and $\mathrm{Ra} = 10^8$, the simulations can be divided into three broad categories. Firstly, for $\Delta x/\lambda_\mathrm{c} \lesssim \delta_b$, all of the global parameters remain virtually unchanged compared to the reference DNS; this is the "high resolution limit". Secondly, for $\Delta x/\lambda_\mathrm{c} \gtrsim 10$ (at $\mathrm{Ra} = 10^5$), $\Delta x/\lambda_\mathrm{c} \gtrsim 30$ (at $\mathrm{Ra} = 10^8$), no convection develops after a long integration time[13], $250T_\mathrm{e}$ for $\mathrm{Ra} = 10^5$, $125T_\mathrm{e}$ for $\mathrm{Ra} = 10^8$. This is the "fully subfilter" limit. The wide range of scales in between, $\delta_b \lesssim \Delta x \lesssim 10\lambda_\mathrm{c}$, is the grey zone of constant viscosity RBC. As δ_b depends on Ra, a practical definition of the grey zone adopted for the rest of this thesis is $10^{-1} \lesssim \Delta x/\lambda_\mathrm{c} \lesssim 10$.

At the high resolution end of this grey zone, heat and momentum transports decrease monotonically with increasing grid spacing at both $\mathrm{Ra} = 10^5$ (Figs. 2.8a,c) and 10^8 (Figs. 2.8b,d). Convection initiates marginally earlier in the $\mathrm{Ra} = 10^8$ simulations compared with the DNS for grid spacings $0.03 \lesssim \Delta x/\lambda_\mathrm{c} \lesssim 0.09$, however by $\Delta x/\lambda_\mathrm{c} \simeq 0.2$ the initiation time is $\approx 10\%$ later than the DNS for both Rayleigh numbers. Similar behaviour has been observed in studies of resolution requirements for cloud resolving models: Petch et al. (2002) performed simulations of both shallow (precipitating and non-precipitating) and deep cumulus convection, finding that in all cases grid spacings $\lesssim 0.25H$ (where their H is the sub-cloud layer depth) were required to avoid significant delays to convection initiation.

For grid spacings $\gtrsim 0.4H$, the behaviour of the Nusselt and Reynolds numbers ceases to be monotonic with increasing grid spacing. This is the *hard* grey zone, where the grid spacing is comparable to the most energetic mode, $\ell_L \approx \lambda_\mathrm{c}$. (Although ℓ_L does vary with Ra, and between 2D and 3D convection, it is always of order λ_c.) Here we see a strong dependence of both Nu and Re on the exact grid spacing, with the Nusselt number sometimes *over*predicted compared to the reference DNS.We therefore further divide the grey zone into a "hard" and a "soft" grey zone. For this thesis, a practical definition of the "hard" grey zone is the range $10^{-1}\lambda_\mathrm{c} \lesssim \Delta x \lesssim \lambda_\mathrm{c}$, while the "soft" grey zone spans the remainder of the grey zone: $\lambda_\mathrm{c} \lesssim \Delta x \lesssim 10\lambda_\mathrm{c}$.

[13]Note that the ratio between the diffusive and convective timescales is $T_\kappa/T_B = \mathrm{Ra}^{1/2}\,\mathrm{Pr}^{1/2}$, so for $\mathrm{Ra} = 10^5$ a full diffusive timescale was simulated, while for $\mathrm{Ra} = 10^8$, only $\approx 1/16^{\mathrm{th}}$ of a diffusive timescale was simulated. However for high-Rayleigh number RBC ($\mathrm{Ra} \gg \mathrm{Ra_c}$), the characteristic time for the growth of perturbations is $\propto T_B$.

In this range of grid spacings, multiple equilibria were also observed. Figure 2.9 shows a time series of instantaneous values of Nu in RBC with $\mathrm{Ra} = 10^5$; a) shows the time series from the DNS, while b) shows the time series from a run with $\Delta x/\lambda_\mathrm{c} \approx 1$. The DNS spins up to an equilibrium, with decaying periodic oscillations about the central equilibrium value. The coarse grid simulation spins up to an initial equilibrium (though convection initiation is delayed, as noted earlier), but this equilibrium turns out to be unstable, as after $\approx 10T_\mathrm{e}$ there is a sharp increase in Nu towards a second, higher-Nu equilibrium.

To qualitatively understand these behaviours, Figs. 2.10 and 2.11 show example buoyancy fields in fully-developed RBC at $\mathrm{Ra} = 10^5$ and 10^8 respectively, for a range of horizontal grid spacings. In both figures a) is from the reference DNS, while b)-d) are grey zone simulations with grid spacings of $\Delta x/\lambda_\mathrm{c} \simeq 0.2, 0.45, 1$ respectively.

At $\mathrm{Ra} = 10^5$, the circulation is still crudely resolved at $\Delta x/\lambda_\mathrm{c} \simeq 0.2$ (Figure 2.10b), although the buoyancy field is more diffuse and the plumes wider than in the DNS — this is expected as $\Delta x > \delta_b$. This helps to explain the monotonically-decreasing Nu and Re in the range $0.05 \lesssim \Delta x/\lambda_\mathrm{c} \lesssim 0.3$: as the circulation is resolved more and more poorly, the buoyancy gradients become ever weaker, leading to weaker velocities and thus weaker advective heat transport.

At $\Delta x/\lambda_\mathrm{c} \simeq 0.45$ (Figure 2.10c), the details of the circulation are not resolved at all, and the convective instability projects directly onto the grid scale, as predicted by the analysis of B. Zhou et al. (2014). Since our simulations use a constant viscosity at all grid spacings, the effective Rayleigh number remains the same at all Δx, but the effective critical Rayleigh number increases due to the true critical wavelength being unresolvable, $\lambda_\mathrm{c} < 2\Delta x$. This means that a convective circulation still develops, but is forced to occur at the grid scale. This results in artificially large velocities and Nusselt numbers, reminiscent of the phenomenon of grid point storms observed in NWP when running without a mass-flux convection scheme (e.g. Deng and Stauffer 2006).

Because the effective Rayleigh number remains the same, a circulation still develops even at very coarse grid spacings $\Delta x \gg \lambda_\mathrm{c}$ if Ra is sufficiently greater than Ra_c. We can see why by analysing the marginal stability curve for RBC at large wavelengths. The marginal stability curve for free-slip RBC is given by $\mathrm{Ra}_\mathrm{c}(a) = (1+a^2)^3\pi^4/a^2$, where $a = 2/(\lambda/H)$ is the horizontal wavenumber of a small perturbation to the resting reference solution (2.20) (Chandrasekhar 1961). For large wavelengths, $\lambda/H \gg 1$, this reduces to $\mathrm{Ra}_\mathrm{c} \approx \lambda^2\pi^4/4H^2$. If the horizontal resolution is very coarse, the smallest resolvable wavelength is $\lambda_\mathrm{c}^\mathrm{eff} = 2\Delta x > \lambda_\mathrm{c}$, making the effective critical Rayleigh number equal to $\mathrm{Ra}_\mathrm{c}^\mathrm{eff} = \pi^4(\Delta x/H)^2$. (The analysis is similar for no-slip boundary conditions, but the algebra is messier; the $\mathrm{Ra}_\mathrm{c} \propto \Delta x^2$ result remains the same, with some proportionality constant $\mathcal{O}(100)$.)

This result means that for $\mathrm{Ra} = 10^5$, the effective critical Rayleigh number only exceeds Ra for grid spacings $\Delta x \approx 10\sqrt{10}H \approx 30H$, which is what we observe in our simulations — see Figure 2.8, and the listed Reynolds numbers at 25 and $250T_\mathrm{e}$ in Table 2.3. For $\mathrm{Ra} = 10^8$, however, we could not expect the simulations to become subcritical due to the grid spacing until grid spacings $\Delta x \approx 1000H$; simulations with such coarse grids were not performed, as they would be of limited applicability to atmospheric modelling, and are not expected to give rise to any new behaviour.

Therefore the results for the Nusselt and Reynolds numbers after $25T_\mathrm{e}$ are also shown in Figs. 2.8a)-d). Note that $25T_\mathrm{e}$ equates to approximately 8 hours if we use the values for ΔB and H appropriate to the CBL; this is long enough for simulations of the cumulus-capped marine boundary layer to spin up to an approximate equilibrium (Siebesma et al. 2003). The results and their interpretation remain similar to the long-integration time results for $\Delta x/\lambda_\mathrm{c} \lesssim 0.5$ for both Rayleigh numbers considered; however for $\Delta x/\lambda_\mathrm{c} \gtrsim 1$ ($\mathrm{Ra} = 10^5$), $\Delta x/\lambda_\mathrm{c} \gtrsim 2$ ($\mathrm{Ra} = 10^8$) the severe delays to convection initiation significantly affect the circulation developed by $25T_\mathrm{e}$. For both cases, no convection develops by $25T_\mathrm{e}$ for $\Delta x/\lambda_\mathrm{c} \gtrsim 10$.

At $\mathrm{Ra} = 10^8$, the same behaviour is exhibited for very coarse grid spacings $\Delta x \gtrsim \lambda_\mathrm{c}$ as was observed at $\mathrm{Ra} = 10^5$ (Figure 2.11d): the critical wavelength cannot be resolved, but the the effective Rayleigh number is still greater than the effective critical Rayleigh number, and so convection develops at the grid scale with $\lambda_\mathrm{c}^\mathrm{eff} = 2\Delta x$. However for smaller grid spacings within the grey zone, an interesting behaviour is observed: for $\delta_b \lesssim \Delta x \lesssim H$, a full convective circulation develops, but with the wrong inter-plume spacing, $\lambda > \lambda_\mathrm{c}$. Furthermore, this wavelength depends on the grid spacing, with $\lambda(\Delta x_1) > \lambda(\Delta x_2)$ for $\Delta x_1 > \Delta x_2$ (Figs. 2.11b,c). This is very similar to behaviour found in grey zone studies of the CBL (Beare 2014) and in NWP (Lean et al. 2008), where models with insufficient resolution develop reasonable-looking convective circulations, simply on the wrong length scales. This is despite the fact that the models tend to have Δx significantly less than the expected inter-plume/inter-cloud spacing, so they "should" be able to resolve the correct smaller scale.

It has been postulated (B. Zhou et al. 2014) that this resolution-dependence of the outer length scale (inter-cloud or inter-plume spacing) is related to anisotropic mixing in the eddy diffusivity closures for the turbulent fluxes. It can be shown (Ray 1965; P. Clark, pers. comm.) that the marginal linear stability curve in RBC with anisotropic mixing is given by:

$$\mathrm{Ra} = \frac{\pi^4(\gamma_\nu a^2 + 1)(\gamma_\kappa a^2 + 1)(a^2 + 1)}{a^2}, \tag{2.31}$$

where $\gamma_\nu \coloneqq \nu_x/\nu_z$, $\gamma_\kappa \coloneqq \kappa_x/\kappa_z$ are diffusion anisotropy coefficients, and a is the

horizontal wavenumber of the perturbation to the basic state. This expression reduces to the standard RBC stability criterion when $\gamma_\nu = \gamma_\kappa = 1$. The critical Rayleigh number is the minimum of this curve with respect to a, given by setting $\partial\,\mathrm{Ra}/\partial a = 0$. After a little algebra the following 6th-order polynomial results:

$$2\gamma_\nu\gamma_\kappa(a^2)^3 + (\gamma_\nu\gamma_\kappa + \gamma_\nu + \gamma_\kappa)(a^2)^2 - 1 = 0. \tag{2.32}$$

The general case $\gamma_\nu \neq \gamma_\kappa$ is difficult to analyse by hand, but if $\gamma_\nu = \gamma_\kappa =: \gamma$ (which we would expect in the context of Smagorinsky-type eddy diffusivity closures), the single positive real root may be written:

$$a = \frac{1}{2}\sqrt{\sqrt{1 + \frac{8}{\gamma}} - 1} \tag{2.33}$$

This is a strictly decreasing function of γ (for $\gamma > 0$), meaning that the critical wavelength, $\lambda_\mathrm{c} \propto 1/a$, is a strictly *increasing* function of the anisotropy parameter γ.

To better interpret this expression, it is instructive to consider the cases $\gamma > 1$ and $\gamma < 1$ separately. If $\gamma > 1$, horizontal mixing is stronger than vertical mixing, which is expected from the extension of an LES-like filter scale-dependent pure eddy diffusivity scheme to the grey zone of resolutions. In the simplest case of a Smagorinsky scheme, γ is effectively the square of the ratio of horizontal to vertical grid spacings. As the anisotropy increases, i.e. the horizontal mixing/grid spacing increases relative to the vertical, the critical wavelength also increases. Quantitatively, for large γ, we have $a = 1/\gamma^{1/2} - 1/\gamma^{3/2} + 7/(2\gamma^{5/2}) + \mathcal{O}(\gamma^{-7/2})$; the leading term approximates (2.33) to within 10% for $\gamma \gtrsim 8$, giving $\lambda/H \to 2\sqrt{\gamma}$ as $\gamma \to \infty$ (the two-term truncation is accurate to within 1% for $\gamma \gtrsim 17$). If instead $\gamma < 1$, vertical mixing is stronger than horizontal mixing, which is the case in most non-grey zone parametrizations of the CBL to account for the strong nonlocal mixing due to the unresolved convective circulation. In this case, the critical wavelength is expected to *decrease* as the ratio of vertical to horizontal mixing (i.e. $1/\gamma$) increases. Quantitatively, for small γ, we have $a = 1/(2^{1/4}\gamma^{1/4}) - \gamma^{1/4}/(4\cdot 2^{3/4}) + \gamma^{3/4}/(64\cdot 2^{1/4}) + \mathcal{O}(\gamma^{5/4})$, giving $\lambda/H \to 2^{5/4}\gamma^{1/4}$ as $1/\gamma \to \infty$; the leading term is accurate to within 10% for $1/\gamma \gtrsim 3$. While there are limits to approximating the nonlocal vertical convective mixing by a simple eddy diffusivity, the analogy is sufficient to show that the critical wavelength of the convection that develops is directly dependent on the parametrization of the mixing. In particular, enhanced horizontal mixing is expected to widen the convective overturning circulation, while enhanced vertical mixing is expected to narrow it.

However, since we use the same viscosity at all grid spacings, this argument

does not appear to explain our grey zone results, especially since the ratio of plume width (Δx) to the inter-plume spacing (λ) remains remarkably constant at ≈ 10 throughout the range of grid spacings where $\lambda > \lambda_c$ and $\lambda \neq 2\Delta x$ is observed. If the behaviour were due to numerical diffusion, we would not expect to observe the transition to direct grid projection at $\Delta x \gtrsim \lambda_c/2$, as this projection implies the effective critical wavelength is still $\lambda_c^{\text{eff}} \approx 2$. Transitional behaviour *is* observed around $\Delta x = \lambda_c/2$, as seen in Figure 2.11c), where a circulation with $\lambda \approx 10H$ is produced, although there are also strong variations visible at the grid scale.

2.4 Discussion & conclusions

In this Chapter, we have considered the simple case of Rayleigh-Bénard convection as an analogue of atmospheric convection. We have reproduced a wide range of established results for RBC to verify our numerical implementation, in particular reproducing the expected scalings of the Nusselt and Reynolds numbers with the Rayleigh number. We have then studied what happens when the problem is systematically under-resolved, including quantitative analyses of the global parameters Re and Nu, as well as convection initiation, as functions of grid spacing. This was followed by a qualitative investigation of some example simulations throughout the grey zone.

Simulations at both $\text{Ra} = 10^5$ and 10^8 exhibit delayed initiation of convection when resolution is insufficient, as frequently observed in partially-resolved simulations of atmospheric convection. At coarse enough grid spacings the solution reverts to the diffusive regime with no motion — the filter implied by the grid has effectively reduced the Rayleigh number enough to render the problem sub-critical. However at intermediate grid spacings we find that the solution exhibits interesting dependence on the grid spacing, including strong projection of the convection pattern onto the grid. This is reminiscent of grid-point storms in numerical weather prediction.

At $\text{Ra} = 10^8$, further interesting behaviour is seen at horizontal grid spacings intermediate between the width of thermal plumes and the depth of the domain: the size of the circulation that develops increases with increasing grid spacing, a behaviour which is also observed in NWP and in partially-resolved simulations of the convective boundary layer.

We therefore conclude that, even in two dimensions, the simple case of Rayleigh-Bénard convection is a promising testbed for grey-zone convection parametrizations. These results will be the reference for later investigations into two-fluid parametrization of the grey-zone convective regime.

Future work should investigate the sensitivity of these results to the numerical

model used for the simulations, as well as perform analysis of higher-order statistics (for instance, variances and covariances) in comparison to spatially filtered reference solutions. Further, for a true weather prediction, we need to predict coherent structures in the correct locations in space and time; turning again to Lorenz (1963),

> The short-range weather forecaster, however, is forced willy-nilly to predict the details of the large-scale turbulent eddies—the cyclones and anticyclones—which continually arrange themselves into new patterns. Thus there are occasions when more than the statistics of irregular flow are of very real concern.

Reproducing the correct statistics is merely the first step in building a transient parametrization.

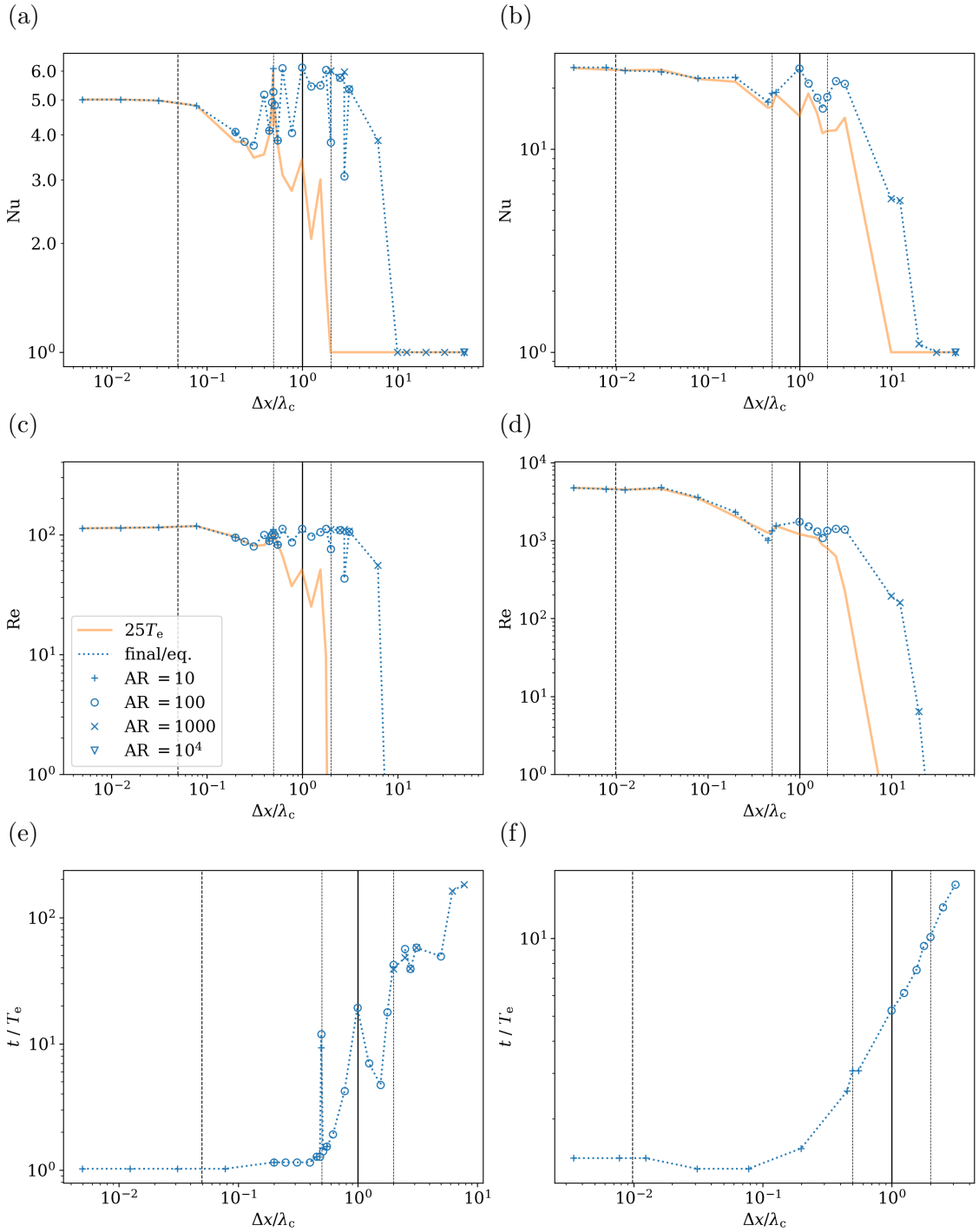

Figure 2.8: Nusselt numbers (a,b), Reynolds numbers (c,d), and time to initiation of convection (e,f) as functions of grid spacing for simulations of RBC at $\mathrm{Ra} = 10^5$ (left column) and $\mathrm{Ra} = 10^8$ (right column). Grid spacings are nondimensionalized by the critical wavelength, $\lambda_c \simeq 2.02H$. Nusselt numbers are volume-averaged (Equation (2.21)), the velocity scale for the Reynolds number is taken to be U_3 (Equation 2.28), and time to initiation is defined as the first time for which the instantaneous value of $\mathrm{Nu} > 1.1$. The blue dotted lines plot the values of Nu and Re (averaged over $5T_e$) after an equilibrium has been reached, or after $250T_e$ ($\mathrm{Ra} = 10^5$) or $125T_e$ ($\mathrm{Ra} = 10^8$), whichever is arrived at first. The solid translucent orange lines plot the values of Nu and Re after $25T_e$. Different marker styles correspond to different domain aspect ratios. The vertical lines mark out length scales of interest: the solid black line marks the critical wavelength, $\Delta x/\lambda_c = 1$; thin densely-dotted black lines mark a factor of two either side, $\Delta x/\lambda_c = 0.5, 2$; the dashed black line towards the left of each plot marks the thermal boundary layer depth, a proxy for the thermal plume width.

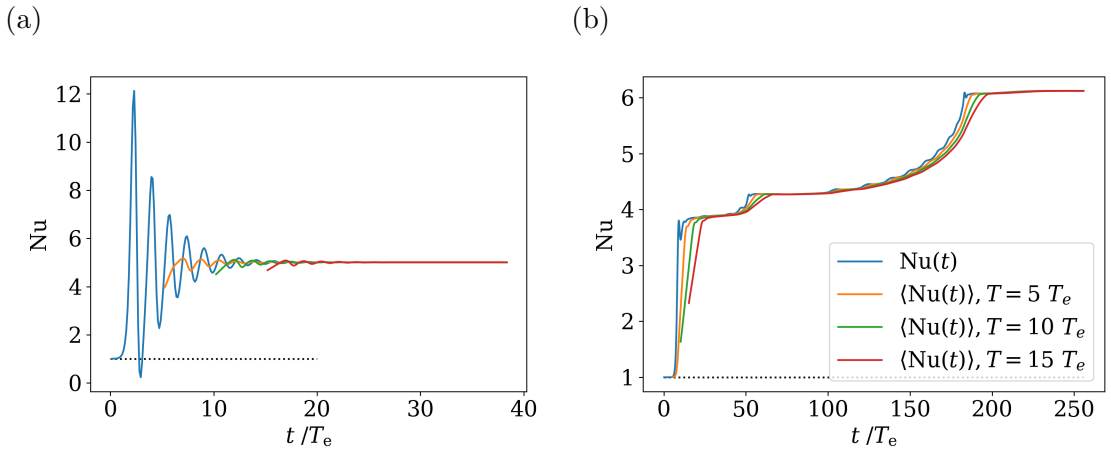

Figure 2.9: Comparison of Nusselt number time series for simulations run at different horizontal grid spacings. In (a), the simulation is the over-resolved simulation with $\Delta x \Delta z = 0.01H$ uniformly; in (b), the horizontal grid spacing is $\Delta x = 2H \approx \lambda_c$.

(a) $\Delta x = 0.02H \simeq 0.01\lambda_c$

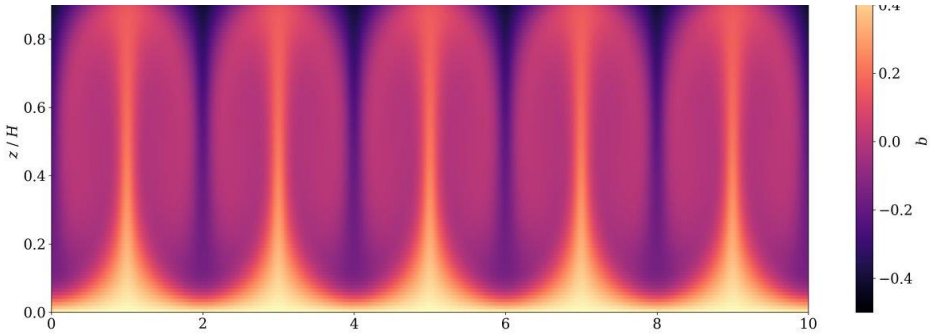

(b) $\Delta x = 0.4H \simeq 0.2\lambda_c$

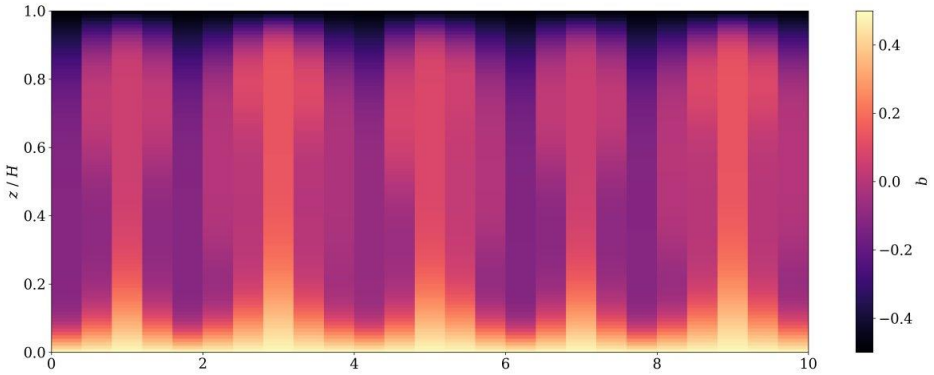

(c) $\Delta x \simeq 0.91H \simeq 0.45\lambda_c$

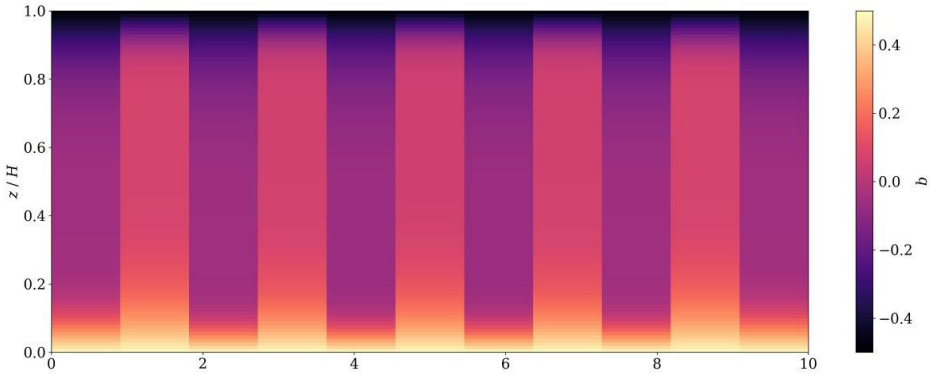

(d) $\Delta x = 2H \simeq \lambda_c$

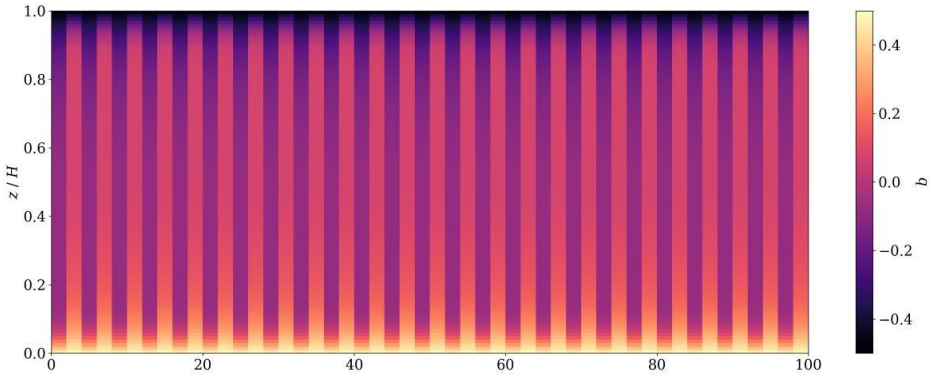

Figure 2.10: Buoyancy fields in fully-developed RBC at Ra = 10^5 at a range of horizontal grid spacings.

(a) $\Delta x = 6.9 \times 10^{-3} H \simeq 3.4 \times 10^{-3} \lambda_c$

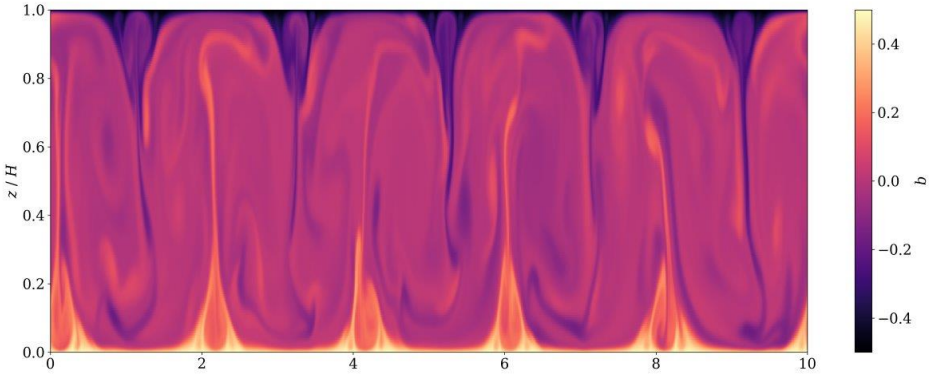

(b) $\Delta x = 0.4H \simeq 0.2\lambda_c$

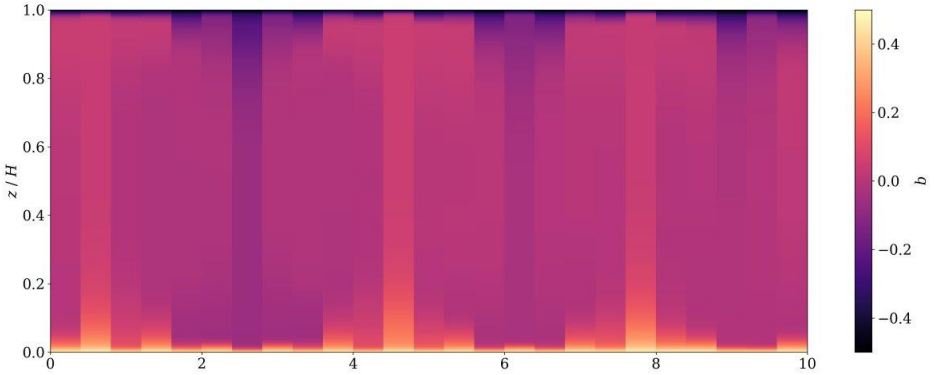

(c) $\Delta x \simeq 0.91H \simeq 0.45\lambda_c$

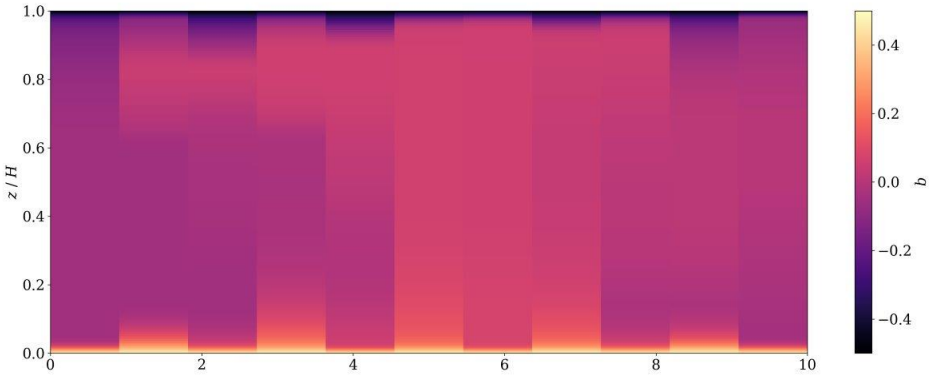

(d) $\Delta x = 2H \simeq \lambda_c$

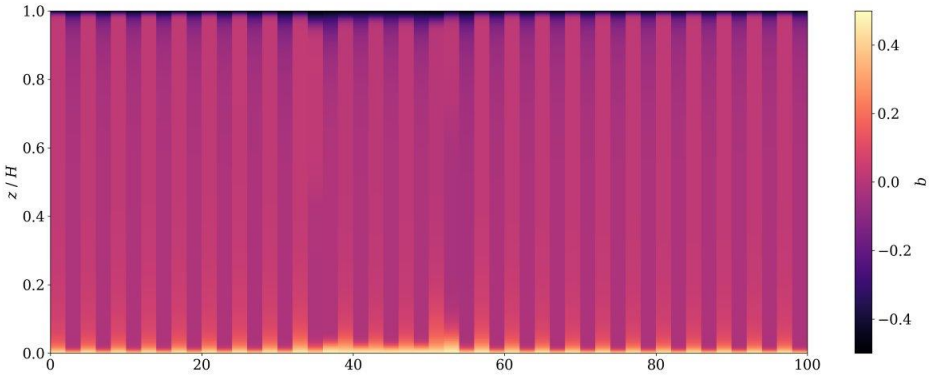

Figure 2.11: Buoyancy fields in fully-developed RBC at Ra = 10^8 at a range of horizontal grid spacings.

Chapter 3

Multi-fluid modelling for atmospheric convection

3.1 Introduction

We noted in Chapter 1 that traditional convection parametrization approaches make use of a conceptual split of the atmosphere into clouds (or updrafts) and their environment. Conceptually similar splits are used in scaling theories for Rayleigh-Bénard convection, where the convecting fluid is partitioned into filamentary plumes (analogous to updrafts and downdrafts) where the buoyancy flux and thermal dissipation is locally very strong, and their incoherent turbulent environment which occupies most of the volume (Chillà and Schumacher 2012). The properties of the fluid in these different regions are very different, which makes the partitioning useful. Similar ideas have been used to derive dynamical equations for intermittent turbulent flows (Dopazo 1977; McComb 1990 §§11.2, 11.5), where the flow is partitioned into turbulent and non-turbulent regions and then volume averaged. So-called "phase averaging" has also been proposed to conditionally split a turbulent flow into turbulent and non-turbulent parts, and then to split the turbulent part into its coherent and incoherent parts (Hussain 1983).

The resulting equations are very similar to equations governing "multi-phase" flows[1] — for instance flows containing both liquid and gas, or several species of liquid and gas. These flows are commonly studied in engineering (Brennen 2005; Städtke 2007).

Within the context of intermittent turbulent flows, conditional averaging was once thought of as a promising way forward (McComb 1990, p.413):

> Attempts to reduce the arbitrariness of decisions about the turbulent–non-turbulent interface, by working from the equation of motion in order

[1] We say "multi-phase" as this is an umbrella term used for many flows, some of which contain multiple species of liquid, gas, or plasma, but not necessarily multiple *phases* of matter.

> to obtain a conservation equation for the intermittency function (Libby 1976) or conditionally averaged transport equations (Dopazo 1977), are undoubtedly the right way forward. While at present this subject is in its infancy, in the future we can expect to see it develop as an important aspect of the usual closure problem.

Alas, conditional averaging as a theoretical tool for turbulence research never did catch on in the way McComb hoped — especially interesting since *all* of his references on conditional averaging are pre-1980, more than 10 years before the publication of the book, suggesting that the field was already dormant.

A "multi-fluid" or "conditional filtering" approach has been proposed (Thuburn et al. 2018) for modelling atmospheric convection in the grey zone, based on conditional averaging ideas for intermittent turbulent fluids (Dopazo 1977). A similar equation set was derived by Yano (2014). Multi-fluid modelling borrows conceptually from the widely-used traditional mass-flux approach, envisaging a partition of the convective system into "updraft" and "environment", but applies this systematically to the governing fluid dynamical equations. This yields fully prognostic and 3D equations for each "fluid", and does not rely on the assumptions of traditional approaches which break down at high resolutions. In particular, neither quasi-equilibrium nor small updraft fraction are assumed in the derivation. The equations are coupled by terms representing the exchange of mass, momentum, energy, and tracers. In this framework convection is fundamentally a part of the dynamics — there is no separate "convection scheme" which is called by the dynamical core.

The skewness of (joint) probability distribution functions of variables in convective flows is well known to be important (Larson et al. 2002; Zhu and Zuidema 2009) and is often poorly treated in first or second-order turbulence closures; one approach to modelling this variability is assuming bi-Gaussian joint probability distributions in PDF-based convective closures (Fitch 2019; Larson et al. 2012). Each Gaussian can be thought of as a different component of the fluid. A potential advantage of the multi-fluid approach is that even the simplest possible multi-fluid model, a two fluid model, intrinsically captures information about odd-order moments. It is therefore possible that the multi-fluid method can provide a better low-order approximation for flows with bimodal distributions, or large skewness.

Closures for the unknown terms must be provided in order to complete the multi-fluid equation set. Previous work has largely used closures borrowed from mass flux-type parametrizations. For instance, Thuburn et al. (2019) presented a two-fluid single-column model of the dry CBL based on the Thuburn et al. (2019) equation set, which used a modified form of the entraining-plume based closure of Cheinet (2003) for entrainment, and a detrainment closure formed from a combination of the

eddy-diffusivity mass-flux (EDMF) closure of Siebesma et al. (2007), who prescribed a mass flux profile, and a buoyancy-sorting based closure that Rio et al. (2010) proposed based on LES results. They found that the obtained solutions were largely similar to those using diagnostic EDMF closures, to be expected given the similarity of their closures to EDMF closures, the 1D nature of the scheme, and the smallness of the eddy turnover time compared to time-scales of boundary layer development reducing the impact of prognostic vs. diagnostic parametrization.

Tan et al. (2018) presented a less-general equation set based on the ideas of Yano (2014), explicitly assuming an anelastic equation set and neglecting horizontal subfilter variability. Conceptually the authors regard this as an extension to the EDMF framework to make it prognostic, and allow for non-vanishing convective area fraction. They use entrainment and detrainment rates which are modifications of expressions proposed by Gregory (2001) based on linking the entrainment rate to the buoyant generation of (vertical) TKE, obtaining results which are similar to a diagnostic EDMF closure for a shallow-cumulus test case.

Both Tan et al. (2018) and Thuburn et al. (2019) use equation sets which assume the pressure in all partitions is identical. This is known to lead to an ill-posed equation set in the inviscid case with no transfers between fluid partitions (Gidaspow et al. 1973); Thuburn et al. (2019) related this ill-posedness to a Kelvin-Helmholtz–like instability. To stabilize the equations, Thuburn et al. (2019) proposed using diffusion of vertical velocity, which directly damps the Kelvin-Helmholtz instability. This is effectively the introduction of an eddy diffusivity; Tan et al. (2018) use an eddy diffusivity from the outset.

Other methods have been proposed to mollify the multi-fluid instability. Notably, McIntyre (2020) showed that parametrizing the mass transfers between fluids via the convergence within a fluid partition is sufficient to stabilize the equation set. This was used by Weller et al. (2020) in a two-fluid single-column model of both the Bryan and Fritsch (2002) dry rising bubble, and a 2D CBL-like problem. The authors also used a parametrization for the pressure differences between fluid partitions based on the divergence within a partition; this was inspired by similar parametrizations used in some engineering multi-phase flows, for instance Baer and Nunziato (1986). These transfer parametrizations gave good predictions of the profiles of buoyancy, vertical velocity, and volume fraction compared to those diagnosed from horizontally-averaged reference simulations.

The principal difference between multi-phase modelling, which is well-developed for studying engineering flows, and multi-fluid modelling for turbulence, which is relatively under-developed, is that in the former it is usually obvious what the different phases are. In the context of *general* multi-fluid modelling, we are free to choose what each fluid represents, which vastly changes the burden of modelling.

The overarching purpose of this chapter is to say as much as possible about multi-fluid modelling without introducing a specific fluid partition. We begin by deriving the multi-fluid Boussinesq equations, which will be central to our investigation of multi-fluid modelling of convection for the remainder of the thesis. The derivation proceeds in a similar way to the derivation in Thuburn et al. (2018), but we retain the fluid relabelling and viscous terms from the outset. After a brief discussion of the terms requiring parametrization, we take a close look at the fluid relabelling (or "transfer") terms, deriving several exact integral expressions for them. These aid in the interpretation of the transfer terms, as well as providing a method for their calculation from reference data for arbitrary fluid partitions.These expressions are compared with similar expressions derived earlier; the more general nature of the expressions presented here is emphasized. We also sketch some ideas for how these terms could be used to provide physically-based heuristic, or formal asymptotic, derivations of conditionally-filtered transfer terms.

Armed with the exact integral results for expressions involving the indicator function, we return to a more complete discussion of all the terms requiring closure in the multi-fluid Boussinesq system. We show that retaining fluid relabelling terms from the outset allows for the conditionally-filtered transfer terms to arise naturally, and further that the suggested definition of transferred fluid properties in Thuburn et al. (2018) has some deficiencies and should be generalized. We also show that for any stress tensor linearly and isotropically related to the rate-of-strain tensor, an additional isotropic stress arises in the multi-fluid equations. Since such stress tensors are not only present in the Navier-Stokes equations, but also often used as low-order approximations of *turbulent* stress tensors, this result is of wide-ranging importance in multi-fluid modelling of turbulent flows. By analogy with compressible fluids, we propose that the nonzero divergence within a fluid partition should give rise to a further isotropic stress which can be used to parametrize (part of) the pressure differences between the fluid partitions. The energetic consequences of the conditionally-filtered stress terms are discussed, showing again that the nonzero divergence within fluid partitions has important consequences. Finally, we demonstrate the usefulness of some of the results by application to a simple problem: explicit conditional filtering of the first normal mode of Rayleigh-Bénard convection.

3.2 Derivation of the multi-fluid Boussinesq equation set

In this section a derivation of the multi-fluid Boussinesq equations is presented. This derivation differs from both Weller et al. (2020) and Thuburn et al. (2018) in explicitly including diffusive terms and relabelling terms from the outset. As in Chapter 2, we choose the Boussinesq equation set as this is the simplest fluid dynamical equation set which permits buoyant convection. The simplicity makes many of the points regarding closure clearer in section 3.4; however all of these points are still relevant in the case of fully compressible equations[2].

Our starting point is the viscous Boussinesq equation set introduced in Chapter 2:

$$\frac{\mathrm{D}\mathbf{u}}{\mathrm{D}t} = b\hat{\mathbf{k}} - \boldsymbol{\nabla} P + \nu \boldsymbol{\nabla}^2 \mathbf{u}, \tag{2.4}$$

$$\frac{\mathrm{D}b}{\mathrm{D}t} = \kappa \boldsymbol{\nabla}^2 b, \tag{2.5}$$

$$\boldsymbol{\nabla} \cdot \mathbf{u} = 0. \tag{2.6}$$

Here $\mathbf{u}$ is the velocity field, b is the buoyancy field, P is the pressure field, ν is the fluid's kinematic viscosity, and κ its buoyancy diffusivity. We envisage solving this equation set in the space-time domain $D \times [0, T]$, where $D \subseteq \mathbb{R}^d, T \in \mathbb{R}_{>0}$.

Indicator functions are used to label different regions of the flow (2.4)-(2.6) based on some set of conditions, indexed by $i, 0 \leq i < n$:

$$I_i(\mathbf{x}, t) \coloneqq \begin{cases} 1 & \text{if condition } i \text{ true at location}(\mathbf{x}, t) \\ 0 & \text{if condition } i \text{ false at location}(\mathbf{x}, t) \end{cases} \tag{3.1}$$

In practice, these conditions should be based on physically motivated arguments — for instance, some definition of "updraft" or "coherent structure" — but for now the derivation is left general. The labels are mutually exclusive, that is, only one label can be nonzero for a particular fluid parcel at a given time:

$$\sum_i I_i(\mathbf{x}, t) = 1 \qquad \forall \mathbf{x}, t \in D \times [0, T]. \tag{3.2}$$

A fluid parcel will be relabelled if the parcel no longer satisfies the condition defining the label. Thus the indicator functions satisfy Lagrangian conservation, except at the interfaces where I_i jumps from 1 to 0 (or vice versa):

$$\frac{\mathrm{D}I_i}{\mathrm{D}t} = \mathcal{S}_i^+ - \mathcal{S}_i^-, \tag{3.3}$$

[2]Conditional filtering of compressible equation sets is discussed in Appendix B.

where $\mathcal{S}_i^+, \mathcal{S}_i^- \in \mathbb{R}_{\geq 0}$ formally denote sources and sinks of the indicator function I_i. This will be made more precise in section 3.3.

Here our derivation differs from those in e.g. Weller et al. (2020) and Thuburn et al. (2018) in that we choose to retain source and sink terms on the right-hand side of equation (3.3) (the relabelling of fluid from one partition to another). This clarifies the origin of transfer terms in the spatially-filtered equations, foregoing the need to justify their re-introduction at a later stage in the derivation. Since the transfer terms are crucial to the multi-fluid method — the analogue of entrainment and detrainment in traditional convection models — it is important to be clear about where they arise.

Governing equations for each region of the fluid are found by multiplying each of equations (2.4)-(2.6) by I_i, then adding $\mathbf{u} \times$ (3.3) to equation (2.4), and $b \times$ (3.3) to equation (2.5). Assuming that the usual product rule holds for I_i,[3] this gives:

$$\frac{\partial I_i \mathbf{u}}{\partial t} + \boldsymbol{\nabla} \cdot (I_i \mathbf{u} \otimes \mathbf{u}) = I_i b \hat{\mathbf{k}} - I_i \boldsymbol{\nabla} P + I_i \nu \boldsymbol{\nabla}^2 \mathbf{u} + \mathbf{u} \left(\mathcal{S}_i^+ - \mathcal{S}_i^- \right), \tag{3.4}$$

$$\frac{\partial I_i b}{\partial t} + \boldsymbol{\nabla} \cdot I_i \mathbf{u} b = I_i \kappa \boldsymbol{\nabla}^2 b + b \left(\mathcal{S}_i^+ - \mathcal{S}_i^- \right), \tag{3.5}$$

$$\boldsymbol{\nabla} \cdot I_i \mathbf{u} - \mathbf{u} \cdot \boldsymbol{\nabla} I_i = 0. \tag{3.6}$$

To be of any use for the modelling of unresolved scales, some sort of average or filter must be applied to this equation set. As in Chapter 1, we denote the operation of filtering by angle brackets, $\langle \ldots \rangle$, and assume that the application of the filter is linear, constant-preserving, and commutes with space and time partial derivatives (see equations (1.18)-(1.19)). Boundary effects can be included in the same way as for usual single-fluid modelling (Fureby and Tabor 1997); we will not discuss such effects here. For the desired application to atmospheric convection, filtering only in the horizontal removes the boundary non-commutation issues for the top and bottom boundaries.

Before filtering the governing equations, let us make some definitions that will tidy up the resulting expressions:

Definition 7 (Resolved fluid fraction)**.** For an indicator function I_i and filtering operation $\langle \ldots \rangle_g$, we define the ***resolved fluid fraction in partition*** i by:

$$\sigma_i \coloneqq \langle I_i \rangle_g . \tag{3.7}$$

Recall that, in Chapter 1, we defined the resolved part of a variable φ by: $\varphi^{\mathrm{r}} \coloneqq \langle \varphi \rangle_g$ (Definition 4). Having introduced the indicator function I_i, this definition

[3] This is true when treating I_i as a generalized step function, which is enough for our purposes since the domain occupied by partition i is assumed non-pathological — see section 3.3.

naturally extends to conditionally filtered variables:

Definition 8 ("Resolved" variables (multi-fluid))**.** Given a variable φ, a filtering operation $\langle \dots \rangle_g$, and an indicator function I_i, we define the ***resolved part of*** φ ***in partition*** i by:

$$\varphi_i^{\mathrm{r}} \coloneqq \frac{\langle I_i \varphi \rangle_g}{\sigma_i}. \tag{3.8}$$

Note that this means φ_i^{r} is undefined wherever $\sigma_i = 0$.

In Chapter 1, we also defined the subfilter flux $s(\varphi, \psi) \coloneqq \langle \varphi\psi \rangle_g - \langle \varphi \rangle_g \langle \psi \rangle_g$ (Definition 5). Anticipating the similarity of the conditionally-filtered subfilter flux terms to the single-fluid subfilter fluxes suggests also the following definition for brevity of notation:

Definition 9 (Generalized second centred moment/"subfilter flux" (multi-fluid))**.** Given any two flow variables φ, ψ, and a conditional filtering operation $(\dots)_i^{\mathrm{r}}$, we define the **subfilter flux in partition** i, $s_i(\varphi, \psi)$ by:

$$s_i(\varphi, \psi) \coloneqq (\varphi\psi)_i^{\mathrm{r}} - \varphi_i^{\mathrm{r}} \psi_i^{\mathrm{r}}. \tag{3.9}$$

This multi-fluid extension retains linearity in both its arguments[4]. Note that the sum of the within-partition fluxes is *not* equal to the unconditioned subfilter flux: $\sum_i \sigma_i s_i(\varphi, \psi) = (\varphi\psi)^{\mathrm{r}} - \sum_i \sigma_i \varphi_i^{\mathrm{r}} \psi_i^{\mathrm{r}} \neq s(\varphi, \psi)$. This is the difference between multi-fluid and multi-moment representations of the subfilter flow.

Since $\sum_i I_i = 1$, we therefore have

$$\sum_i \sigma_i = 1, \qquad \sum_i \sigma_i \varphi_i^{\mathrm{r}} = \varphi^{\mathrm{r}}. \tag{3.10}$$

In addition, if the filter is positive semidefinite, these definitions ensure $\sigma_i \in [0, 1] \forall \mathbf{x}, t$. In order to avoid dealing with negative fluid "fractions", we will therefore assume in the foregoing that the filter kernel *is* positive semidefinite. This may seem like a small restriction, but it actually rules out the commonly-used spectral cutoff filter. Here $\sigma_i(\mathbf{x}, t)$ is the fraction of fluid fulfilling condition i in the vicinity of a point $(\mathbf{x}, t)$, where the "vicinity" is defined by the filter scale. For a 3D filter, this vicinity will be a volume, but for a 2D filter would instead be an area. For shorthand throughout the remainder of the thesis we will refer to σ_i merely as the "fluid fraction". The associated velocity field and buoyancy field of fluid fulfilling condition i in the vicinity of $(\mathbf{x}, t)$ are denoted $\mathbf{u}_i^{\mathrm{r}}, b_i^{\mathrm{r}}$. Filtering the governing equations (3.4)-(3.6), along with the indicator function evolution equation (3.3), gives prognostic

[4]So long as the wavefront sets of no pair of φ, ψ, I_i overlap. This poses issues for the definition of subfilter fluxes directly containing indicator functions, e.g. $s_i(I_i, \varphi)$; these issues are surmountable, but beyond the scope of this Chapter.

equations for each of the conditionally resolved variables:

$$\frac{\partial \sigma_i}{\partial t} + \boldsymbol{\nabla} \cdot (\sigma_i \mathbf{u}_i^{\mathrm{r}}) = (\mathcal{S}_i^+)^{\mathrm{r}} - (\mathcal{S}_i^-)^{\mathrm{r}}, \tag{3.11}$$

$$\begin{aligned}\frac{\partial \sigma_i \mathbf{u}_i^{\mathrm{r}}}{\partial t} + \boldsymbol{\nabla} \cdot (\sigma_i \mathbf{u}_i^{\mathrm{r}} \otimes \mathbf{u}_i^{\mathrm{r}}) = \sigma_i b_i^{\mathrm{r}} \hat{\mathbf{k}} - (\boldsymbol{\nabla} P)_i^{\mathrm{r}} + \nu (\boldsymbol{\nabla}^2 \mathbf{u})_i^{\mathrm{r}} + (\mathbf{u}\mathcal{S}_i^+)^{\mathrm{r}} - (\mathbf{u}\mathcal{S}_i^-)^{\mathrm{r}} \\ - \boldsymbol{\nabla} \cdot \sigma_i s_i(\mathbf{u}, \mathbf{u}),\end{aligned} \tag{3.12}$$

$$\frac{\partial \sigma_i b_i^{\mathrm{r}}}{\partial t} + \boldsymbol{\nabla} \cdot (\sigma_i \mathbf{u}_i^{\mathrm{r}} b_i^{\mathrm{r}}) = \kappa (\boldsymbol{\nabla}^2 b)_i^{\mathrm{r}} + (b\mathcal{S}_i^+)^{\mathrm{r}} - (b\mathcal{S}_i^-)^{\mathrm{r}} - \boldsymbol{\nabla} \cdot \sigma_i s_i(\mathbf{u}, b), \tag{3.13}$$

$$\boldsymbol{\nabla} \cdot \sigma_i \mathbf{u}_i^{\mathrm{r}} = (\mathbf{u} \cdot \boldsymbol{\nabla} I_i)^{\mathrm{r}}. \tag{3.14}$$

As with ordinary single-fluid modelling, the operation of filtering introduces many unknown terms. Evolution equations for the unknown terms can be derived, but they contain further unknown terms, and so on *ad infinitum*. Thus, at any finite order, the filtered equation set is not closed, in the sense that there are more unknowns than independent equations. So, in order to close the multi-fluid Boussinesq equations, we must postulate expressions for the following terms in relation to the resolved variables:

- Transfer terms: $(\mathcal{S}_i^{\pm})^{\mathrm{r}}$, $(\mathbf{u}\mathcal{S}_i^{\pm})^{\mathrm{r}}$, $(b\mathcal{S}_i^{\pm})^{\mathrm{r}}$;
- Pressure gradient: $(\boldsymbol{\nabla} P)_i^{\mathrm{r}}$;
- Viscous & diffusive terms: $(\boldsymbol{\nabla}^2 \mathbf{u})_i^{\mathrm{r}}$, $(\boldsymbol{\nabla}^2 b)_i^{\mathrm{r}}$;
- Subfilter fluxes: $\boldsymbol{\nabla} \cdot \sigma_i s_i(\mathbf{u}, \mathbf{u})$, $\boldsymbol{\nabla} \cdot \sigma_i s_i(\mathbf{u}, b)$.

While the transfer terms are the most obvious different from an ordinary filtered equation set (c.f. Equation (1.24)), the subfilter fluxes are the only terms that have a *direct* analogue in ordinary single-fluid modelling. Further, although the form of the subfilter fluxes looks the same, the applicable modelling assumptions may be very different.

There are a few things we can immediately say about this equation set before manipulating any of the unknown terms or introducing any closure assumptions. Firstly, (3.14) shows that even though the mean flow, $\sum_i \sigma_i \mathbf{u}_i^{\mathrm{r}} = \mathbf{u}^{\mathrm{r}}$, is non-divergent, the resolved velocity field within each partition i *is* divergent. This divergence is exactly the filtered advection of the indicator function associated with that partition — that is, "divergence" within fluid partition i arises entirely due to the transport of the label field I_i by the whole flow field $\mathbf{u}$. It is thus intricately linked with the transfer terms $\langle \mathcal{S}_i^{\pm} \rangle$, in that parametrizing both $\langle \mathcal{S}_i^{\pm} \rangle$ and $\langle \mathbf{u} \cdot \boldsymbol{\nabla} I_i \rangle$ would overconstrain the model. This point becomes obvious when treating the indicator function evolution equation more rigorously, as we will see in Section 3.3.

Secondly, though there are lots of unknown terms requiring parametrization, many of those terms are subject to *sum constraints*: their sum over all fluid partitions

must match the corresponding term in the *un*conditionally-filtered equation set. Summing each of these equations over all partitions i yields the filtered Boussinesq equation set, i.e. the result of applying the filter $\langle \ldots \rangle$ directly to (2.4)-(2.6). First note that, by their definition in (3.3), $\sum_i (\mathcal{S}_i^+ - \mathcal{S}_i^-) = 0$. Then:

$$\begin{aligned}\frac{\partial \mathbf{u}^{\mathrm{r}}}{\partial t} + \boldsymbol{\nabla}\cdot(\mathbf{u}^{\mathrm{r}} \otimes \mathbf{u}^{\mathrm{r}}) = b^{\mathrm{r}}\hat{\mathbf{k}} - \boldsymbol{\nabla} P^{\mathrm{r}} + \nu \boldsymbol{\nabla}^2 \mathbf{u}^{\mathrm{r}} - \boldsymbol{\nabla}\cdot\left(\sum_i \sigma_i s_i(\mathbf{u},\mathbf{u})\right) \\ - \boldsymbol{\nabla}\cdot\left(\sum_i \sigma_i \left[\mathbf{u}_i^{\mathrm{r}} - \mathbf{u}^{\mathrm{r}}\right] \otimes \left[\mathbf{u}_i^{\mathrm{r}} - \mathbf{u}^{\mathrm{r}}\right]\right),\end{aligned} \tag{3.15}$$

$$\begin{aligned}\frac{\partial b^{\mathrm{r}}}{\partial t} + \boldsymbol{\nabla}\cdot(\mathbf{u}^{\mathrm{r}} b^{\mathrm{r}}) = \kappa \boldsymbol{\nabla}^2 b^{\mathrm{r}} - \boldsymbol{\nabla}\cdot\left(\sum_i \sigma_i s_i(\mathbf{u},b)\right) \\ - \boldsymbol{\nabla}\cdot\left(\sum_i \sigma_i \left[\mathbf{u}_i^{\mathrm{r}} - \mathbf{u}^{\mathrm{r}}\right] \left[b_i^{\mathrm{r}} - b^{\mathrm{r}}\right]\right),\end{aligned} \tag{3.16}$$

$$\boldsymbol{\nabla}\cdot\mathbf{u}^{\mathrm{r}} = 0. \tag{3.17}$$

Here we have used the exact relation

$$\begin{aligned} s(a,b) &= \sum_i \sigma_i s_i(a,b) + \sum_i \sigma_i \left(a_i^{\mathrm{r}} - a^{\mathrm{r}}\right)\left(b_i^{\mathrm{r}} - b^{\mathrm{r}}\right) \\ \implies \sum_i \sigma_i a_i^{\mathrm{r}} b_i^{\mathrm{r}} - a^{\mathrm{r}} b^{\mathrm{r}} &= s(a,b) - \sum_i \sigma_i s_i(a,b) = \sum_i \sigma_i \left(a_i^{\mathrm{r}} - a^{\mathrm{r}}\right)\left(b_i^{\mathrm{r}} - b^{\mathrm{r}}\right)\end{aligned} \tag{3.18}$$

to express the residual between the sum over all partitions of the within-partition resolved fluxes, e.g. $\sum_i \sigma_i \mathbf{u}_i^{\mathrm{r}} \otimes \mathbf{u}_i^{\mathrm{r}}$, and the single-fluid resolved fluxes, e.g. $\mathbf{u}^{\mathrm{r}} \otimes \mathbf{u}^{\mathrm{r}}$, in a more meaningful way; see Appendix B.3 for a proof of equation (3.18). This expresses the total single-fluid subfilter fluxes, $s(\mathbf{u},\mathbf{u}), s(\mathbf{u},b)$, as the sum of two contributions: firstly, the sum of subfilter fluxes *within each partition*; and secondly, the sum of the *exact* resolved fluxes due to the difference between the conditionally-resolved flow variables and the *un*conditionally resolved variables. That is, the first term represents intra-partition variability, while the second represents inter-partition variability. This form therefore facilitates comparison between multi-fluid and single-fluid turbulence models.

We can now read off the sum constraints for the unknown terms:

$$\sum_i \left([\mathcal{S}_i^+]^{\mathrm{r}} - [\mathcal{S}_i^-]^{\mathrm{r}}\right) = 0 \tag{3.19}$$

$$\sum_i \left([\mathbf{u}\mathcal{S}_i^+]^{\mathrm{r}} - [\mathbf{u}\mathcal{S}_i^-]^{\mathrm{r}}\right) = 0 \tag{3.20}$$

$$\sum_i \left([b\mathcal{S}_i^+]^{\mathrm{r}} - [b\mathcal{S}_i^-]^{\mathrm{r}}\right) = 0 \tag{3.21}$$

$$\sum_i (\boldsymbol{\nabla} P)_i^{\mathrm{r}} = \boldsymbol{\nabla} P^{\mathrm{r}} \tag{3.22}$$

$$\sum_i (\boldsymbol{\nabla}^2 b)_i^{\mathrm{r}} = \boldsymbol{\nabla}^2 b^{\mathrm{r}} \tag{3.23}$$

$$\sum_i (\boldsymbol{\nabla}^2 \mathbf{u})_i^{\mathrm{r}} = \boldsymbol{\nabla}^2 \mathbf{u}^{\mathrm{r}} \tag{3.24}$$

$$\sum_i \sigma_i = 1 \tag{3.25}$$

$$\sum_i \boldsymbol{\nabla} \cdot (\sigma_i \mathbf{u}_i^{\mathrm{r}}) = 0. \tag{3.26}$$

The only terms which are not constrained are the subfilter fluxes of momentum and buoyancy; this should not surprise us, since it is the ability of a multi-fluid model to provide a fundamentally different representation of the subfilter flow which makes it an intriguing candidate for turbulence modelling. For instance, note that for a horizontally-averaged Boussinesq flow, $\boldsymbol{\nabla} \cdot \mathbf{u}^{\mathrm{r}} = 0$ implies $\partial w^{\mathrm{r}}/\partial z = 0$; presuming impermeable boundaries, this implies $\mathbf{u}^{\mathrm{r}} = w^{\mathrm{r}} \hat{\mathbf{k}} = \mathbf{0}$. Therefore in a single-fluid model, there can be no contribution to the turbulent momentum or buoyancy fluxes from the resolved velocity. However, in a multi-fluid model, $\boldsymbol{\nabla} \cdot \mathbf{u}_i^{\mathrm{r}} \neq 0$ allows a circulation to exist even in a horizontally-averaged flow, leading to a part of the turbulent momentum and buoyancy fluxes being captured by the *resolved* partitioned variables. This idea has been exploited by Efstathiou et al. (2020) to find "optimal" partitions for a flow into two fluids, based on maximizing the amount of turbulent tracer flux that is transported by the resolved two-fluid velocity fields.

To summarize, in this section we have presented a derivation of the multi-fluid Boussinesq equations, which are the basis for the multi-fluid parametrizations to be developed in the remaining chapters of this thesis.

3.3 Indicator function evolution equation

Because they are so central to multi-fluid modelling, we wish to study the sources and sinks of the indicator function in more detail. To do this, we need to be able to make sense of derivatives of the indicator function; but indicator functions are discontinuous by definition, so their derivatives in the usual sense do not exist. The general theory which makes sense of derivatives of discontinuous functions is the theory of distributions[5]: "the space of distributions is essentially the smallest extension

[5]Distributions (also known as "generalized functions") were introduced piecemeal in the early- to mid-20$^{\mathrm{th}}$ century by various mathematicians, as well as used informally by physicists (such as Paul Dirac's infamous "δ-function", but certain earlier work can also be interpreted as heuristically using distributions, for instance Green's functions and some relations in Fourier analysis). The most complete contributions were the pioneering work of Laurent Schwartz, whose 1951 monograph *Théorie des distributions* (Schwartz 1951) was the first major work on distributions. An excellent

of the space of continuous functions where differentiation is always well defined" (Hörmander 2003, p. 1). This is what allows us to make precise the statement that "source terms [for the Lagrangian labels I_i] would necessarily have a δ-function structure" (Thuburn et al. 2018), enabling the derivation of formal expressions for sources and sinks of the indicator function that may, at the very least, be useful in analysing reference simulations.

Therefore let us recast the definition of the indicator function into more useful language. The indicator function I_i, Equation (3.1), defines a (time-dependent) subset of the solution domain, $D_i(t) \subset D$:

$$I_i(\mathbf{x}, t) \coloneqq \begin{cases} 1 & \mathbf{x} \in D_i(t) \\ 0 & \mathbf{x} \notin D_i(t) \end{cases}, \qquad D_i \cap D_j = \emptyset \ \forall i, j. \tag{3.27}$$

Let us assume that D_i is a countable union of disjoint, connected, measurable subsets of D, $\bigcup_\alpha D_{i,\alpha} = D_i, D_{i,\alpha} \cap D_{i,\beta} = \emptyset$, each with piecewise smooth boundary (such that we may use the divergence theorem). The indicator function I_i is then the sum of the indicators for each of these subsets, i.e. $I_i \coloneqq I_{\mathbf{x}\in D_i} = \sum_\alpha I_{\mathbf{x}\in D_{i,\alpha}}$.

In practice, we will always be interested in spatiotemporally-filtered variables and equations; filtering of this sort was defined via integration against a filter kernel in Equation (1.30). Let us therefore consider the integral of some function $f(\mathbf{x}, t)$ times the material derivative of the indicator function; for convenience, we will consider the domain of integration to be $\mathbb{R}^d$ to avoid the consideration of boundary terms. When f represents a filter kernel, we will assume for simplicity that its width is uniform in both space and time. (Boundary terms can be handled by the addition of another indicator function, this time used to indicate the whole domain $D \subseteq \mathbb{R}^d$; non-uniform filter kernels can also be considered. Both add non-commutation terms between the operations of filtering and taking partial derivatives; see Fureby and Tabor 1997.) Then:

$$\int_{\mathbb{R}^d} f \frac{\mathrm{D}I_i}{\mathrm{D}t} \,\mathrm{d}V = \int_{\mathbb{R}^d} f \frac{\partial I_i}{\partial t} \,\mathrm{d}V + \int_{\mathbb{R}^d} f\mathbf{u} \cdot \boldsymbol{\nabla} I_i \,\mathrm{d}V \tag{3.28}$$

$$= \int_{\mathbb{R}^d} f\mathbf{V}_{\partial D_i} \cdot \hat{\mathbf{n}}_{\partial D_i} \delta(\mathbf{x} \in \partial D_i) \,\mathrm{d}V + \int_{\mathbb{R}^d} f\mathbf{u} \cdot \boldsymbol{\nabla} I_i \,\mathrm{d}V \tag{3.29}$$

$$= -\int_{\mathbb{R}^d} f\mathbf{V}_{\partial D_i} \cdot \boldsymbol{\nabla} I_i \,\mathrm{d}V + \int_{\mathbb{R}^d} f\mathbf{u} \cdot \boldsymbol{\nabla} I_i \,\mathrm{d}V \tag{3.30}$$

$$= -\int_{\mathbb{R}^d} (\mathbf{V}_{\partial D_i} - \mathbf{u}) f \cdot \boldsymbol{\nabla} I_i \,\mathrm{d}V \tag{3.31}$$

$$= \oint_{\partial D_i} (\mathbf{V}_{\partial D_i} - \mathbf{u}) f \cdot \hat{\mathbf{n}}_{\partial D_i} \,\mathrm{d}(\partial D_i). \tag{3.32}$$

modern resource on the theory of distributions is Hörmander (2003).

In the second equality we have used $\partial I_i/\partial t = \mathbf{V}_{\partial D_i} \cdot \hat{\mathbf{n}}_{\partial D_i} \delta(\mathbf{x} \in \partial D_i)$, where $\mathbf{V}_{\partial D_i}$ is the velocity of the boundary of the domain D_i, and $\hat{\mathbf{n}}_{\partial D_i}$ is the outward unit normal at the boundary. This follows from $\partial I_i/\partial t = \partial \mathbf{x}/\partial t \,|_{\partial D_i} \cdot \hat{\mathbf{n}}_{\partial D_i} \delta(\mathbf{x} \in \partial D_i)$, using the chain rule for distributions; we then note that $\partial \mathbf{x}/\partial t \,|_{\partial D_i}$ defines the velocity of the interface, $\mathbf{V}_{\partial D_i} \coloneqq \partial \mathbf{x}/\partial t \,|_{\partial D_i}$.

In the third (and again in the fifth) equality we have used the relation that the gradient of the indicator of a domain D_i is a "surface delta function":

$$\boldsymbol{\nabla} I_i = -\hat{\mathbf{n}}_{\partial D_i} \delta(\mathbf{x} \in \partial D_i), \tag{3.33}$$

$$\text{where} \qquad \int_{\mathbb{R}^d} f(\mathbf{x}) \delta(\mathbf{x} \in \partial D_i) \,\mathrm{d}V = \oint_{\partial D_i} f(\mathbf{x}_i) \,\mathrm{d}(\partial D_i). \tag{3.34}$$

This relation is often heuristically used or implied in literature on conditional filtering, for instance in Dopazo (1977) where to make sense of the source terms an integral is taken over a control volume (subsequently taken to 0) in the neighbourhood of the interface, or in §4 of Fureby and Tabor (1997) where the relationship is stated but not proven. However, the relationship *is* derived and the surface delta function formally defined (in the context of particle physics) in Lange (2012). Arguing heuristically, the relationship makes sense since the indicator of a domain is constant both inside and outside the domain, but discontinuous at the boundary. Therefore we expect that the derivative should point along the *in*ward normal to the boundary, and only be nonzero at the boundary.

All that equation (3.31) really says is that changes in indicator function on a material parcel (must) result in a movement of the interface ∂D_i relative to the parcel. We can identify a relative velocity associated with this movement, $\mathbf{v}_{\partial D_i} \coloneqq \mathbf{V}_{\partial D_i} - \mathbf{u}$, and hence express the changes in indicator function in the form of advection by that relative velocity. This relation also means that the total derivative following the interface is identically zero,

$$\int_{\mathbb{R}^d} \left(\frac{\partial I_i}{\partial t} + \mathbf{V}_{\partial D_i} \cdot \boldsymbol{\nabla} I_i \right) f \,\mathrm{d}V = 0. \tag{3.35}$$

Using the notation for spatial filtering introduced in Definition 6, and interpreting f as a filter kernel, equation (3.31) may be re-written as:

$$\left\langle \frac{\mathrm{D}I_i}{\mathrm{D}t} \right\rangle_g = \left\langle (\mathbf{u} - \mathbf{V}_{\partial D_i}) \cdot \boldsymbol{\nabla} I_i \right\rangle_g . \tag{3.36}$$

To make more sense of this we must be able to express the left hand side in terms of the filtered indicator function, $\langle I_i \rangle_g$. Note that the distributional derivative of the

product of a function and a distribution obeys the usual product rule, i.e.

$$\partial(fG) = f(\partial G) + (\partial f)G \tag{3.37}$$

for f a function and G a distribution. Then we can write

$$\left\langle \frac{\mathrm{D}I_i}{\mathrm{D}t} \right\rangle_g = \left\langle \frac{\partial I_i}{\partial t} \right\rangle_g + \langle \mathbf{u} \cdot \boldsymbol{\nabla} I_i \rangle_g \tag{3.38}$$

$$= \left\langle \frac{\partial I_i}{\partial t} \right\rangle_g + \langle \boldsymbol{\nabla} \cdot (I_i \mathbf{u}) \rangle_g \tag{3.39}$$

$$= \frac{\partial \sigma_i}{\partial t} + \boldsymbol{\nabla} \cdot \sigma_i \mathbf{u}_i^{\mathrm{r}}, \tag{3.40}$$

since $\boldsymbol{\nabla} \cdot \mathbf{u} = 0$. Equating the final expression with equation (3.36) gives the *fluid fraction conservation equation*:

$$\frac{\partial \sigma_i}{\partial t} + \boldsymbol{\nabla} \cdot \sigma_i \mathbf{u}_i^{\mathrm{r}} = \langle (\mathbf{u} - \mathbf{V}_{\partial D_i}) \cdot \boldsymbol{\nabla} I_i \rangle_g \,. \tag{3.41}$$

For a compressible medium, the conservation equation for the resolved *mass* fraction in fluid i, $\sigma_i \rho_i^{\mathrm{r}}$, takes exactly the same form, but with the resolved velocity defined as density-weighted — see the Appendix B for details of how to extend the above derivation to compressible media. Note that comparison with (3.11) gives the formal identification

$$(\mathcal{S}_i^+)^{\mathrm{r}} - (\mathcal{S}_i^-)^{\mathrm{r}} = \langle (\mathbf{u} - \mathbf{V}_{\partial D_i}) \cdot \boldsymbol{\nabla} I_i \rangle_g \,. \tag{3.42}$$

Aside. *Before moving on, let us use the definitions of the resolved variables to clean up our expression for the total derivative of the indicator function following the interface:*

$$\frac{\partial \sigma_i}{\partial t} + (\mathbf{V}_{\partial D_i})^{\mathrm{r}} \cdot \boldsymbol{\nabla} \sigma_i = -\left[(\mathbf{V}_{\partial D_i} \cdot \boldsymbol{\nabla} I_i)^{\mathrm{r}} - (\mathbf{V}_{\partial D_i})^{\mathrm{r}} \cdot \boldsymbol{\nabla} \sigma_i \right]. \tag{3.43}$$

This is a form of the filtered indicator function evolution equation that is often used in modelling of multi-phase systems; all modelling reduces to modelling of the motion of the interface between partitions. As a specific example, if the right hand side is set to zero (trivially true if the interface is stationary), the evolution equation for the Holm and Kupershmidt (1984) model results.

With some effort, the expression on the right hand side of Equation (3.41) can be split up into sources and sinks, and then again into exchanges between every pair of fluids (neglecting interactions of three or more fluids); for details, see the

Appendix B. The result is:

$$\frac{\partial \sigma_i}{\partial t} + \boldsymbol{\nabla} \cdot \sigma_i \mathbf{u}_i^{\mathrm{r}} = \sum_{j \neq i} \left(\sigma_j S_{ji} - \sigma_i S_{ij} \right), \tag{3.44}$$

where

$$\sigma_i S_{ij} \coloneqq \int_{\partial D_{ij}} g\, \mathcal{H}(-\mathbf{v}_{\partial D_{ij}} \cdot \hat{\mathbf{n}}_{\partial D_{ij}}) \left(-\mathbf{v}_{\partial D_{ij}} \cdot \hat{\mathbf{n}}_{\partial D_{ij}} \right) \mathrm{d}(\partial D_i) \tag{3.45}$$

$$= \int_{\partial D_{ji}} g\, \mathcal{H}(\mathbf{v}_{\partial D_{ji}} \cdot \hat{\mathbf{n}}_{\partial D_{ji}}) \left(\mathbf{v}_{\partial D_{ji}} \cdot \hat{\mathbf{n}}_{\partial D_{ji}} \right) \mathrm{d}(\partial D_j), \tag{3.46}$$

$$\sigma_j S_{ji} \coloneqq \int_{\partial D_{ji}} g\, \mathcal{H}(-\mathbf{v}_{\partial D_{ji}} \cdot \hat{\mathbf{n}}_{\partial D_{ji}}) \left(-\mathbf{v}_{\partial D_{ji}} \cdot \hat{\mathbf{n}}_{\partial D_{ji}} \right) \mathrm{d}(\partial D_j) \tag{3.47}$$

$$= \int_{\partial D_{ij}} g\, \mathcal{H}(\mathbf{v}_{\partial D_{ij}} \cdot \hat{\mathbf{n}}_{\partial D_{ij}}) \left(\mathbf{v}_{\partial D_{ij}} \cdot \hat{\mathbf{n}}_{\partial D_{ij}} \right) \mathrm{d}(\partial D_i), \tag{3.48}$$

with $\sum_j \sigma_i S_{ij} = (\mathcal{S}_i^-)^{\mathrm{r}}, \sum_j \sigma_j S_{ji} = (\mathcal{S}_i^+)^{\mathrm{r}}$ (within the two-fluid interaction approximation). Here ∂D_{ij} denotes the part of the boundary of D_i which is in contact only with D_j and no other partitions; $\hat{\mathbf{n}}_{\partial D_{ij}}$ is the outward-pointing unit normal at the boundary ∂D_{ij} (i.e. it points from domain D_i into domain D_j; $\mathbf{v}_{\partial D_{ij}}$ is the velocity of the boundary relative to a fluid parcel; and $\mathcal{H}(x)$ is the Heaviside step function. Thus $\sigma_i S_{ij}$ is the rate of fluid fraction transferred from fluid i into fluid j. We make the distinction here between "relabelling terms" and "transfer terms": "relabelling" describes the source and sink terms for the fluid parcel labels in the unfiltered flow, whereas "transfer terms" describes the source and sink terms for the fluid fractions of the conditionally-filtered flow. This conceptual distinction merits thinking of the conditionally-filtered partitions as separate, but interacting, fluids, with different physical properties.

Equation (3.44) makes precise the ad-hoc introduction of transfer terms of this form in Thuburn et al. (2018) (for compressible fluids) and Weller et al. (2020) (for a multi-fluid Boussinesq system); we have defined the transfers as fluid fraction-weighted to match the conventions in these papers. It also provides an explicit link between these transfer terms — often called "entrainment" and "detrainment" — and the motion of the interface between partitions. This is a generalization and unification of results from various areas of fluid mechanics.

In prior work on mass flux convection parametrization, for instance, Siebesma (1998) derived the relation (their equation (42), in our notation):

$$(\mathcal{S}_i^+)^{\mathrm{r}} - (\mathcal{S}_i^-)^{\mathrm{r}} = -\frac{1}{A} \int_{\partial D_i} (\mathbf{u} - \mathbf{V}_{\partial D_i}) \cdot \hat{\mathbf{n}}_{\partial D_i} \, \mathrm{d}\ell \tag{3.49}$$

without explicitly introducing indicator functions for the subdomains indexed by

i. Yano (2014) and Tan et al. (2018) derived similar relations[6] using essentially the same argument as Siebesma (1998). Comparison with (3.42) shows that our result is equivalent if the filter kernel is a horizontal average kernel, i.e. if $g(\mathbf{x}, \mathbf{x}') = (1/A)\delta(z - z')$, then

$$\int g(\mathbf{x}, \mathbf{x}') f(\mathbf{x}') \, \mathrm{d}V = \int_A \mathrm{d}x' \, \mathrm{d}y' \int \mathrm{d}z' \frac{1}{A} \delta(z - z') f(x', y', z') \tag{3.50}$$

$$= \frac{1}{A} \int_A f(x', y', z) \, \mathrm{d}x' \, \mathrm{d}y' \tag{3.51}$$

and so

$$\left\langle (\mathbf{u} - \mathbf{V}_{\partial D_i}) \cdot \boldsymbol{\nabla} I_i \right\rangle_g = \int_D g(\mathbf{x}, \mathbf{x}') (\mathbf{u} - \mathbf{V}_{\partial D_i}) \cdot \boldsymbol{\nabla} I_i \, \mathrm{d}D \tag{3.52}$$

$$= \frac{1}{A} \int_A (\mathbf{u} - \mathbf{V}_{\partial D_i}) \cdot \boldsymbol{\nabla} I_i \, \mathrm{d}x \, \mathrm{d}y \tag{3.53}$$

$$= -\frac{1}{A} \int_\ell (\mathbf{u} - \mathbf{V}_{\partial D_i}) \cdot \hat{\mathbf{n}}_{\partial D_i} \, \mathrm{d}\ell. \tag{3.54}$$

Here $\ell \coloneqq \partial D_i \cap \{\mathbf{x} | z = \text{const.}\}$ is the intersection of the partition boundary ∂D_i with a plane of fixed z.

This shows that the expressions for entrainment and detrainment in earlier work on mass-flux convection parametrization are special cases of the more general framework presented here. The generalization is not of purely formal interest: for applications to the grey zone, filters of finite width *must* be considered. Performing the derivation in the way above, including explicitly introducing indicator functions for the subdomains, is the only way this author can conceive to correctly account for finite filter width in a conditional averaging context. That the expressions retain near identical form is another demonstration of the so-called "averaging invariance" of the Navier-Stokes equations (Germano 1992).

Siebesma (1998), Yano (2014), and Tan et al. (2018) all proceed to split the expression on the right hand side of (3.49) into entrainment and detrainment based on the sign of $(\mathbf{u} - \mathbf{V}_{\partial D_i}) \cdot \hat{\mathbf{n}}_{\partial D_i}$. This has been used by e.g. de Rooy et al. (2013) to compute entrainment and detrainment terms from LES reference. The generalization (3.48) to give explicit integral expressions for mass sources and sinks between

[6] Discrepancies in the final expressions (e.g. compare equation (40) of Siebesma 1998 with equation (4.9) of Yano 2014 and equation (A6) of Tan et al. 2018) may be reconciled by accounting for differences in the definitions of the normal vectors, interface velocities, and the line elements to be integrated over at the partition boundary. Explicitly, in this Chapter and in Siebesma (1998), the velocities entering the expressions are full 3D velocities, and the normal vector is the actual outward-pointing normal of domain D_i. Neither of these is necessarily horizontal, as Siebesma notes. However, the normal vector entering the expressions in Yano (2014) and Tan et al. (2018) is the normal to the curve defined by the intersection of the boundary of D_i with a horizontal plane, which is horizontal; this requires the introduction of "effective"/"apparent" horizontal velocities which take into account the fact that really the boundary is not necessarily vertical.

each pair of partitions is new, as far as we are aware, but fairly trivial.

The developments presented in the remainder of this section, however, are entirely new, and rely crucially on the explicit introduction of the indicator function. These results differ in spirit from earlier presentations in the cumulus parametrization literature as they aim to provide a starting point for theoretical investigations about entrainment and detrainment, rather than serving purely as calculational tools, or for completeness of description.

Returning to equation (3.32), another useful relation follows if we allow the indicator function to be written as a Heaviside step function on a single[7] real-valued differentiable function $\psi_i : D \to \mathbb{R}$. This is always possible for subdomains which satisfy the conditions already assumed, but an explicit example would be e.g. $\psi_0 = w, \psi_1 = -w$, corresponding to a two-fluid partition based on the sign of the vertical velocity; this partition will be used extensively in later chapters of this thesis. Then

$$I_i(\mathbf{x}, t) = \mathcal{H}(\psi_i) \implies \partial I_i = \delta(\psi_i)\partial\psi_i, \tag{3.55}$$

where by $\partial\mathcal{H}(\psi_i)$ the distributional derivative of $\mathcal{H}(\psi_i)$ is understood. This allows us to write

$$\int_{\mathbb{R}^d} \mathbf{V}_{\partial D_i} \cdot \hat{\mathbf{n}}_{\partial D_i} \delta(\mathbf{x} \in \partial D_i)\, \mathrm{d}V = \int_{\mathbb{R}^d} \frac{\partial I_i}{\partial t}\, \mathrm{d}V = \int_{\mathbb{R}^d} \delta(\psi_i) \frac{\partial \psi_i}{\partial t}\, \mathrm{d}V \tag{3.56}$$

$$= \int_{\mathbb{R}^d} \frac{\delta(\psi_i)|\boldsymbol{\nabla}\psi_i|}{|\boldsymbol{\nabla}\psi_i|} \frac{\partial \psi_i}{\partial t}\, \mathrm{d}V \tag{3.57}$$

$$= \int_{\mathbb{R}^d} \frac{\delta(\mathbf{x} \in \partial D_i)}{|\boldsymbol{\nabla}\psi_i|} \frac{\partial \psi_i}{\partial t}\, \mathrm{d}V \tag{3.58}$$

$$\implies \mathbf{V}_{\partial D_i} \cdot \hat{\mathbf{n}}_{\partial D_i} = \frac{\frac{\partial \psi_i}{\partial t}}{|\boldsymbol{\nabla}\psi_i|}, \tag{3.59}$$

where in the second equality we have used that $\delta(\mathbf{x} \in \partial D_i) = \delta(\psi_i)|\boldsymbol{\nabla}\psi_i|$, and made use of the fact that for $\mathbf{x} \in \partial D_i$, $|\boldsymbol{\nabla}\psi_i| \neq 0$. This is an exact expression for the (relevant part of) the velocity of the partition interface, which may be substituted wherever $\mathbf{V}_{\partial D_i} \cdot \hat{\mathbf{n}}_{\partial D_i}$ appears. For instance, the transfer term S_{ij} becomes:

$$\sigma_i S_{ij} = \int_{\partial D_{ij}} g\ H\left(\frac{\frac{\partial \psi_i}{\partial t}}{|\boldsymbol{\nabla}\psi_i|} - \mathbf{u} \cdot \hat{\mathbf{n}}_{\partial D_{ij}}\right)\left(\frac{\frac{\partial \psi_i}{\partial t}}{|\boldsymbol{\nabla}\psi_i|} - \mathbf{u} \cdot \hat{\mathbf{n}}_{\partial D_{ij}}\right) \mathrm{d}(\partial D_i). \tag{3.60}$$

If ψ_i is calculable based on flow variables, this removes the need for object tracking algorithms in order to calculate the transfer terms, since all of the terms in the

[7] This can be extended to indicator functions that are countable products of such step functions, though some care must be taken to define these products in order to correctly account for potential overlap of singularities in the distributions. While relatively straightforward, the details are technical and beyond the scope of this thesis.

integral are known at any single time.This could be useful as the determination of the interface velocity numerically from reference data is a difficult problem (see Section 3.6 of de Rooy et al. 2013).

An alternative use for writing the indicator function in terms of a step function on a single real variable is more theoretical. All we need do is write

$$\frac{\mathrm{D}I_i}{\mathrm{D}t} = \frac{\mathrm{D}\mathcal{H}(\psi_i)}{\mathrm{D}t} = \delta(\psi_i)\frac{\mathrm{D}\psi_i}{\mathrm{D}t} \tag{3.61}$$

$$\implies \sum_{j\neq i}(\sigma_j S_{ji} - \sigma_i S_{ij}) = \oint_{\partial D_i} g\ \frac{1}{|\boldsymbol{\nabla}\psi_i|}\frac{\mathrm{D}\psi_i}{\mathrm{D}t}\,\mathrm{d}(\partial D_i). \tag{3.62}$$

This may seem obvious, but expressing the transfer terms this way is attractive for theoretical work: if ψ_i is a physical field, then we can derive an equation for $\mathrm{D}\psi_i/\mathrm{D}t$. Then equation (3.62) is amenable to formal asymptotic analysis, or physically-based scale analysis, in terms of what is known about the source and sink terms for $\mathrm{D}\psi_i/\mathrm{D}t$. Those source and sink terms can then be mapped on to the earlier definitions of S_{ij}.

As a concrete example, consider partitioning turbulent Rayleigh-Bénard convection into two fluids based on the sign of the buoyancy, b. Let fluid 0 be negatively buoyant, and fluid 1 be positively buoyant. Then the fluid fraction transfers are:

$$\sigma_1 S_{10} - \sigma_0 S_{01} = \oint_{\partial D_0} g\ \frac{1}{|\boldsymbol{\nabla}b|}\frac{\mathrm{D}b}{\mathrm{D}t}\,\mathrm{d}(\partial D_0) \tag{3.63}$$

$$= \oint_{\partial D_0} g\ \frac{1}{|\boldsymbol{\nabla}b|}\kappa\boldsymbol{\nabla}^2 b\,\mathrm{d}(\partial D_0). \tag{3.64}$$

Therefore the *only* places where fluid is transferred based on buoyancy are where the diffusion term is important. This easily decomposes into positive contributions from locations where $\boldsymbol{\nabla}^2 b > 0$, and negative contributions where $\boldsymbol{\nabla}^2 b < 0$:

$$\sigma_1 S_{10} = \oint_{\partial D_0} g\ \frac{1}{|\boldsymbol{\nabla}b|}\mathcal{H}(\boldsymbol{\nabla}^2 b)\kappa\boldsymbol{\nabla}^2 b\,\mathrm{d}(\partial D_0), \tag{3.65}$$

$$\sigma_0 S_{01} = -\oint_{\partial D_0} g\ \frac{1}{|\boldsymbol{\nabla}b|}\mathcal{H}(-\boldsymbol{\nabla}^2 b)\kappa\boldsymbol{\nabla}^2 b\,\mathrm{d}(\partial D_0). \tag{3.66}$$

Splitting the underlying flow into thermal plumes (including the boundary layers) with characteristic buoyancy scale ΔB over a characteristic length of δ, and a homogeneous turbulent bulk with characteristic buoyancy scale ΔB over a characteristic length of H, we can scale the contributions to the integrand:

$$\kappa\frac{\boldsymbol{\nabla}^2 b}{|\boldsymbol{\nabla}b|} \sim \frac{\kappa}{\delta} = \frac{\kappa}{H}\cdot\mathrm{Nu} \qquad \text{(plumes)}, \qquad \kappa\frac{\boldsymbol{\nabla}^2 b}{|\boldsymbol{\nabla}b|} \sim \frac{\kappa}{H} \qquad \text{(bulk)}. \tag{3.67}$$

For turbulent convection, $\mathrm{Nu} \gg 1$, so contributions from the plumes dominate the transfer terms. Gradients parallel to the plumes will be much smaller in magnitude than gradients perpendicular to the plumes. Defining a Cartesian co-ordinate system orientated following a plume, such that at each location $\tilde{\mathbf{z}}$ points normal to the plume, this allows us to write

$$|\boldsymbol{\nabla} b| \approx \left|\frac{\partial b}{\partial \tilde{z}}\right|, \quad \boldsymbol{\nabla}^2 b \approx \frac{\partial^2 b}{\partial \tilde{z}^2}. \tag{3.68}$$

By their nature as thermal plumes, i.e. regions where buoyancy magnitude is greater than the surroundings (recall for instance Figure 2.2), $\partial b/\partial \tilde{z} < 0$, so we may replace $|\partial b/\partial \tilde{z}| \to -\partial b/\partial \tilde{z}$. Further, we know that at the wall, $-\partial b/\partial z = \mathrm{Nu}\ \Delta B/H$. Expanding in a power series in $\tilde{z}$, we can write:

$$-\frac{\partial b}{\partial z}\Big|_{z=0} \approx \mathrm{Nu}\,\frac{\Delta B}{H}\left(1 - a_1\frac{\tilde{z}}{\delta} + \mathcal{O}\left(\frac{\tilde{z}^2}{\delta^2}\right)\right) \tag{3.69}$$

which should be approximately valid for thermal plumes in the interior, since they are merely detached thermal boundary layers. The constant $a_1 > 0$ depends on the shape of the buoyancy profile in the plume. (There will also be a modulating factor depending on the lifetime of the plumes, since their buoyancy will diffuse as the plumes advect.) Collecting results, we have:

$$\begin{aligned}
\kappa\frac{\boldsymbol{\nabla}^2 b}{|\boldsymbol{\nabla} b|} &\approx \kappa\frac{\partial^2 b/\partial \tilde{z}^2}{\mathrm{Nu}(\Delta B/H)\,(1 - a_1\tilde{z}/\delta + \mathcal{O}(\tilde{z}^2/\delta^2))} \\
&\approx \frac{\kappa H}{\Delta B}\cdot\frac{1}{\mathrm{Nu}}\frac{\partial^2 b}{\partial \tilde{z}^2}\left(1 + a_1\frac{\tilde{z}}{\delta} + \mathcal{O}\left(\frac{\tilde{z}^2}{\delta^2}\right)\right) \\
&\approx \frac{\kappa H}{\Delta B}\cdot\frac{1}{\mathrm{Nu}}\cdot\frac{\Delta B}{\delta^2}\frac{\partial^2 \hat{b}}{\partial \hat{\tilde{z}}^2}\left(1 + a_1\hat{\tilde{z}} + \mathcal{O}\left(\hat{\tilde{z}}^2\right)\right) \\
&\approx \frac{\kappa H}{\Delta B}\cdot\frac{2\delta}{H}\cdot\frac{\Delta B}{\delta^2}\frac{\partial^2 \hat{b}}{\partial \hat{\tilde{z}}^2}\left(1 + a_1\hat{\tilde{z}} + \mathcal{O}\left(\hat{\tilde{z}}^2\right)\right) \\
&\approx \frac{2\kappa}{\delta}\frac{\partial^2 \hat{b}}{\partial \hat{\tilde{z}}^2}\left(1 + a_1\hat{\tilde{z}}\right).
\end{aligned} \tag{3.70}$$

In going from the first line to the second line we Taylor expanded $(1 - a_1\tilde{z}/\delta + \mathcal{O}(\tilde{z}^2/\delta^2))^{-1}$; in going from the second to the third we introduced nondimensionalized variables $\hat{b} \coloneqq b/\Delta B, \hat{\tilde{z}} \coloneqq \tilde{z}/\delta$; from the third to the fourth, we used $1/\mathrm{Nu} = 2\delta/H$; and in the final line we truncated the Taylor expansion at first order.

Let us now assume that the vertical dependence of the filter kernel is a delta function; then we can further split the plumes into parts where $\tilde{\mathbf{z}}\cdot\mathbf{z} \approx 1$, and parts where $\tilde{\mathbf{z}}\cdot\mathbf{z} \approx 0$ — i.e. parts where the edge of the plume is approximately horizontal, and parts where the edges are approximately vertical. The integral for the positive

transfer term can then be split into (defining $\hat{x} \coloneqq x/H, \hat{z} \coloneqq z/H$):

$$\begin{aligned}\sigma_1 S_{10} \approx \frac{2\kappa H}{\delta} \cdot \frac{1}{H} \int_{\partial D_i \| x} g(\hat{x} - \hat{x}'; \Delta) \frac{\partial^2 \hat{b}}{\partial \hat{\tilde{z}}^2} \left(1 + a_1 \hat{\tilde{z}}\right) \mathrm{d}\hat{x} \\ + \frac{2\kappa H}{\delta} \int_{\partial D_i \perp x} g(\hat{x} - \hat{x}'; \Delta) \delta(\hat{z} - \hat{z}') \frac{\partial^2 \hat{b}}{\partial \hat{\tilde{z}}^2} \left(1 + a_1 \hat{\tilde{z}}\right) \mathrm{d}\hat{z} \\ + \text{plume separation regions.}\end{aligned} \tag{3.71}$$

Restoring dimensions, the first integral is approximately equal to $(2\kappa\delta/(\Delta B\ H))(1+ a_1\ \tilde{z}/\delta)\ \partial^2 b^{\mathrm{r}}/\partial z^2$, but is only applicable close to the top and bottom boundaries. The second is approximately $\sum_{x_\alpha \in \partial D_i} (2\kappa\delta/(\Delta B\ H))\ g(x - x_\alpha; \Delta)(1 + a_1\ \tilde{z}/\delta)\ \partial^2 b/\partial x^2$, where the sum is over points on distinct disconnected regions of the boundary, and is applicable sufficiently far from the top and bottom boundaries. The first expression is written entirely in terms of resolved variables, if we allow $\delta = H/(2\,\mathrm{Nu}) = -\Delta B/(2\ \partial b^{\mathrm{r}}/\partial z\ |_{z=0})$; all that remains is the setting of the closure constant a_1. The second integral is more problematic, and still requires closure arguments which will depend quite strongly on the filter scale. And we have yet to develop arguments for the plume separation regions.

We have no doubt that with more effort, more complete and more elegant closures could be argued; however, the above hopefully serves to illustrate that explicitly considering derivatives of the indicator function can be useful for the development of theories for the transfer terms.We see the intersection of these new results and classical entraining plume-based entrainment studies as an interesting area of future cross-fertilization. Expressions like (3.42) have to date only been used in a diagnostic context, to calculate entrainment and detrainment from idealized simulations (e.g. de Rooy et al. 2013). However, explicitly considering the indicator functions allows writing the entrainment and detrainment terms as (3.62), allowing for process-based theoretical considerations. Comparison of these two expressions for different possible definitions of cloud/coherent structure has the potential to, at the very least, shed light on some of major discrepancies between different formulations of entrainment and detrainment rates (again, see the excellent review by de Rooy et al. 2013). Further, for the desired unified modelling of all types of atmospheric convection, (3.62) can provide physics-based justifications for potentially different formulations of entrainment and detrainment, given the potentially different (local) definitions of coherent structure required in different regimes.

It would also likely be instructive to directly compare the dynamical relabelling expression (3.62) with the theoretical entraining plume studies upon which almost all mass flux entrainment and detrainment closures are based. Theoretical work on this problem can be traced back (at least) to Taylor (1945), Morton et al. (1956),

and Turner (1962); the first numerical cloud model based on plume theory followed shortly after in Simpson and Wiggert (1969)[8]. These classical references consider dry, axisymmetric, steady-state plumes in stationary, neutral environments. Savre and Herzog (2019) is an important step forward in plume theory to account for processes which are important in atmospheric moist convection that have previously been neglected; however they still consider a steady-state, axisymmetric, Reynolds-averaged plume. Entraining plume considerations form the backbone of most mass flux entrainment and detrainment parametrizations, and it would therefore be very useful to compare these entrainment and detrainment expressions with dynamical expressions in the general multi-fluid framework. This could be especially useful for consideration of memory terms, which are necessarily absent from steady-state plume theory. It would also be very useful to directly compare the predictions of steady, axisymmetric plume theory with even the equilibrium response of a system like RBC, where the large-scale circulation is crucial to the plume dynamics, and even in 3D the structures tend to be quasi-two-dimensional and sheet-like.

One potential criticism of considering explicit indicator functions in the derivations of expressions like (3.62) is that it (potentially unnecessarily) introduces an element of human choice into the modelling. Firstly, we believe that this human choice is implicit in any direct modelling of coherent structures, there being no universal, objective definition of "coherent structures", and it does no harm to make that choice explicit. This should make it easier to avoid problems arising due to unstated assumptions, which are likely to differentiate more strongly between choices of condition in the grey zone, non-steady state regime.

Perhaps more fundamentally, however, explicitly introducing indicator functions allows one to express uncertainty as to the exact nature of the partitioning by considering the indicator to be the indicator of a "fuzzy set" (Zadeh 1965). Such an indicator function can take any value in the unit interval, rather than just zero or 1, and hence expresses a *degree* of membership of a set. One way this could be useful in our application is to inherently express uncertainty as to the exact value of a threshold for distinguishing membership of a partition, or complementarily to express uncertainty as to the exact location of the boundary. The simplest way to implement this would be to convolve the indicator functions with a smooth mollifying function of finite, specified width (this need not have any relation to the width of the spatial filter); indeed, this is one way of making the expressions in this section suitable for numerical computation. Crucially, this would turn the surface integrals over the domain boundaries into volume integrals.

In summary, in this section we have used some results from the theory of distri-

[8]Note that the first author here, Joanne Simpson, is the same groundbreaking scientist who pioneered the hot tower hypothesis under the surname Malkus.

butions to make precise statements about the fluid relabelling or "transfer" terms arising in multi-fluid modelling. These link two conceptual ways of thinking about the transfers — tracking the motion of the interface between partitions, and the macroscopic "entrainment" and "detrainment" point of view which relates directly to traditional convection parametrization approaches in meteorology. Additionally, we provided exact integral results which express quantitatively how these two approaches relate, giving expressions which allow for the computation of transfer terms from reference data. Finally, we suggested a potential route for using the expressions for *deriving* closures for transfer terms in multi-fluid models.

3.4 Terms requiring closure

To recap, the terms of (3.12)-(3.13) which require closing are:

- Transfer terms: $(\mathcal{S}_i^{\pm})^{\mathrm{r}}$, $(\mathbf{u}\mathcal{S}_i^{\pm})^{\mathrm{r}}$, $(b\mathcal{S}_i^{\pm})^{\mathrm{r}}$;
- Pressure gradient: $(\boldsymbol{\nabla} P)_i^{\mathrm{r}}$;
- Viscous & diffusive terms: $(\boldsymbol{\nabla}^2\mathbf{u})_i^{\mathrm{r}}$, $(\boldsymbol{\nabla}^2 b)_i^{\mathrm{r}}$;
- Subfilter fluxes: $\boldsymbol{\nabla}\cdot s_i(\mathbf{u},\mathbf{u})$, $\boldsymbol{\nabla}\cdot\sigma_i s(\mathbf{u},b)$.

We shall now discuss each of these in turn. It is useful to express the unknowns in terms of resolved variables as much as possible. The physical interpretation of the remaining unknown terms can then be discussed.

In the subsequent analysis, boundary terms and terms arising from spatiotemporal variations in the filter kernel $g(\varepsilon)$ are neglected.

3.4.1 Exchange terms

In the preceding section, we split sources and sinks of the indicator function into their contributions from all two-partition interactions, and labelled these "fluid fraction transfer terms". Recall that similar terms arise in the momentum and buoyancy equations, representing the transfers of momentum and buoyancy which occur when mass is transferred. To avoid repetition, in this section we shall manipulate expressions for a general variable φ, which may be b or $\mathbf{u}$. The earlier split of sources and sinks of fluid fraction (3.48) straightforwardly extends to transfers of any fluid property φ:

$$\begin{aligned}(\varphi\mathcal{S}_i^{+})^{\mathrm{r}} - (\varphi\mathcal{S}_i^{-})^{\mathrm{r}} = \sum_{j\neq i}\Bigg(&\int_{\partial D_{ij}} g\varphi\mathcal{H}(-\mathbf{v}_{\partial D_{ij}}\cdot\hat{\mathbf{n}}_{\partial D_{ij}})(-\mathbf{v}_{\partial D_{ij}}\cdot\hat{\mathbf{n}}_{\partial D_{ij}})\,\mathrm{d}(\partial D_i)\\ &-\int_{\partial D_{ij}} g\varphi\mathcal{H}(\mathbf{v}_{\partial D_{ij}}\cdot\hat{\mathbf{n}}_{\partial D_{ij}})(\mathbf{v}_{\partial D_{ij}}\cdot\hat{\mathbf{n}}_{\partial D_{ij}})\,\mathrm{d}(\partial D_i)\Bigg).\end{aligned} \tag{3.72}$$

Rather than modelling these transfers of φ directly, separately from the fluid fraction transfer terms S_{ij}, it makes sense to define transferred values of φ. This shifts the burden of modelling: instead of modelling a separate exchange term for each prognostic equation, we choose to model the mass exchanges S_{ij}, and what properties are exchanged along with these mass transfers, b_{ij}^{T} and $\mathbf{u}_{ij}^{\mathrm{T}}$.

The definition of transferred properties, $\varphi_{ij}^{\mathrm{T}}$, which matches those used in Thuburn et al. (2018) is:

$$\begin{aligned} \sigma_i \varphi_{ij}^{\mathrm{T}} S_{ij} &\coloneqq \langle \varphi \mathcal{S}_{ij} \rangle \\ &\iff \\ \varphi_{ij}^{\mathrm{T}} \langle \mathcal{S}_{ij} \rangle &= \langle \varphi \mathcal{S}_{ij} \rangle . \end{aligned}$$

However, really the transfer $\langle \varphi \mathcal{S}_{ij} \rangle$ can only be matched to the transfer $\langle \mathcal{S}_{ij} \rangle$ on each piecewise-continuous subset of the boundary of partition i. The reason this matters is that very different processes can contribute to the relabelling of fluid parcels; for instance, for fluid partitions based on the sign of vertical velocity, there are buoyancy-based transfers, viscous transfers, and pressure gradient transfers. For Rayleigh-Bénard convection, the analysis of Togni et al. (2015) suggests that the viscous transfers should be most important in the boundary layers, pressure transfers to be the most important in regions of plume separation and impingement, and combined buoyancy and viscous transfers to be required in the fluid interior. However, for turbulent convection, regions of recirculation develop in the plume separation regions where multiple types of transfer occur in quite close proximity. A bulk definition of mass transfers, and transferred fluid properties, misses this subtlety. The buoyancy and horizontal momentum of fluid parcels is very different for those different transfers, and therefore different transferred values of buoyancy and horizontal momentum should be associated with the different sources of relabelling.

Possible alternative definitions are messy to write down explicitly, but involve either associating a $\varphi_{ij}^{\mathrm{T}}$ with each piecewise-continuous part of the boundary ∂D_{ij}, or with each different process which contributes to the transfers. The latter is easiest to define via the version of the indicator function evolution equation which writes the indicator in terms of step functions, for then the processes contributing to the relabelling are transparent.

3.4.2 Diffusive terms

The diffusion term in the buoyancy equation can be rewritten using the product rule:

$$\kappa\sigma_i(\boldsymbol{\nabla}^2 b)_i^{\mathrm{r}} = \kappa\left(\boldsymbol{\nabla}\cdot\boldsymbol{\nabla}\sigma_i b_i^{\mathrm{r}} - (\boldsymbol{\nabla}\cdot b\boldsymbol{\nabla}I_i)^{\mathrm{r}} - (\boldsymbol{\nabla}I_i\cdot\boldsymbol{\nabla}b)^{\mathrm{r}}\right) \tag{3.73}$$

$$= \kappa\sigma_i\boldsymbol{\nabla}^2 b_i^{\mathrm{r}} + \kappa\boldsymbol{\nabla}\cdot(b_i^{\mathrm{r}}\boldsymbol{\nabla}\sigma_i) + \kappa\boldsymbol{\nabla}\sigma_i\cdot\boldsymbol{\nabla}b_i^{\mathrm{r}} - \kappa(\boldsymbol{\nabla}\cdot b\boldsymbol{\nabla}I_i)^{\mathrm{r}} - \kappa(\boldsymbol{\nabla}I_i\cdot\boldsymbol{\nabla}b)^{\mathrm{r}}. \tag{3.74}$$

The last two terms require parametrization, but sum to zero over all partitions and therefore may be neglected without adding a spurious source or sink to the mean buoyancy equation. The last term is the filtered buoyancy gradient along the outward-pointing normal at the boundary of domain D_i:

$$-\kappa(\boldsymbol{\nabla}I_i\cdot\boldsymbol{\nabla}b)^{\mathrm{r}} = -\kappa\int_{\mathbb{R}^d} g(\varepsilon)\boldsymbol{\nabla}I_i\cdot\boldsymbol{\nabla}b\,\mathrm{d}V \tag{3.75}$$

$$= \kappa\int_{\partial D_i} g(\varepsilon)\hat{\mathbf{n}}_{\partial D_i}\cdot\boldsymbol{\nabla}b\,\mathrm{d}(\partial D_i), \tag{3.76}$$

while the second to last term is the divergence of the filtered buoyancy times the outward pointing normal vector at the boundary of domain D_i:

$$-\kappa(\boldsymbol{\nabla}\cdot b\boldsymbol{\nabla}I_i)^{\mathrm{r}} = \kappa\boldsymbol{\nabla}\cdot\int_{\partial D_i} g(\varepsilon)b\hat{\mathbf{n}}_{\partial D_i}\,\mathrm{d}(\partial D_i) \tag{3.77}$$

$$= \kappa\int_{\partial D_i} g(\varepsilon)\hat{\mathbf{n}}_{\partial D_i}\cdot\boldsymbol{\nabla}b\,\mathrm{d}(\partial D_i) + \kappa\int_{\partial D_i} g(\varepsilon)b\boldsymbol{\nabla}\cdot\hat{\mathbf{n}}_{\partial D_i}\,\mathrm{d}(\partial D_i). \tag{3.78}$$

The last term here includes the divergence of the surface normal, $\boldsymbol{\nabla}\cdot\hat{\mathbf{n}}_{\partial D_i}$, which is equal to the sum of the principal curvatures of the surface ∂D_i. If the interface is a real interface between two phases, this can be related to the pressure jump across the interface and surface tension effects via the Young-Laplace equation. It is unclear whether a similar relation should be used when there is no real interface, as for the desired application to modelling convection. However, if the interface is expected to be definitely concave, or definitely convex, that tells us the sign the term must take, and therefore whether it acts as a buoyancy source or sink. For instance, buoyancy contours in classical entraining plume solutions tend to be mostly convex, so $\boldsymbol{\nabla}\cdot\hat{\mathbf{n}} > 0$ on the boundary of a buoyancy-based partition, making the term a source of buoyancy.

Here we see again that directly considering the "δ-function structure" of derivatives of the indicator function actually produces expressions which are both physically interpretable, and calculable.

3.4.3 Stress

Viscous terms

More care is required with the viscous terms due to their tensorial nature. Before considering the viscous terms it is worth remembering that we generally wish to express tensors as *symmetric* tensors in fluid dynamics, since a nonzero antisymmetric part implies that there is a net torque locally on fluid elements (Gilbert et al. 2014). In incompressible fluid dynamics, this is often forgotten because $\boldsymbol{\nabla}\cdot(\boldsymbol{\nabla}\mathbf{u}+(\boldsymbol{\nabla}\mathbf{u})^{\mathsf{T}}) = \boldsymbol{\nabla}\cdot(\boldsymbol{\nabla}\mathbf{u})^{\mathsf{T}} = \boldsymbol{\nabla}^2\mathbf{u}$ when $\boldsymbol{\nabla}\cdot\mathbf{u}=0$[9]. Since $\boldsymbol{\nabla}\cdot\mathbf{u}_i^{\mathrm{r}} \neq 0$ in a multi-fluid system, it is instructive to re-insert the symmetric part. We also note that any tensor can be split into its isotropic and deviatoric parts; this is worth mentioning because, although the pressure is the only isotropic stress in the incompressible Navier-Stokes equations, other isotropic stresses will arise when conditionally filtering the equations. This is already apparent when *un*conditionally spatially filtering the equation set; the Reynolds stress has a nonzero isotropic part: the turbulent kinetic energy(!). This requires some more notation:

Definition 10 (Tensor decompositions)**.** For any rank 2 tensor $\mathbf{A}$, we define:

1. the *symmetric part of* $\mathbf{A}$:

$$\mathbf{symm}(\mathbf{A}) \coloneqq \frac{1}{2}\left(\mathbf{A}+\mathbf{A}^{\mathsf{T}}\right); \tag{3.79}$$

2. the *antisymmetric part of* $\mathbf{A}$:

$$\mathbf{asymm}(\mathbf{A}) \coloneqq \frac{1}{2}\left(\mathbf{A}-\mathbf{A}^{\mathsf{T}}\right); \tag{3.80}$$

3. the *isotropic part of* $\mathbf{A}$:

$$\mathbf{iso}(\mathbf{A}) \coloneqq \frac{1}{d}\mathbf{tr}(\mathbf{A})\mathbf{I}_d; \tag{3.81}$$

4. the *deviatoric part of* $\mathbf{A}$:

$$\mathbf{dev}(\mathbf{A}) \coloneqq \mathbf{A}-\mathbf{iso}(\mathbf{A}). \tag{3.82}$$

Note that all of the defined operations are *linear*, i.e. $\mathbf{f}(c\mathbf{A}+\mathbf{B}) = c\mathbf{f}(\mathbf{A})+\mathbf{f}(\mathbf{B})$ for constant c, tensors $\mathbf{A},\mathbf{B}$, and $\mathbf{f}(\cdot)\in\{\mathbf{symm}(\cdot),\mathbf{asymm}(\cdot),\mathbf{iso}(\cdot),\mathbf{dev}(\cdot)\}$. For reference, in other texts $\mathbf{asymm}(\mathbf{A})$ is sometimes called the "rotational part", $\mathbf{iso}(\mathbf{A})$ is sometimes called the "hydrostatic part", and $\mathbf{dev}(\mathbf{A})$ is sometimes called the "anisotropic part".

An immediate corollary is $\mathbf{A} = \mathbf{symm}(\mathbf{A})+\mathbf{asymm}(\mathbf{A}) = \mathbf{iso}(\mathbf{A})+\mathbf{dev}(\mathbf{A})$. We

[9]Here we use the convention $[\boldsymbol{\nabla}\mathbf{u}]_{\mu\nu} = \partial u_\mu/\partial x_\nu$.

further note that $\mathbf{asymm}(\mathbf{iso}(\mathbf{A})) = \mathbf{0}$ for any $\mathbf{A}$. These definitions are co-ordinate independent, meaning that the decomposition into symmetric and antisymmetric parts, or into isotropic and deviatoric parts, is independent of reference frame.

With that in mind, we use the product rule to rewrite the viscous term in equation (3.12):

$$\begin{aligned}\nu\sigma_i(\boldsymbol{\nabla}^2\mathbf{u})_i^{\mathrm{r}} &= \nu(\boldsymbol{\nabla}\cdot 2\,\mathbf{symm}[\boldsymbol{\nabla}I_i\mathbf{u}])^{\mathrm{r}} - \nu(\boldsymbol{\nabla}\cdot 2\,\mathbf{symm}[\mathbf{u}\otimes\boldsymbol{\nabla}I_i])^{\mathrm{r}} \\ &\quad - \nu(\boldsymbol{\nabla}I_i\cdot 2\,\mathbf{symm}[\boldsymbol{\nabla}\mathbf{u}])^{\mathrm{r}} \\ &= \nu\boldsymbol{\nabla}\cdot 2\,\mathbf{symm}(\boldsymbol{\nabla}\sigma_i\mathbf{u}_i^{\mathrm{r}}) - \nu\boldsymbol{\nabla}\cdot 2\,\mathbf{symm}[\mathbf{u}\otimes\boldsymbol{\nabla}I_i]^{\mathrm{r}} \\ &\quad - \nu(\boldsymbol{\nabla}I_i\cdot 2\,\mathbf{symm}[\boldsymbol{\nabla}\mathbf{u}])^{\mathrm{r}}.\end{aligned} \tag{3.83}$$

It is worth noting here that $\mathbf{symm}(\mathbf{u}\otimes\boldsymbol{\nabla}I_i)^{\mathrm{r}} = \mathbf{symm}(\boldsymbol{\nabla}\sigma_i\mathbf{u}_i^{\mathrm{r}}) - (\mathbf{symm}\boldsymbol{\nabla}\mathbf{u})_i^{\mathrm{r}}$, i.e. the difference between the conditionally-filtered strain rate tensor, and the strain rate tensor for the conditionally-filtered velocity field. Analogously to the expression for the diffusive terms, Equation (3.74), the second and third terms in the final expression above sum to zero over all fluids and therefore could be neglected without introducing a spurious source or sink to the mean momentum equation. The isotropic part of $\mathbf{symm}(\boldsymbol{\nabla}\mathbf{u})$ is zero, since $\boldsymbol{\nabla}\cdot\mathbf{u} = 0$, and the isotropic parts of $\mathbf{symm}(\boldsymbol{\nabla}\sigma_i\mathbf{u}_i^{\mathrm{r}})$ and $\mathbf{symm}[\mathbf{u}\otimes\boldsymbol{\nabla}I_i]^{\mathrm{r}}$ are both equal to $\boldsymbol{\nabla}\cdot\sigma_i\mathbf{u}_i^{\mathrm{r}}$. Thus all the isotropic parts cancel and we can write:

$$\begin{aligned}\nu\sigma_i(\boldsymbol{\nabla}^2\mathbf{u})_i^{\mathrm{r}} &= \nu\boldsymbol{\nabla}\cdot\mathbf{dev}\{2\,\mathbf{symm}(\boldsymbol{\nabla}\sigma_i\mathbf{u}_i^{\mathrm{r}})\} - \nu\boldsymbol{\nabla}\cdot\mathbf{dev}\{2\,\mathbf{symm}[\mathbf{u}\otimes\boldsymbol{\nabla}I_i]^{\mathrm{r}}\} \\ &\quad - \nu(\boldsymbol{\nabla}I_i\cdot 2\,\mathbf{dev}\{\mathbf{symm}[\boldsymbol{\nabla}\mathbf{u}]\})^{\mathrm{r}}.\end{aligned} \tag{3.84}$$

This means we can expand the first term on the right-hand side without worrying about cancellations of its isotropic part with isotropic parts of the other two terms:

$$\begin{aligned}\boldsymbol{\nabla}\cdot\mathbf{dev}\{2\,\mathbf{symm}(\boldsymbol{\nabla}\sigma_i\mathbf{u}_i^{\mathrm{r}})\} &= \boldsymbol{\nabla}\cdot\sigma_i\mathbf{dev}\{2\,\mathbf{symm}(\boldsymbol{\nabla}\mathbf{u}_i^{\mathrm{r}})\} \\ &\quad + \boldsymbol{\nabla}\cdot\mathbf{dev}\{2\,\mathbf{symm}(\mathbf{u}_i^{\mathrm{r}}\otimes\boldsymbol{\nabla}\sigma_i)\} \\ &= \sigma_i\boldsymbol{\nabla}\cdot\mathbf{dev}\{2\,\mathbf{symm}(\boldsymbol{\nabla}\mathbf{u}_i^{\mathrm{r}})\} \\ &\quad + \boldsymbol{\nabla}\sigma_i\cdot\mathbf{dev}\{2\,\mathbf{symm}(\boldsymbol{\nabla}\mathbf{u}_i^{\mathrm{r}})\} \\ &\quad + \boldsymbol{\nabla}\cdot\mathbf{dev}\{2\,\mathbf{symm}(\mathbf{u}_i^{\mathrm{r}}\otimes\boldsymbol{\nabla}\sigma_i)\} \\ &= \sigma_i\boldsymbol{\nabla}\cdot\left\{\boldsymbol{\nabla}\mathbf{u}_i^{\mathrm{r}} + (\boldsymbol{\nabla}\mathbf{u}_i^{\mathrm{r}})^{\mathsf{T}} - \frac{2}{d}(\boldsymbol{\nabla}\cdot\mathbf{u}_i^{\mathrm{r}})\mathbf{I}_d\right\} \\ &\quad + \boldsymbol{\nabla}\sigma_i\cdot\mathbf{dev}\{2\,\mathbf{symm}(\boldsymbol{\nabla}\mathbf{u}_i^{\mathrm{r}})\} \\ &\quad + \boldsymbol{\nabla}\cdot\mathbf{dev}\{2\,\mathbf{symm}(\mathbf{u}_i^{\mathrm{r}}\otimes\boldsymbol{\nabla}\sigma_i)\}\end{aligned}$$

$$
\begin{aligned}
&= \sigma_i \boldsymbol{\nabla}^2 \mathbf{u}_i^{\mathrm{r}} + \left(\frac{d-2}{d}\right) \sigma_i \boldsymbol{\nabla}(\boldsymbol{\nabla} \cdot \mathbf{u}_i^{\mathrm{r}}) \\
&\quad + \boldsymbol{\nabla}\sigma_i \cdot \mathbf{dev}\{2\ \mathbf{symm}(\boldsymbol{\nabla}\mathbf{u}_i^{\mathrm{r}})\} \\
&\quad + \boldsymbol{\nabla} \cdot \mathbf{dev}\{2\ \mathbf{symm}(\mathbf{u}_i^{\mathrm{r}} \otimes \boldsymbol{\nabla}\sigma_i)\}.
\end{aligned} \tag{3.85}
$$

The final line uses that $\boldsymbol{\nabla}\cdot(f\mathbf{I}_d) \equiv \boldsymbol{\nabla} f$ for any scalar function f, as well as $\boldsymbol{\nabla}\cdot\boldsymbol{\nabla}\mathbf{A} \equiv \boldsymbol{\nabla}(\boldsymbol{\nabla}\cdot\mathbf{A})$, $\boldsymbol{\nabla}\cdot[\boldsymbol{\nabla}\mathbf{A}]^{\mathsf{T}} \equiv \boldsymbol{\nabla}^2\mathbf{A}$ for any vector function $\mathbf{A}$. Substituting this back into equation (3.84) for the full viscous term gives:

$$
\begin{aligned}
\nu\sigma_i(\boldsymbol{\nabla}^2\mathbf{u})_i^{\mathrm{r}} &= \nu\sigma_i \boldsymbol{\nabla}^2 \mathbf{u}_i^{\mathrm{r}} + \left(\frac{d-2}{d}\right) \nu\sigma_i \boldsymbol{\nabla}(\boldsymbol{\nabla} \cdot \mathbf{u}_i^{\mathrm{r}}) \\
&\quad + \nu\boldsymbol{\nabla}\sigma_i \cdot \mathbf{dev}\{2\ \mathbf{symm}(\boldsymbol{\nabla}\mathbf{u}_i^{\mathrm{r}})\} - \nu(\boldsymbol{\nabla} I_i \cdot \mathbf{dev} 2\ \mathbf{symm}[\boldsymbol{\nabla}\mathbf{u}])^{\mathrm{r}} \\
&\quad + \nu\boldsymbol{\nabla} \cdot \mathbf{dev}\{2\ \mathbf{symm}(\mathbf{u}_i^{\mathrm{r}} \otimes \boldsymbol{\nabla}\sigma_i)\} - \nu\boldsymbol{\nabla} \cdot \mathbf{dev}\{2\ \mathbf{symm}[\mathbf{u} \otimes \boldsymbol{\nabla} I_i]^{\mathrm{r}}\} \\
&= \sigma_i\nu \boldsymbol{\nabla}^2 \mathbf{u}_i^{\mathrm{r}} + \left(\frac{d-2}{d}\right) \sigma_i \boldsymbol{\nabla}(\nu\boldsymbol{\nabla} \cdot \mathbf{u}_i^{\mathrm{r}}) \\
&\quad - [(\boldsymbol{\nabla} I_i \cdot 2\nu\ \mathbf{dev}\{\mathbf{symm}[\boldsymbol{\nabla}\mathbf{u}]\})^{\mathrm{r}} - \boldsymbol{\nabla}\sigma_i \cdot \mathbf{dev}\{2\nu\ \mathbf{symm}(\boldsymbol{\nabla}\mathbf{u}_i^{\mathrm{r}})\}] \\
&\quad - [\boldsymbol{\nabla} \cdot \mathbf{dev}\{2\nu\ \mathbf{symm}[\mathbf{u} \otimes \boldsymbol{\nabla} I_i]^{\mathrm{r}}\} - \boldsymbol{\nabla} \cdot \mathbf{dev}\{2\nu\ \mathbf{symm}(\mathbf{u}_i^{\mathrm{r}} \otimes \boldsymbol{\nabla}\sigma_i)\}] .
\end{aligned} \tag{3.86}
$$

Written in this way, each term is explicitly Galilean invariant. The unknown terms have been grouped with their corresponding expressions involving resolved variables, analogous to the construction of the Reynolds stress tensor in traditional turbulence modelling.

The first term on the right hand side is the usual form of diffusion added in multi-fluid models (e.g. Thuburn et al. 2019; Weller et al. 2020). The third and fourth terms require closure; both arise directly from spatial variations in I_i (representing momentum transfer across the interface, which we will discuss further shortly). However, the second term is an additionalmomentum stress which depends only on resolved variables within fluid partition i. This term is missed when diffusion is added post-hoc, as when the underlying equation set is assumed to be inviscid (which is the case in Thuburn et al. 2018).For $d > 2$ the interpretation of this term is clear[10]: it is a resistance to compression or expansion of the fluid. This is easiest to see if we restrict to flow along one dimension; thus consider the acceleration of a fluid parcel along the $\hat{\mathbf{x}}$ direction due to $\boldsymbol{\nabla}(\boldsymbol{\nabla}\cdot\mathbf{u})$. We have $\mathrm{D}u/\mathrm{D}t \propto \partial(\boldsymbol{\nabla}\cdot\mathbf{u})/\partial x$. Assume that the divergence is increasing along the $\mathbf{x}$ direction; this accelerates the fluid parcel in the $\mathbf{x}$ direction, which increases $\boldsymbol{\nabla}\cdot\mathbf{u}$ behind the fluid parcel and decreases $\boldsymbol{\nabla}\cdot\mathbf{u}$ in front of it, acting to smooth out differences in the divergence.

[10]Note that d here is the dimension of the underlying fluid. Therefore we need not consider the pathological case $d = 1$; the case $d = 2$ is simple because the term vanishes.

A term identical in form arises in compressible fluid dynamics. As a bulk viscous stress, this term not only has consequences for the momentum budget, but also introduces a positive-semidefinite sink of energy — see Section 3.4.4. This is an important consequence of the fact that conditionally filtering a fluid introduces a source of divergence within each partition due to relabelling of fluid at the interface, even when the underlying fluid is divergence free.

With the exception of terms involving the spatial variation of ν, the above derivation holds for the conditional filtering of *any* stress tensor which linearly and isotropically depends on the rate-of-strain tensor. Notably, this includes a lot of turbulence models: any turbulence model using so-called "down-gradient diffusion" to model the Reynolds stress tensor. This includes the Smagorinsky model widely used in LES reference simulations of the atmosphere — so the extra bulk viscous term should be included when developing multi-fluid models of convection.

We now take a closer look at the interpretation of the unknown terms in Equation (3.86). Recalling the relation between the gradient of the indicator and the surface delta function, Equation (3.34), we have for the first term:

$$\begin{aligned} -(\boldsymbol{\nabla} I_i \cdot 2\nu \,\mathsf{dev}\{\mathsf{symm}[\boldsymbol{\nabla}\mathbf{u}]\})^{\mathrm{r}} &= \int_{\mathbb{R}^d} g\ \delta(\mathbf{x} \in \partial D_i)\mathbf{n}_{\partial D_i} \cdot 2\nu\ \mathsf{dev}\{\mathsf{symm}[\boldsymbol{\nabla}\mathbf{u}]\}\,\mathrm{d}V \\ &= \int_{\partial D_i} g\ \mathbf{n}_{\partial D_i} \cdot 2\nu\ \mathsf{symm}[\boldsymbol{\nabla}\mathbf{u}]\,\mathrm{d}(\partial D_i). \end{aligned} \tag{3.87}$$

The integrand is the projection of the rate-of-strain tensor onto the boundary of partition i, i.e. the resolved viscous momentum flux through the interface. If there is shear *at* the interface, this term accounts for its contribution to the momentum budget. It is exactly cancelled by the corresponding term at the boundary of other partitions (because, for a point $\mathbf{x} \in \partial D_i \cap \partial D_j$, $\mathbf{n}_{\partial D_i} = -\mathbf{n}_{\partial D_j}$). For the second term we have:

$$-\boldsymbol{\nabla} \cdot \mathsf{dev}\{2\nu\ \mathsf{symm}[\mathbf{u} \otimes \boldsymbol{\nabla} I_i]^{\mathrm{r}}\} \tag{3.88}$$

$$= \boldsymbol{\nabla} \cdot \mathsf{dev}\left\{2\nu\ \mathsf{symm}\left(\int_{\mathbb{R}^d} g\ \mathbf{u} \otimes \mathbf{n}_{\partial D_i} \delta(\mathbf{x} \in \partial D_i)\,\mathrm{d}V\right)\right\}$$

$$= \boldsymbol{\nabla} \cdot \mathsf{dev}\left\{2\nu\ \mathsf{symm}\left(\int_{\partial D_i} g\ \mathbf{u} \otimes \mathbf{n}_{\partial D_i}\,\mathrm{d}(\partial D_i)\right)\right\}. \tag{3.89}$$

Dopazo (1977) arrives at a similar expression (their equation (17), which is defined in a Reynolds-averaging context, and includes the isotropic part), which they describe as "an additional viscous force of the turbulent on the non-turbulent region", going on to say that "[t]he physical meaning [of this expression] as well as a different mathematical way to recover it may be clearly seen in Landau and Lifshitz (1987, p. 74) and Batchelor (1970) in connexion with the viscosity of suspensions." That

the integrand represents an additional viscous force is obvious, given how it arises. However, its interpretation beyond that is tricky; in this author's opinion, neither resource quoted by Dopazo gives a clear explanation of what this term represents. It perhaps helps to remember that $\mathbf{dev}\ \mathbf{symm}(\mathbf{u} \otimes \boldsymbol{\nabla} I_i)^{\mathrm{r}} = \mathbf{dev}\ \mathbf{symm}\boldsymbol{\nabla}(\sigma_i \mathbf{u}_i^{\mathrm{r}}) - \mathbf{dev}\ \mathbf{symm}\sigma_i(\boldsymbol{\nabla}\mathbf{u})_i^{\mathrm{r}}$, i.e. the difference between the resolved rate of shear in partition i, and the rate of shear computed using resolved variables. For a control volume entirely within the domain D_i this difference is zero, so the difference must arise purely from the boundaries between fluid partitions.

Beyond that, explicit geometric interpretation is useful, which requires more breaking down:

$$-\boldsymbol{\nabla} \cdot \mathbf{dev}\{2\nu\ \mathbf{symm}[\mathbf{u} \otimes \boldsymbol{\nabla} I_i]^{\mathrm{r}}\} = \int_{\partial D_i} g\ 2\nu\ \Big[(\mathbf{u} \cdot \boldsymbol{\nabla})\mathbf{n}_{\partial D_i} + (\mathbf{n}_{\partial D_i} \cdot \boldsymbol{\nabla})\mathbf{u} + \mathbf{u}(\boldsymbol{\nabla} \cdot \mathbf{n}_{\partial D_i}) - \frac{2}{d}\boldsymbol{\nabla}(\mathbf{u} \cdot \mathbf{n}_{\partial D_i})\Big]\, \mathrm{d}(\partial D_i). \tag{3.90}$$

Now we can interpret all of the terms geometrically. The first term, $(\mathbf{u} \cdot \boldsymbol{\nabla})\mathbf{n}_{\partial D_i}$, is the gradient of the normal vector in the direction of the velocity field. Since the gradient of the normal is in the tangent plane of the interface, this projects the velocity vector onto the tangent plane of the interface. The second term, $(\mathbf{n}_{\partial D_i} \cdot \boldsymbol{\nabla})\mathbf{u}$, is the gradient of the velocity vector in the direction of the surface normal. The third term includes the divergence of the surface normal, which appeared in our expressions for the diffusive terms. Again, this can be interpreted in terms of the curvature of the interface, and related to any relevant surface tension effects. The final term is the gradient of the normal component of the velocity vector. Clearly all of these terms depend on the detailed dynamics of the interface.

The resources quoted by Dopazo (1977) do give interesting methods for approximating the volume-averaged contribution of this term for the case of dilute suspensions of particles. Clearly this is not directly relevant to the modelling of atmospheric convection, but similar techniques may be useful for studying the limiting behaviour of these terms for idealized convective flows in the fully-parametrized limit.

Pressure terms

The pressure gradient term $\langle I_i \boldsymbol{\nabla} P \rangle$ can be rewritten as:

$$\sigma_i \boldsymbol{\nabla} P_i^{\mathrm{r}} = \boldsymbol{\nabla} \langle I_i P \rangle_g - \langle P \boldsymbol{\nabla} I_i \rangle_g \tag{3.91}$$

$$= \boldsymbol{\nabla}(\sigma_i P_i^{\mathrm{r}}) - \langle P \boldsymbol{\nabla} I_i \rangle_g \tag{3.92}$$

$$= \sigma_i \boldsymbol{\nabla} P^{\mathrm{r}} + \boldsymbol{\nabla}(\sigma_i p_i) + \left[P^{\mathrm{r}} \boldsymbol{\nabla}\sigma_i - (P\boldsymbol{\nabla} I_i)^{\mathrm{r}}\right], \tag{3.93}$$

where $\sigma_i p_i \coloneqq \sigma_i P_i^{\mathrm{r}} - \sigma_i P^{\mathrm{r}} = (I_i P)^{\mathrm{r}} - (I_i)^{\mathrm{r}}(P)^{\mathrm{r}}$, and $P^{\mathrm{r}} = \sum_i \sigma_i P_i^{\mathrm{r}}$ by definition. The total pressure P^{r} is the pressure which satisfies the divergence-free constraint for the total velocity field $\mathbf{u}^{\mathrm{r}} \coloneqq \sum_i \sigma_i \mathbf{u}_i^{\mathrm{r}}$. The deviation pressures p_i are the difference between the resolved pressure in each fluid and the total resolved pressure, and so their fluid fraction-weighted sum over all fluids is zero.

The term $-(P\boldsymbol{\nabla} I_i)^{\mathrm{r}}$ is the resolved pressure gradient force acting at the interface between partitions. This can be seen by noting that $\boldsymbol{\nabla} I_i = -\delta(\mathbf{x} \in \partial D_i)\hat{\mathbf{n}}_{\partial D_i}$, i.e. a unit vector pointing *in*wards from the domain boundary of fluid i, and existing only at that boundary. This boundary is a 2D surface, so $-P\boldsymbol{\nabla} I_i$ is exactly the pressure force pushing outwards from the domain of fluid i, and $-(P\boldsymbol{\nabla} I_i)^{\mathrm{r}}$ is just the resolved part of this. We choose to decompose the pressure gradient term in this way so that the term in square brackets gives zero contribution when summed over all fluids. This term represents the difference between resolved pressure drag due to the mean pressure and resolved fluid fraction, and the actual filtered pressure drag at the interface between partitions. Since it sums to zero over all partitions, we may neglect it without introducing a spurious contribution to the total momentum equation.

Combined stress tensor

We have shown that careful treatment of the conditionally filtered viscous term gives rise to a resolved bulk viscous stress: a term depending on the divergence of the resolved velocity field within a fluid. In this section, we wish to recast the above treatment in terms of a general stress tensor $\boldsymbol{\varsigma}$, and then argue that applying the Newton-Stokes conditions to the stress tensor within each fluid partition suggests that (part of) the pressure differences between the partitions can be accounted for with an additional bulk viscous stress.

We denote the full stress tensor by $\boldsymbol{\varsigma}$; in general continuum mechanics this is called the "Cauchy stress tensor", usually denoted by $\boldsymbol{\sigma}$. We use the alternate lowercase sigma in order to avoid confusion with the fluid fraction σ_i. For a fluid, it is customary to split the stress tensor into its equilibrium and non-equilibrium parts, $\boldsymbol{\varsigma}_{\mathrm{e}}$ and $\boldsymbol{\varsigma}_{\mathrm{n}}$. The non-equilibrium part is often written $\boldsymbol{\tau}$, and we will use that notation from here. The equilibrium (or hydrostatic) part is the stress which would exist for the fluid at rest, and is therefore determined by the thermodynamic pressure field (see §3.4 of Batchelor 1967, or §§15, 49 of Landau and Lifshitz 1987). The non-equilibrium part can be further decomposed into its isotropic, symmetric

deviatoric, and antisymmetric parts:

$$\boldsymbol{\varsigma} = -P\mathbf{I}_d + \boldsymbol{\tau} \tag{3.94}$$

$$= -P\mathbf{I}_d + \frac{1}{d}\mathbf{tr}(\boldsymbol{\tau}) + \mathbf{dev\ symm}(\boldsymbol{\tau}) + \mathbf{asymm}(\boldsymbol{\tau}). \tag{3.95}$$

These respectively represent the response of a material fluid element to isotropic compression/expansion, shear, and net torque. The additional resistance to isotropic compression/expansion is also a pressure, in the sense that the pressure is the normal force on a surface element — which is precisely the full isotropic part of the stress tensor, not just the equilibrium part. If the non-equilibrium part of the stress has no isotropic part, which is true for an incompressible Newtonian fluid, then there is no difference between these two senses of the pressure.

Why does this matter? First let us recover the stress tensor for our Boussinesq fluid[11]. We assume that no net torque acts on an infinitesimal fluid element, so the non-equilibrium part of the stress tensor must be symmetric: $\mathbf{asymm}(\boldsymbol{\tau}) = \mathbf{0}$. We then note that the only difference between the stresses felt by a fluid at rest and a fluid in motion is the presence of the velocity field; therefore the non-equilibrium part of the stress must only be related to the velocity field. It cannot be directly related to the velocity because this would break Galileian invariance; the next-simplest choice is that it is related to the gradient of the velocity, the rate-of-strain tensor: $\mathbf{symm}(\boldsymbol{\tau}) \sim \mathbf{symm}(\boldsymbol{\nabla}\mathbf{u})$. (This construction can be thought of as expanding $\boldsymbol{\varsigma}$ as a Taylor series in $\boldsymbol{\nabla}\mathbf{u}$.) We then suppose that the fluid is *Newtonian*: the non-equilibrium part of the momentum stress tensor is *linearly* and *isotropically* related to the rate-of-strain tensor (these are sometimes called the "Newton-Stokes conditions"). "Linear" means that the proportionality factor between the two must be a tensor; "isotropic" requires this tensor to be isotropic. At this point we briefly switch to index notation for clarity. The most general tensor relationship between two rank two tensors is provided by an arbitrary rank four tensor, $\Gamma_{\mu\nu\rho\lambda}$; we require this rank four tensor to be isotropic:

$$[\boldsymbol{\tau}]_{\mu\nu} = \Gamma_{\mu\nu\rho\lambda}\frac{1}{2}\left(\partial_\rho u_\lambda + \partial_\lambda u_\rho\right). \tag{3.96}$$

Because $\boldsymbol{\tau}$ is supposed symmetric, $\Gamma_{\mu\nu\rho\lambda} = \Gamma_{\nu\mu\rho\lambda}$. The only isotropic rank four tensor is constructed of products of the rank-two identity tensor:

$$\begin{aligned}\Gamma_{\mu\nu\rho\lambda} &= a\delta_{\mu\rho}\delta_{\nu\lambda} + b\delta_{\mu\lambda}\delta_{\nu\rho} + c\delta_{\mu\nu}\delta_{\rho\lambda} \\ &= 2a\delta_{\mu\rho}\delta_{\nu\lambda} + c\delta_{\mu\nu}\delta_{\rho\lambda},\end{aligned} \tag{3.97}$$

[11] This section closely follows derivations which can be found elsewhere; for instance, §§3.3-3.4 of Batchelor (1967).

for scalars a, c. Substituting this into Equation (3.96) gives:

$$\boldsymbol{\tau} = 2a\frac{1}{2}\mathbf{symm}(\boldsymbol{\nabla}\mathbf{u}) + c(\boldsymbol{\nabla}\cdot\mathbf{u})\mathbf{I}_d. \tag{3.98}$$

Since $\boldsymbol{\nabla}\cdot\mathbf{u} = 0$ for a Boussinesq fluid, $\boldsymbol{\nabla}\cdot\boldsymbol{\tau} = \boldsymbol{\nabla}\cdot\left(a(\boldsymbol{\nabla}\mathbf{u} + (\boldsymbol{\nabla}\mathbf{u})^{\mathsf{T}})\right) = a\boldsymbol{\nabla}^2\mathbf{u}$ (for constant a). Identifying $a \to \nu$, this is the correct expression for the stress tensor.

Why bother with all of this? Well, in a multi-fluid system, we do not know the correct expression for the conditionally-filtered stress tensor. All we can write is:

$$\langle I_i\boldsymbol{\nabla}\cdot\boldsymbol{\varsigma}\rangle = \boldsymbol{\nabla}\cdot(\sigma_i\boldsymbol{\varsigma}_i^{\mathrm{r}}) - \langle\boldsymbol{\nabla}I_i\cdot\boldsymbol{\varsigma}\rangle\,. \tag{3.99}$$

Conditionally filtering $\boldsymbol{\varsigma}$ (using (3.95) with $\boldsymbol{\tau}$ given by (3.98)) gives:

$$\sigma_i\boldsymbol{\varsigma}_i^{\mathrm{r}} = \langle -I_iP\mathbf{I}_d\rangle + 2\nu\ \mathbf{symm}(\langle I_i\boldsymbol{\nabla}\mathbf{u}\rangle) \tag{3.100}$$

$$= \sigma_i\left(-P_i^{\mathrm{r}}\mathbf{I}_d + 2\nu\ \mathbf{symm}(\boldsymbol{\nabla}\mathbf{u}_i^{\mathrm{r}})\right) - 2\nu\ \mathbf{symm}\left(\mathbf{u}_i^{\mathrm{r}}\otimes\boldsymbol{\nabla}\sigma_i - (\mathbf{u}\otimes\boldsymbol{\nabla}I_i)^{\mathrm{r}}\right). \tag{3.101}$$

But what if we presumed that, to first order, the stress within each fluid is Newtonian? Then the conditionally-filtered stress would be:

$$\boldsymbol{\varsigma}_i^{\mathrm{r}} = -P_{(\mathrm{e})i}^{\mathrm{r}}\mathbf{I}_d + c_i(\boldsymbol{\nabla}\cdot\mathbf{u}_i^{\mathrm{r}})\mathbf{I}_d + 2a_i\ \mathbf{symm}(\boldsymbol{\nabla}\mathbf{u}_i^{\mathrm{r}}), \tag{3.102}$$

plus higher order terms. Comparing with Equation (3.101) shows that, for the partitioned stress to be fully Newtonian, either $2\nu\ \mathbf{symm}\left(\mathbf{u}_i^{\mathrm{r}}\otimes\boldsymbol{\nabla}\sigma_i - (\mathbf{u}\otimes\boldsymbol{\nabla}I_i)^{\mathrm{r}}\right) = \mathbf{0}$, or $2\nu\ \mathbf{symm}\left(\mathbf{u}_i^{\mathrm{r}}\otimes\boldsymbol{\nabla}\sigma_i - (\mathbf{u}\otimes\boldsymbol{\nabla}I_i)^{\mathrm{r}}\right) \propto 2\nu\ \sigma_i\mathbf{symm}(\boldsymbol{\nabla}\mathbf{u}_i^{\mathrm{r}})$. But even if the stress is *not* fully Newtonian, unless $\mathbf{symm}\left(\mathbf{u}_i^{\mathrm{r}}\otimes\boldsymbol{\nabla}\sigma_i - (\mathbf{u}\otimes\boldsymbol{\nabla}I_i)^{\mathrm{r}}\right)$ is very large, there is clearly an important Newtonian part.

This tells us that, in a multi-fluid system, the divergence due to relabelling of fluid contributes an isotropic stress, with associated bulk viscosity c_i. But how do we relate $P_{(\mathrm{e})i}^{\mathrm{r}}$, the "equilibrium" pressure in fluid i, to the full resolved pressure P_i^{r}? Part of this equilibrium pressure must arise from P^{r}, the pressure satisfying the only explicit continuity constraint. Beyond that, some of the difference will be thermodynamic, i.e. due to the different buoyancy fields in each partition. But some of it must be kinematic: the different partitions have different velocity fields also. Assuming that this kinematic difference between P_i^{r} and $P_{(\mathrm{e})i}^{\mathrm{r}}$ is, to first order, just the difference between P_i^{r} and P^{r}, this suggests that $p_i = -c_i\boldsymbol{\nabla}\cdot\mathbf{u}_i^{\mathrm{r}}$. What we are arguing is: all fluids in a multi-fluid system have separate pressures P_i^{r}; these deviate from the common pressure experienced by all fluids, P_{c}, at any location due to the presence of different velocity fields, $\mathbf{u}_i^{\mathrm{r}}$. We assume that the difference between the pressures is, to first order, linearly dependent on the gradient of the

difference between the velocity field in the partition and the mean velocity:

$$P_i^{\mathrm{r}} - P_{\mathrm{c}} = \boldsymbol{\Gamma}' : \boldsymbol{\nabla}\left(\mathbf{u}_i^{\mathrm{r}} - \sum_i \sigma_i \mathbf{u}_i^{\mathrm{r}}\right) + \text{higher order \& nonlinear terms.} \tag{3.103}$$

Here the bold colon notation means the complete contraction of two rank-2 tensors, i.e. $\mathbf{A} : \mathbf{B} \coloneqq A_{ab}B^{ab}$ for any two rank 2 tensors $\mathbf{A}, \mathbf{B}$. Since the pressure is isotropic, the expression on the right hand side must also be isotropic, requiring the proportionality tensor $\boldsymbol{\Gamma}'$ to be proportional to the identity tensor $\boldsymbol{\Gamma}' \propto \mathbf{I}_d$. Thus $P_i^{\mathrm{r}} - P_{\mathrm{c}} = -\gamma_i \boldsymbol{\nabla} \cdot \mathbf{u}_i^{\mathrm{r}}$ to first order, as the mean velocity is divergence-free. Note that γ_i need not be the same in each fluid partition, nor is it required to be homogeneous.

By definition, $\sigma_i p_i$ must sum to zero over all fluids, but in order for the bulk viscous contribution to satisfy this constraint, a correction term must be added:

$$p_i = -\gamma_i \boldsymbol{\nabla} \cdot \mathbf{u}_i^{\mathrm{r}} + \sum_j (\sigma_j \gamma_j \boldsymbol{\nabla} \cdot \mathbf{u_j}). \tag{3.104}$$

This correction suggests that the "common pressure experienced by all fluids" is $P_c = P^{\mathrm{r}} + \sum_i (\sigma_i \gamma_i \boldsymbol{\nabla} \cdot \mathbf{u_i})$, though the correction will only be large if the resolved advection of σ_i is large. The derivation of $P_i^{\mathrm{r}} - P_c \propto \boldsymbol{\nabla} \cdot \mathbf{u}_i^{\mathrm{r}}$ still holds.

To summarize, *the correct application of the Newton-Stokes conditions directly suggests that the difference between the equilibrium pressure and the dynamic pressure in each fluid partition is given by a bulk viscous stress.* This gives us a parametrization for the leading-order kinematic differences in pressure between the fluid partitions, as a so-called "bulk viscous pressure". It should be noted that such isotropic stresses do not conserve filter scale energy. This should be obvious since they arise due to the viscous stress, not the filtering of the pressure gradient term.

It is usually argued that this "bulk viscous pressure" is negligible in the sorts of weakly compressible flow encountered in the geosciences, or else, if non-negligible in magnitude, that it may be subsumed entirely into the definition of the (dynamical) pressure with at most second-order inconsistencies (Papalexandris 2020). However, in the case of a multi-fluid system neither of these arguments hold. Firstly, there is no reason to believe that the divergences within each partition will be small, since they arise due to advection of the label functions, which are not necessarily negligible. Secondly, the divergences will be different in each partition, so cannot simply be subsumed into the definition of the pressure. Thus the bulk viscous contribution to the pressure difference between fluid partitions should be a generic feature of multi-fluid modelling, even for flows where the underlying fluid is assumed divergence-free.

Since the divergence within a partition is dependent on the advection of the

indicator labels, the accuracy of the bulk viscous pressure is expected to depend directly on the accuracy of the transfer term formulation.

3.4.4 Energetics

Thuburn and Vallis (2018) discussed the energetics of the conditionally-filtered Euler equations; the energetics of the Boussinesq system are similar, except for the treatment of the viscous terms, which do not appear in the Euler equations.

The contribution of the viscous terms to the kinetic energy of the resolved flow in partition i is:

$$\begin{aligned}
\mathbf{u}_i^{\mathrm{r}} \cdot \langle I_i \boldsymbol{\nabla} \cdot \boldsymbol{\tau} \rangle &= \mathbf{u}_i^{\mathrm{r}} \cdot \{ \boldsymbol{\nabla} \cdot (\sigma_i \boldsymbol{\tau}_i^{\mathrm{r}}) - \langle \boldsymbol{\nabla} I_i \cdot \boldsymbol{\tau} \rangle \} && (3.105)\\
&= \boldsymbol{\nabla} \cdot (\sigma_i \mathbf{u}_i^{\mathrm{r}} \cdot \boldsymbol{\tau}_i^{\mathrm{r}}) - \sigma_i \boldsymbol{\tau}_i^{\mathrm{r}} : \boldsymbol{\nabla} \mathbf{u}_i^{\mathrm{r}} - \mathbf{u}_i^{\mathrm{r}} \cdot \langle \boldsymbol{\nabla} I_i \cdot \boldsymbol{\tau} \rangle && (3.106)\\
&= \boldsymbol{\nabla} \cdot (\sigma_i \mathbf{u}_i^{\mathrm{r}} \cdot \boldsymbol{\tau}_i^{\mathrm{r}}) - \sigma_i \mathsf{iso}[\boldsymbol{\tau}_i^{\mathrm{r}}] : \boldsymbol{\nabla} \mathbf{u}_i^{\mathrm{r}} - \sigma_i \mathsf{dev\ symm}[\boldsymbol{\tau}_i^{\mathrm{r}}] : \boldsymbol{\nabla} \mathbf{u}_i^{\mathrm{r}} \\
&\quad - \sigma_i \mathsf{dev\ asymm}[\boldsymbol{\tau}_i^{\mathrm{r}}] : \boldsymbol{\nabla} \mathbf{u}_i^{\mathrm{r}} - \mathbf{u}_i^{\mathrm{r}} \cdot \langle \boldsymbol{\nabla} I_i \cdot \boldsymbol{\tau} \rangle && (3.107)
\end{aligned}$$

Decomposing the viscous stress tensor in this way allows us to maximize the amount of the dissipation rate which can be directly expressed in terms of resolved variables. For our incompressible Newtonian fluid, $\boldsymbol{\tau} = \nu(\boldsymbol{\nabla}\mathbf{u})^{\mathsf{T}}$, $\mathsf{iso}[\boldsymbol{\tau}_i^{\mathrm{r}}] = \mathbf{0}, \mathsf{asymm}[\boldsymbol{\tau}_i^{\mathrm{r}}] = \mathbf{0}$, and $\mathsf{dev\ symm}[\sigma_i \boldsymbol{\tau}_i^{\mathrm{r}}] = \mathsf{symm}[\sigma_i \boldsymbol{\tau}_i^{\mathrm{r}}] = \nu\sigma_i 2\ \mathsf{symm}[\boldsymbol{\nabla}\mathbf{u}_i^{\mathrm{r}}] - 2\nu\ \mathsf{symm}[\langle \mathbf{u} \otimes \boldsymbol{\nabla} I_i \rangle - \mathbf{u}_i^{\mathrm{r}} \otimes \boldsymbol{\nabla}\sigma_i]$. This simplifies the kinetic energy term to:

$$\begin{aligned}
\mathbf{u}_i^{\mathrm{r}} \cdot \langle I_i \boldsymbol{\nabla} \cdot \boldsymbol{\tau} \rangle &= \boldsymbol{\nabla} \cdot (\sigma_i \mathbf{u}_i^{\mathrm{r}} \cdot \boldsymbol{\tau}_i^{\mathrm{r}}) - \nu\sigma_i 2\ \mathsf{symm}[\boldsymbol{\nabla}\mathbf{u}_i^{\mathrm{r}}] : \boldsymbol{\nabla}\mathbf{u}_i^{\mathrm{r}} \\
&\quad - 2\nu\ \mathsf{symm}[\langle \mathbf{u} \otimes \boldsymbol{\nabla} I_i \rangle - \mathbf{u}_i^{\mathrm{r}} \otimes \boldsymbol{\nabla}\sigma_i] : \boldsymbol{\nabla}\mathbf{u}_i^{\mathrm{r}} - \mathbf{u}_i^{\mathrm{r}} \cdot \langle \boldsymbol{\nabla} I_i \cdot \boldsymbol{\tau} \rangle \\
&= \boldsymbol{\nabla} \cdot (\sigma_i \mathbf{u}_i^{\mathrm{r}} \cdot \boldsymbol{\tau}_i^{\mathrm{r}}) - \nu\sigma_i 2\ \|\mathsf{symm}[\boldsymbol{\nabla}\mathbf{u}_i^{\mathrm{r}}]\|^2 \\
&\quad - 2\nu\ \mathsf{symm}[\langle \mathbf{u} \otimes \boldsymbol{\nabla} I_i \rangle - \mathbf{u}_i^{\mathrm{r}} \otimes \boldsymbol{\nabla}\sigma_i] : \boldsymbol{\nabla}\mathbf{u}_i^{\mathrm{r}} \\
&\quad - \mathbf{u}_i^{\mathrm{r}} \cdot \langle \boldsymbol{\nabla} I_i \cdot \boldsymbol{\tau} \rangle
\end{aligned} \tag{3.108}$$

If a viscous term of the form $\nu\sigma_i \boldsymbol{\nabla}^2 \mathbf{u}_i^{\mathrm{r}}$ had been used instead, as is done when the viscous terms are added post-hoc (Tan et al. 2018; Thuburn et al. 2019; Weller et al. 2020), the dissipation rate would be different; we would instead have:

$$\begin{aligned}
\mathbf{u}_i^{\mathrm{r}} \cdot \sigma_i \nu \boldsymbol{\nabla} \cdot (\boldsymbol{\nabla}\mathbf{u}_i^{\mathrm{r}})^{\mathsf{T}} &= \boldsymbol{\nabla} \cdot \left(\sigma_i \mathbf{u}_i^{\mathrm{r}} \cdot (\boldsymbol{\nabla}\mathbf{u}_i^{\mathrm{r}})^{\mathsf{T}}\right) - \nu\sigma_i (\boldsymbol{\nabla}\mathbf{u}_i^{\mathrm{r}})^{\mathsf{T}} : \boldsymbol{\nabla}\mathbf{u}_i^{\mathrm{r}} - \nu\,(\mathbf{u}_i^{\mathrm{r}} \otimes \boldsymbol{\nabla}\sigma_i) : \boldsymbol{\nabla}\mathbf{u}_i^{\mathrm{r}} \\
&= \boldsymbol{\nabla} \cdot \left(\sigma_i \mathbf{u}_i^{\mathrm{r}} \cdot (\boldsymbol{\nabla}\mathbf{u}_i^{\mathrm{r}})^{\mathsf{T}}\right) - \nu\sigma_i \|\mathsf{symm}[\boldsymbol{\nabla}\mathbf{u}_i^{\mathrm{r}}]\|^2 + \nu\sigma_i \|\mathsf{asymm}[\boldsymbol{\nabla}\mathbf{u}_i^{\mathrm{r}}]\|^2 \\
&\quad - \nu\,(\mathbf{u}_i^{\mathrm{r}} \otimes \boldsymbol{\nabla}\sigma_i) : \boldsymbol{\nabla}\mathbf{u}_i^{\mathrm{r}}.
\end{aligned} \tag{3.109}$$

Clearly $\|\mathsf{symm}[\boldsymbol{\nabla}\mathbf{u}_i^{\mathrm{r}}]\|^2 - \|\mathsf{asymm}[\boldsymbol{\nabla}\mathbf{u}_i^{\mathrm{r}}]\|^2 \leq 2\ \|\mathsf{symm}[\boldsymbol{\nabla}\mathbf{u}_i^{\mathrm{r}}]\|^2$ in general, so the viscous dissipation rate calculated entirely in terms of resolved variables is therefore

incorrect if the symmetrization of the stress tensor is not properly accounted for[12]. The reason is because *not* having a symmetric stress tensor implies that there may be net torques on fluid elements — this can both add and subtract kinetic energy from the flow, meaning that the "dissipation" is no longer even negative semi-definite! Thus there is a direct energetic consequence to missing this term from the momentum equation. This is important: getting the correct dissipation is crucial in turbulence models, since the dissipation rate is used to set the turbulence length scales.

The contribution to the kinetic energy of the resolved flow from the pressure gradient terms is:

$$-\mathbf{u}_i^{\mathrm{r}} \cdot \langle I_i \boldsymbol{\nabla} P \rangle = -\boldsymbol{\nabla} \cdot (\sigma_i \mathbf{u}_i^{\mathrm{r}} P_i^{\mathrm{r}}) + \sigma_i P_i^{\mathrm{r}} \boldsymbol{\nabla} \cdot \mathbf{u}_i^{\mathrm{r}} + \mathbf{u}_i^{\mathrm{r}} \cdot \langle P \boldsymbol{\nabla} I_i \rangle \,. \tag{3.110}$$

The first term is a transport term; the final term is the work done against the resolved pressure drag by the resolved velocity. The middle term is a pressure work term, caused by the non-zero divergence of the conditionally filtered velocity fields. In form, this term is exactly like that which appears in compressible fluid dynamics. The difference here is that the underlying fluid is incompressible, and so instead of appearing as source terms in a budget for the internal energy, the term appears as a source in the *subfilter* kinetic energy equation, i.e. in the transport equation for the quantity $1/\sigma_i \, ((\mathbf{u} \cdot \mathbf{u})_i^{\mathrm{r}} - \mathbf{u}_i^{\mathrm{r}} \cdot \mathbf{u}_i^{\mathrm{r}})$:

$$\begin{aligned} -\langle I_i \boldsymbol{\nabla} \cdot (P\mathbf{u}) \rangle + \mathbf{u}_i^{\mathrm{r}} \cdot \langle I_i \boldsymbol{\nabla} P \rangle &= -\boldsymbol{\nabla} \cdot \langle I_i P \mathbf{u} \rangle + \langle P\mathbf{u} \cdot \boldsymbol{\nabla} I_i \rangle + \boldsymbol{\nabla} \cdot (\sigma_i \mathbf{u}_i^{\mathrm{r}} P_i^{\mathrm{r}}) \\ &\quad - \sigma_i P_i^{\mathrm{r}} \boldsymbol{\nabla} \cdot \mathbf{u}_i^{\mathrm{r}} - \mathbf{u}_i^{\mathrm{r}} \cdot \langle P \boldsymbol{\nabla} I_i \rangle \\ &= -\boldsymbol{\nabla} \cdot (\sigma_i [\langle (P\mathbf{u}) \rangle_i - P_i^{\mathrm{r}} \mathbf{u}_i^{\mathrm{r}}]) - \sigma_i P_i^{\mathrm{r}} \boldsymbol{\nabla} \cdot \mathbf{u}_i^{\mathrm{r}} \\ &\quad + [\langle \mathbf{u} \cdot P \boldsymbol{\nabla} I_i \rangle - \mathbf{u}_i^{\mathrm{r}} \cdot \langle P \boldsymbol{\nabla} I_i \rangle] \,. \end{aligned} \tag{3.111}$$

This subtlety is easily missed when working with the fully compressible equations, since in that case the divergence within a fluid partition is a sum of the contributions from the advection of the indicator function and the real divergence of the underlying fluid.

If we model the pressure differences between partitions by a bulk viscous stress, the contribution to the within-partition kinetic energy is:

$$\sigma_i p_i \boldsymbol{\nabla} \cdot \mathbf{u}_i^{\mathrm{r}} = -\sigma_i (\gamma_i \boldsymbol{\nabla} \cdot \mathbf{u}_i^{\mathrm{r}} - \sum_j \gamma_j \sigma_j \boldsymbol{\nabla} \cdot \mathbf{u}_j) \boldsymbol{\nabla} \cdot \mathbf{u}_i^{\mathrm{r}} \tag{3.112}$$

$$= -\sigma_i \gamma_i (\boldsymbol{\nabla} \cdot \mathbf{u}_i^{\mathrm{r}})^2 + \sigma_i \boldsymbol{\nabla} \cdot \mathbf{u}_i^{\mathrm{r}} \sum_j \gamma_j \sigma_j \boldsymbol{\nabla} \cdot \mathbf{u}_j. \tag{3.113}$$

[12]It is possible to show the same result without explicitly requiring the within-partition stress tensors to be symmetric; however, we believe that directly accounting for the symmetry makes the calculation clearer and its physical interpretation more transparent.

The first term is a definite dissipation, however the second term could take either sign. Summing over all fluids however allows us to write the contribution of the bulk viscous pressure term to the kinetic energy summed over all fluids, $\sum_i \mathbf{u}_i^{\mathrm{r}} \cdot \mathbf{u}_i^{\mathrm{r}}$:

$$\sum_i \sigma_i p_i \boldsymbol{\nabla} \cdot \mathbf{u}_i^{\mathrm{r}} = -\sum_i \sigma_i \gamma_i (\boldsymbol{\nabla} \cdot \mathbf{u}_i^{\mathrm{r}})^2 + \left(\sum_i \sigma_i \boldsymbol{\nabla} \cdot \mathbf{u}_i^{\mathrm{r}} \right) \left(\sum_j \gamma_j \sigma_j \boldsymbol{\nabla} \cdot \mathbf{u}_j \right). \quad (3.114)$$

By the Cauchy-Schwartz inequality, the first term may be rewritten as:

$$\sum_i \sigma_i \gamma_i (\boldsymbol{\nabla} \cdot \mathbf{u}_i^{\mathrm{r}})^2 = \sum_j \sigma_j \sum_i \sigma_i \gamma_i (\boldsymbol{\nabla} \cdot \mathbf{u}_i^{\mathrm{r}})^2 \quad (3.115)$$

$$\geq \left(\sum_i \sigma_i \sqrt{\gamma_i} \boldsymbol{\nabla} \cdot \mathbf{u}_i^{\mathrm{r}} \right)^2. \quad (3.116)$$

If the bulk viscosities are the same in all fluids, $\gamma_i = \gamma \ \forall i$, then $\sum_i \sigma_i p_i \boldsymbol{\nabla} \cdot \mathbf{u}_i^{\mathrm{r}} \leq 0$, showing that the bulk viscous pressure parametrization acts as a sink of the within-partition kinetic energy summed over all fluids — and therefore as a source of subfilter kinetic energy.

3.4.5 Subfilter fluxes

The "subfilter flux" terms $\boldsymbol{\nabla} \cdot \sigma_i ((\mathbf{u} \otimes \mathbf{u})_i^{\mathrm{r}} - \mathbf{u}_i^{\mathrm{r}} \otimes \mathbf{u}_i^{\mathrm{r}})$ and $\boldsymbol{\nabla} \cdot \sigma_i ((\mathbf{u}b)_i^{\mathrm{r}} - \mathbf{u}_i^{\mathrm{r}} b_i)$ are analogous to similar terms which arise in single-fluid modelling of turbulence. It is important to note two differences, however; firstly, $(\mathbf{u} \otimes \mathbf{u})_i^{\mathrm{r}}$ and $(\mathbf{u}b)_i^{\mathrm{r}}$ contain contributions from all partitions, *not just partition i*. Secondly, the sum of the fluxes over all partitions is not equal to the corresponding flux from the filtered single-fluid equations, due to the difference between $\sum_i \sigma_i \mathbf{u}_i^{\mathrm{r}} \otimes \mathbf{u}_i^{\mathrm{r}}$ and $\mathbf{u}^{\mathrm{r}} \otimes \mathbf{u}^{\mathrm{r}}$. The ramifications of this for modelling the fluxes are beyond the scope of this chapter.

However, if one wishes to parametrize the subfilter momentum flux by analogy with viscous stress, as is very often done in both LES and RANS turbulence modelling with a so-called "downgradient" closure, the correct way to do so is by assuming that the subfilter momentum flux is linearly and isotropically related to the strain tensor $2\,\mathbf{symm}(\boldsymbol{\nabla} \mathbf{u}_i^{\mathrm{r}})$. Since the individual fluid partitions are not divergence free, careful application of this choice must also introduce an extra isotropic stress, as discussed in the previous sections.

3.5 Boundary conditions

The boundary conditions must also be filtered in order to provide a complete equation set. Periodic conditions are not affected by the conditional filtering, they simply

pass through to the filtered fields. Other boundary conditions are affected by a) the usual problems of the finite extent of spatial filters close to a boundary (Fureby and Tabor 1997), and b) Neumann boundary conditions are additionally affected by non-commutation of spatial derivatives with multiplication by the indicator functions.

The former effect, (a), would in general require the replacement of boundary conditions by so-called "wall functions" (standard practice in LES) which are dependent on the grid spacing in the vicinity of the boundary. For instance, in the case of velocity boundary conditions, the correct form for the boundary condition depends on whether the closest grid point to the boundary lies in the viscous sublayer, the buffer layer, or the log-layer.

This problem can be partially negated by using an anisotropic filter, with characteristic width much smaller in the direction perpendicular to the boundary than in the direction parallel. Such anisotropic filters are generally implied in modelling of the atmosphere.

The second effect is relevant regardless of filter scale. For a Neumann boundary condition of the form

$$\hat{\mathbf{n}} \cdot \boldsymbol{\nabla} \varphi = \chi, \tag{3.117}$$

where $\hat{\mathbf{n}}$ is a unit vector field normal to the boundary, multiplication by an indicator function I_i gives:

$$I_i \hat{\mathbf{n}} \cdot \boldsymbol{\nabla} \varphi = I_i \chi \tag{3.118}$$

$$\implies \hat{\mathbf{n}} \cdot \boldsymbol{\nabla} (I_i \varphi) - \varphi \hat{\mathbf{n}} \cdot \boldsymbol{\nabla} I_i = I_i \chi, \tag{3.119}$$

where the product rule has been used in going from the first line to the second. Neglecting the non-commutation of a spatial filter with the spatial derivative, and assuming that $\hat{\mathbf{n}}$ varies slowly on the filter scale, the conditionally filtered Neumann boundary condition is:

$$\hat{\mathbf{n}} \cdot \boldsymbol{\nabla} \varphi_i + \frac{1}{\sigma_i} \left[\varphi_i \hat{\mathbf{n}} \cdot \boldsymbol{\nabla} \sigma_i - \overline{\varphi \hat{\mathbf{n}} \cdot \boldsymbol{\nabla} I_i} \right] = \chi_i. \tag{3.120}$$

The terms in square brackets are not in general zero, and rely on the boundary conditions for σ_i and I_i. To determine both of these conditions, knowledge of the behaviour of the indicator function in the vicinity of the boundary is required. This behaviour will depend on asymptotics of whatever variables define the indicator, and will therefore in general be different for different choices of indicator function.

Clearly the above expression simplifies to

$$\hat{\mathbf{n}} \cdot \boldsymbol{\nabla} \varphi_i = \chi_i \tag{3.121}$$

if either $\varphi = 0$ or $\hat{\mathbf{n}} \cdot \boldsymbol{\nabla} I_i = 0$ on the boundary.

An exact integral expression for $-\overline{\varphi \hat{\mathbf{n}} \cdot \boldsymbol{\nabla} I_i}$ follows from the results of Section 3.3:

$$-\overline{\varphi \hat{\mathbf{n}} \cdot \boldsymbol{\nabla} I_i} = \int_{\partial D_i \cap \partial D} g(\varepsilon) \varphi \hat{\mathbf{n}} \cdot \hat{\mathbf{n}}_{\partial D_i} \, \mathrm{d}(\partial D_i \cap \partial D), \tag{3.122}$$

where $\partial D_i \cap \partial D$ is the intersection of the physical boundary of the domain, ∂D, with the boundary of fluid partition i, ∂D_i. Clearly this is only generally zero if those two boundaries either do not intersect, or are orthogonal wherever they do intersect.

The boundary conditions for the fluid fractions themselves depend on the limit of $\overline{I_i}$ as the boundary is approached. No more can be said without specifying what the I_i represent, which is beyond the scope of this chapter.

3.6 Conditional horizontal averaging of the first normal mode of Rayleigh-Bénard convection

To make the preceding analysis more concrete, we shall explicitly conditionally filter a simple flow. Consider the problem of Rayleigh-Bénard convection between two free boundaries; after subtracting a horizontally homogeneous, time-independent, zero-flow reference state (see Section 2.1), the first normal mode solutions for the buoyancy, b, and vertical velocity, w, are (Chandrasekhar 1961, p. 23):

$$b = B \cos\left(\frac{\pi x}{\sqrt{2}H}\right) \sin\left(\frac{\pi z}{H}\right), \tag{3.123}$$

$$w = W \cos\left(\frac{\pi x}{\sqrt{2}H}\right) \sin\left(\frac{\pi z}{H}\right), \tag{3.124}$$

where H is the depth of the domain, and $B, W \in \mathbb{R}_{>0}$ are constants. The flow is periodic in x, with period $2\sqrt{2}H$ (for the most unstable mode). The same analysis can be performed for the case of no-slip boundaries; nothing significant changes, as the horizontal dependence of the solution is still sinusoidal, simply with a different wavelength for the most unstable mode. However, the vertical dependence is more cumbersome; see p. 39 of Chandrasekhar (1961).

The divergence of the momentum equation gives

$$\boldsymbol{\nabla}^2 P = \frac{\partial b}{\partial z}, \tag{3.125}$$

giving the corresponding expression for the pressure:

$$P = \Pi \cos\Big(\frac{\pi x}{\sqrt{2}H}\Big)\cos\Big(\frac{\pi z}{H}\Big), \tag{3.126}$$

with $\Pi = -B\ 2H/3\pi$. From the mass continuity equation we find

$$u = -\sqrt{2}W \sin\Big(\frac{\pi x}{\sqrt{2}H}\Big)\cos\Big(\frac{\pi z}{H}\Big) \tag{3.127}$$

for the horizontal velocity. It is easily confirmed that this is a solution to the Boussinesq equations (2.4)-(2.6) on the domain $\{x, z, t\} \in D = [0, 2\sqrt{2}H] \times [0, H] \times [0, \infty)$, with periodic boundaries in the x direction and stress-free boundaries in the z-direction, once a stationary hydrostatically balanced solution dependent only on z has been factored out.

Let us now partition the flow into rising and falling parts: by inspection of $w(x, z)$ we find

$$w > 0 \quad \text{in the region} \quad -\frac{\sqrt{2}H}{2} < x < \frac{\sqrt{2}H}{2}, \tag{3.128}$$

$$w < 0 \quad \text{in the region} \quad \frac{\sqrt{2}H}{2} < x < \frac{3\sqrt{2}H}{2}, \tag{3.129}$$

so the indicator function does not depend on z. Let us conditionally average in the horizontal. From equations (3.11)–(3.14), the full conditionally horizontally averaged two-fluid 2D Boussinesq equation set is (making the replacements $\varphi_i^{\mathrm{r}} \to \varphi_i$, $\mathcal{S}_i^{+\mathrm{r}} \to \sigma_j S_{ji}$, and replacing $(\dots)^{\mathrm{r}} \to \overline{(\dots)}$):

$$\frac{\partial \sigma_i}{\partial t} + \frac{\partial}{\partial z}(\sigma_i w_i) = \sigma_j S_{ji} - \sigma_i S_{ij}, \tag{3.130}$$

$$\begin{aligned}\frac{\partial \sigma_i w_i}{\partial t} + \frac{\partial}{\partial z}\big(\sigma_i w_i^2\big) = {} & \sigma_i b_i - \sigma_i \frac{\partial \overline{P}}{\partial z} - \frac{\partial}{\partial z}(\sigma_i p_i) - \left[\overline{P}\frac{\partial \sigma_i}{\partial z} - \overline{\left(P\frac{\partial I_i}{\partial z}\right)}\right] + \nu\frac{\partial^2}{\partial z^2}(\sigma_i w_i) \\ & - \nu\frac{\partial}{\partial z}\overline{\left(w\frac{\partial I_i}{\partial z}\right)} - \nu\left\{\overline{\frac{\partial I_i}{\partial x}\frac{\partial w}{\partial x}} + \overline{\frac{\partial I_i}{\partial z}\frac{\partial w}{\partial z}}\right\} \\ & + \sigma_j w_{ji}^{\mathrm{T}} S_{ji} - \sigma_i w_{ij}^{\mathrm{T}} S_{ij} - \frac{\partial}{\partial z}\left(\sigma_i s_i(w, w)\right),\end{aligned} \tag{3.131}$$

$$\begin{aligned}\frac{\partial \sigma_i b_i}{\partial t} + \frac{\partial}{\partial z}(\sigma_i w_i b_i) = {} & \kappa\frac{\partial^2}{\partial z^2}(\sigma_i b_i) - \kappa\frac{\partial}{\partial z}\overline{\left(b\frac{\partial I_i}{\partial z}\right)} - \kappa\left\{\overline{\frac{\partial I_i}{\partial x}\frac{\partial b}{\partial x}} + \overline{\frac{\partial I_i}{\partial z}\frac{\partial b}{\partial z}}\right\} \\ & + \sigma_j b_{ji}^{\mathrm{T}} S_{ji} - \sigma_i b_{ij}^{\mathrm{T}} S_{ij} - \frac{\partial}{\partial z}\left(\sigma_i s_i(b, w)\right),\end{aligned} \tag{3.132}$$

$$\sum_i \frac{\partial}{\partial z}(\sigma_i w_i) = 0. \tag{3.133}$$

Clearly the fluid fraction in each partition is equal to 1/2 everywhere,

$$\sigma_{w>0} = \sigma_{w<0} = \tfrac{1}{2}. \tag{3.134}$$

For the pressure, we get:

$$\begin{aligned} P_{w>0}(z) &= \frac{1}{\sigma_{w>0}} \frac{1}{2\sqrt{2}H} \int_{-\frac{H}{\sqrt{2}}}^{\frac{H}{\sqrt{2}}} \Pi \cos\left(\frac{\pi x}{\sqrt{2}H}\right) \cos\left(\frac{\pi z}{H}\right) \mathrm{d}x \\ &= \frac{2\Pi}{\pi} \cos\left(\frac{\pi z}{H}\right), \end{aligned} \tag{3.135}$$

$$P_{w<0}(z) = -\frac{2\Pi}{\pi} \cos\left(\frac{\pi z}{H}\right). \tag{3.136}$$

The mean pressure, i.e. the un-conditioned horizontally-averaged pressure, is zero.

For the vertical velocity, we get:

$$w_{w>0}(z) = \frac{2W}{\pi} \sin\left(\frac{\pi z}{H}\right), \qquad w_{w<0}(z) = -\frac{2W}{\pi} \sin\left(\frac{\pi z}{H}\right) \tag{3.137}$$

$$\implies \frac{\mathrm{d}w_{w>0}}{\mathrm{d}z} = \frac{2W}{H} \cos\left(\frac{\pi z}{H}\right), \qquad \frac{\mathrm{d}w_{w<0}}{\mathrm{d}z} = -\frac{2W}{H} \cos\left(\frac{\pi z}{H}\right). \tag{3.138}$$

Therefore the difference between the pressure in each partition and the mean pressure is equal to minus the divergence of the velocity field in that partition, multiplied by a constant. The constant is given by

$$\begin{aligned} \gamma &= \frac{P_{w>0}}{-\,\mathrm{d}w_{w>0}/\mathrm{d}z} \\ &= \frac{2}{3\pi} \frac{BH^2}{W}. \end{aligned} \tag{3.139}$$

Assuming a free convective scaling, $B = \Delta B, W = \sqrt{\Delta B\ H}$, this gives

$$\begin{aligned} \frac{\gamma}{\nu} &= \frac{2}{3\pi} \sqrt{\frac{\Delta B\ H^3}{\kappa\nu}}\, \mathrm{Pr}^{-1/2} \\ &= \frac{2}{3\pi}\, \mathrm{Ra}^{1/2}\, \mathrm{Pr}^{-1/2}\,. \end{aligned} \tag{3.140}$$

This result is exactly the expected scaling of $\gamma(\mathrm{Ra}, \mathrm{Pr})$ (see Section 4.2.2), with the width of the plumes, δ, set to scale with H: $\delta \sim H$. This is the only possible scaling δ can take in this simple example.

Now we horizontally average the advection of the indicator function:

$$\frac{1}{2\sqrt{2}H} \int_0^{2\sqrt{2}H} \mathbf{u} \cdot \boldsymbol{\nabla} I_{w>0}\, \mathrm{d}x = -\frac{1}{2\sqrt{2}H} \int_0^{2\sqrt{2}H} \mathbf{u} \cdot \hat{\mathbf{n}}_{\partial D_{w>0}} \delta(\mathbf{x} \in \partial D_{w>0})\, \mathrm{d}x$$

$$= -\frac{1}{2\sqrt{2}H}\int_0^{2\sqrt{2}H} (\mathbf{u}\cdot\hat{\mathbf{n}}_{\partial D_{w>0}})\left[\delta(x-\tfrac{\sqrt{2}H}{2})+\delta(x-\tfrac{3\sqrt{2}H}{2})\right]\mathrm{d}x$$
$$= -\frac{1}{2\sqrt{2}H}\left(u(\tfrac{\sqrt{2}H}{2})-u(\tfrac{3\sqrt{2}H}{2})\right)$$
$$= \frac{W}{H}\cos\Big(\frac{\pi z}{H}\Big) \tag{3.141}$$
$$= \frac{\mathrm{d}(\sigma_{w>0}w_{w>0})}{\mathrm{d}z} \tag{3.142}$$
$$= \sigma_{w>0}\frac{\mathrm{d}w_{w>0}}{\mathrm{d}z}, \tag{3.143}$$

so the filtered advection of the indicator function gives rise to a divergence within the conditionally-filtered velocity field, precisely as expected.

We can also use the results of section 3 to directly calculate the exchange terms between the two fluids. For the fluid fraction transfer rate, S_{ij}, we can use (3.60) with a horizontal-average kernel to get:

$$\sigma_{w<0}S_{<>} = \frac{1}{2\sqrt{2}H}\int_{\partial D_{<>}} \mathcal{H}(-\mathbf{u}\cdot\hat{\mathbf{n}}_{\partial D_{<>}})\times(-\mathbf{u}\cdot\hat{\mathbf{n}}_{\partial D_{<>}})\,\mathrm{d}(x\cap\partial D_{w<0})$$
$$= \frac{W}{H}\mathcal{H}(z-\tfrac{H}{2})(-\cos\big(\tfrac{\pi z}{H}\big)), \tag{3.144}$$
and $$\sigma_{w>0}S_{><} = \frac{W}{H}\mathcal{H}(\tfrac{H}{2}-z)(\cos\big(\tfrac{\pi z}{H}\big)). \tag{3.145}$$

Here $<>$ is shorthand for $w<0\to w>0$. This expression matches exactly with the previous result for the advection of the indicator function $I_{w>0}$, as expected given that $\partial\sigma_i/\partial t = 0$ for this problem, and so $\langle\mathbf{u}\cdot\boldsymbol{\nabla}I_i\rangle = \sigma_j S_{ji} - \sigma_i S_{ij}$.

From (3.60) with the function g equal to a horizontal average kernel times b or w it follows that

$$b_{ij}^T = 0, \qquad w_{ij}^T = 0. \tag{3.146}$$

This is clear from inspection since ∂D_0 is made up of $w=0$ surfaces, which coincide with $b=0$ surfaces. Note that since we subtracted the reference solution from the normal mode solutions, the actual transferred buoyancy is equal to the reference buoyancy, $b_{\mathrm{R}} \coloneqq (\Delta B/2)(1-(2z)/H)$.

The analysis of this simple normal mode solution shows that the pressure differences between the fluid partitions can be important; that for this simple flow, it can be shown explicitly that the pressure differences are proportional to a constant times the divergence of the fluid flow within a partition; and that the divergence is exactly equal to the filtered advection of the indicator function.

This section also demonstrated the use of several of the exact results concerning gradients of the indicator function, showing that they are useful calculational tools.

3.7 Discussion and conclusions

In this chapter we have:

- provided a derivation of a multi-fluid Boussinesq equation set, which will be the focus of work for the remainder of this thesis, taking particular care with viscous and relabelling terms;
- used the results for derivatives of the indicator function to provide integral expressions for many of the unknown subfilter terms requiring closure, aiding in their interpretation;
- (semi-)rigorously treated the material derivative of the indicator function in terms of the theory of distributions, leading to useful expressions for exchange terms between the fluids, and also unifying and extending previous work on conditionally-averaged/filtered fluid dynamics (Dopazo 1977; Thuburn et al. 2018; Yano 2014);
- shown that a careful treatment of the viscous terms introduces a new isotropic viscous stress dependent entirely on resolved variables (missed in previous studies);
- argued that the above results suggest modelling pressure differences between the partitions as bulk viscous stresses — even in flows where the underlying fluid is incompressible;
- discussed the energetic consequences of this model, showing it to be consistent;
- directly calculated the conditionally filtered flow for a very simple problem, showing explicitly that a divergent conditionally-filtered flow appears from a divergence-free underlying flow; directly shown that the pressure differences between the fluid partitions are a) large, and b) exactly equal to a constant times the divergence within the fluid partition; shown that this constant scales consistently with the scaling argument to be presented in Section 4.2.2.

Chapter 4

Two-fluid modelling of Rayleigh-Bénard convection in a single column

Note that the work in this Chapter has been published in Shipley et al. (2022).

4.1 Introduction

Multi-fluid modelling has recently been proposed as an approach to representing convection in the grey zone (Tan et al. 2018; Thuburn et al. 2018; Yano 2014); similar equation sets are used for the modelling of multi-phase flows in engineering (e.g. Städtke 2007). In the convection context, this takes inspiration from traditional mass-flux parametrizations in splitting the fluid into multiple components, which may represent updrafts, environment, downdrafts etc.. The split is applied directly to the governing equations, which are then spatially filtered, allowing a fully 3D and time-dependent framework to be derived (Thuburn et al. 2018; Chapter 3 of this thesis). Neither quasi-equilibrium nor small updraft fraction are assumed in the derivation. Each "fluid" evolves according to its own prognostic equations, interacting with other fluids via the pressure gradient, and terms involving the exchange of mass, momentum, energy, and tracers. These exchange terms are the analogue of entrainment, detrainment, and cloud-base mass-flux in traditional models, and must be parametrized. Convection is inherently a part of the dynamics in this framework: there is no separate convection scheme which is called by the dynamical core.

In order to build a multi-fluid model of atmospheric convection, the multi-fluid equation set must be closed. The form of these closures directly depends on the definition of the fluid partitions (Chapter 3; see also de Rooy et al. 2013). For example, the single-column two-fluid model of Thuburn et al. (2019) contains entrainment and detrainment closures designed to capture coherent structures in the convective boundary layer, whereas the closures in Cohen et al. (2020) are designed to model a second fluid in the cloud layer only. Perturbation pressure closures for

the latter approach were suggested in J. He et al. (2020). Entrainment and detrainment closures based on velocity divergence, and a bulk viscous parametrization for the perturbation pressure, were proposed and tested in Weller et al. (2020), but the test cases used forevaluation were non-turbulent, unlike the real atmosphere. All of these multi-fluid models have been single-column, and used standard atmospheric test cases (e.g. dry rising bubble, dry convective boundary layer, oceanic and continental shallow cumulus, diurnal deep convection) for verification. While prior work shows the considerable promise of the multi-fluid method, little work has been done testing the response of a specific multi-fluid scheme to a variety of forcings, or suggested how the closure constants should scale with that forcing. Such investigation could lead to more consistent results compared to tuning a model to a handful of test cases.

One motivation for multi-fluid modelling is that, given that it reduces to mass flux under certain additional assumptions, we can draw on the wealth of previous work on closures for mass flux schemes. Indeed, this has been the starting point for most multi-fluid models to date (Tan et al. 2018; Thuburn et al. 2019), especially for entrainment and detrainment. As this work progresses it will be important to discover which features can carry over from the homogeneous equilibrium setting, and which must be replaced. A very important difference between the two approaches, however, is that the multi-fluid approach includes both time-dependence and horizontal fluxes, which must be inserted ad-hoc in traditional mass flux schemes. Therefore despite the decades of research on mass flux approaches, it can tell us little about how to model the horizontal fluxes and memory terms which are so vital in the grey zone.

To gain a better understanding of the multi-fluid equations, and how some of the new closure terms affect the solution, we present a single-column model of dry Rayleigh-Bénard convection with one rising and one falling fluid. RBC is the simplest relevant convection problem: the equations and boundary conditions are as simple as possible while still allowing for a fully turbulent convective solution. RBC has been extensively studied, and a wealth of experimental, numerical, and theoretical results make it a well-constrained starting point (Ahlers et al. 2009; Chandrasekhar 1961; Chillà and Schumacher 2012). In particular, the scaling of bulk buoyancy (Nu) and momentum (Re) transport with the applied buoyancy forcing (Ra) is well understood over at least ten decades. For a more detailed overview of RBC, refer back to Chapter 2.

Any two-fluid parametrization of RBC should therefore aim to capture these bulk features of RBC, in particular the described scaling behaviour of Nu and Re with Ra. It is important to understand the response of the model in a fully-parametrized equilibrium setting before moving to the grey zone. This will help pin down the

physics of a multi-fluid model of convection, free of the complexities — especially microphysics and phase changes — of the real atmosphere.Although single-column, this model retains full time dependence, and places no restrictions on the magnitude of the area fraction, distinguishing it from a traditional mass flux closure.

The chapter begins with a review of the multi-fluid Boussinesq equation set derived in Chapter 3. Closures for one rising and one falling fluid which attempt to capture the large-scale overturning circulation are presented in Section 4.2.1, and a scaling argument is presented for the magnitude of the pressure differences between the fluids in Section 4.2.2. The numerical method is then described in Section 4.3. In Section 4.4, results of the two-fluid single-column model (Section 4.2.1) are compared with horizontally-averaged results from the DNS (Chapter 2, Section 2.2) over a range of buoyancy forcing spanning eight decades ($10^2 \leq \mathrm{Ra} \leq 10^{10}$), and the sensitivity of the model to its two dimensionless closure constants is investigated. The chapter concludes with a summary of its results and their relevance to convection parametrizations, and a discussion of avenues for future research.

4.2 Multi-fluid equation set and closure choices

As a first step towards building a multi-fluid parametrization of convective turbulence, we motivate and present a two-fluid single-column model of dry Rayleigh-Bénard convection. The full viscous multi-fluid Boussinesq equation set is (derived in Chapter 3):

$$\frac{\partial \sigma_i}{\partial t} + \boldsymbol{\nabla} \cdot (\sigma_i \mathbf{u}_i) = \overline{\mathcal{S}_i^+} - \overline{\mathcal{S}_i^-}, \tag{3.11}$$

$$\begin{aligned} \frac{\partial \sigma_i \mathbf{u}_i}{\partial t} + \boldsymbol{\nabla} \cdot (\sigma_i \mathbf{u}_i \otimes \mathbf{u}_i) &= \sigma_i b_i \mathbf{k} - \sigma_i \boldsymbol{\nabla} \overline{P} - \boldsymbol{\nabla}(\sigma_i p_i) - \left[\overline{P} \boldsymbol{\nabla} \sigma_i - \overline{P \boldsymbol{\nabla} I_i}\right] \\ &\quad + \nu \boldsymbol{\nabla}^2 \sigma_i \mathbf{u}_i - \nu \boldsymbol{\nabla} \cdot \overline{(\mathbf{u} \otimes \boldsymbol{\nabla} I_i)^\mathsf{T}} - \nu \overline{\boldsymbol{\nabla} I_i \cdot (\boldsymbol{\nabla} \mathbf{u})^\mathsf{T}} \\ &\quad + \overline{\mathbf{u} \mathcal{S}_i^+} - \overline{\mathbf{u} \mathcal{S}_i^-} - \boldsymbol{\nabla} \cdot (\sigma_i s_i(\mathbf{u}, \mathbf{u})), \end{aligned} \tag{3.12}$$

$$\begin{aligned} \frac{\partial \sigma_i b_i}{\partial t} + \boldsymbol{\nabla} \cdot (\sigma_i \mathbf{u}_i b_i) &= \kappa \boldsymbol{\nabla}^2 \sigma_i b_i - \kappa \overline{\boldsymbol{\nabla} I_i \cdot \boldsymbol{\nabla} b} - \kappa \boldsymbol{\nabla} \cdot \overline{b \boldsymbol{\nabla} I_i} \\ &\quad + \overline{b \mathcal{S}_i^+} - \overline{b \mathcal{S}_i^-} - \boldsymbol{\nabla} \cdot (\sigma_i s_i(\mathbf{u}, b)), \end{aligned} \tag{3.13}$$

$$\sum_i \boldsymbol{\nabla} \cdot (\sigma_i \mathbf{u}_i) = 0. \tag{3.26}$$

$$\sum_i \sigma_i = 1. \tag{3.25}$$

Here an overbar denotes a spatial filter (Germano 1992); $i \in \{0, 1, \ldots, n\}$ indexes the fluid partitions; I_i is an indicator function for fluid i; $\sigma_i \coloneqq \overline{I_i}$ is the fraction of fluid i contained within a characteristic filter volume; $\mathbf{u}_i \coloneqq \overline{I_i \mathbf{u}} / \sigma_i$ and $b_i \coloneqq \overline{I_i b} / \sigma_i$ are the

velocity and buoyancy fields of fluid i; $p_i \coloneqq \overline{I_i P}/\sigma_i - \overline{P}$ is the difference between the conditionally-filtered pressure in fluid i and the unconditionally filtered pressure $\overline{P}$; $\overline{\mathcal{S}_i^{\pm}}, \overline{\mathbf{u}\mathcal{S}_i^{\pm}}, \overline{b\mathcal{S}_i^{\pm}}$ are respectively sources and sinks of fluid fraction, momentum, and buoyancy in fluid i arising from the relabelling of fluid. The unconditionally-filtered pressure, $\overline{P}$, ensures the incompressibility of the mean flow, equation (3.26).

Equations (3.11)-(3.25) are derived by conditionally spatially filtering the Boussinesq equations (2.4)-(2.6) in the manner set out by Thuburn et al. (2018); however, here viscous terms and sources and sinks of fluid fraction are retained from the outset. The only terms neglected here are those arising from possible non-commutation of the spatial filter with the partial derivatives. For a full derivation and discussion of the terms requiring closure, see Chapter 3.

The multi-fluid analogues of the exact integral relations (2.23)-(2.22) are much more complex, and will not be used in this chapter. However, it is worth noting that averaging Equation (3.13) over a horizontal area and over time, then assuming a stationary state, gives:

$$\begin{aligned} \boldsymbol{\nabla} \cdot \langle \sigma_i \mathbf{u}_i b_i - \kappa \boldsymbol{\nabla}(\sigma_i b_i^{\mathrm{r}}) + \kappa (b \boldsymbol{\nabla} I_i)^{\mathrm{r}} + \sigma_i s_i(\mathbf{u}, b) \rangle_{A,t} \\ = - \langle \kappa (\boldsymbol{\nabla} I_i \cdot \boldsymbol{\nabla} b)^{\mathrm{r}} \rangle_{A,t} + \left\langle (b\mathcal{S}_i^+)^{\mathrm{r}} - (b\mathcal{S}_i^-)^{\mathrm{r}} \right\rangle_{A,t} \end{aligned} \tag{4.1}$$

$$\begin{aligned} \implies \frac{\partial}{\partial z} \langle \sigma_i \mathbf{u}_i b_i - \kappa \boldsymbol{\nabla}(\sigma_i b_i^{\mathrm{r}}) + \kappa (b \boldsymbol{\nabla} I_i)^{\mathrm{r}} + \sigma_i s_i(\mathbf{u}, b) \rangle_{A,t} \\ = - \langle \kappa (\boldsymbol{\nabla} I_i \cdot \boldsymbol{\nabla} b)^{\mathrm{r}} \rangle_{A,t} + \left\langle (b\mathcal{S}_i^+)^{\mathrm{r}} - (b\mathcal{S}_i^-)^{\mathrm{r}} \right\rangle_{A,t} . \end{aligned} \tag{4.2}$$

Therefore the analogue of the Nusselt number in multi-fluid RBC must include two extra contributions, one due to the subfilter flux of buoyancy (which would exist in a similar form in spatially filtered RBC), and the other purely due to the conditional filtering. (This assumes that the buoyancy transfers may not be written inside a divergence.) Of course, this within-partition Nusselt number will not generally be independent of height due to the relabelling of fluid and the non-conservative part of the subfilter viscous term. However, the Nusselt number of the total flow (i.e. summed over all partitions) remains independent of height. This has the important consequence that parametrizations of $\kappa(\boldsymbol{\nabla} I_i \cdot \boldsymbol{\nabla} b)^{\mathrm{r}}$ and $\boldsymbol{\nabla} \cdot \kappa (b \boldsymbol{\nabla} I_i)^{\mathrm{r}}$ must sum to zero over all partitions, and parametrizations of the second term must remain flux divergences, otherwise the exact constraint on the Nusselt number will be violated. It is obvious from their form that these constraints should apply; this is merely an example of an explicit consequence arising from not respecting exact constraints when building parametrizations.

4.2.1 Closures

The terms in equations (3.11)-(3.13) that require closure can be split into:

- p_i, the difference between the conditionally-filtered pressure in fluid i and the unconditionally filtered pressure;
- $\overline{P}\boldsymbol{\nabla}\sigma_i - \overline{P\boldsymbol{\nabla}I_i}$, $-\nu\boldsymbol{\nabla}\cdot\overline{(\mathbf{u}\otimes\boldsymbol{\nabla}I_i)^\mathsf{T}} - \nu\overline{\boldsymbol{\nabla}I_i\cdot(\boldsymbol{\nabla}\mathbf{u})^\mathsf{T}}$, and $-\kappa\overline{\boldsymbol{\nabla}I_i\cdot\boldsymbol{\nabla}b} - \kappa\boldsymbol{\nabla}\cdot\overline{b\boldsymbol{\nabla}I_i}$, which arise from conditionally-filtering the pressure gradient, viscous diffusion, and buoyancy diffusion terms;
- $-\boldsymbol{\nabla}\cdot\left(\overline{I_i\mathbf{u}\otimes\mathbf{u}} - \sigma_i\mathbf{u}_i\otimes\mathbf{u}_i\right)$, and $-\boldsymbol{\nabla}\cdot\left(\overline{I_i\mathbf{u}b} - \sigma_i\mathbf{u}_i b_i\right)$, which are often termed "subfilter fluxes" and are akin to the Reynolds stress and subfilter buoyancy flux, respectively, in normal higher-order modelling of turbulence;
- $\overline{\mathcal{S}_i^\pm}$, $\overline{\mathbf{u}\mathcal{S}_i^\pm}$, $\overline{b\mathcal{S}_i^\pm}$, which arise from filtering the re-labelling of fluid parcels.

The physical interpretations of these terms were discussed in Section 3.4. Here we present closures that attempt to model the dominant coherent overturning structures of RBC (seen in the DNS, Figure 2.2).

For this study, differences between conditionally-filtered and unconditionally-filtered pressures are parametrized as $p_i = \left(\sum_j \sigma_j\gamma_i\boldsymbol{\nabla}\cdot\mathbf{u}_j\right) - \gamma_i\boldsymbol{\nabla}\cdot\mathbf{u}_i$, where γ_i is a volume (or "bulk") viscosity. This form was derived in Chapter 3 by analogy with the "bulk viscous pressure" which arises in compressible fluid dynamics (see e.g. Batchelor 1967).We also showed in Chapter 3 that this form is exactly correct for the first normal mode of free-slip RBC. This parametrization has successfully been used by Weller et al. (2020), where it was argued that such a form is plausible since, in the underlying Boussinesq flow, the pressure is simply a Lagrange multiplier to enforce the divergence-free condition.Parametrizing the pressure differences in this way then serves to restrict the divergences within each partition from becoming too large.

Residual terms arising from conditionally-filtering the pressure gradient and diffusion terms are closed via a mean-field approximation:

- $\overline{P}\boldsymbol{\nabla}\sigma_i - \overline{P\boldsymbol{\nabla}I_i} \to \overline{P}\boldsymbol{\nabla}\sigma_i - \overline{P}\boldsymbol{\nabla}\sigma_i = 0$;
- $-\nu\boldsymbol{\nabla}\cdot\overline{(\mathbf{u}\otimes\boldsymbol{\nabla}I_i)^\mathsf{T}} - \nu\overline{\boldsymbol{\nabla}I_i\cdot(\boldsymbol{\nabla}\mathbf{u})^\mathsf{T}} \to -\nu\boldsymbol{\nabla}\cdot(\overline{\mathbf{u}}\otimes\boldsymbol{\nabla}\sigma_i)^\mathsf{T} - \nu\boldsymbol{\nabla}\sigma_i\cdot(\boldsymbol{\nabla}\overline{\mathbf{u}})^\mathsf{T}$;
- $-\kappa\overline{\boldsymbol{\nabla}I_i\cdot\boldsymbol{\nabla}b} - \kappa\boldsymbol{\nabla}\cdot\overline{b\boldsymbol{\nabla}I_i} \to -\kappa\boldsymbol{\nabla}\sigma_i\cdot\boldsymbol{\nabla}\overline{b} - \kappa\boldsymbol{\nabla}\cdot\overline{b}\boldsymbol{\nabla}\sigma_i$.

These choices retain the correct sum over all fluids for the entire pressure, viscous, and diffusive terms, respectively. They also cause the fluid fractions to behave passively in the case of two identical fluids, and in the absence of transfers: the Eulerian derivatives for $\mathbf{u}_i$ and b_i do not depend on σ_i if the two fluids have the same $\mathbf{u}_i$ and b_i.

We assume that the internal subfilter fluxes of momentum and buoyancy within each partition are negligible, i.e. $s_i(\mathbf{u},\mathbf{u}) \approx \mathbf{0}, s_i(\mathbf{u},b) \approx \mathbf{0}$. Via the decomposition of subfilter fluxes into contributions from coherent structures and internal

variability, equation (3.18), this implies assuming that the multi-fluid split captures *all* of the subfilter variability in the full momentum and buoyancy fluxes[1], i.e.$|\sum_i \sigma_i(\mathbf{u}_i - \overline{\mathbf{u}}) \otimes (\mathbf{u}_i - \overline{\mathbf{u}})| \gg |\sum_i \sigma_i s_i(\mathbf{u}, \mathbf{u})|$, $\left|\sum_i \sigma_i(\mathbf{u}_i - \overline{\mathbf{u}})(b_i - \overline{b})\right| \gg |\sum_i \sigma_i s_i(\mathbf{u}, b)|$. While this will never be exactly true — some further representation of internal subfilter variability is likely to be required — it is instructive to see how well a multi-fluid model with no extra subfilter modelling can perform when simulating a fully turbulent flow. In the single column context this requires the vertical grid to adequately resolve the boundary layers, as in the DNS, to avoid the introduction of wall functions.

To proceed further, we must decide what the labels I_i represent. The simplest choice is to restrict to two fluids; the symmetries of the Rayleigh-Bénard problem suggest choosing one falling and the other rising: let $i = 0$ denote fluid with $w \leq 0$, and $i = 1$ denote fluid with $w > 0$ (as in Weller et al. 2020). Then fluid 1 represents "updrafts" while fluid 0 represents "downdrafts". This choice of definitions for the two fluids, coupled with the discrete symmetry of the unfiltered equations under the simultaneous transformations $z \to H - z$, $b \to -b$, forces $\int_{\mathcal{D}} \sigma_i \, \mathrm{d}V = \frac{1}{2}$. This constraint can be used as a "sanity check" for both the initial conditions and the transfer terms $\mathcal{S}_i^{\pm}$. The discrete symmetry of the fluids under exchange also forces $\gamma_i = \gamma_j$ if γ is not a function of z.

Specializing to two fluids allows the sources of fluid fraction i to be written as $\overline{\mathcal{S}_i^+} = \sigma_j S_{ji}$, where $\sigma_j S_{ji}$ is the rate of transfer of fluid fraction from j to i; similarly, the sinks may be written as $\overline{\mathcal{S}_i^-} = \sigma_i S_{ij}$. We choose to model the exchanges of momentum and buoyancy from fluid i to j as a characteristic value, $\mathbf{u}_{ij}^T$ or b_{ij}^T, times the rate of transfer of fluid fraction from i to j, $\sigma_i S_{ij}$. This aligns with the modelling approach taken in other recent works on multi-fluid modelling (McIntyre et al. 2020; Thuburn et al. 2019, 2018; Weller and McIntyre 2019; Weller et al. 2020).

Partitioning the flow based on the sign of w forces $w_{ij}^T = 0$. For a single-column model, it remains only to specify the form of the fluid fraction transfer rate, S_{ij}, and the transferred buoyancy, b_{ij}^T (for a 2D or 3D model, the horizontal components of the transferred velocity would also need to be specified). For the fluid fraction transfer rate we choose

$$S_{ij} = \max(-\boldsymbol{\nabla} \cdot \mathbf{u}_i, 0), \tag{4.3}$$

which in 1D is similar to dynamical entrainment (Houghton and Cramer 1951), and follows the successful implementation of the same divergence-based transfer in

[1]Note that the converse is not necessarily true, i.e. $\sum_i \sigma_i s_i(a, b) = 0 \not\Rightarrow s_i(a, b) = 0$ for any i. Therefore there may well be flows where a multi-fluid split dominates the subfilter fluxes, yet the partitioned subfilter fluxes $s_i(a, b)$ are not small and need to be retained.

Weller et al. (2020). This aims to capture the large-scale overturning circulation, and is exactly correct for the first normal mode of RBC with stress-free boundaries (shown in Chapter 3). McIntyre (2020, chapter 2) also shows that this choice of transfer rate removes the problematic Kelvin-Helmholtz–like instability for a two-fluid Boussinesq system (Thuburn et al. 2019).

The transferred buoyancy must depend on the distribution of buoyancy within each fluid, and on the detailed dynamics of the relabelling. In the absence of this information, we choose a simple model:

$$b_{ij}^T = b_i + (-1)^i C|b_i|, \tag{4.4}$$

with some dimensionless constant $C \geq 0$. That is, the buoyancy of fluid parcels relabelled from i to j is modelled as the mean buoyancy within the fluid i plus or minus some constant times the magnitude of the buoyancy, to crudely approximate the subfilter buoyancy variability. The signs are chosen to model the fact that the fluid transferred from the falling (0) to the rising (1) fluid is expected to be more buoyant than the average falling fluid parcel for that height, while the reverse should be true for transfers from the rising (1) to the falling (0) fluid. This is a similar formulation to that used by Thuburn et al. (2019), though in theirs the transferred value depends on both the initial and destination fluids, rather than just the initial fluid.

Making these closure assumptions reduces the equation set to:

$$\frac{\partial \sigma_i}{\partial t} + \boldsymbol{\nabla} \cdot (\sigma_i \mathbf{u}_i) = \sigma_j S_{ji} - \sigma_i S_{ij}, \tag{4.5}$$

$$\begin{aligned} \frac{\partial \sigma_i \mathbf{u}_i}{\partial t} + \boldsymbol{\nabla} \cdot (\sigma_i \mathbf{u}_i \otimes \mathbf{u}_i) = {} & \sigma_i b_i \mathbf{k} - \sigma_i \boldsymbol{\nabla} \overline{P} - \boldsymbol{\nabla}(\sigma_i p_i) \\ & + \nu \boldsymbol{\nabla}^2 \sigma_i \mathbf{u}_i - \nu \boldsymbol{\nabla} \cdot (\overline{\mathbf{u}} \otimes \boldsymbol{\nabla} \sigma_i)^\mathsf{T} - \nu \boldsymbol{\nabla} \sigma_i \cdot (\boldsymbol{\nabla} \overline{\mathbf{u}})^\mathsf{T} \\ & + \sigma_j \mathbf{u}_{ji}^T S_{ji} - \sigma_i \mathbf{u}_{ij}^T S_{ij}, \end{aligned} \tag{4.6}$$

$$\begin{aligned} \frac{\partial \sigma_i b_i}{\partial t} + \boldsymbol{\nabla} \cdot (\sigma_i \mathbf{u}_i b_i) = {} & \kappa \boldsymbol{\nabla}^2 \sigma_i b_i - \kappa \boldsymbol{\nabla} \sigma_i \cdot \boldsymbol{\nabla} \overline{b} - \kappa \boldsymbol{\nabla} \cdot \overline{b} \boldsymbol{\nabla} \sigma_i \\ & + \sigma_j b_{ji}^T S_{ji} - \sigma_i b_{ij}^T S_{ij}, \end{aligned} \tag{4.7}$$

with $i, j \in \{0, 1\}$, and the specific parametrization choices:

$$S_{ij} = \max(-\boldsymbol{\nabla} \cdot \mathbf{u}_i, 0), \tag{4.8}$$

$$w_{ij}^T = 0, \tag{4.9}$$

$$b_{ij}^T = b_i + (-1)^i C|b_i| \tag{4.10}$$

$$p_i = \left(\sum_j \sigma_j \gamma \boldsymbol{\nabla} \cdot \mathbf{u}_j \right) - \gamma \boldsymbol{\nabla} \cdot \mathbf{u}_i. \tag{4.11}$$

The equations are given in vector form because of the desire to eventually create a 3D grey-zone convection parametrization; to that end the subsequent numerical method is also three-dimensional. Note, however, that in the form (4.5)-(4.11), the horizontal components of the transferred velocity still require closure.

Boundary conditions

As noted in Section 3.5, the boundary conditions for multi-fluid equations are non-trivial. Conditionally filtering the boundary conditions for RBC gives $\mathbf{u}_i(z = 0, H) = \mathbf{0}$, $b_i(z = 0, H) = \pm\,\Delta B/2$. The Neumann boundary condition for the unconditionally filtered pressure (required for the numerical solution, which solves elliptic equations for the pressures) is hydrostatic, $\mathrm{d}\overline{P}/\mathrm{d}z = \overline{b}(z = 0, H)$. Boundary conditions on the perturbation pressures are chosen to be zero-gradient, $\mathrm{d}p_i/\mathrm{d}z = 0$.

Because the σ_i equation is a transport equation with no diffusion, boundary values of σ_i are not in the domain of dependence of its solution. The asymptotic boundary behaviour of σ_i is thus entirely dependent on the asymptotic behaviour of the transfer terms as the boundaries are approached. Boundary values of σ_i are however required for the momentum and buoyancy equations, which do contain second derivatives of σ_i. These boundary values should be set by extrapolated values of σ_i from the interior of the domain. However, for this study we choose zero-gradient conditions for σ_i for better numerical behaviour. Heuristically this means that we are imposing no creation of fluid in either partition at the boundary.

4.2.2 Scaling of pressure differences between fluids

In single-column form, equations (4.5)-(4.11) contain two free parameters: γ and C. C is dimensionless and should be $\mathcal{O}(1)$, but γ has the dimensions of (bulk) viscosity and does not have an obvious magnitude. In this section we present a scaling argument for γ with the external dimensionless control parameters Ra, Pr, thus reducing the model to the choice of two dimensionless constants which should both be $\mathcal{O}(1)$.

In convection, a distinction is often made between filamentary plumes and a well-mixed environment; this distinction is clearly seen in the example RBC buoyancy fields of Figure 2.2, and is the basis of the conceptual "updraft"-"environment" partition. We assume that such a plume has a length $\sim H$, a width δ (to be determined), and the along-plume flow scales with the large-scale circulation $U \sim U_B = \sqrt{\Delta B\ H}$. Orienting a local Cartesian co-ordinate system such that $\hat{\mathbf{x}}$ points parallel to the plume and $\hat{\mathbf{z}}$ points normal to it, the scaled continuity equation gives:

$$\frac{U}{H}\frac{\partial \tilde{u}}{\partial \tilde{x}} = -\frac{W}{\delta}\frac{\partial \tilde{w}}{\partial \tilde{z}} \quad \Longrightarrow \quad W \sim U\frac{\delta}{H}. \tag{4.12}$$

Splitting the buoyancy equation similarly into its plume-parallel and -normal parts gives:

$$\left(\frac{\partial\tilde{b}}{\partial\tilde{t}}+\frac{\partial\tilde{u}\tilde{b}}{\partial\tilde{x}}+\frac{\partial\tilde{w}\tilde{b}}{\partial\tilde{z}}\right)=\frac{\kappa T_b}{\delta^2}\left(\frac{\delta^2}{H^2}\frac{\partial^2\tilde{b}}{\partial\tilde{x}^2}+\frac{\partial^2\tilde{b}}{\partial\tilde{z}^2}\right). \tag{4.13}$$

Note the buoyancy scaling cancels here. The simplest choice of the time scale isthe diffusive scaling $T_b = \delta^2/\kappa$, which makes the coefficient of the final term on the right-hand side one, consistent with filamentary plumes being diffusion-limited in well-developed turbulent flows. Scaling the plume-parallel momentum equation witha *viscous* time scale $T_m \coloneqq \delta^2/\nu = T_b/\operatorname{Pr}$, buoyancy with ΔB and pressure with $P \sim U^2$ (Bernoulli scaling), leads to:

$$\frac{\partial\tilde{u}}{\partial\tilde{t}}+\frac{\partial\tilde{u}\tilde{u}}{\partial\tilde{x}}+\frac{\partial\tilde{u}\tilde{w}}{\partial\tilde{z}}=\operatorname{Re}\frac{\delta^2}{H^2}\left(-\frac{\partial\tilde{p}}{\partial\tilde{x}}+\tilde{b}\;\hat{\mathbf{g}}\cdot\hat{\mathbf{x}}\right)+\left(\frac{\delta^2}{H^2}\frac{\partial^2\tilde{u}}{\partial\tilde{x}^2}+\frac{\partial^2\tilde{u}}{\partial\tilde{z}^2}\right), \tag{4.14}$$

where $\operatorname{Re} = UH/\nu = \operatorname{Pr}^{-1/2}\operatorname{Ra}^{1/2}$. The pressure gradient and buoyancy terms are assumed to drive the flow, and so $\operatorname{Re}\,\delta^2/H^2 = \mathcal{O}(1)$ and:

$$\frac{\delta}{H}=\operatorname{Re}^{-1/2}. \tag{4.15}$$

Applying the same scalings to the plume-perpendicular momentum equation, we find that the across-plume pressure contrast — i.e. the difference in pressure between the plume and the bulk — must scale as $P_z = P\delta/H = \Delta B\delta$.[2]

These results are the standard Prandtl-Blasius results with δ the boundary-layer depth, consistent with the presumption that plumes in RBC are simply detached from the boundary layers. This is a standard assumption for the kinetic boundary layer depth in scaling analysis of RBC, for example in the successful theory of Grossmann and Lohse (2000) for the Nusselt and Reynolds number scalings. The $\operatorname{Re}\propto\operatorname{Ra}^{1/2}$ result is also expected for RBC in the parameter regimes under study in this chapter (Ahlers et al. 2009, table 2).

From these results we find that the advection time, H/U, is equal to the momentum diffusion time $T_m = \delta^2/\nu$ (and, to an $\mathcal{O}(1)$ factor of the Prandtl number, the buoyancy diffusion time T_b), meaning that advection stretches the plume at the same rate at which diffusion broadens it.

We wish to parametrize the difference between the conditionally-filtered pressure in partition i, and the unconditionally-filtered pressure, as a bulk viscous stress: $p_i = -\gamma(\boldsymbol{\nabla}\cdot\mathbf{u}_i - \sum_j \sigma_j \boldsymbol{\nabla}\cdot\mathbf{u}_j)$, equation (4.11). Assuming that the multi-fluid

[2]Note that this argument only applies where $\hat{\mathbf{g}}\cdot\hat{\mathbf{x}} = \mathcal{O}(1)$, which is expected to be in the vicinity of the boundaries, including the plume recirculation regions. Therefore we might expect a more careful argument to be required to get the scaling of P_z correct in the interior of the flow.

split is dominated by a plume vs. bulk contrast, then $\mathbf{u}_i$ scales with the velocity of the plumes, $\sqrt{\Delta B\ H}$, and the divergence within each fluid should then scale as $\boldsymbol{\nabla}\cdot\mathbf{u}_i = (U/H)\widetilde{\boldsymbol{\nabla}}\cdot\tilde{\mathbf{u}}_i$ (so long as the filter width is $\gtrsim H$). Collecting the nondimensionalized expressions for the pressure and the bulk viscous stress gives:

$$\begin{aligned}
&\gamma\frac{U}{H}\widetilde{\boldsymbol{\nabla}}\cdot\tilde{\mathbf{u}}_i = \Delta B\ \delta\frac{\partial\tilde{p}}{\partial\tilde{z}} \\
&\quad\implies \frac{\gamma}{\nu} = \mathcal{O}(1)\times\frac{\Delta B H}{\nu U}\delta = \mathcal{O}(1)\times\frac{U^2 H}{\nu U}\frac{\delta}{H} = \mathcal{O}(1)\times\mathrm{Re}^{\frac{1}{2}} \\
&\quad\implies \frac{\gamma}{\nu} = \hat{\gamma}_0\,\mathrm{Ra}^{1/4}\,\mathrm{Pr}^{-1/4},
\end{aligned} \tag{4.16}$$

introducing the $\mathcal{O}(1)$, dimensionless constant $\hat{\gamma}_0$.

This scaling law for $\gamma(\mathrm{Ra},\mathrm{Pr})$ reduces the model for the pressure perturbation to the specification of an $\mathcal{O}(1)$ constant, $\hat{\gamma}_0$. Although $\hat{\gamma}_0$ must be determined empirically, this determination need only be performed at one Rayleigh number. Since $\mathrm{Pr} = 0.707$ is constant throughout our experiments, we choose to subsume the factor of $\mathrm{Pr}^{-1/4} \simeq 1.09$ into the definition of $\hat{\gamma}_0$ from now on.

4.3 Numerical method

The two-fluid Boussinesq equation set (4.7)-(4.11) is solved in advective form using the finite volume solver `multiFluidBoussinesqFoam`; this is part of the AtmosFOAM library of CFD codes for atmospheric fluid dynamics, based onVersion 7 of the OpenFOAM open-source CFD library (The OpenFOAM Foundation 2019). The code for the solver is available on GitHub at `http://www.github.com/AtmosFOAM/AtmosFOAM-multiFluid`; code required to set up, run, and analyse the simulations may be found at `http://www.github.com/AtmosFOAM/danRun`. The method is similar to that detailed in section 3 of Weller et al. (2020); an overview, and choices specific to this chapter, are presented below.

The spatial discretization uses Arakawa C-grid staggering in the horizontal and Lorenz staggering in the vertical. Temporal discretization is Crank-Nicolson with off-centring coefficient $\alpha = 0.55$.

Prognostic variables are b_i and σ_i at cell centres, and the volume flux $\phi_i \coloneqq \mathbf{u}_i\cdot\mathbf{S}_f$ at cell faces, where $\mathbf{S}_f$ is the outward-pointing area vector of face f. Advection of b_i and σ_i is total variation-diminishing (with a van Leer limiter) to preserve boundedness.Advection of ϕ_i uses linear-upwind (Shaw et al. 2017) which corrects first-order upwind using linear approximations to the velocity gradient. The terms involving Laplacians calculate the Gauss divergence of two-point gradients (Weller and Shahrokhi 2014). Both of these discretizations are second-order accurate on a uniform grid.

Diagnostic variables are the pressures P and p_i at cell centres. Solutions for both P and p_i are implicit but not simultaneous: first a Poisson equation is solved for P, which maintains a divergence-free mean velocity field (i.e. it ensures Equation (3.26) is satisfied), followed by a Helmholtz equation for each p_i. These solutions are then iterated to convergence. The generalized Geometric-Algebraic MultiGrid (GAMG) method is used for the implicit pressure solves, with an absolute tolerance of 10^{-6}.Preliminary tests suggest that the multi-fluid elliptic problems are not significantly more stiff than the single-fluid problems.

Spatial discretizations and the iterative pressure solvers use standard OpenFOAM operators, detailed in the OpenFOAM User Guide (The OpenFOAM Foundation 2019).

The transfer terms S_{ij} are handled explicitly, while the momentum and buoyancy transfers are implicit and operator-split, as in Weller et al. (2020).This handling of the transfer terms guarantees boundedness and conservation of energy and momentum (McIntyre et al. 2020).

Two outer iterations (for the whole of the above method) and two inner iterations (for the implicit pressure solves) are performed per time-step.

With the exception of the transfer terms (which are specifically defined for a two-fluid system), the described numerical method is suitable for an arbitrary number of fluid partitions, in up to three spatial dimensions.

Computational cost

Compared to the single-fluid Boussinesq solver, the two-fluid solver detailed above is slightly more than twice as computationally expensive at a given resolution; this makes sense, since the two-fluid algorithm solves two copies of the Boussinesq equations, plus extra terms coupling those equations, as well as two extra equations for the conservation of fluid fraction. Since this is a development code to explore the properties and behaviour of multi-fluid models of convection, modularity is prized over computational efficiency, so the code has not been optimized.

We may however remark that a comparison of the computational cost of two-fluid code against a single-fluid code with no parametrization of subfilter scales on the same grid is unhelpful. If the flow is fully resolved, there is no need for parametrization of any kind, and so the extra fluids are superfluous. If the flow is fully subfilter – i.e. a single-column model – a single-fluid code cannot produce any flow, due to the divergence constraint, and so all heat (and moisture) transport must be by diffusion and by representation of the subfilter flow. This subfilter representation is traditionally performed via a mass flux-type scheme in atmospheric convection problems. Multi-fluid modelling is envisaged as a unified framework for

representing convection from the fully-parametrized to the fully-resolved limit, and at all scales in between. This means that a two-fluid scheme may potentially be much cheaper than a single-fluid scheme in the grey zone: consider a two-fluid scheme which performs as well as a single-fluid scheme which requires twice the (horizontal) resolution. Despite computing a second fluid, a crude estimate suggests that the two-fluid scheme would be approximately 4 times cheaper to run.

4.4 Two-fluid single-column model results

For $10^2 \leq \mathrm{Ra} \leq 10^{10}$, single-column two-fluid simulations were run with the same vertical resolution as the reference DNS (see Table 2.1) for various values of $\hat{\gamma}_0$ and C. The qualitative nature of the solutions is described in section 4.4.1, followed by an analysis of sensitivity to the choice of $\hat{\gamma}_0$ and C in section 4.4.2. In section 4.4.3 the global buoyancy and momentum transport, Nu and Re, is examined as a function of the buoyancy forcing Ra.

For all simulations, the initial state was constructed from a resting hydrostatically-balanced solution with a linear buoyancy profile and uniform $\sigma_i = 0.5$ in both fluids. Small non-zero velocities equal to $\pm 10^{-3}\ U_B$ were added to ensure correct labeling, and random perturbations of magnitude $|\delta b| \leq 0.0008\ \Delta B$ drawn from a uniform distribution were added to the initial linear profile to seed instability[3]. Simulations were run until a steady state was reached (9–12 T_e); the steady-state profiles of buoyancy, pressure, vertical velocity, and fluid fraction, were then compared with the corresponding statistically steady-state time-mean conditionally horizontally averaged DNS profiles. Resolutions, time-step size, and total simulation run time for each simulation are given in Table 4.1.

The single column model spins up to equilibrium in a remarkably similar manner to the horizontally-averaged DNS; this is demonstrated in Figure 4.1, which shows the Nusselt number vs. time for both DNS and single-column simulations at $\mathrm{Ra} = 10^5$ and 10^8. For these simulations, $\hat{\gamma}_0 = 1.861$, and $C = 0.5, 0$ for $\mathrm{Ra} = 10^5, 10^8$, respectively (see section 4.4.3). At each Ra, convection initiates at a similar time ($\approx 2T_\mathrm{e}$) in both the single-column and DNS flows, seen in the sharp increase in Nu above the purely diffusive value of 1. This initial convective surge causes a strong peak in the Nusselt number (slightly overestimated by the single-column model), before the system gradually settles down towards equilibrium with decaying Nusselt number under- and overshoots. The under- and overshoots appear stochastic for the

[3]This value was chosen in order to approximate the same initial available potential energy in both the DNS and the single-column simulations. However, the (linear) growth rate of instabilities in a single fluid is not dependent on the size of the initial perturbation, and so the exact magnitude of the initial perturbations does not matter so long as it is small.

Ra	$T_{\text{tot}}/4T_B$	$\Delta t/4T_B$
10^2	19	1.998×10^{-4}
10^3	63	3.197×10^{-4}
2×10^3	38	2.557×10^{-4}
10^4	19	1.279×10^{-3}
10^5	19	1.279×10^{-3}
10^6	19	7.992×10^{-4}
10^7	19	3.197×10^{-4}
2×10^7	19	5.115×10^{-4}
10^8	19	3.197×10^{-4}
10^9	19	1.598×10^{-4}
10^{10}	19	5.115×10^{-5}

Table 4.1: Details of time-step size and total simulation time for the two-fluid single-column results (section 4.4). Resolutions are the same as the vertical resolution of the DNS, explained in section 2.2 and given in Table 2.1. All two-fluid single-column simulations at a given Ra required similar time-steps regardless of $\hat{\gamma}_0$ and C, therefore only the values for $\hat{\gamma}_0 = 1.861$, $C = 0.5$ ($\text{Ra} \leq 10^7$), $\hat{\gamma}_0 = 1.861$, $C = 0$ ($\text{Ra} > 10^7$) are given.

DNS, whereas they are periodic for the single-column model; that the single-column model appears less chaotic than the DNS is unsurprising.

The same steady state was reached when initializing from other initial conditions (e.g. initializing from the DNS reference profiles), provided the identities of the fluids were initialized correctly and the initial column-integrated fraction of fluid in each fluid was equal to 0.5. This suggests that the steady state is robust. Similar qualitative spin-up behaviour is also observed with different values of $\hat{\gamma}_0$ and C. Thus, for the remainder of the chapter we consider only the steady state, and not the spin-up.Given the convergence of time averages over 5, 10, and $15T_{\text{e}}$ shown in Figure 4.1, for the remainder of this chapter all figures and quoted statistics are from steady-state simulations averaged over $10T_{\text{e}}$ (unless otherwise stated).

We begin our study of the two-fluid single-column model steady-state by looking at the qualitative behaviour of the equilibrium profiles in different Rayleigh number regimes. We then investigate the sensitivity of those profiles to the two closure constants, C and $\hat{\gamma}_0$. Finally we examine the scaling of the global parameters Nu and Re with Ra produced by the model.

4.4.1 Phenomenology

For each of the characteristic Rayleigh numbers $\text{Ra} = 10^5, 10^8, 10^{10}$ (as in Figure 2.2), we present and discuss an example two-fluid single column simulation.In this section the value of $\hat{\gamma}_0$ was chosen to give a good qualitative fit to the conditionally horizontally averaged DNS buoyancy, pressure, and vertical velocity profiles at $\text{Ra} = 10^5$.

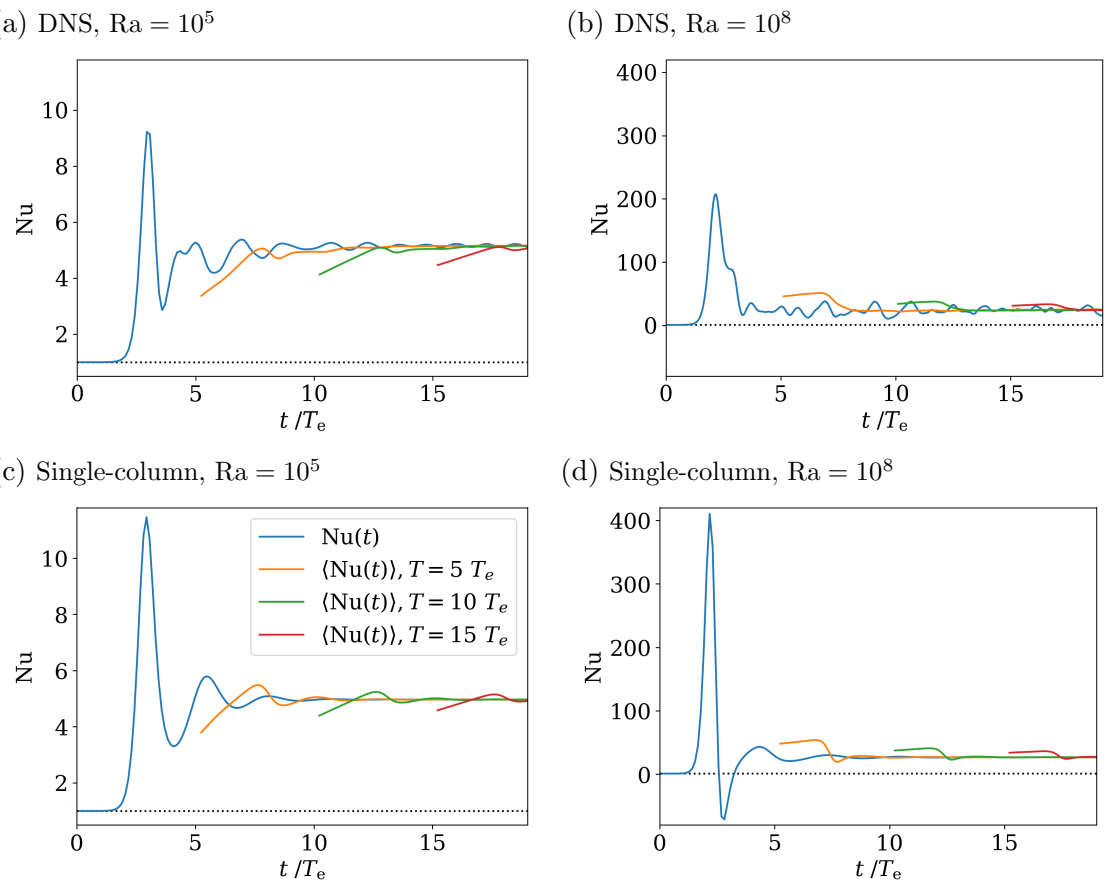

Figure 4.1: Nondimensionalized vertical heat flux vs. time for (a,b) DNS and (c,d) single-column models. In each subfigure, the blue curve shows the instantaneous nondimensionalized vertical buoyancy flux, $H \times (wb - \kappa\frac{\partial b}{\partial z})/\kappa\Delta B$, while the orange, green, and red curves show Nusselt numbers (domain- and time-averaged nondimensionalized buoyancy flux) for different averaging times. In each plot, Nu = 1 is shown as a black dotted line. In (c) and (d) $\gamma/\nu = 1.861 \times \mathrm{Ra}^{1/4}$, with $C = 0.5$ for (c) and $C = 0$ for (d) (see Figure 4.8a).

To avoid possible confusion, this value of $\hat{\gamma}_0$ was retained for the simulations at $\mathrm{Ra} = 10^8, 10^{10}$. The value of C is varied between the turbulent and non-turbulent simulations. The discussion for each of these examples qualitatively applies to all simulations within the characteristic Rayleigh number regime.

Laminar (Ra = 10^5)

At $\mathrm{Ra} = 10^5$, the DNS exhibits laminar convective rolls (see Figure 2.2a). This solution is qualitatively characteristic of the flow for all laminar Ra, $\mathrm{Ra_c} < \mathrm{Ra} \lesssim 10^7$. Steady state results of a two-fluid single-column model governed by equations (4.5)-(4.11) with $\hat{\gamma}_0 \simeq 0.75$, $C = 0.5$ are shown in Figure 4.2. The mean buoyancy (a) and pressure (b) profiles match closely between the DNS and the single column model; in particular the model correctly predicts a well-mixed buoyancy in the fluid interior, with a sharp buoyancy gradient close to the top and bottom boundaries. The shape

of the pressure profile is also correct, though the maxima are slightly too high close to the boundaries.

Good agreement is also seen between the DNS and two-fluid single column model for the individual fluid buoyancy profiles: the overall shape is correct, though the profiles are too far apart in the middle of the domain, leading to surplus buoyancy transport for a given velocity profile. Experiments varying C (see section 4.4.2) demonstrated $C > 0$ was required to reproduce a buoyancy overshoot at the top (bottom) of the rising (falling) fluid. By overshoot, we mean the part of the buoyancy profile at the interface between the bulk and the buoyancy boundary layer where $\mathrm{d}b_i/\mathrm{d}z$ changes sign. These overshoots can be seen in the 2D buoyancy field of the DNS flow of Figure 2.2a and are a general feature of $\mathcal{O}(1)$ Prandtl number laminar RBC. (For $\mathrm{Pr} > 1$, the overshoots become so strong that they begin to be seen even in the mean buoyancy profile; such profiles can be seen in e.g. Figure 4b of Schmalzl et al. 2004.) The value $C = 0.6$ gives the best shape for $b_i(z)$ for $\mathrm{Ra} = 10^5$, but $C \simeq 0.5$ works for all laminar Ra.

The individual fluid velocity profiles are roughly the correct shape; the slight asymmetry in the location of the maxima in each fluid in the DNS is due to the gradient of the volume fraction profile in the DNS (i.e. forcing the correct gradient of σ_i reproduces the asymmetry in the vertical velocity profiles).

The pressure profiles within each fluid are captured by the scheme, suggesting that to leading order $p_i \propto -\gamma \boldsymbol{\nabla} \cdot \mathbf{u}_i$ is an appropriate model of the pressure differences. The model is particularly good close to the boundaries, but the fluids are better mixed in the interior of the domain in the DNS, causing the pressure differences there to be smaller than predicted by the single column model. This could possibly be remedied by using a z-dependent γ parametrization,either directly or through dependence on other properties of the flow such as the TKE, which would fit well with the discussion of LES in section 2.1.3.

The two-fluid model keeps area fractions, $\sigma_i(z)$, close to 0.5. This is expected as the divergence-based transfer is known to keep $\sigma_i(z)$ roughly constant (Weller et al. 2020). In contrast, the area fractions diagnosed from the DNS diverge from 0.5 either side of the centre (where symmetry demands equal fractions), reaching a maximum close to the boundaries approaching 0.3 and 0.7.

Transition to turbulence ($\mathrm{Ra} = 10^8$)

Between $10^7 < \mathrm{Ra} \lesssim 5 \times 10^8$, the DNS solutions transition from laminar flow to fully developed turbulence. The buoyancy field of Figure 2.2b is characteristic of this transitional regime. Besides the solutions becoming intermittent and transient rather than (quasi-)periodic, the plume separation from the boundary layer funda-

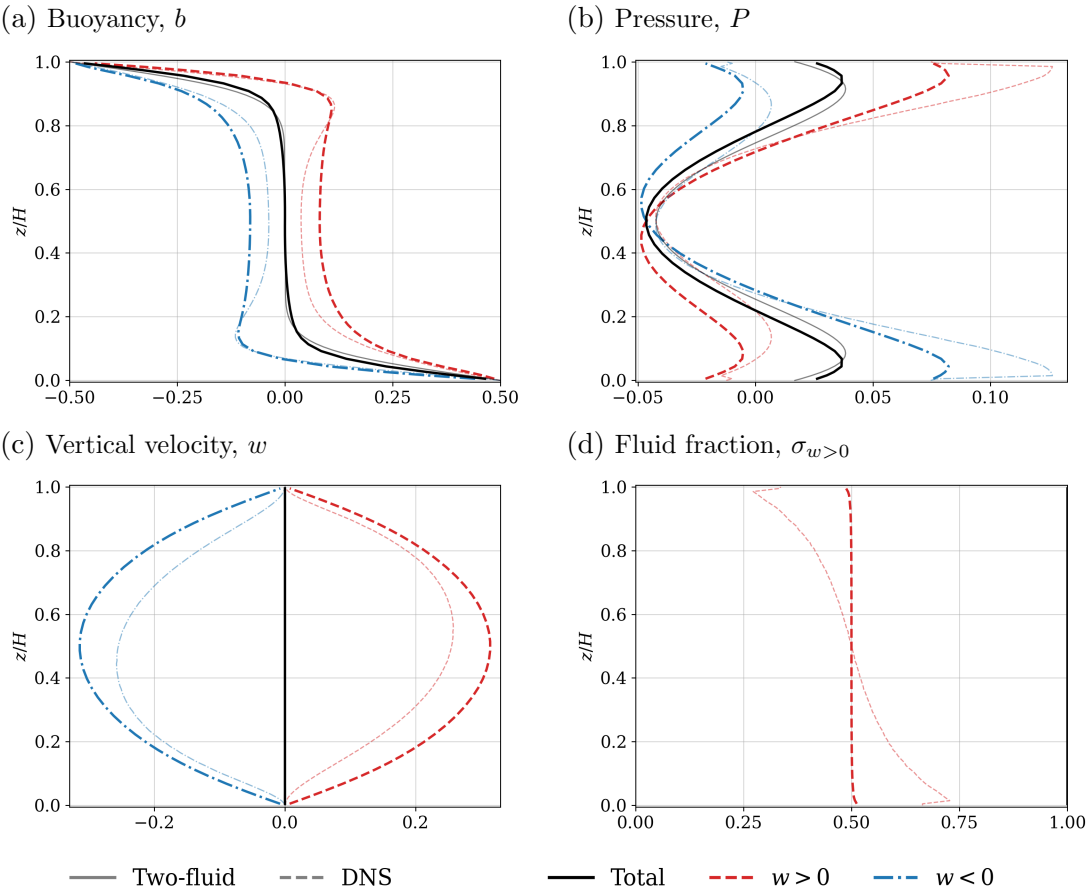

Figure 4.2: Two-fluid single-column model of $\mathrm{Ra} = 10^5$ RBC governed by equations (4.5)-(4.11) and (4.16), with closure constants $\hat{\gamma}_0 \simeq 0.75, C = 0.5$. Conditionally horizontally- and time-averaged profiles from the DNS are shown for reference. $\mathrm{Nu} = 7.1$, reference $\mathrm{Nu}_{\mathrm{DNS}} = 5.0$.

mentally changes: above $\mathrm{Ra} \approx 10^7$, regions of recirculation develop at the base of the plumes.

Results of a two-fluid single-column model with $\hat{\gamma}_0 \simeq 0.75$, $C = 0$ are compared with those from the horizontally-averaged DNS in Figure 4.3. Better prediction of the pressure differences between the fluids near the boundaries is achieved by increasing $\hat{\gamma}_0$ by a factor of ≈ 1.5; however this degrades the agreement of the mean pressure profile with the DNS profile, and significantly decreases the magnitude of the vertical velocity profiles.Conversely, better prediction of the mean pressure profile is achieved by decreasing $\hat{\gamma}_0$ by a factor of approximately 2/3, though this reduces the agreement in the vicinity of the boundaries. This again suggests that γ should be a function of z(i.e. it should depend on the distance from the boundaries).

We can better understand the relationship between the mean pressure profile and the within-partition velocity profiles by considering the steady-state horizontally-averaged vertical momentum equation. The mean vertical velocity must be zero due to continuity. For $\mathrm{Ra} \gg \mathrm{Ra}_c$, the viscous terms are negligible outside of the kinetic

boundary layers, and the mean buoyancy is also approximately zero outside of the thermal boundary layers. Thus in the bulk of the fluid the equation reduces to a balance between the pressure gradient and the turbulent momentum stress:

$$\frac{\partial \overline{P}}{\partial z} \approx -\frac{\partial s(w,w)}{\partial z}. \tag{4.17}$$

Therefore away from the boundaries, the pressure (up to an arbitrary constant) is entirely determined by the turbulent momentum stress. Using the exact decomposition (3.18) we can rewrite this in terms of the within-partition vertical velocities as (choosing the arbitrary constant to be zero):

$$-\overline{P} = \sum_i \sigma_i \left(w_i - \overline{w}\right)^2 + \sum_i \sigma_i s_i(w,w) \tag{4.18}$$

$$= \sigma_0 w_0^2 + \sigma_1 w_1^2 + \sigma_0 s_0(w,w) + \sigma_1 s_1(w,w). \tag{4.19}$$

Thus in our two fluid system, differences between the simulated mean pressure profile and the DNS profile arise either from incorrectly capturing the within-partition vertical velocity profiles, or from neglecting the internal variability within each partition, $s_i(w,w)$.

As can be seen in Figure 4.3c, the agreement between the simulated vertical velocity profiles and the DNS profiles is good, showing that at least part of the discrepancy between the simulated and DNS mean pressure profiles must be due to neglecting the internal variability. However, in the very centre of the domain, the vertical velocity profiles are significantly sharper in the DNS than in our simulations; if the two-fluid simulations captured this effect, it would significantly deepen the central pressure minimum, as seen in the DNS.

We can also see that a naïve eddy viscosity parametrization of the neglected internal variability cannot directly explain the discrepancy. Since $\sigma_0 \approx \sigma_1, b_0 \approx b_1, w_0 \approx -w_1$ in the bulk of the domain, we would expect $\sigma_0 \nu_{\mathrm{t},0}\, \partial w_0/\partial z \approx -\sigma_1 \nu_{\mathrm{t},1}\, \partial w_1/\partial z$. Thus a simple downgradient parametrization of the residual turbulent momentum flux cancels out in the mean momentum equation in the bulk of the domain. However, it is certainly possible that even a simple downgradient closure could significantly change the dynamics in the vicinity of the boundaries such that the indirect effect propagates to the velocity profiles in the bulk.

Apart from the pressure profiles, comparisons with the DNS reference profiles are mostly the same as for the laminar case, except that the additional mixing caused by the recirculation regions at the base of the plumes modifies the profiles in the near-boundary regions. This has the most obvious effect on the buoyancy profiles within each fluid, which no longer overshoot, and on the volume fraction profile,

which is no longer monotonic. The lack of overshoots is reproduced by transferring the mean buoyancy, $C = 0$, a suitable model for well-mixed turbulent flow. The detailed differences to the profiles caused by these recirculation regions are however not reproduced by this simple parametrization: better representation of the mass exchanges S_{ij} is required. The recirculation is counter to the large-scale circulation, and hence is not captured either by our arguments for the scaling of γ, or by the divergence-based mass transfer.

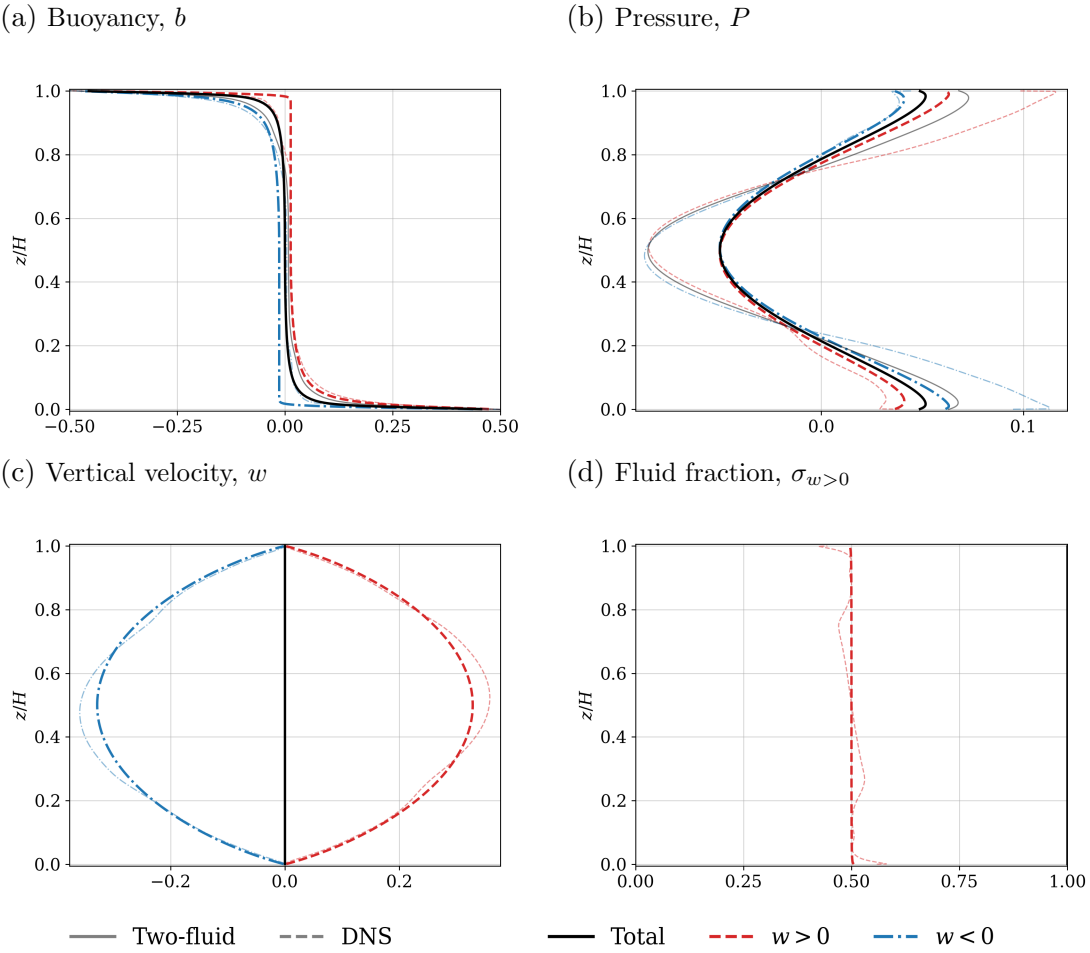

Figure 4.3: Two-fluid single-column model of $\mathrm{Ra} = 10^8$ RBC governed by equations (4.5)-(4.11) and (4.16), with closure constants $\hat{\gamma}_0 \simeq 0.75$, $C = 0$. Conditionally horizontally- and time-averaged profiles from the DNS are shown for reference. $\mathrm{Nu} = 36.9$; reference $\mathrm{Nu}_{\mathrm{DNS}} = 27.9$.

Fully developed turbulence ($\mathrm{Ra} = 10^{10}$)

Above $\mathrm{Ra} \approx 5 \times 10^8$, the DNS flow is fully turbulent, exhibiting structures on many scales from the domain depth down to the exceptionally thin boundary layers, shown in Figs. 2.2c-d for $\mathrm{Ra} = 10^{10}$. The recirculations at plume base first exhibited in the transitional regime divide into multiple small plumes which organize into a larger-scale circulation. The bulk of the domain is statistically well-mixed.

Results from a two-fluid single-column model with $\hat{\gamma}_0 \simeq 0.75$, $C = 0$ are shown in Figure 4.4. Qualitative agreement with the buoyancy and vertical velocity profiles is still good, but the mean pressure profile predicted by the model now has too little curvature in the centre of the domain.Better agreement with the mean pressure in the centre of the domain is achieved with $\hat{\gamma}_0$ decreased by approximately a factor of 2/3, while the best agreement between DNS and two-fluid model for both the mean pressure profile and the within-partition profiles close to the boundaries is found for $\hat{\gamma}_0$ larger by approximately a factor of 2. As with the $\mathrm{Ra} = 10^8$ simulation, these discrepancies are closely linked to errors in the vertical velocity profiles.

Again, the complex mixing of the turbulent flow has strong effects on the volume fraction profile, causing the volume fraction of rising (falling) fluid to be less than 0.5 close to the lower (upper) boundary. These larger discrepancies between the DNS and the two-fluid model model are possibly because the $w = 0$ interface is now very complex. Figure 4.5 shows the $w = 0$ interface superimposed on the DNS buoyancy fields at $\mathrm{Ra} = 10^8$ and $\mathrm{Ra} = 10^{10}$. Although the dominant rising/falling two-fluid split is still into columns of falling and rising air with an approximately vertical interface even in the higher Ra case, the simple split is increasingly complicated by the complex vortical motions in the bulk of the fluid, and especially close to the base of the plumes. The intricate dynamics of these interfaces are not accounted for by our single-column model.

While there are quantitative discrepancies, for all three Rayleigh numbers the overall agreement between horizontally-averaged DNS and the two-fluid single-column model is good. Approximately the correct profiles are captured even in the highly turbulent regime of $\mathrm{Ra} = 10^{10}$. The model performs remarkably well given it has no representation of sub-filter variability beyond the two-fluid split, showing that the model captures the essential coherent overturning structures of Rayleigh-Bénard convection in all three characteristic regimes.

4.4.2 Sensitivity to $\hat{\gamma}_0$ and C

In this section, the sensitivity of the model to the dimensionless closure parameters $\hat{\gamma}_0$ and C is investigated. The effects of changing $\hat{\gamma}_0$ and C are similar at all Rayleigh numbers, so for brevity only $\mathrm{Ra} = 10^5$ is presented.

Sensitivity to $\hat{\gamma}_0$

Figure 4.6 shows the effect on the two-fluid single-column steady-state of varying $\hat{\gamma}_0$ from $10^{-1} \lesssim \hat{\gamma}_0 \lesssim 10^1$, along with examples in the asymptotically-large and -small $\hat{\gamma}_0$ regimes. The experiments were performed with $C = 0.5$ at fixed $\mathrm{Ra} = 10^5$, but the results are similar for all Ra.

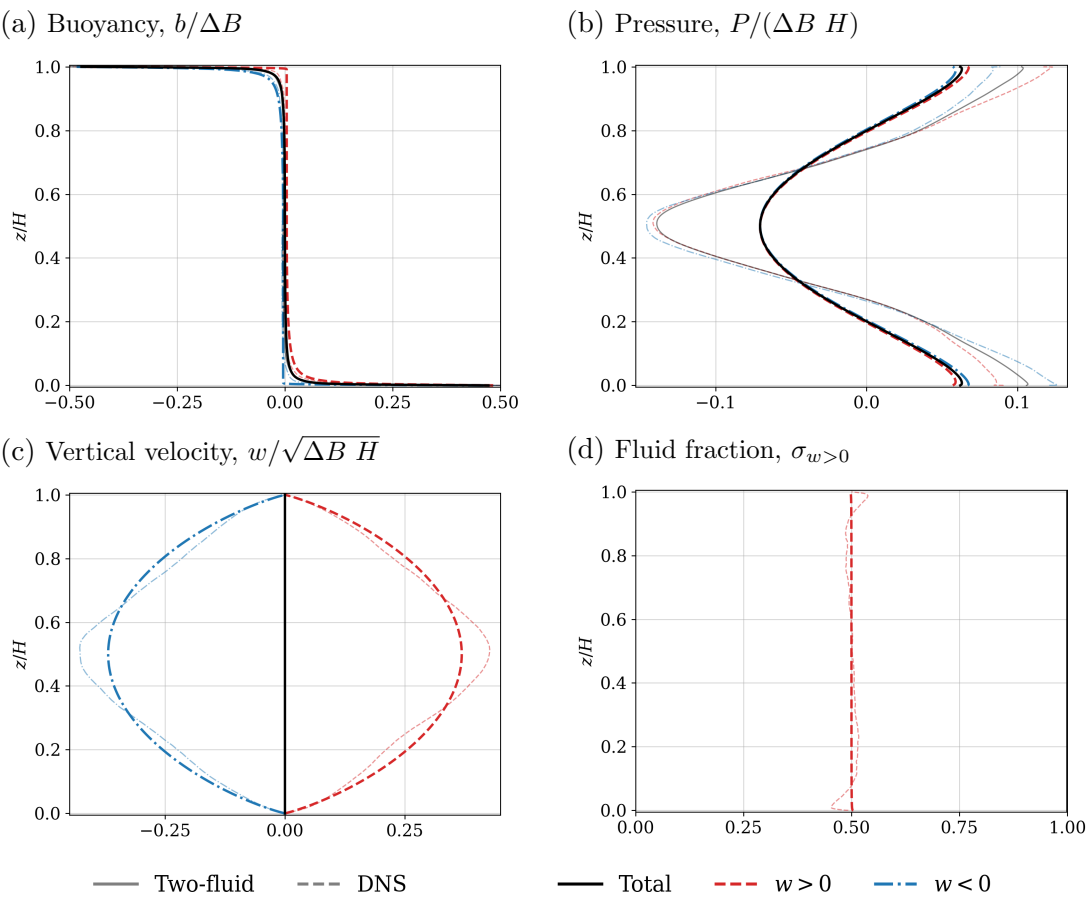

Figure 4.4: Two-fluid single-column model of $\mathrm{Ra} = 10^{10}$ RBC governed by equations (4.5)-(4.11) and (4.16), with closure constants $\hat{\gamma}_0 \simeq 0.75$, $C = 0$. Conditionally horizontally- and time-averaged profiles from the DNS are shown for reference. $\mathrm{Nu} = 130$; reference $\mathrm{Nu}_{\mathrm{DNS}} = 94.5$.

The best qualitative match between the single-column and DNS profiles is found when $\hat{\gamma}_0 \simeq 0.75$, as discussed earlier, while the correct heat flux is predicted at $\hat{\gamma}_0 \simeq 1.861$. These values are both $\mathcal{O}(1)$, as expected. Agreement with the reference profiles degrades sharply as $\hat{\gamma}_0$ moves away from this range.

Increasing $\hat{\gamma}_0$ increases the buoyancy difference between the fluids, and damps the vertical velocities — which makes sense since in 1D this parametrization of p_i *is* similar to diffusion of the vertical velocity within a fluid, even though the sum correction means no extra viscous term is added to the mean momentum budget. This effect is already clear at $\hat{\gamma}_0 = 2$, where the vertical velocities are only $\approx 2/3$ of those in the DNS, and the pressure profile is much shallower, though still with the correct number of turning points. By $\hat{\gamma}_0 = 10$, the pressure profile loses the minimum in the centre of the domain, and the vertical velocities are almost zero. At asymptotically large $\hat{\gamma}_0$, the system becomes subcritical and the solution is purely diffusive.

Decreasing $\hat{\gamma}_0$ rapidly increases the pressure gradient, and deepens the minimum

(a)

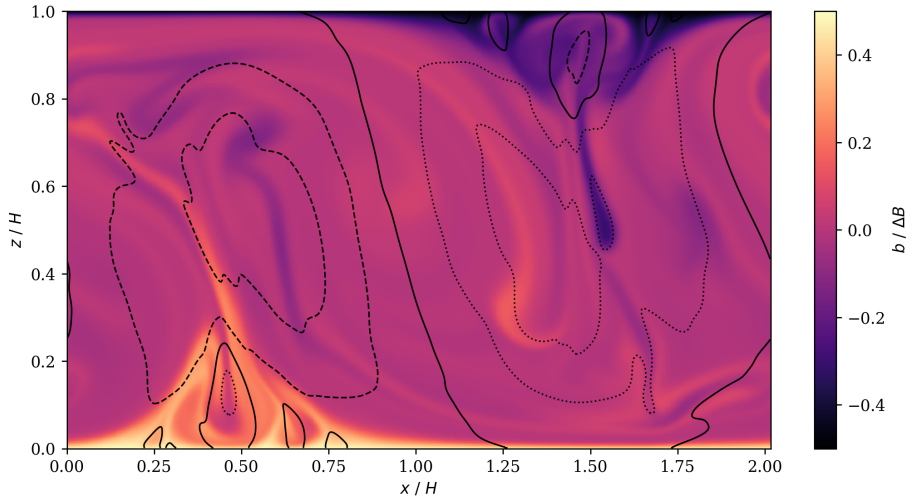

(b)

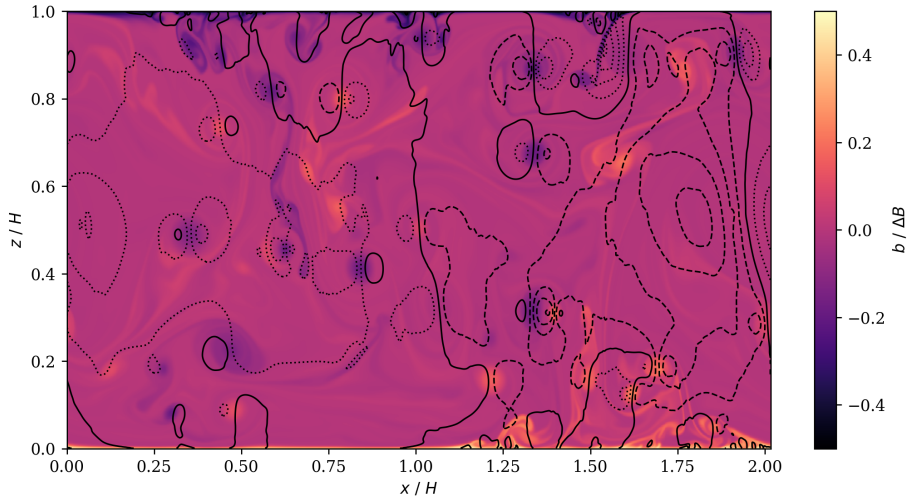

Figure 4.5: Snapshots of DNS buoyancy fields with overlaid vertical velocity contours at Ra = 10^8 (a) and Ra = 10^{10} (b). Dashed contours denote $w > 0$, dotted $w < 0$, and the solid contour denotes $w = 0$. Contours above and below $w = 0$ are spaced at intervals of $U_B/4$.

of the mean pressure in the centre of the domain. This drastically increases the vertical velocities — by $\hat{\gamma}_0 = 10^{-1}$, the maximum vertical velocities are over three times those of the DNS, and over twice those of the simulations with $\hat{\gamma}_0 = 0.75$ discussed in detail earlier. Decreasing $\hat{\gamma}_0$ further only slightly changes these results, as seen for the asymptotically-small case of $\hat{\gamma}_0 = \times 10^{-5}$.

Sensitivity to C

Figure 4.7 shows the steady-state effect of varying C from 0 (mean buoyancy is transferred: $b_{ij}^T = b_i$) to 1 (zero buoyancy is transferred over most of the domain:

$b_{ij}^T = 0$ wherever $b_i = |b_i|$). Transfers with $C > 1$ amount to transferring buoyancies with magnitude greater than ΔB close to the boundaries, which causes the solution to become unstable at $C \approx 1.3$.

The main effect of increasing C is to generate the aforementioned overshoots in the within-fluid buoyancy profiles; this also steepens the pressure gradient, deepens the central pressure minimum, and increases the magnitude of the vertical velocities in each fluid. These effects are small compared to the order-of-magnitude effects associated with varying $\hat{\gamma}_0$: for example, the maximum velocity increases monotonically from 0.3 to 0.45 as C increases from 0 to 1. These effects are qualitatively similar at all Ra, but for $\mathrm{Ra} \gtrsim 10^7$, the individual fluid buoyancy profiles no longer exhibit overshoots, so $C = 0$ provides a better fit with the DNS buoyancy profiles.

4.4.3 Scaling of Nusselt number with Rayleigh number

To investigate the performance of the two-fluid single column model more systematically, the scaling of the Nusselt number for single-column models across the Rayleigh number range $10^2 \leq \mathrm{Ra} \leq 10^{10}$ is compared with the DNS results. The scaling $\gamma/\nu \propto \mathrm{Ra}^{1/4}$ (section 4.2.2) is evaluated, along with two choices of the transferred buoyancy, $C = 0$ and $C = 0.5$. For each transferred buoyancy, the dimensionless proportionality factor $\hat{\gamma}_0$ was fixed by finding the value which gave the correct Nusselt number at $\mathrm{Ra} = 10^5$. Fixing this constant at different Rayleigh numbers changes the prefactor of the Nu(Ra) scaling, but does not change the scaling itself.

Figure 4.8a shows Nu against Ra for the different values of C and scalings for γ. The DNS results are shown for comparison, along with results from the single column model run with both tunable parameters set to zero, $C = \hat{\gamma}_0 = 0$. All models with $\hat{\gamma}_0 > 0$ perform significantly better than the model with $\hat{\gamma}_0 = 0$, which becomes supercritical for $\mathrm{Ra} < 10^3$ and follows a Nu(Ra) scaling with exponent everywhere > 0.33.

Models with $\gamma/\nu \propto \mathrm{Ra}^{1/4}$ show exceptional agreement with the DNS heat fluxes for $\mathrm{Ra} \geq 10^4$, giving $\mathrm{Nu} \sim \mathrm{Ra}^{2/7}$ with both $C = 0$ (upwards-pointing triangles) and $C = 0.5$ (downward-pointing triangles). This shows that the Nusselt number scaling exponent depends on γ/ν but not on C; this makes sense since C is a crude parametrization for *how* the flow produces a given heat flux, and should not affect the scaling of the heat flux itself. Below $\mathrm{Ra} = 10^4$, models with different values of C and $\hat{\gamma}_0$ produce slightly different behaviour: the $C = 0, \hat{\gamma}_0 = 1.108$ simulations become convective at $\mathrm{Ra} < 10^3$, inconsistent with the known $\mathrm{Ra_c} \simeq 1708$. While the $C = 0.5, \hat{\gamma}_0 = 1.861$ simulations are still diffusive at $\mathrm{Ra} = 10^3$, the heat flux at $\mathrm{Ra} = 2 \times 10^3$ is roughly 30% too high, suggesting either a critical Rayleigh number < 1708, or incorrect scaling of Nu with Ra close to the onset of convection.

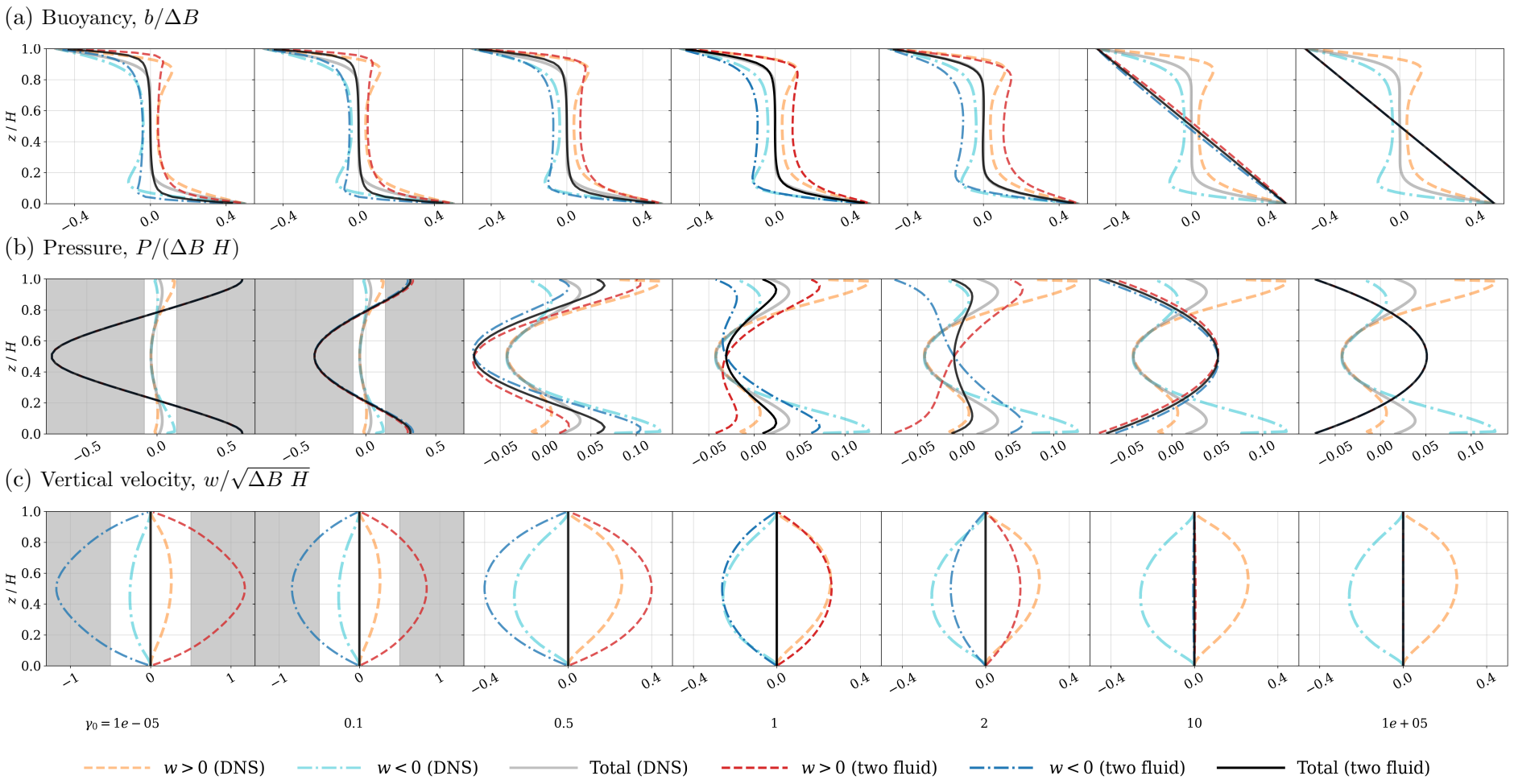

Figure 4.6: Two-fluid single-column model of $\mathrm{Ra} = 10^5$ RBC governed by equations (4.5)-(4.11) and (4.16), with $C = 0.5$, showing sensitivity to $\hat{\gamma}_0$ (defined in Equation (4.16)) over the range $10^{-1} \leq \hat{\gamma}_0 \leq 10^1$. Profiles in the limit of asymptotically large (10^5) and small (10^{-5}) $\hat{\gamma}_0$ are also shown for reference. $\hat{\gamma}_0 = \mathcal{O}(1)$ is expected based on the scale analysis of section 4.2.2. Small values of $\hat{\gamma}_0$ ($\lesssim \mathcal{O}(10^{-1})$) are shown in the first two columns, values of order 1 in the centre three columns, and large magnitudes ($\gtrsim \mathcal{O}(10)$) in the final two columns. Grey shaded regions in plots in the first two columns highlight areas which are not in the domain of plots to their right.

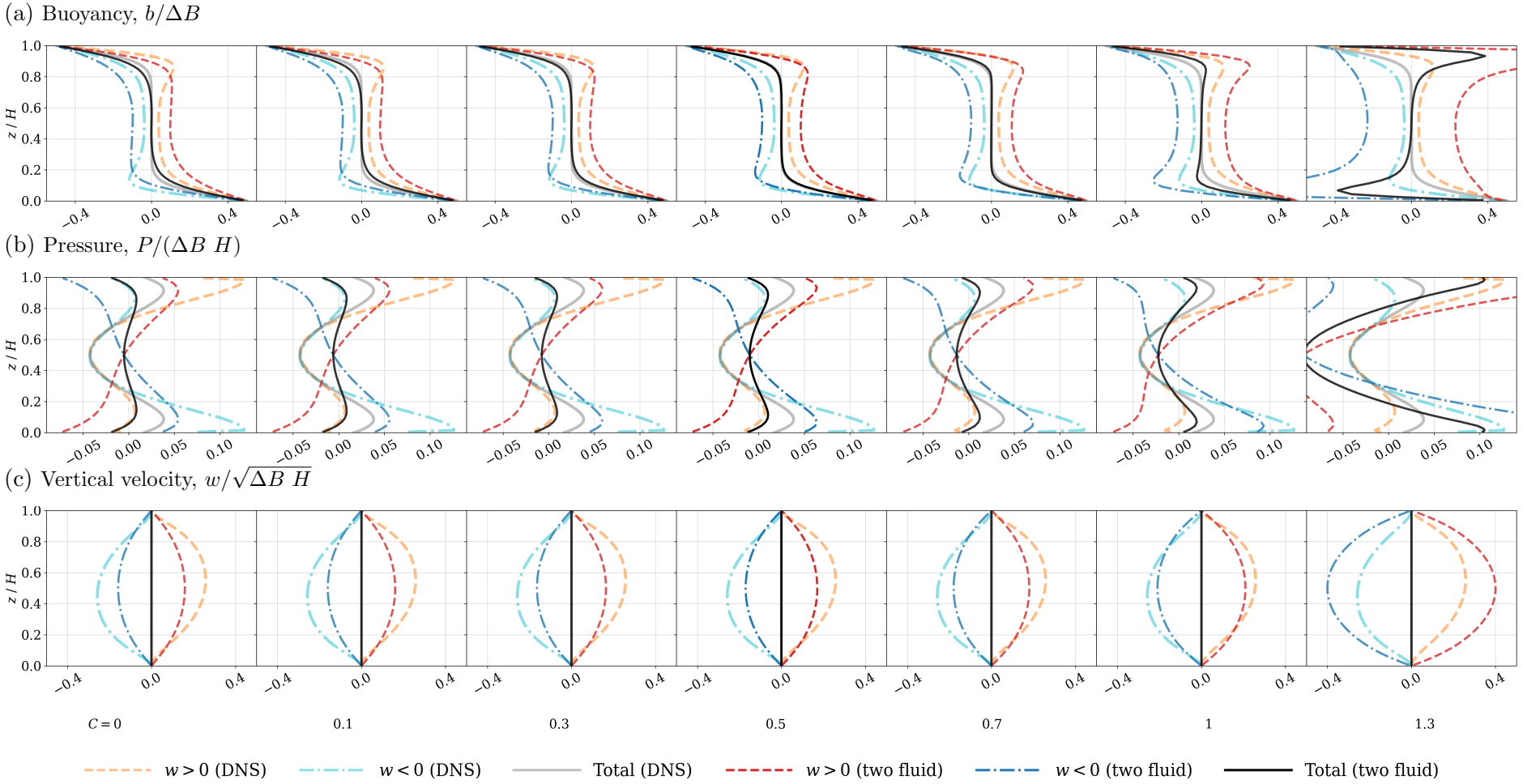

Figure 4.7: Two-fluid single-column model of $\mathrm{Ra} = 10^5$ RBC governed by equations (4.5)-(4.11) and (4.16), with $\hat{\gamma}_0 \simeq 0.75$, showing sensitivity to the transferred buoyancy parameter C (defined in Equation (4.10)) over the range $0 \leq C \leq 1.3$. $C = 0.5$ corresponds to the profiles in Figure 4.2. For $C \gtrsim 1.3$, the solution becomes unstable. Results for small values of C $(= 0, 0.1)$ are shown in the left column; for values around the central value of 0.5 in the middle column; and for large values (≥ 1) in the right column (see text for interpretation). Grey shaded regions in plots in the right column highlight areas which are not in the domain of plots in the left and centre columns.

These discrepancies suggest that the scaling used for γ/ν is not quite correct in the low Ra regime; unsurprising since the scaling argument assumed $\mathrm{Re} \gg 1$. For the intended application to highly turbulent atmospheric convection, however, this does not present a severe problem.

The single-column model does not naturally capture the drop in the prefactor of the Nusselt number scaling which occurs as the flow transitions to turbulence around $\mathrm{Ra} \sim 10^7$. The drop in the Nusselt number scaling prefactor may not be a robust feature of the convective flow, so it is far more important to get the scaling exponent correct. Such drops in the scaling prefactor are found in other RBC experiments (see Johnston and Doering 2009 for a 2D numerical example; Roche et al. 2004 for a 3D experimental example), but appear to be dependent on the nature of the flow configuration, rather than global in nature like the scaling exponent. However, this drop *can* be accurately reproduced by using $C = 0.5$ for $\mathrm{Ra} \leq 10^7$ and $C = 0$ for $\mathrm{Ra} > 10^7$, retaining the value of $\hat{\gamma}_0 \simeq 1.861$. With this parametrization, the Nusselt number is correctly predicted to within 5% across six decades of buoyancy forcing, $10^4 \leq \mathrm{Ra} \leq 10^{10}$, and approximately the correct transitional behaviour is found for $\mathrm{Ra} < 10^4$. This could be diagnostically incorporated into the parametrization by, for instance, reducing C to 0 whenever the vertical velocity maximum gives a turbulent $\mathrm{Re} \gtrsim 2 \times 10^3$.

The Reynolds number in the single-column simulations was estimated from the maximum magnitude of the vertical velocity in each partition; this should scale with the large-scale circulation, so makes sense for a bulk Reynolds number.We can see more rigorously why this should match the RMS velocity scales used to estimate the bulk Reynolds number of the single-fluid flow by considering again the decomposition of the flow into coherent structures and internal variability:

$$w_{\mathrm{RMS}} \coloneqq \sqrt{s(w,w)} = \sqrt{\sum_i \sigma_i s_i(w,w) + \sum_i \sigma_i (w_i - \overline{w})^2} \tag{4.20}$$

$$\approx \sqrt{\sigma_0 w_0^2 + \sigma_1 w_1^2} \approx |w_0| \approx |w_1| \tag{4.21}$$

in the centre of the domain. That is, neglecting the internal variability, the within-partition velocities describe the vertical velocity variance, and so the maximum of $\sqrt{\sigma_0 w_0^2 + \sigma_1 w_1^2}$ ($\approx |w_0|$ due to symmetry once bulk well-mixed) should be a good estimator of the bulk Reynolds number. Using this estimate, the scaling behaviour of the Reynolds number is also well-captured (Figure 4.8b), in particular giving the same scaling exponent as the DNS. Notably, the change in C required to capture the correct behaviour of Nu does not cause a corresponding kink in the Reynolds number scaling. This suggests that C really is just a crude measure of the flow state. Future work would hope to capture these flow states dynamically through

representing the sub-filter scale variability of the variables within each fluid.

4.5 Summary and conclusions

In this chapter we have shown that the simple two-fluid single column model (4.5)-(4.11) can qualitatively reproduce horizontal-mean DNS buoyancy, vertical velocity, and pressure profiles in all three characteristic regimes of Rayleigh-Bénard convection. A scaling argument for the pressure differences between the fluids allows the model to predict the correct power-law scalings of $\mathrm{Nu} \sim \mathrm{Ra}^{2/7}$and $\mathrm{Re} \sim \mathrm{Ra}^{1/2}$, and after measuring a dimensionless constant at one Rayleigh number the magnitude of Nu can be predicted to within 5% over 6 decades of Ra. The closure set is minimal, requiring only two constants to be set; and not finely-tuned, as both closure constants may be varied significantly from their central values without destroying the solution. Intriguingly, the model also captures approximately the correct spin-up behaviour, and approximately the correct critical Rayleigh number, despite being designed as an equilibrium parametrization for the high-Rayleigh number regime. Understanding the reasons for this will form the basis of future work.

Although we use a similar equation set and identical fluid definitions to Weller et al. (2020), this is the first such study to model a fully turbulent regime with these fluid definitions. It is also the first multi-fluid convection study to considerably vary the applied forcing, testing the robustness of the parametrization.

This demonstrates the essential validity of the multi-fluid concept: the model directly captures the dominant overturning circulation of convection, present even in the fully turbulent regime, by allowing for a circulation even in a single column. It is important to note that this performance is achieved without even a minimal treatment of fluxes due to variability within each fluid (i.e. conventional 'turbulent' or 'subfilter' fluxes) apart from the fixed viscosity and Prandtl number of the fluid.

With the current model the mean buoyancy profile (and therefore the Nusselt number), the vertical velocity maxima in each fluid (and therefore the implied Reynolds number), and the pressure profile, cannot all simultaneously have the correct magnitude. It is unclear whether this is due to neglected subfilter variability (in the form of exchanged buoyancy or neglected subfilter stresses, for example), or due to inadequate representation of the fluid fraction transfers. A more accurate and flexible representation of these transfers is essential to progressing beyond single-column modelling.

A limitation of this study is that our reference simulations are 2D, whereas real-world convection is 3D. For this reason we have limited our analysis to global properties of the solutions, such as scalings of Nu and Re with Ra, which do not

depend on dimension. We have also attempted to formulate our closures in a way which does not directly depend on the dimensionality of the simulated domain; given that there is no representation of turbulence in our model beyond the partition into two fluids, the differences between 2D and 3D cascades do not directly enter our model.

For the intended application to atmospheric convection, 3D convective turbulence must be considered. This will marginally alter the magnitudes of the Nusselt and Rayleigh numbers (the Nu prefactor is larger in 3D, while the Re prefactor is smaller), though the scaling with Ra and the shapes of the mean profiles are expected to be the same. However the qualitative nature of the flow will be different; pronounced, long-lived small-scale vortices would not exist in the 3D case due to vortex stretching, and the solution is expected to be far more intermittent. Due to the different cascades in 2D and 3D, the required closures at grey zone resolutions similar to the plume widths could also be quite different.

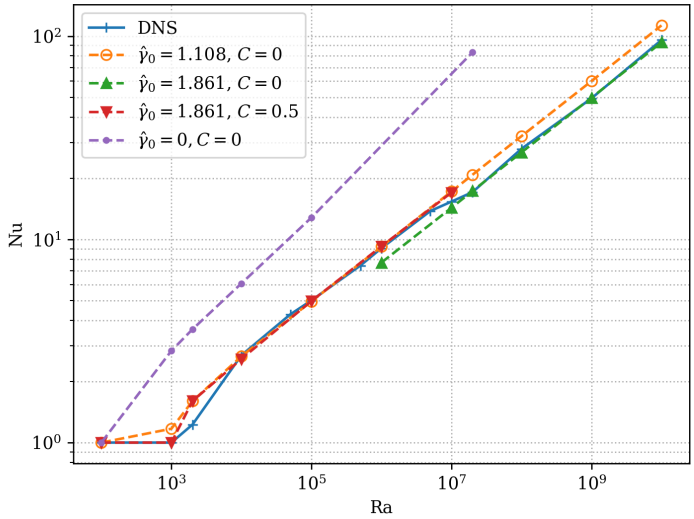

(a) Nusselt number vs. Rayleigh number over the range $10^2 \leq \mathrm{Ra} \leq 10^{10}$ for two-fluid single column models with various values of $\hat{\gamma}_0$ and C. Setup of the two-fluid single-column model is described in Section 4.2. The crosses joined by a solid blue curve show the reference DNS results (as 2.3a), while the closed circles joined by a dashed purple curve show the results of running the single column model with $C = 0$ (mass exchanges transfer the mean buoyancy) and $\gamma = 0$ (no pressure differences between the fluids). Three further dashed curves (orange with with open circles; green with upward-pointing triangles; red with downward-pointing triangles) show the results for $\gamma = \nu\hat{\gamma}_0 \,\mathrm{Ra}^{1/4}$ with different values of $\hat{\gamma}_0$; all give scalings of $\mathrm{Nu} \sim \mathrm{Ra}^{2/7}$. Single-column Nusselt numbers are calculated from the buoyancy gradient at the boundaries, and checked against the column-integrated buoyancy flux.

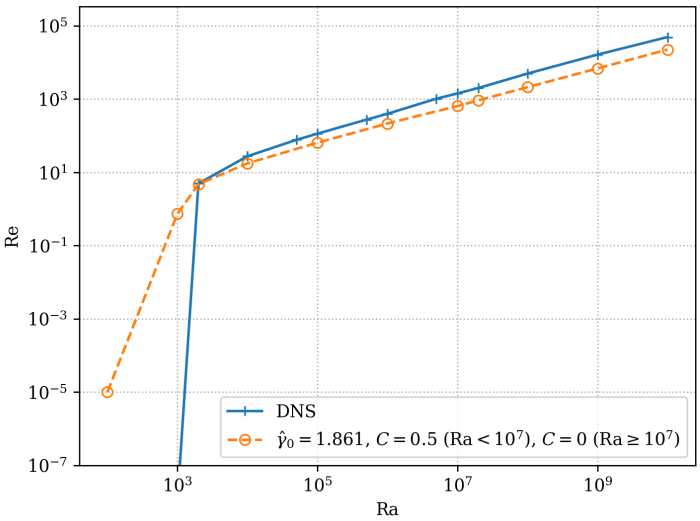

(b) Reynolds number vs. Rayleigh number for $10^2 \leq \mathrm{Ra} \leq 10^{10}$. The crosses joined by a solid blue curve show the reference DNS results (as 2.3b), while the open circles joined by a dashed orange curve show results from a two fluid single column model (described in Section Setup of the two-fluid single-column model is described in Section 4.2.), with $\gamma/\nu = 1.861\,\mathrm{Ra}^{1/4}$ and $C = 0.5$ for $\mathrm{Ra} \leq 10^7$, $C = 0$ for $\mathrm{Ra} > 10^7$; these constants give the best fit for Nu as a function of Ra (Figure 4.8a). Both curves exhibit scalings of $\mathrm{Re} \sim \mathrm{Ra}^{1/2}$ for $\mathrm{Ra} \gtrsim 10^4$. Single-column Reynolds numbers are calculated using the maxima of the individual fluid vertical velocity profiles for the velocity scale.

Figure 4.8

Chapter 5

Beyond single-column: Two-fluid modelling in the grey zone of RBC

5.1 Introduction

In this chapter we explore the multi-fluid approach to modelling Rayleigh-Bénard convection at grey zone resolutions. Chapter 2 presented simulations of RBC at varying horizontal resolution using the single-fluid Boussinesq equations. In this chapter we will present simulations of RBC using the two-fluid model developed in Chapter 4, analysing its performance from fully-subfilter convection, through the grey zone, to the resolved limit. We consider where the model performs better (and worse) than a single-fluid model with no parametrization, and crucially we look for signs as to whether — and if so, *why* — the multi-fluid approach may tame the grey zone.

5.2 Performance of two-fluid model formulation in 2D

5.2.1 Review of the grey zone

In Chapter 2, the grey zone of Rayleigh-Bénard convection was investigated by simulating convection at varying horizontal resolutions and comparing the results of these simulations to DNS. We also argued that these simulations may be taken as a crude proxy for atmospheric models with so-called "explicit convection". For a given energy injection length scale (i.e. the length scale of the peak in the power spectrum), ℓ, we defined the (2D) grey zone to range from $10^{-1}\ell \lesssim \Delta x \lesssim 10\ell$, where Δx is the grid spacing; for our purposes ℓ is taken to be the critical wavelength, $\ell \approx \lambda_c \approx 2H$.We also defined the "hard" grey zone to be the range $10^{-1}\ell \lesssim \Delta x \lesssim \ell$, and the "soft" grey zone to be $\ell \lesssim \Delta x \lesssim 10\ell$. A summary of the problems with the

single-fluid grey zone simulations is:

- **Incorrect (local) length scales:** Convection projects onto the grid scale, even when Δx is smaller than the width of convective plumes.
- **Incorrect (global) time scales:** Initiation of convection is delayed, particularly in the soft grey zone.
- **Strong dependence on initial conditions:** Direct numerical simulations show a negligible difference between initialization with purely random perturbations to the buoyancy field, versus a sinusoidal perturbation to force the most unstable mode, after roughly $10T_\mathrm{e}$. Some grey zone simulations show strong sensitivity to the initialization at times over $100T_\mathrm{e}$ (though the final statistically stationary equilibrium solution is not dependent on the initial conditions).
- **Multiple equilibria:** Many grey zone simulations reach what appears to be a stationary state after $\gtrsim 10T_\mathrm{e}$, followed by a jump to another steady state at much later times (i.e. at least $10T_\mathrm{e}$ after the initial "equilibrium" was reached). This jump to a different equilibrium is often associated with a "period-halving" – the dominant length scale of the simulated convection collapses from L to $L/2$. If $L/2$ is still greater than Δx, further jumps to other equilibria may occur until the dominant simulated length scale is equal to the horizontal grid spacing.
- **Different dynamical states:** If the grid spacing Δx is not sufficiently small to resolve the inner turbulence length scale ℓ_t — i.e. the boundary layer/coherent structure thickness — then the simulation will be laminar rather than intermittent/turbulent.
- **Incorrect global response:** Grey zone simulations will produce the wrong global heat and momentum transports.

As noted in Chapter 1, analytical and numerical modelling of the atmosphere (as well as many observations) takes place within the grey zone of atmospheric convection, meaning that an understanding of the grey zone must be developed in order to understand and correctly predict convection and its effects on the length and time scales that humans are interested in. Traditional convection parametrizations are fundamentally one-dimensional (so-called "single-column models"), relying on assumptions which are only valid over large length and time scales and under assumptions of horizontal homogeneity and the existence of a time scale separation between large-scale forcing and the convection. Horizontal transports *cannot* be neglected in the grey zone, however, and the assumptions of many clouds within a

grid volume and scale separation between forcing and convective response cannot be made.

Therefore there are many attempts to modify traditional convection parametrizations to work in the grey zone, or else the mass-flux schemes are removed and convection is handled explicitly via the dynamical core and a Smagorinsky-type eddy diffusivity closure (to simulate the enhanced mixing due to turbulence). Though this "explicit" convection often works better than traditional mass flux-type parametrizations at grey zone resolutions, systematic errors remain and results do not necessarily converge as grid spacing decreases (Clark et al. 2016; Lean et al. 2008; Stein et al. 2015). Because convection is marked out from other atmospheric turbulence by the importance of nonlocal fluxes, modifications to eddy diffusivity-type closures (usually local and down-gradient) are required in order to accurately model convection.

Within the context of Rayleigh-Bénard convection, the simplest single-column downgradient (isotropic) eddy diffusivity closure simply renormalizes the buoyancy diffusivity such that the Nusselt number of the horizontally-averaged flow matches the Nusselt number of the DNS: $\kappa \to \kappa_\mathrm{t} : \kappa_\mathrm{t}/\kappa = \mathrm{Nu} = \left\langle wb - \kappa\frac{\partial b}{\partial z}\right\rangle_{V,t} \Big/ (\kappa \Delta B/H)$, which works because in a single-column $\langle w \rangle_A = 0$. This first-order closure gives the wrong profiles of buoyancy and pressure, however — higher-order thinking is required to represent the shapes of the profiles correctly in a single column.

For the reasons outlined in the introduction and Chapter 3, multi-fluid modelling is a promising framework for overcoming these problems, compared to modifying existing convection schemes for use in the grey zone. But one cannot expect an arbitrary multi-fluid scheme to work in the convective grey zone purely *because* it is a multi-fluid scheme. Therefore in this section we analyse the performance of closures used in the simple two-fluid single-column model of RBC developed in Chapter 4 when applied across the grey zone of RBC.

5.2.2 Two-fluid model formulation

In Chapter 4 we developed a two-fluid model for Rayleigh-Bénard convection based on one rising and one falling fluid. No further accounting for subfilter fluxes was made beyond the partition into two fluids. The closures were designed to capture the dominant coherent overturning structures of RBC. As emphasized in Chapter 4, the form of the equation set and closures only explicitly assumes a single column in the specification of the transferred momentum, since no closure for the horizontal components of the transferred momentum is required in a single-column. We repeat the equation set and chosen closures here, before discussing their applicability to the grey zone, and adding the remaining closure required for 2D simulation.

$$\sum_i \boldsymbol{\nabla} \cdot (\sigma_i \mathbf{u}_i) = 0. \tag{3.26}$$

$$\sum_i \sigma_i = 1 \tag{3.25}$$

$$\frac{\partial \sigma_i}{\partial t} + \boldsymbol{\nabla} \cdot (\sigma_i \mathbf{u}_i) = \sigma_j S_{ji} - \sigma_i S_{ij}, \tag{4.5}$$

$$\begin{aligned} \frac{\partial \sigma_i \mathbf{u}_i}{\partial t} + \boldsymbol{\nabla} \cdot (\sigma_i \mathbf{u}_i \otimes \mathbf{u}_i) = {} & \sigma_i b_i \hat{\mathbf{k}} - \sigma_i \boldsymbol{\nabla} \overline{P} - \boldsymbol{\nabla}(\sigma_i p_i) \\ & + \nu \boldsymbol{\nabla}^2 \sigma_i \mathbf{u}_i - \nu \boldsymbol{\nabla} \cdot (\overline{\mathbf{u}} \otimes \boldsymbol{\nabla} \sigma_i)^{\mathsf{T}} - \nu \boldsymbol{\nabla} \sigma_i \cdot (\boldsymbol{\nabla} \overline{\mathbf{u}})^{\mathsf{T}} \\ & + \sigma_j \mathbf{u}_{ji}^T S_{ji} - \sigma_i \mathbf{u}_{ij}^T S_{ij}, \end{aligned} \tag{4.6}$$

$$\begin{aligned} \frac{\partial \sigma_i b_i}{\partial t} + \boldsymbol{\nabla} \cdot (\sigma_i \mathbf{u}_i b_i) = {} & \kappa \boldsymbol{\nabla}^2 \sigma_i b_i - \kappa \boldsymbol{\nabla} \sigma_i \cdot \boldsymbol{\nabla} \overline{b} - \kappa \boldsymbol{\nabla} \cdot \overline{b} \boldsymbol{\nabla} \sigma_i \\ & + \sigma_j b_{ji}^T S_{ji} - \sigma_i b_{ij}^T S_{ij}, \end{aligned} \tag{4.7}$$

with $i, j \in \{0, 1\}$, and the specific parametrization choices:

$$S_{ij} = \max(-\boldsymbol{\nabla} \cdot \mathbf{u}_i, 0), \tag{4.8}$$

$$w_{ij}^T = 0, \tag{4.9}$$

$$b_{ij}^T = b_i + (-1)^i C |b_i| \tag{4.10}$$

$$p_i = \left(\sum_j \sigma_j \gamma \boldsymbol{\nabla} \cdot \mathbf{u}_j \right) - \gamma \boldsymbol{\nabla} \cdot \mathbf{u}_i, \tag{4.11}$$

$$\frac{\gamma}{\nu} = \hat{\gamma}_0 \, \mathrm{Ra}^{1/4} \, \mathrm{Pr}^{-1/4} \, . \tag{4.16}$$

The only additional closure required to complete the equation set in 2D is a closure for the exchanged horizontal momenta; we choose:

$$u_{ij}^T = u_i, \tag{5.1}$$

i.e. the mean horizontal velocity within a partition is transferred. This has the correct high-resolution limit, as well as the correct fully-parametrized limit, and is the closure explicitly chosen in the derivation of the extended EDMF equations in Tan et al. (2018). We may note in addition that in RBC the horizontal velocity is approximately symmetrically distributed on either side of the $w = 0$ interface, so this may even be a reasonable assumption for the transfers within the grey zone of RBC.

Although this is the same equation set as in a single column, there are some crucial differences which manifest when applying it to a 2D problem rather than 1D. Perhaps most importantly, the divergence constraint no longer forces the mean

velocity to be zero — that is, there can (indeed, *must*) be resolved horizontal and vertical velocities in 2D or 3D. This amounts to stating that there will in general be net mass transports in both the horizontal and vertical. Specifically, in 1D the divergence-free mean velocity constraint, Equation (3.26) requires $\partial\overline{w}/\partial z = 0 \implies \partial\sigma_0 w_0/\partial z = -\partial\sigma_1 w_1/\partial z$, i.e. the mass fluxes have to cancel. Coupled with the no-normal flow boundary conditions, this forces $\overline{w} = 0 \implies \sigma_0 w_0 = -\sigma_1 w_1$. In 2D, the horizontal divergence no longer disappears, so there can and in general will be net mass transport in both the horizontal and vertical.

Before simulating anything, there are a few remarks we can make about the suitability of this model formulation for the grey zone of RBC. Firstly, the overarching multi-fluid framework developed in Chapter 3 is in principle suitable for any filter scale and any fluid dynamical problem. It is expected to be of most use when coherent structures play an important role in the dynamics of the flow, which is clearly the case for RBC. However the partition we have chosen is unlikely to be optimal; as shown in Figure 4.5 of Chapter 4, partitioning the turbulent DNS flow based on the sign of w gives only a first approximation to the coherent structures. Because this partition is not optimal, the variability *within* the partitions will be relatively more important for a good description of the flow than if a better partition were chosen. Therefore the assumptions that $s_i(\mathbf{u}, \mathbf{u}) \approx \mathbf{0}, s_i(\mathbf{u}, b) \approx \mathbf{0}$ are likely to be problematic, especially within the grey zone. Further, as already noted, the chosen closures for the transfer terms are fundamentally incompatible with the chosen partition in high-resolution limit.

5.2.3 Simulation setup and experiment design

Having noted these potential incompatibilities, we will nevertheless examine the performance of the two-fluid model with the single-column closures in the grey zone of 2D RBC. In Chapter 2, we explored the grey zone of RBC by systematically decreasing the horizontal resolution of numerical simulations from DNS resolution ($\Delta x \sim \eta_\mathrm{K}$) to such coarse resolution that no circulations develop ($\Delta x \sim 100\ H$). We shall now repeat these simulations with the two-fluid model governed by equations (3.26)-(3.25), (4.5)-(4.7), with the closures (4.8)-(4.11), (4.16), and (5.1).

We present simulations at $\mathrm{Ra} = 10^5, \mathrm{Pr} = 0.707$. The two closure constants are set equal to the values which gave the correct Nusselt number in the single-column simulations of Chapter 4 at $\mathrm{Ra} = 10^5$: $C = 0.5, \hat{\gamma}_0 = 1.861$.

The numerical method is identical to that detailed in Section 4.3 of Chapter 4. The conditions at the top and bottom boundaries are also identical to the single-column model (i.e. no normal flow, no-slip for the velocity; hydrostatic for the mean pressure; zero gradient for the perturbation pressure; fixed buoyancy; and

zero-gradient for the fluid fraction). The lateral boundary conditions are periodic in all fields.

Initialization is the same as for the single-column simulations[1]: velocity perturbations equal to $\pm 10^{-3} U_B$ were added to a resting velocity field, with random perturbations of magnitude $|\delta b| \leq 0.0008 \Delta B$ (drawn from a uniform distribution) added to a horizontally-uniform linear buoyancy profile in hydrostatic balance with the (also horizontally uniform) pressure field. The fluid fractions were initially uniformly equal to 0.5 throughout the domain. Simulations were run until a statistically stationary, yet convective, state was reached, decided from the tendency of the Nusselt number over $20T_\mathrm{e}$, or until $t = 250T_\mathrm{e}$ if no convecting stationary state had been reached. Note that the ratio between the diffusive and convective timescales is $T_\kappa / T_B = \mathrm{Ra}^{1/2} \mathrm{Pr}^{1/2}$, so $250T_\mathrm{e} = (1000/(\mathrm{Ra}\,\mathrm{Pr})^{1/2}) T_\kappa$, so for $\mathrm{Ra} \lesssim 1.4 \times 10^6$ a full diffusive timescale is simulated.

The vertical resolution of the simulations was kept the same as the vertical resolution of the DNS, detailed in Table 2.1. The horizontal resolutions range from DNS resolution, $\Delta x \approx 2\eta_\mathrm{K}$, through to $\Delta x = 100H$. Since the DNS simulations were run at an aspect ratio ($\mathrm{AR} \coloneqq L/H$) of 10, the coarser-resolution simulations were required to be run at larger aspect ratios; sensitivity to aspect ratio was checked by running the same resolution at multiple aspect ratios, with no discernible differences. Full details of the horizontal resolutions and simulation times are given in Table 5.1.

5.2.4 Results

In this section we present and discuss the results of the simulations described in the previous section. The key questions are:

1. How well do the single-column closures work in 2D? (For instance, do they cause numerical instabilities?)
2. How does the two-fluid model perform in the grey zone compared to the single-fluid experiments of Chapter 2?
3. If there are any differences between the performance of the two-fluid and single-fluid models in the grey zone, how and why do they arise?

First we consider global properties of the simulations over all resolutions at $\mathrm{Ra} = 10^5$: Nu, and the time to convection initiation (defined as the first time for which $\mathrm{Nu} > 1.1$). Figure 5.1 shows the Nusselt number at $t = 25T_\mathrm{e}$[2] (after which the

[1] It is worth noting that this initialization is demonstrably incorrect for the fully-resolved limit, and therefore likely does not make sense either for the hard grey zone. However, this should not matter for the fully-developed state unless the system permits multiple equilibria.

[2] $25T_\mathrm{e}$ corresponds to a period of $\approx$ 8 hours for atmospheric shallow convection, assuming $T_\mathrm{e} \approx 20$ min. These estimates derive from the same scaling parameters as used in discussions of the atmospheric convective boundary layer in Chapters 1 and 2.

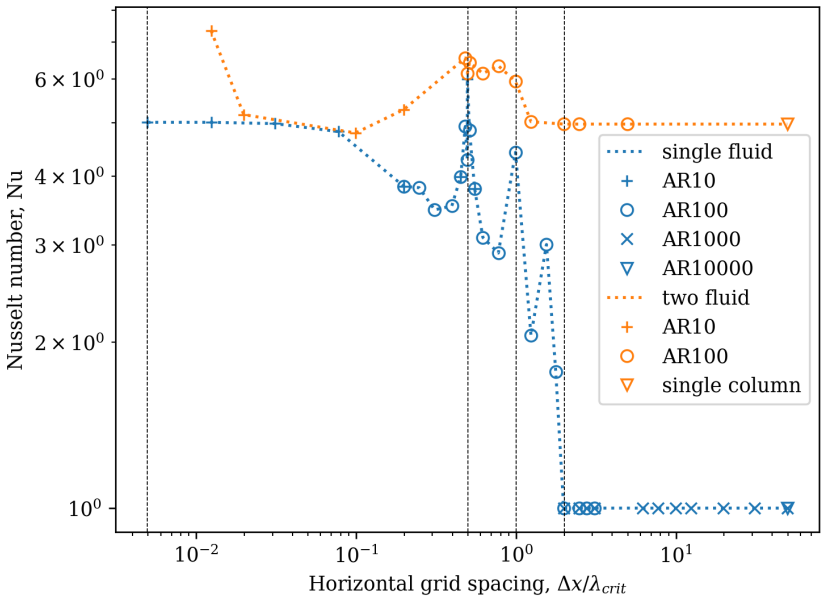

Figure 5.1: Nusselt number in Ra $\simeq 10^5$ RBC at $t = 25T_e$ as a function of horizontal grid spacing. The blue dashed line denotes results from the single-fluid simulations described in Chapter 2; results from the two-fluid model are represented by the orange dashed line. Different domain aspect ratios are denoted by different markers.

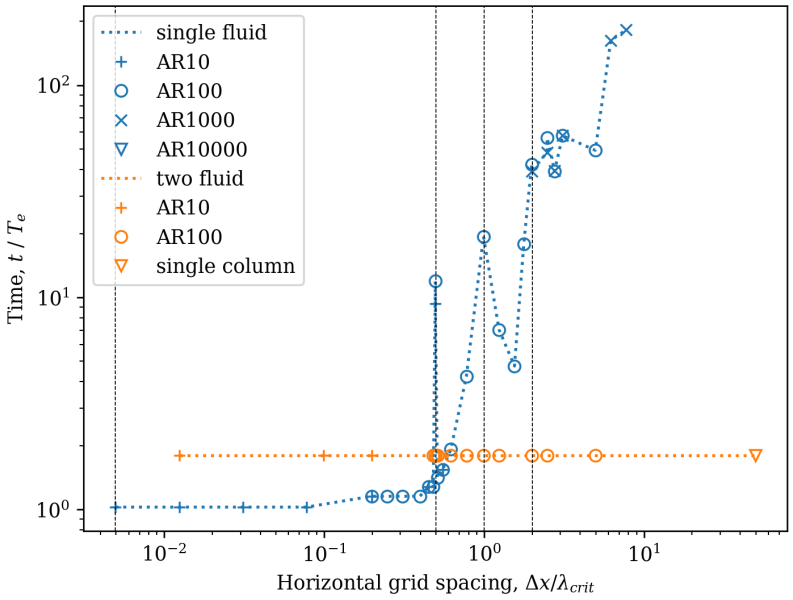

Figure 5.2: Time to the initiation of convection, defined as the first time at which Nu > 1.1. The blue dashed line denotes results from the single-fluid simulations described in Chapter 2; results from the two-fluid model are represented by the orange dashed line. Different domain aspect ratios are denoted by different markers.

$\Delta x/H$	AR	$T_{\text{tot}}/4T_B$	$\Delta t/4T_B$	Nu($25T_{\text{e}}$)	Re($25T_{\text{e}}$)	Nu(eqm.)	Re(eqm.)
2.5×10^{-2}	10	38	1.28×10^{-3}	7.34	200	7.34	200
4×10^{-2}	10	25	1.28×10^{-3}	5.17	200	5.17	200
1×10^{-1}	10	25	1.28×10^{-3}	4.94	200	4.94	200
2×10^{-1}	10	25	1.28×10^{-3}	4.79	190	4.79	190
4×10^{-1}	10	127	1.28×10^{-3}	5.28	170	5.28	170
9.7×10^{-1}	100	25	1.28×10^{-3}	6.55	210	6.55	210
1	100	25	1.28×10^{-3}	6.14	200	6.14	200
1.03	100	25	1.28×10^{-3}	6.43	210	6.43	210
1.25	100	25	1.28×10^{-3}	6.14	200	6.14	200
1.5625	100	125	1.28×10^{-3}	6.34	210	6.34	240
2	100	250	1.28×10^{-3}	5.94	170	7.42	240
2.5	100	250	1.28×10^{-3}	5.02	120	7.45	250
4	100	250	1.28×10^{-3}	4.97	120	5.58	142
5	100	250	1.28×10^{-3}	4.97	120	7.35	250
10	100	250	1.28×10^{-3}	4.97	120	4.97	120
100	10^4	250	1.28×10^{-3}	4.97	120	4.97	120

Table 5.1: Details of horizontal grid spacing, time-step size, domain aspect ratios, and simulation times for the two-fluid grey zone simulations at $\text{Ra} = 10^5$. Times are nondimensionalized by the (approximate) eddy turnover time, $T_{\text{e}} \approx 4T_B = 4\sqrt{H/\Delta B}$. Vertical resolutions are identical to those used in the DNS; see Table 2.1 for details. The final four columns give the Nusselt and Reynolds numbers for the simulations, first at $t = 25T_{\text{e}}$, and secondly at the final equilibrium (or at $t = 250T_{\text{e}}$ if no resolved convective equilibrium was reached).

DNS has reached a stable equilibrium), and Figure 5.2 shows the time to initiation, for both single-fluid and two-fluid simulations at $\text{Ra} = 10^5$. First we note that convection initiates at the same time for the two-fluid model across all resolutions, suggesting that the chosen parametrizations correctly capture the initial Rayleigh-Bénard instability. The single-fluid model takes longer to initiate convection for larger grid spacings, as the convection requires velocities to be resolved at the grid scale since there is no subfilter parametrization. The "correct" time to initiation in the DNS is between 1 and $3T_{\text{e}}$, depending on the initialization used; the two-fluid model initiates at $t = 1.8T_{\text{e}}$. Similar delays to convection initiation are a common problem with grey zone models of convection (e.g. Lean et al. 2008); therefore the fact that our simple two-fluid model always initiates correctly regardless of horizontal resolution is highly promising. Understanding why this is the case should be a priority for further research.

Looking at the Nusselt number after $25T_{\text{e}}$ (Figure 5.1), the two-fluid model performs well for $\Delta x \gtrsim 4H$, giving the same heat flux and vertical profiles of variables as the single-column model. However, for $4H \gtrsim \Delta x \gtrsim 0.2H$, the model overestimates the heat flux at $t = 25T_{\text{e}}$. As we shall see, this is due to projection onto the grid, as with the single-fluid solver. For $\Delta x \lesssim 0.2H$, the two-fluid model begins to

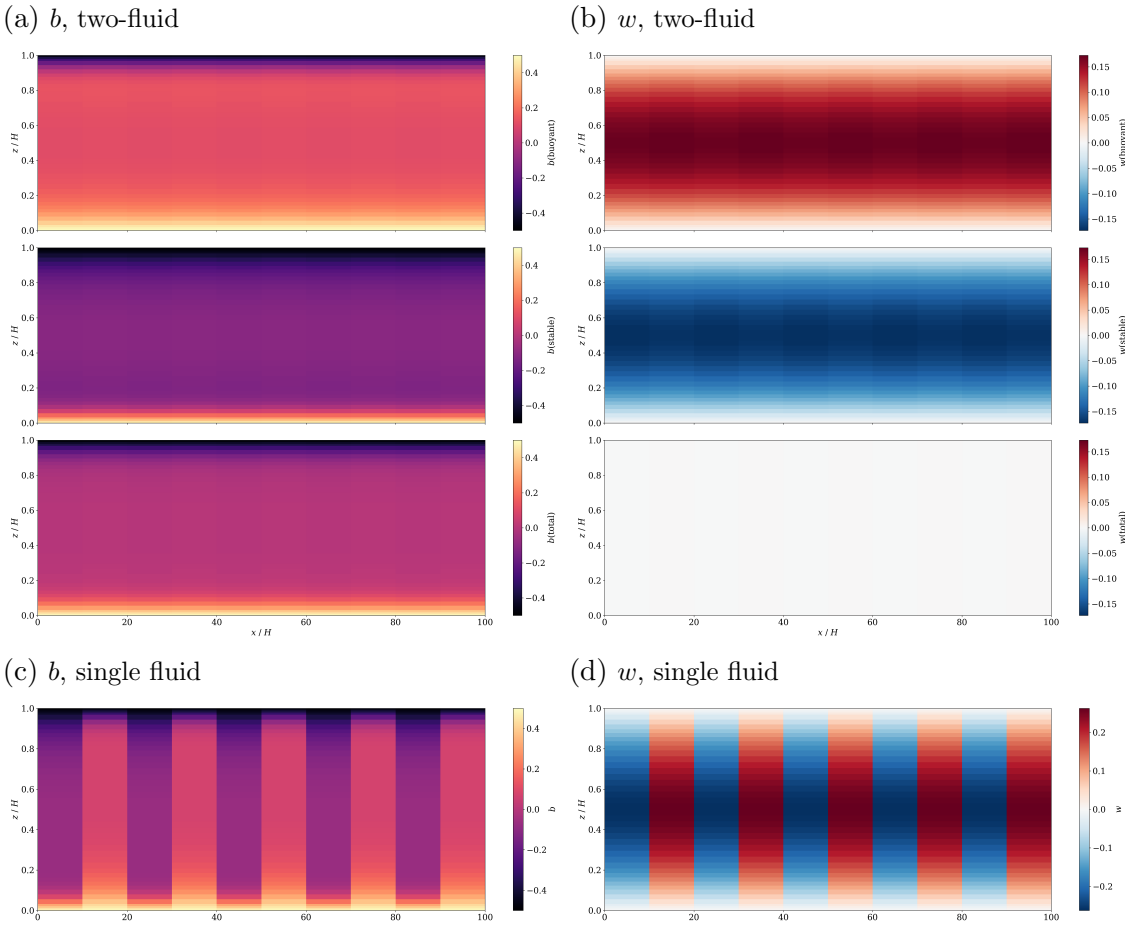

Figure 5.3: Buoyancy (left column) and vertical velocity (right column) fields for Ra $= 10^5$ RBC at a horizontal resolution of $\Delta x = 10H$ for: the two fluid solver with single-column closures (a,b); and the unparametrized single-fluid solver (c,d). The two-fluid fields are arranged top to bottom as: rising, falling, total. Fields are shown at $t \approx 250T_e$. Strong grid projection is seen in the single-fluid case, while only very faint grid projection is visible in the multi-fluid case.

overestimate the heat flux, and by DNS resolution the domain-integrated heat flux in the two-fluid solver is approximately 1.4 times the value for the DNS.

Before discussing the local properties of the simulations — i.e. what the 2D fields actually look like — it is worth considering what the fields *should* look like at different grid spacings. In the fully-parametrized limit ($\ell_f \gg H$), where there are very many complete circulations within a single horizontal filter scale, there should be no visible variation in the horizontal. In the soft grey zone ($10H \lesssim \ell_f \lesssim 100H$), several overturning circulations are contained within a single horizontal filter length; however, if the flow is turbulent ((or even quasi-periodic/chaotic, like Ra $\gtrsim 10^5$ RBC in 3D), not enough are averaged over for all horizontal variation to vanish[3]. Therefore the solution (when projected onto a grid which resolves ℓ_f) should be

[3]Recalling the discussion in Section 1.3.2, this really suggests that we should extend the model to include a stochastic component.

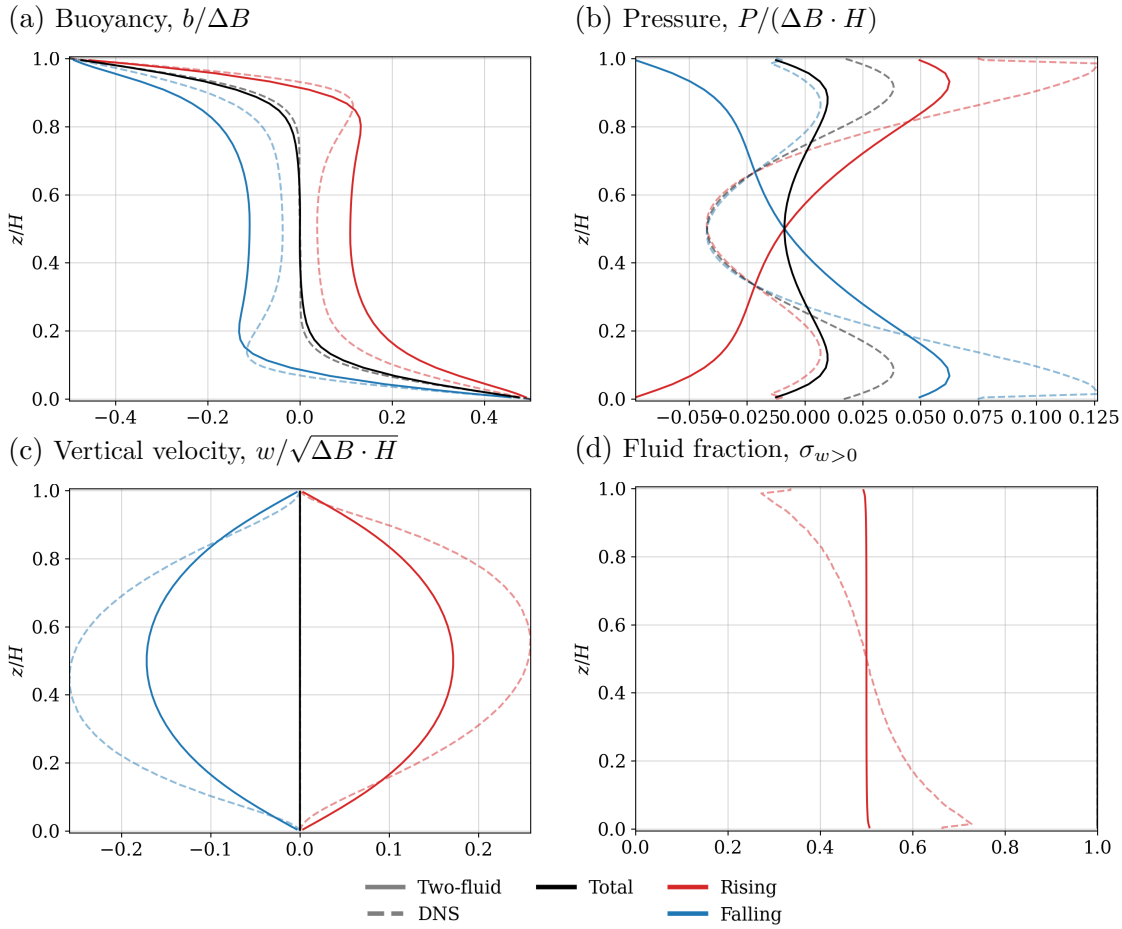

Figure 5.4: Horizontally-averaged profiles of buoyancy, pressure, vertical velocity, and fluid fraction in Ra $= 10^5$ RBC simulated with the two-fluid solver at a horizontal resolution of $\Delta x = 10H$ in a domain of aspect ratio AR $= 100$. Fields are shown at $t \approx 250T_e$. Conditionally horizontally- and time-averaged profiles from the DNS are shown for reference.

fairly horizontally uniform, with some aliasing onto the grid. At higher Rayleigh numbers the true solution should be intermittent, and this intermittency should show up in the (small) horizontal variations. In the hard grey zone ($\delta \lesssim \ell_f \lesssim 10H$), horizontal variations become much more apparent and important, as well as differences between different realizations of the flow. In particular, the instability should not simply project onto the grid scale — i.e. the critical wavelength implied by the model solution should not simply be equal to $2\Delta x$. In the high-resolution limit, the solutions should converge to the DNS.

In the fully parametrized limit, the two-fluid model has the correct behaviour, acting simply as a set of N single-column models, where N is the number of cells in the x-direction. There is no variation in the horizontal; resolved velocities are negligibly small, and damped. Differences of vertical profiles of variables from the single-column case are invisible to the naked eye, and therefore are not shown.

Buoyancy and vertical velocity fields from an example simulation in the soft

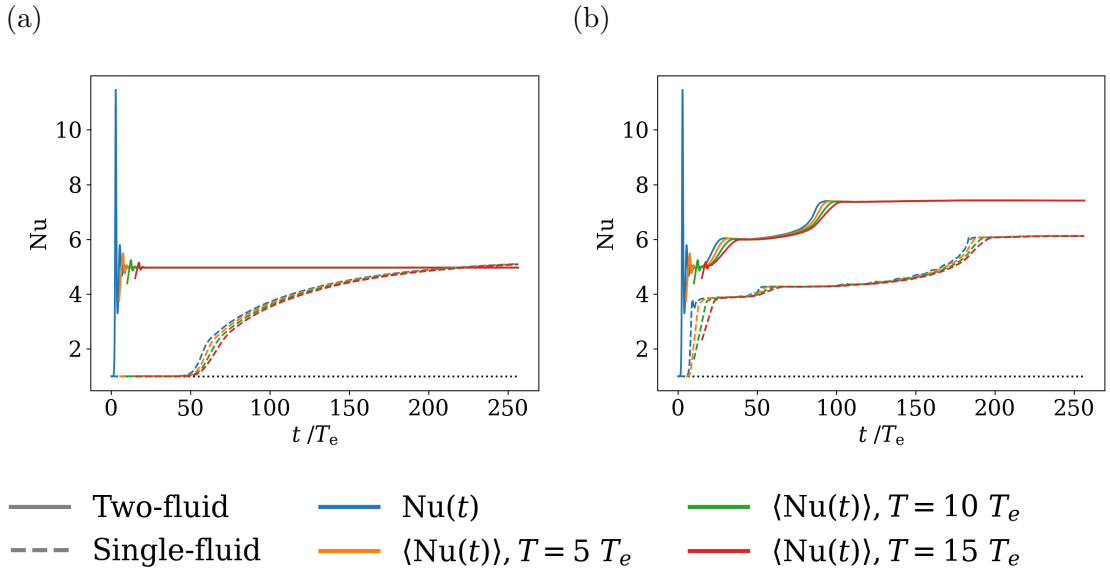

Figure 5.5: Comparison of Nusselt number time series between a simulation using the two-fluid single column closures and one run with the unparametrized single-fluid equations (a) in the soft grey zone of RBC, $\Delta x = 10H$; (b) in the hard grey zone of RBC, $\Delta x = 2H \approx \lambda_c$. The time series of the Nusselt number in the DNS is indistinguishable from the time-series for the two-fluid model in (a) at this temporal resolution. $\mathrm{Nu}_{\mathrm{DNS}} = 5.002$.

grey zone ($\Delta x = 10H$) are shown in Figure 5.3 at $t = 250T_e$. The corresponding vertical profiles of buoyancy, pressure, vertical velocity, and fluid fraction, are shown in Figure 5.4. At this time the Nusselt number and vertical profiles for the two-fluid solver are identical to the single-column model. Very weak projection onto the grid is visible in the buoyancy and vertical velocity fields (a and b), but this is after a very long integration time — assuming $T_e \approx 20$ min in the atmosphere, $250T_e \approx 3.5$ days. In the single-fluid solver (Figure 5.3c-d), there is strong projection onto the grid by this time. Figure 5.5a shows Nusselt number time series for both simulations; clearly the two-fluid solver better captures the dynamics at this resolution; in addition to initiating too late, the Nusselt number is slightly over-predicted by the single-fluid solver by the end of the simulation time. However, the nature of the (admittedly weak) grid projection and the inaccuracy of the mass transfers based on $\boldsymbol{\nabla}\cdot\mathbf{u}_i$ suggest that a parametrization like this may respond poorly to inhomogeneous forcing even in the soft grey zone.To see why the mass transfers based on $\boldsymbol{\nabla}\cdot\mathbf{u}_i$ are incorrect, see Section 5.3.

Buoyancy and vertical velocity fields from an example simulation in the hard grey zone ($\Delta x = 2H$) are shown in Figure 5.6 at $t = 250T_e$; the corresponding vertical profiles are shown in Figure 5.7. Although the two-fluid simulation initially spins up to the correct Nusselt number (Figure 5.5b), with vertical profiles of buoyancy, pressure, and vertical velocity similar to the single-column model, after $\approx 25T_e$ the grey zone instability manifests and projection onto the grid is seen in all fields.

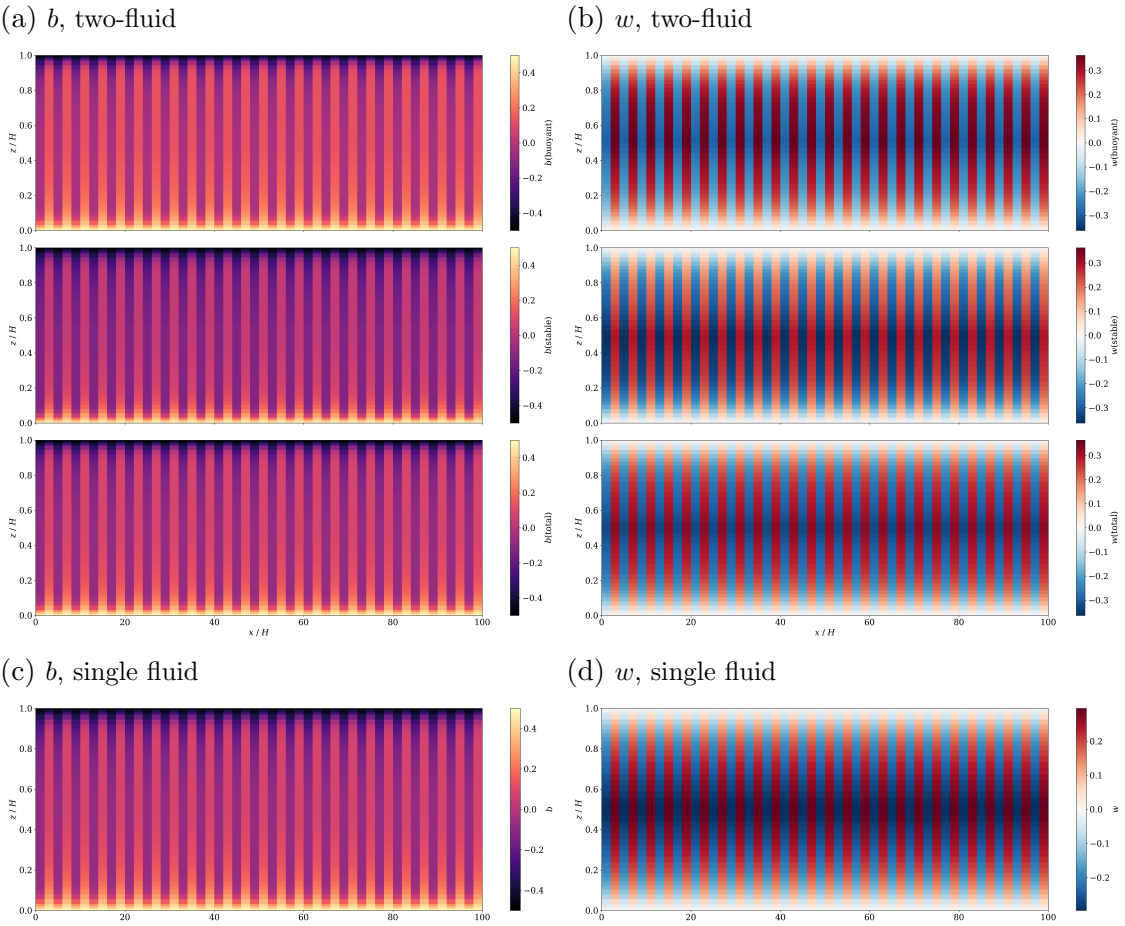

Figure 5.6: Buoyancy (left column) and vertical velocity (right column) fields for $\mathrm{Ra} = 10^5$ RBC at a horizontal grid spacing of $\Delta x = 2H \approx \lambda_c$ for: the two fluid solver with single-column closures (a, b); and the unparametrized single-fluid solver (c, d). The two-fluid fields are arranged top to bottom as: rising, falling, total. Fields are shown at $t \approx 250T_e$. Both simulations have reached a steady state, where no change in the circulation or global properties Nu, Re has been observed for $> 20T_e$. Strong grid projection is obvious in both cases. The two fluids no longer capture the correct sign of vertical velocity.

The Nusselt number continues to increase as the grid-scale instability cascades to the most unstable mode, with strictly alternating columns of rising and falling air throughout the domain. Once the grid projection becomes strong enough, the correct sign of vertical velocity is no longer maintained within each fluid, which leads to a positive feedback, increasing the strength of the velocities within the falling and rising columns. This means that the maximum velocities are greater in the two-fluid model than in the single-fluid model.

The grid projection also causes the vertical profiles to deviate from the single-column profiles (Figure 5.7). The mean buoyancy profile (a) is no longer constant in the bulk of the domain, instead having a weak negative gradient (also observed in the grey zone single-fluid simulations which exhibited grid projection in Chapter 2; not shown).Similar behaviour is also observed in grey zone simulations of the convective

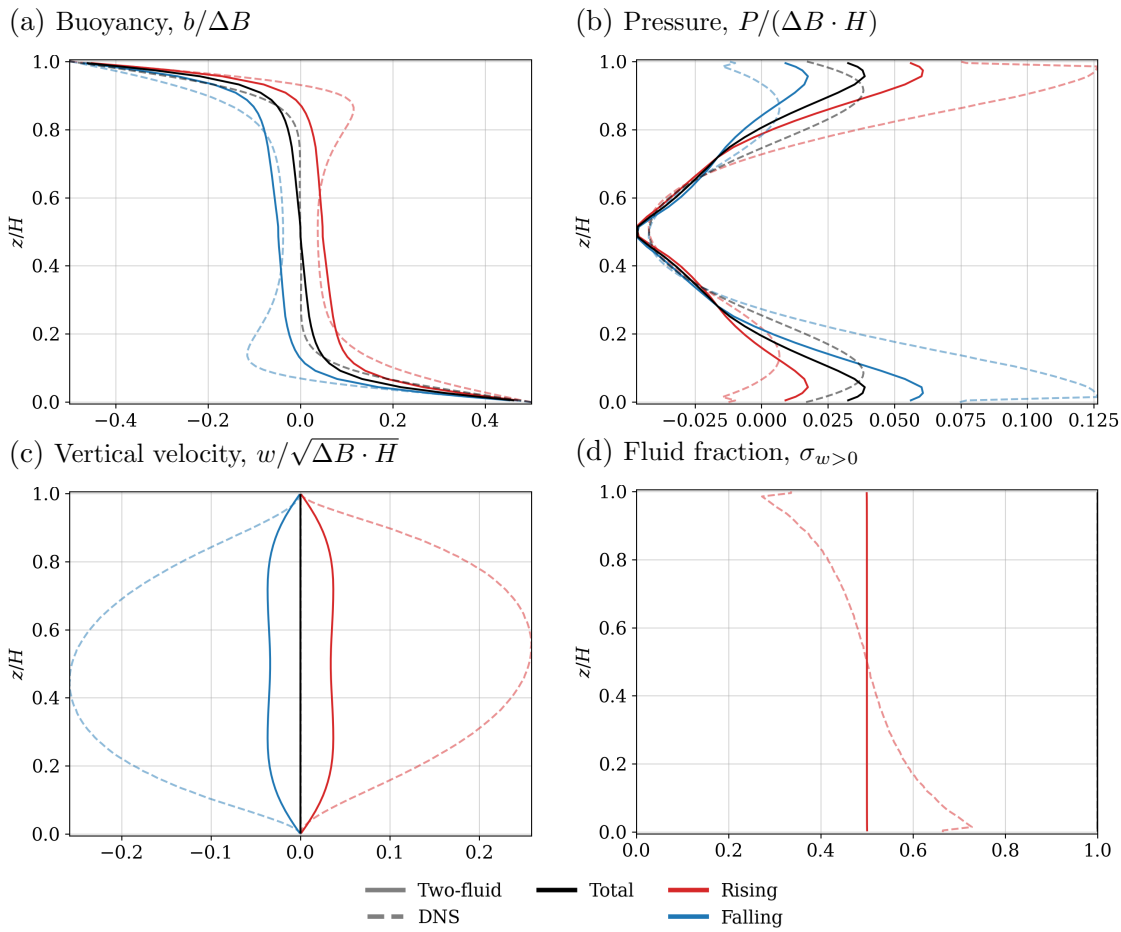

Figure 5.7: Horizontally-averaged profiles of $\mathrm{Ra} = 10^5$ RBC simulated with the two-fluid solver at a horizontal grid spacing of $\Delta x = 2H \approx \lambda_c$ in a domain of aspect ratio $\mathrm{AR} = 100$. Fields are shown at $t \approx 250T_e$. Conditionally horizontally- and time-averaged profiles from the DNS are shown for reference.

boundary layer, where insufficient mixing causes superadiabatic temperature profiles to form (Efstathiou et al. 2016). The buoyancy profiles of both rising and falling fluid lose the overshoots near the boundaries. The mean pressure profile (b) is also similar to the single-fluid grey zone pressure profile at the same horizontal resolution: the sign of the curvature of the pressure profile changes close to the centre of the domain, deepening the lowest pressure due to the unrealistically high vertical velocities. The vertical velocity profiles (c) within each fluid are also qualitatively changed: since the fluids no longer maintain single-signed vertical velocities, the magnitudes of the profiles decrease. This effect is starkest in the centre of the domain, where the maxima of incorrectly-signed velocities are present within each partition, turning the local maximum at the centre of the domain into a local minimum.

Buoyancy and vertical velocity fields from an example simulation in the weakly resolved regime ($\Delta x = 0.4H$) are shown in Figure 5.8 at $t = 125T_e$; the corresponding vertical profiles are shown in Figure 5.9. At first glance, the two-fluid model acts very similarly to the unparametrized single-fluid solver for grid spacings $\Delta x \lesssim 0.4H$;

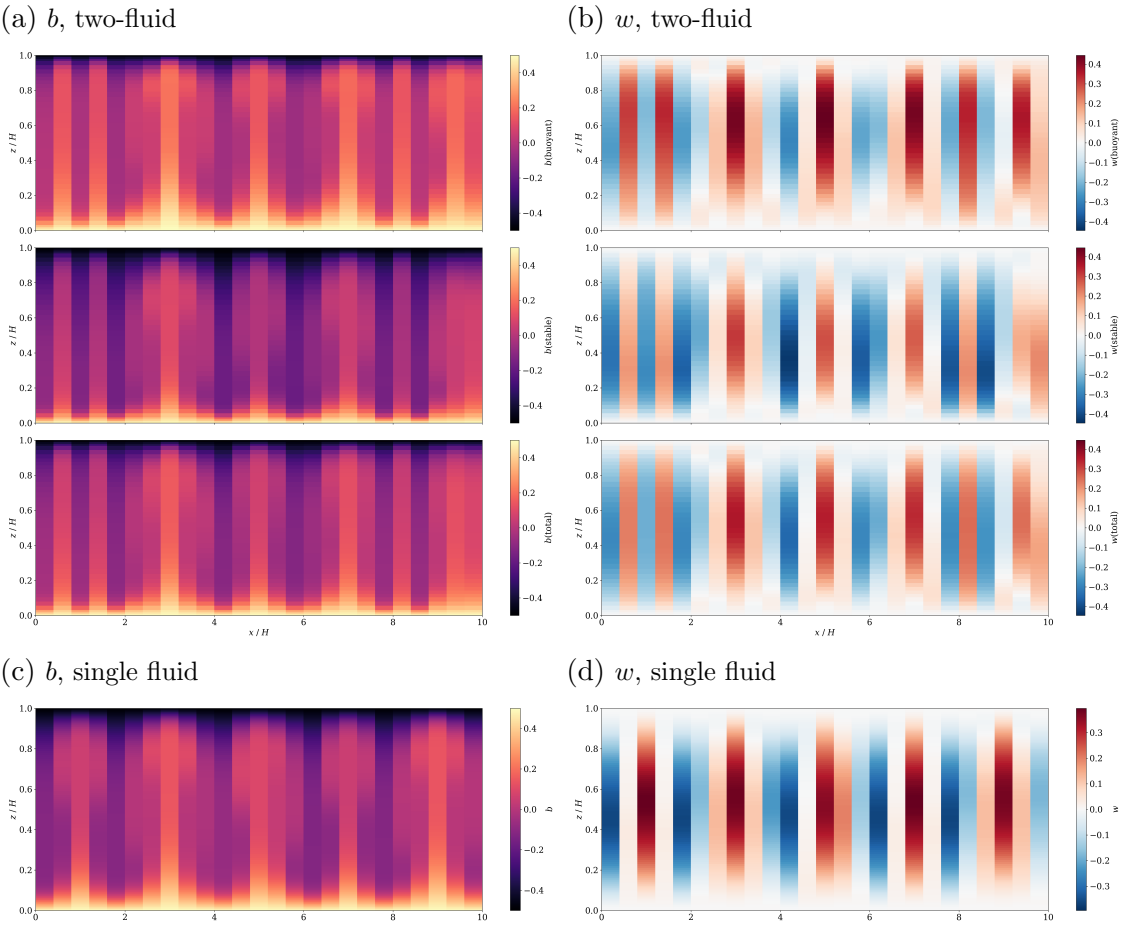

Figure 5.8: Buoyancy (left column) and vertical velocity (right column) fields for $\mathrm{Ra} = 10^5$ RBC at a horizontal grid spacing of $\Delta x = 0.4H \approx 0.2\lambda_c$ for: the two fluid solver with single-column closures (a, b); and the unparametrized single-fluid solver (c, d). The two-fluid fields are arranged top to bottom as: rising, falling, total. Fields are shown at $t \approx 125T_e$. Both simulations have reached a steady state, where no change in the circulation or global properties Nu, Re has been observed for $> 20T_e$. Some grid projection is visible in both cases. The two fluids no longer capture the correct sign of vertical velocity, leading to larger vertical velocity magnitudes in the two-fluid simulation.

the 2D fields and mean profiles look very similar. However, the closures do not keep the vertical velocities single-signed within each fluid, so the solver is effectively acting like two coupled single-fluid solvers with an extra momentum source from the fluid relabelling. This means that the vertical velocity magnitudes are slightly larger in the centre of the domain for the two-fluid solver, leading to the same problems for the vertical velocity profile within each fluid (Figure 5.9c) as observed in the hard grey zone simulations (Figure 5.7c).

In the fully resolved limit (Figure 5.10,5.11), these problems with the two-fluid solver become even more apparent: the buoyancy becomes unbounded (due to the crude closure for the transferred buoyancies being unbounded), with large regions where $|b| > \Delta B/2$, and maximum vertical velocities close to twice those of the single-

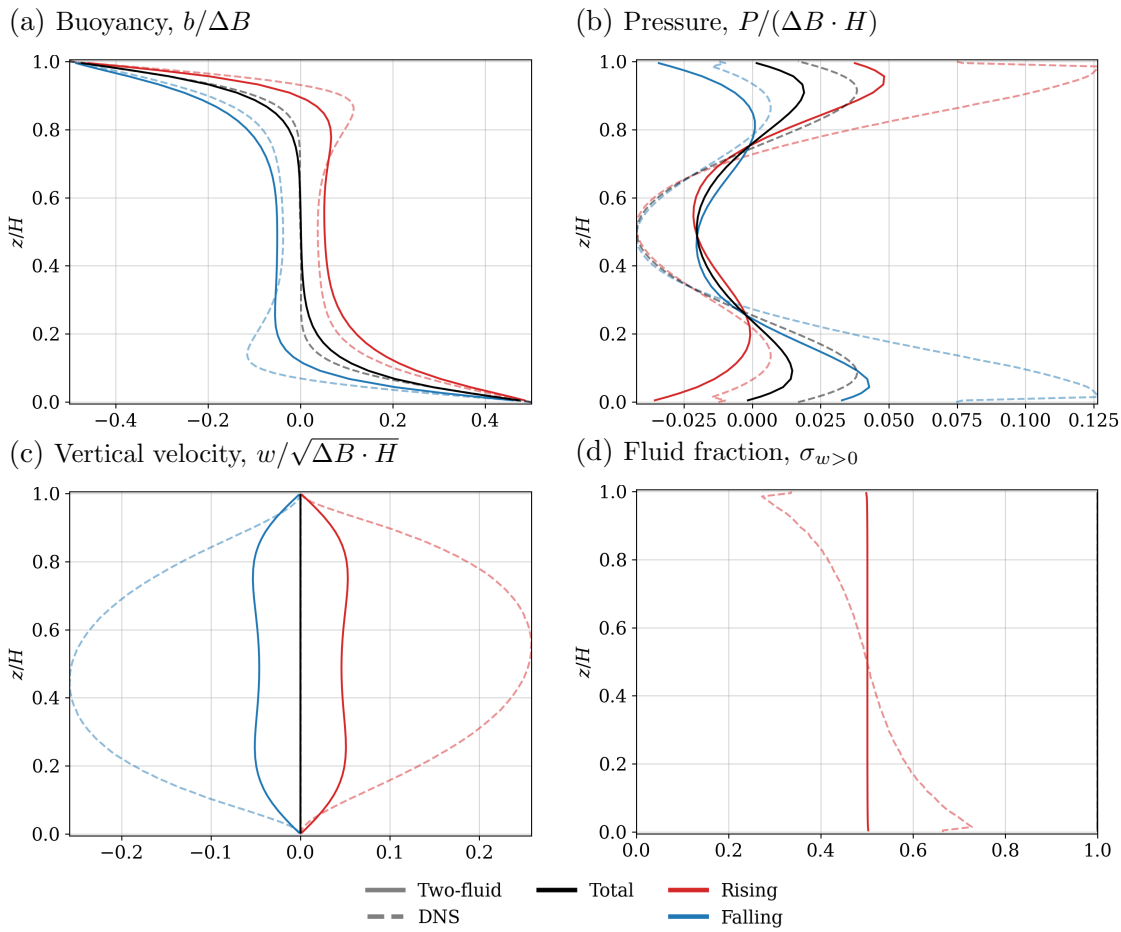

Figure 5.9: Horizontally-averaged profiles of $\mathrm{Ra} = 10^5$ RBC simulated with the two-fluid solver at a horizontal grid spacing of $\Delta x = 0.4H \approx 0.2\lambda_c$ in a domain of aspect ratio $\mathrm{AR} = 10$. Fields are shown at $t \approx 125T_e$. Conditionally horizontally- and time-averaged profiles from the DNS are shown for reference.

fluid DNS. Sharp discontinuities are observed in the profiles of buoyancy, pressure, and fluid fraction (Figure 5.11a,b,d), and nonzero mean vertical velocity is observed (c). Though these features do not actually cause a numerical instability during the period of integration, clearly they are undesirable.

The problems in the high resolution limit can be traced to incorrect limiting behaviour of the closures. The pressure parametrization has the correct limiting behaviour, since $\boldsymbol{\nabla}\cdot\mathbf{u}_i \to 0$ as $\Delta x/H \to 0$. However, the mass transfers proportional to $\boldsymbol{\nabla}\cdot\mathbf{u}_i$ do *not* have the correct limiting behaviour. In the high-resolution limit, we should require $\sigma_i \to I_i$, for consistency with our earlier definitions. This requires that all transfer terms map onto exactly what they should be in the high resolution limit, which may be difficult to achieve in practice.

The essential problem with the single-column closures in the high-resolution limit is that the closure for the vertical momentum transfer is correct at any resolution for fluid partitions based on the sign of the vertical velocity, whereas the divergence-based mass transfer tends to zero in the high-resolution limit. The result is that

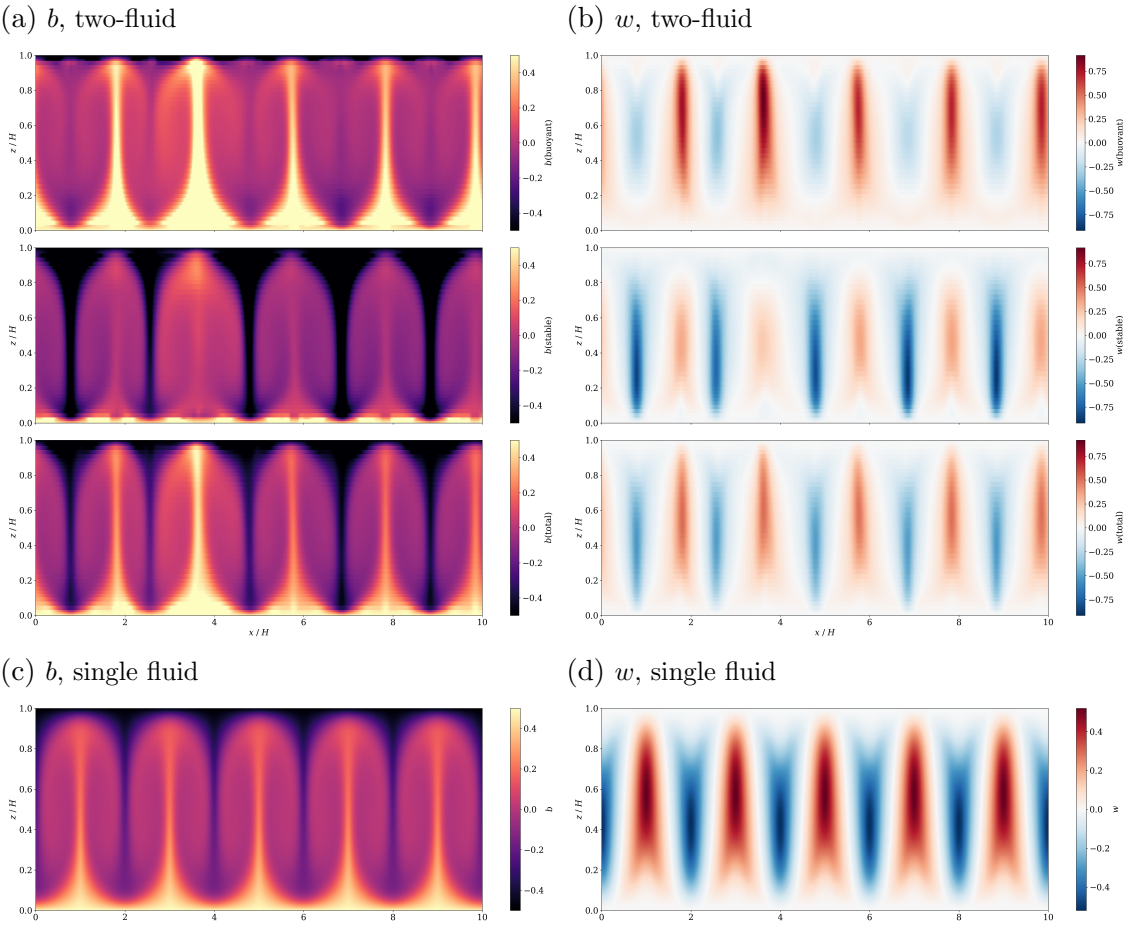

Figure 5.10: Buoyancy (left column) and vertical velocity (right column) fields for $\mathrm{Ra} = 10^5$ RBC at DNS resolution ($\Delta x < 0.028H$) for: the two fluid solver with single-column closures (a, b); and the unparametrized single-fluid solver (c, d). The two-fluid fields are arranged top to bottom as: rising, falling, total. Fields are shown at $t \approx 38T_\mathrm{e}$. Both simulations have reached a steady state, where no change in the circulation or global properties Nu, Re has been observed for $> 20T_\mathrm{e}$. The two fluids do not capture the correct sign of vertical velocity; the buoyancy field has become unbounded (there are large regions where $|b| > \Delta B/2$), and the maximum vertical velocity magnitudes are much greater than in the single-fluid DNS.

the two fluids partially decouple, allowing both signs of vertical velocity within a single partition, but gain an extra momentum source from the residual mass transfers. This is compounded by the buoyancy transfer – at high resolution, the buoyancy transferred from i to j should be equal to the buoyancy in fluid i at that location, but the single-column model transfers $b_{ij}^T = b_i \pm 0.5(-1)^i b_i$, giving a further source of buoyancy, and therefore also of momentum, in the two-fluid model. Running the highest-resolution simulation with transferred buoyancy equal to the mean (simulations not shown), $b_{ij}^T = b_i$, slightly reduces the magnitude of the problem — maximum buoyancies within each partition drop from $\approx 3.4\Delta B/2$ to $\approx 2.9\Delta B/2$ — but the crux of the problem cannot be fixed without changing the

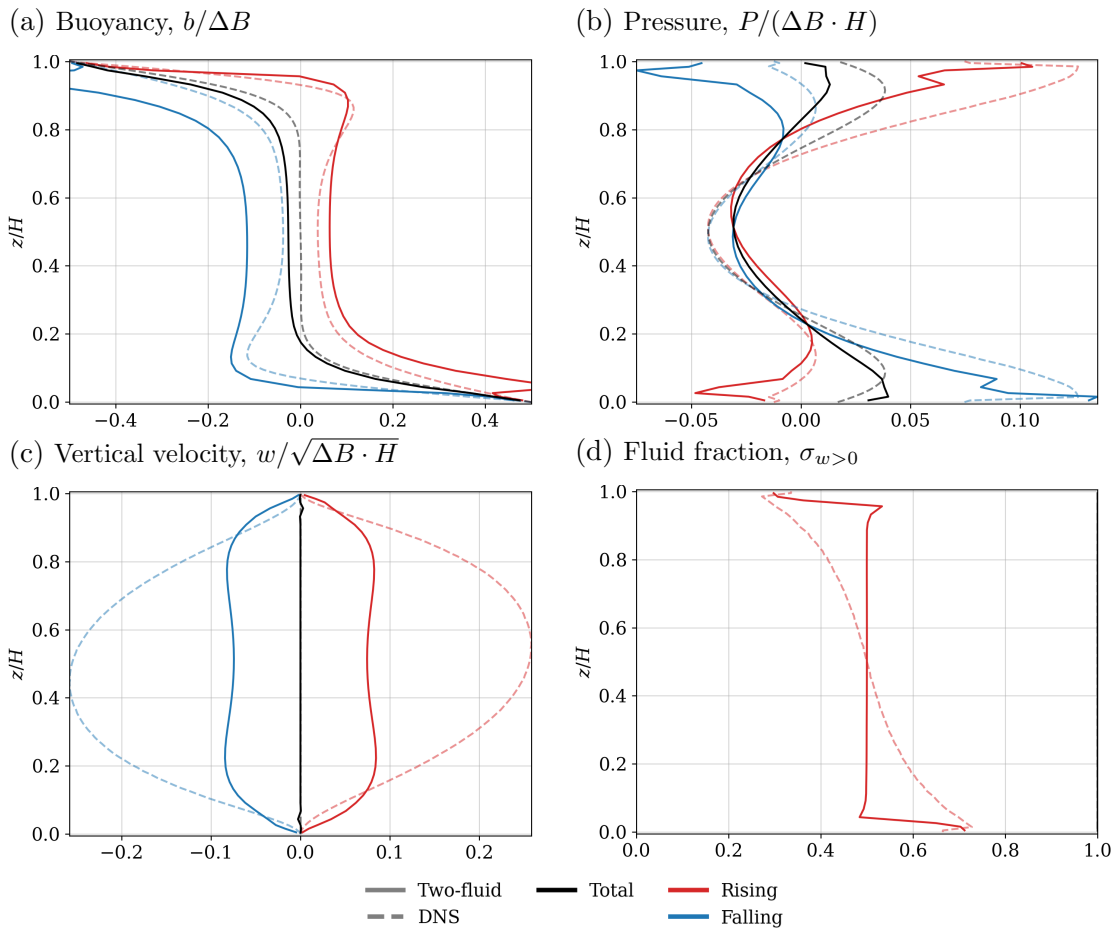

Figure 5.11: Horizontally-averaged profiles of $\mathrm{Ra} = 10^5$ RBC simulated with the two-fluid solver at a horizontal grid spacing of $\Delta x = 0.025H$ in a domain of aspect ratio $\mathrm{AR} = 10$. Fields are shown at $t \approx 38T_\mathrm{e}$. Conditionally horizontally- and time-averaged profiles from the DNS are shown for reference.

mass transfers.

In summary, directly using the single-column closures for the two-fluid equations in 2D achieves limited success in the grey zone of RBC, relative to the unparametrized singe-fluid simulations. Better prediction of the global heat transport is maintained for most of the range of resolutions, from fully parametrized to approaching the high resolution limit. Further, projection onto the grid is often delayed, and the range of resolutions over which grid projection is observed is slightly decreased. Sensitivity to the initial conditions is greatly reduced, since in all cases the single-column parametrizations allow convection to develop at approximately the correct time. We note however that this comparison is somewhat unfair, as even "explicit" convection parametrizations, often claimed to be running "without a convection parametrization", have some awareness of the grid scale (via the Smagorinsky eddy viscosity closure, or similar closures). An LES-type closure may therefore be expected to perform slightly better than the unparametrized single-fluid simulations, though the results should be qualitatively the same.

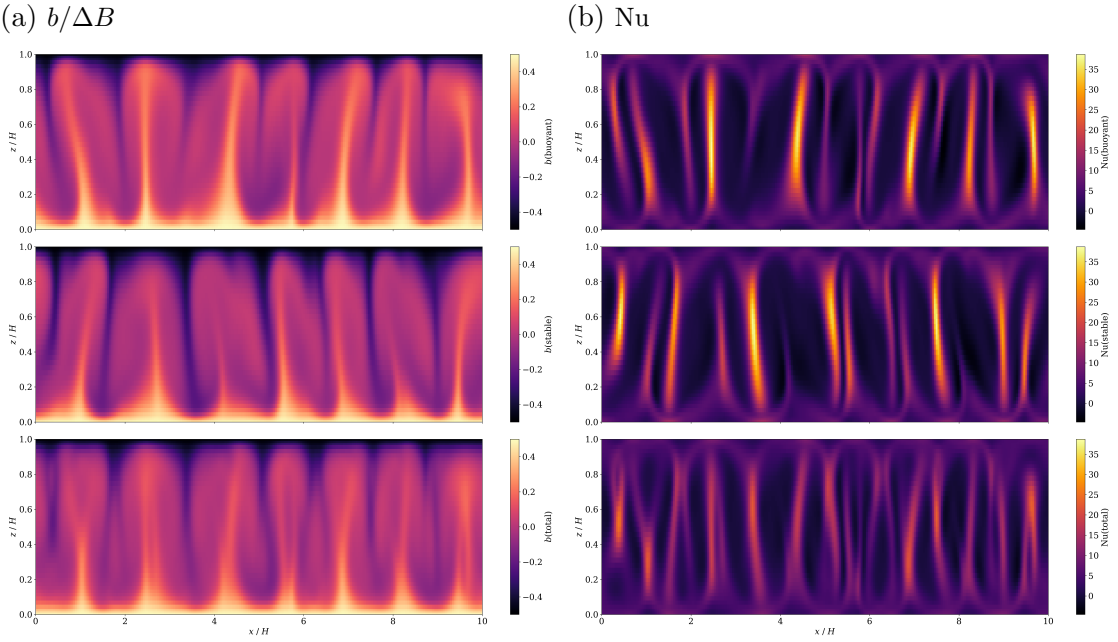

Figure 5.12: Buoyancy (a) and nondimensionalized vertical heat flux (b) fields for Ra $= 10^5$ RBC at approaching-DNS resolution ($\Delta x = 0.04H$) for the two fluid solver with single-column closures. The two-fluid fields are arranged top to bottom as: rising, falling, total. Fields are shown at $t \approx 25T_e$. The two fluids do not capture the correct sign of vertical velocity, and the two fluids have partially decoupled.

However, grid projection still occurs for over a decade of grid spacings, during which the model also produces incorrect global heat and momentum fluxes. Since grid projection is also the cause of multiple equilibria, these are also present within some two fluid simulations which exhibit grid projection. There are also some problems which are unique to a multi-fluid model: at all grid scales smaller than $\approx 10H = 5\lambda_c$, the chosen closures do not guarantee the correct labelling of fluids. This is most obvious in the highest-resolution limit: running a two-fluid model with the single-column closures at the same resolution as the single-fluid DNS yields a complete circulation in each partition. Since the transferred buoyancies and momenta are intended for use with transfers that ensure single-signed velocity in each partition, this eventually leads to unbounded buoyancies and a Nusselt number greater that the DNS by a factor of ≈ 1.4. The decoupling is most clearly seen in the solution for a slightly lower resolution: Figure 5.12 shows the buoyancy and nondimensionalized vertical heat flux in Ra $= 10^5$ RBC at a grid spacing $\Delta x = 0.04H$. In both fields it can be seen that the rising and falling fluids have separate circulations that are slightly out-of-phase with each other. When projected onto the mean field, this gives the appearance of more plumes.

Before moving on, it is worth briefly discussing results at Ra $= 10^8$. We do not include any figures, as the simulations behave qualitatively very similarly to those at

$\mathrm{Ra} = 10^5$ at all resolutions. Initiation is approximately correct, and approximately constant, across all resolutions; the simulations exhibit slightly more intermittency beginning at $\Delta x/H \approx 10$; and the single-column closures break down in the same way at higher resolutions — the two fluids partially decouple, and eventually the mass transfers cause the buoyancies to become unbounded. Importantly, the breakdown occurs at a grid spacing still too coarse to resolve the plumes. In the hard grey zone, similar behaviour is observed as in the single-fluid simulations of Chapter 3: a convective circulation develops with the incorrect length scale, $\lambda_\mathrm{c}^\mathrm{eff} > \lambda_\mathrm{c}$.

While at first this similarity seems surprising, it may be explained by considering the effective Reynolds number at a given filter scale. The grid spacing at which the single-column closures entirely break down is roughly $\Delta x \approx 0.05H$; assuming this is the effective Kolmogorov dissipation scale of the simulation gives an estimated maximum Reynolds number of ~ 50, which is of the same magnitude as the Reynolds number of the $\mathrm{Ra} = 10^5$ DNS (≈ 100). Therefore the simulated Reynolds number is far too low to be expected to exhibit any signs of turbulence. Given that the only Rayleigh number dependence of the parametrization is the weak dependence in γ, we should not expect large differences in grey zone response between the two Rayleigh numbers.

5.3 Discussion of grey-zone applicability of single-column closures

The closures used in the single-column formulation were unlikely to be scale-aware as presented, as there is no dependence on filter scale built into any of the parametrizations. Firstly, the parametrization for the perturbation pressure within each fluid relied on the assumption that the filter scale was greater than the distance between plumes; clearly this is not valid for all filter scales! This assumption was used to scale $\boldsymbol{\nabla}\cdot\mathbf{u}_i \sim (U/H)\widetilde{\boldsymbol{\nabla}}\cdot\tilde{\mathbf{u}}_i$; when the filter scale is smaller than $\sim H$, a more appropriate scaling is $\boldsymbol{\nabla}\cdot\mathbf{u}_i \sim (U/\ell_\mathrm{f})\widetilde{\boldsymbol{\nabla}}\cdot\tilde{\mathbf{u}}_i$, where ℓ_f is the filter length scale. This follows from considerations of $\langle\mathbf{u}\cdot\boldsymbol{\nabla}I_i\rangle$ and $\mathbf{u}_i^\mathrm{r}\cdot\boldsymbol{\nabla}\sigma_i$ at the interface between partitions. Following this through, one obtains instead the scaling:

$$\frac{\gamma}{\nu} = \hat{\gamma}_0 \frac{\min(\ell_\mathrm{f}, H)}{H}\,\mathrm{Ra}^{1/4}\,\mathrm{Pr}^{-1/4}\,. \tag{5.2}$$

Now we come across the problem that the scaling argument assumes that the main pressure contrast is between plume vs. bulk, but the $w = 0$ partition does not capture the plumes well. Therefore for $\ell_\mathrm{f} < H$ the scaling argument should break down for this choice of partition. For partitions which better pick out the coherent

structures, we may potentially extend the argument right down to the width of the plumes, δ, noting that as $\ell_\mathrm{f} \to \delta$, $\gamma/\nu \to \hat{\gamma_0}\,\mathrm{Ra}^{1/8}\,\mathrm{Pr}^{-1/8}$ — i.e. the predicted Rayleigh number dependence weakens.

A similar scale-dependence problem emerges for the closure chosen for the transferred buoyancy. As $\ell_\mathrm{f} \to 0$, we require $\varphi_{ij}^T \to \varphi_i$ — i.e. as the filter scale collapses, the transferred value is just equal to the resolved value in the vicinity of the interface. This is automatically satisfied for w_{ij}^T, since $w = 0$ at the interface and so as $\ell_\mathrm{f} \to 0$, $w_i \to 0$ at the interface. However this limit is *not* captured by the chosen transferred buoyancy closure. We can expect this to cause problems in the high resolution limit. A crude scale awareness can be incorporated by replacing $C \to \left(\frac{\min(\ell_\mathrm{f},H)}{H}\right) C$, such that the correct high resolution limit is obtained.

The biggest problem, however, is the chosen closure for the mass transfers, $S_{ij} = \max(-\boldsymbol{\nabla}\cdot\mathbf{u}_i, 0)$. Though this worked well in a single-column at capturing the dominant coherent overturning structures, an analysis of the indicator function evolution equation, Equation 3.41, shows emphatically that the divergence-based mass transfers are *incorrect* for partitions based on the sign of w:

$$\overline{\frac{\mathrm{D}I_i}{\mathrm{D}t}} = -\overline{\mathbf{V}_{\partial D_i}\cdot\boldsymbol{\nabla}I_i} + \overline{\mathbf{u}\cdot\boldsymbol{\nabla}I_i} \tag{5.3}$$

$$= -\overline{\mathbf{V}_{\partial D_i}\cdot\boldsymbol{\nabla}I_i} + \sigma_i\boldsymbol{\nabla}\cdot\mathbf{u}_i + \mathbf{u}_i\cdot\boldsymbol{\nabla}\sigma_i. \tag{5.4}$$

Therefore $S_{ij} \approx \boldsymbol{\nabla}\cdot\mathbf{u}_i$ requires both $\left|\overline{\mathbf{V}_{\partial D_i}\cdot\boldsymbol{\nabla}I_i}\right| \ll \left|\overline{\mathbf{u}\cdot\boldsymbol{\nabla}I_i}\right|$ and $|\mathbf{u}_i\cdot\boldsymbol{\nabla}\sigma_i| \ll \sigma_i\boldsymbol{\nabla}\cdot\mathbf{u}_i$. The first inequality requires that the location of the interface must move slowly in comparison to the (filtered) advection of fluid across the interface, i.e. that the location of the interface is approximately stationary. The second inequality requires that (fluid fraction times) the divergence of fluid within a partition is much greater than the *resolved* advection of the fluid fraction. Clearly neither of these inequalities hold — either in RBC or in real-world convection — once convection is partially resolved. However, the second inequality is not even necessarily true in the fully parametrized limit; for horizontally conditionally averaged RBC based on the sign of w, $\mathbf{u}_i\cdot\boldsymbol{\nabla}\sigma_i$ is not negligible close to the boundaries. Although w_i tends to zero in the viscous sublayer very close to the boundary, w_i is not negligible in the rest of the boundary layer, and $\partial\sigma_i/\partial z$ is large throughout the boundary layer.

5.4 Discussion and conclusions

We have shown that using a multi-fluid model of RBC with closures formulated for the fully-parametrized limit — i.e. the limit in which assumptions underlying traditional atmospheric convection parametrizations are valid — to simulate RBC

at grey zone resolutions encounters similar problems to running a single-fluid model with no parametrization (Chapter 2).

The formulation correctly captures convective initiation at all resolutions, from the resolved limit to fully parametrized. The formulation works reasonably well in the soft grey zone, although it does not capture any horizontal variability, whereas the true solution filtered and coarse-grained onto grid spacings in this range should show some variability (effectively due to aliasing of an incomplete number of circulations onto the grid).This is precisely the argument we made in Section 1.3.2 to motivate the introduction of stochastic terms in grey zone parametrizations. For this reason, we envisage finding physically-consistent stochastic description of the multi-fluid system vital to its potential success in the grey zone.

In the hard grey zone, the convective instability tends to project onto the grid scale, unrealistically enhancing the heat and momentum transports and producing almost decoupled falling and rising circulations. This is very similar to the observed behaviour of an unparametrized single fluid simulation in the hard grey zone. In the limit of high resolution, the two-fluid solver performs poorly, leading to vertical velocities roughly twice the magnitude of the DNS, unbounded buoyancies, and artificially enhanced vertical buoyancy transport.

The problems in the high resolution limit can be traced back to the mass transfer parametrization: $S_{ij} \propto -\boldsymbol{\nabla} \cdot \mathbf{u}_i$ is *incorrect* for partitions based on the sign of the vertical velocity. We also note that the projection onto the grid in the hard grey zone occurs concurrently with the identities of the two fluids ceasing to be correctly defined, i.e. when horizontal inhomogeneities occur, the current parametrizations can no longer maintain the correct sign of the vertical velocity. Given that this parametrization has the incorrect high resolution limit, and was already the source of some of the deficiencies in the single-column model of Chapter 4, better parametrizations of the mass transfers are required in order to properly test the grey zone behaviour of a two-fluid model of RBC.

One possible way forward would be to introduce two filter scales: the first at an LES scale to smooth out the worst of the (largely) isotropic turbulence, then another at a coarser scale to partition into multiple fluids; in a way this is what has been implicitly done by e.g. Tan et al. 2018. In this vein, the discontinuous indicator function could be generalized to be that of a "fuzzy set", as briefly discussed in Chapter 3. It may also be possible to restrict the possible choice of partitions by requiring that the high-resolution closures are sufficiently well-behaved.

Improvements could also arise from a partition that better selects the coherent structures, and from representation of within-fluid variability by consideration of higher moments of the flow. In particular, DNS data may be used to diagnose $S_{ij}, b_{ij}^T, \mathbf{u}_{ij}^T$ for various filter scales and fluid definitions. Possible closures could be in-

formed by direct analysis of the interactions between coherent structures, boundary layers, and homogeneous, isotropic bulk (Berghout et al. 2021; Togni et al. 2015).

The analysis of the indicator function evolution equation in Section 3.3 of Chapter 3 provides a route to discovering better parametrizations. For instance, when conditionally-filtering based on the sign of the vertical velocity, the indicator function for the rising partition may be written as $I_1 = \mathcal{H}(w)$, where $\mathcal{H}$ is the Heaviside step function. Then, using Equation (3.62), the fluid fraction transfers can be expressed as:

$$\sigma_0 S_{01} - \sigma_1 S_{10} = \int_{\partial D_1} g(\mathbf{x} - \mathbf{x'}, \ell_f) \frac{1}{|\boldsymbol{\nabla} w|} \frac{\mathrm{D}w}{\mathrm{D}t} \,\mathrm{d}(\partial D_1) \tag{5.5}$$

$$= \int_{\partial D_1} g(\mathbf{x} - \mathbf{x'}, \ell_f) \frac{1}{|\boldsymbol{\nabla} w|} \left(b - \frac{\partial P}{\partial z} + \nu \boldsymbol{\nabla}^2 w \right) \mathrm{d}(\partial D_1). \tag{5.6}$$

Beginning with this equation ensures that one can easily impose the correct limiting behaviours. It is unfortunately beyond the scope of this thesis to perform further analysis of this equation, but it is our firm belief that asymptotic analysis of results like Equation (3.62) should form the basis of future work on finding the correct transfer terms for multi-fluid convection parametrization.

Due to the complexity of the flow, and the difference of the unknown terms compared to those traditionally considered either in turbulence modelling or convection closure, multi-fluid modelling is an interesting candidate for "data-driven" closure discovery. Sparse Bayesian regression methods have recently been used to suggest closed-form equations for eddy Reynolds stresses and buoyancy fluxes in ocean mesoscale eddy parametrization (Zanna and Bolton 2020), and to suggest closures for Reynolds stresses in two-phase Reynolds-averaged modelling of disperse multi-phase flow, including partitioning of TKE between the phases (Beetham et al. 2021). Sound physical reasoning is still required by the modeller in order to select reasonable basis functions, and to interpret and validate the resulting closures. Such methods could be used to supplement the analytical and heuristic methods already used to suggest possible closures.

All of the above will develop fundamental understanding of the multi-fluid equations for convection. A thorough understanding of the dry convective grey zone, and of possible multi-fluid approaches to its parametrization, will help sharpen the questions for the much thornier problem of moist convection.

Chapter 6

Conclusions & outlook

Although it is an important part of the global climate system, contributing strongly to both global budgets and local variability, on time scales from hours to centuries, atmospheric convection is not currently well represented in NWP or climate models (e.g. Holloway et al. 2014; Stein et al. 2015; Stevens and Bony 2013). Weather and climate prediction at convection-resolving scales will not be possible for the foreseeable future (nor necessarily *desirable*, even in the long term), so the effects of convection on the scales that *are* resolved must be accounted for by a parametrization. A fundamental barrier to progress is the grey zone: a range of resolutions where coherent convection is neither fully resolved, nor fully sub-filter, meaning that neither traditional convective closures, nor traditional LES closures, can apply.

In this thesis, we have broadly followed two lines of investigation. Firstly, we have attempted to understand the convective grey zone by analysing the grey zone of the simplest convective system: Rayleigh-Bénard convection. Secondly, we have explored the usefulness of multi-fluid modelling for parametrizing turbulent convection, at both resolutions where convection is fully subfilter, and in the grey zone. Since it is not yet understood how best to represent convection with the multi-fluid equations, we chose to focus again on the simplest convective system to build understanding of how to apply the multi-fluid framework to convection modelling.

6.1 Summary of key results

Moist atmospheric convection is a complex problem, involving the dynamics of a turbulent buoyancy-forced fluid over a vast range of spatiotemporal scales, coupled with highly nonlinear first-order phase transitions, non-equilibrium microphysical processes, internal radiative forcing, complex surface exchanges, and an ever-changing large-scale environment which the convection responds and feeds back to. These interwoven complexities make it an exceptionally rich phenomenon, but also exceptionally hard to model. However, the grey zone is a concept which applies to

any nonlinear dynamical system. Therefore in Chapter 2 we chose to analyse the simplest setup that exhibits turbulent convection: dry Rayleigh-Bénard convection (RBC).

RBC consists of a Boussinesq fluid confined between two horizontal planes, each held at a fixed buoyancy. Buoyancy acts to destabilize the flow, while diffusion of momentum and buoyancy act to stabilize the flow. All of the dimensional parameters of the RBC problem can be reduced to a specification of the Rayleigh number (the ratio of buoyancy forcing to viscous diffusion) and the Prandtl number (the ratio of viscosity to buoyancy diffusivity). The stability of the system depends only on the Rayleigh number. The statistically stationary global response of the system, i.e. the kinetic and thermal dissipation rates, is a function only of these dimensionless numbers and a third dimensionless number, the Nusselt number, which is the ratio of the total heat flux through a horizontal layer to the heat flux in a hydrostatically balanced, no-flow reference state.

In Chapter 2 we began by running a suite of direct numerical simulations of fixed Prandtl number 2D RBC over a wide range of Rayleigh numbers, from an order of magnitude lower than the critical Rayleigh number through to fully developed convective turbulence. We showed these simulations to be in good agreement with previous theoretical, numerical, and experimental studies of RBC, allowing them to be used as reference "truth" simulations for the remainder of the thesis.

Our investigation of the grey zone of RBC began by simulating RBC at fixed Rayleigh and Prandtl numbers over a wide range of horizontal resolutions, from fully resolved through to so coarse that no convection takes place. We performed these suites of simulations at $\mathrm{Ra} = 10^5$, which is non-turbulent, and $\mathrm{Ra} = 10^8$, which is turbulent. The behaviour of the simulations in the grey zone of resolutions bears strong similarities to some of the errors observed in numerical weather prediction models run with explicit convection. In the grey zone (for resolutions $\gtrsim H$, or grid spacings $\gtrsim 0.2H$), the convective circulation tends to project strongly onto the grid. This is different from the (expected) *aliasing* onto the grid observed when projecting a filtered, horizontally non-uniform flow onto a grid which resolves the filter scale. This collapsing of the convection onto the smallest available scale is similar to the phenomenon of grid point storms observed in NWP. In both 2D RBC and the convective NWP grey zones, the grey zone simulations have a tendency to initiate convection later, and produce stronger heat fluxes, than the reference truth. This is due to the projection onto the grid, noted by B. Zhou et al. (2014) qualitatively as akin to when the grid scale in Rayleigh-Bénard convection can no longer resolve the length scale of the most unstable convective mode. We quantitatively confirm this for RBC, showing that global statistics such as the Nusselt number and Reynolds number are within 10% of their DNS values for grid spacings

$\sim 0.1\lambda_c \approx 0.2H$ and smaller. This is also consistent with work on cloud-resolving models in the meteorological literature: for instance, Petch et al. (2002) found that grid spacings $\leq 0.25H$ (for $H \sim$ the sub-cloud layer depth) were required to provide adequate representation of fluxes from the sub-cloud layer for cloud-resolving models of both shallow and deep convection. These results show that RBC is a useful testbed for understanding the convective grey zone, which should be used more widely in the meteorological community: although RBC is much simpler than real atmospheric convection, it possesses similar grey zone behaviour. The simplicity, as well as the wealth of available theoretical and experimental results, can and should be exploited to understand the grey zone, and to develop parametrizations which are scale aware and tame the instabilities and strong grid-projection, without the confounding complexities of real-world convection.

In Chapter 3 we introduced the multi-fluid approach to convection parametrization. The original derivations of multi-fluid equation sets for atmospheric convection (e.g. Thuburn et al. 2018; Yano 2014) were motivated by extending the mass flux concept of splitting the flow into convecting and environmental parts (e.g. Arakawa and Schubert 1974). Though the resulting equations sets bear a strong resemblance to those used in the modelling of multi-phase engineering flows, the interpretation and intended use of the multiple fluids are closer to the ideas of conditioned averaging for intermittent turbulent flows (Dopazo 1977) and to pick out coherent structures in turbulent flows (Hussain 1983, 1986).

Chapter 3 attempts to say as much as possible about the closures required for the multi-fluid equation set without considering specific partitions or second (or higher) moments. First we derived the viscous multi-fluid equation set via conditional filtering, a simple extension of the work of Thuburn et al. (2018) for the inviscid compressible Euler equations. The viscous terms are vital for RBC, and also should be included for fluid partitions based on data from LES or observations of the real atmosphere. Though Reynolds numbers are high enough in convection for molecular viscosity and diffusivity to be negligible, the *eddy* viscosities of an LES or diagnosed from observations are not necessarily negligible, and therefore the extra viscous terms should be included in a multi-fluid formulation.

The remainder of Chapter 3 explored the consequences of explicitly considering the exact source and sink terms for the indicator function of a fluid partition. First a correspondence was derived between the representation of the fluid fraction exchanges in terms of entrainment and detrainment, as is used in convection parametrizations, and in terms of the motion of the interface between fluid partitions, which is sometimes used in engineering multi-phase models. Though expressions relating entrainment and detrainment rates to the motion of fluid across the boundary of a convective element have been used before, especially in studies

attempting to diagnose cumulus entrainment and detrainment coefficients, this is — to our knowledge — the first formal derivation applicable to the case of general conditional spatial filtering. This apparatus is necessary for formulating the correspondence in the grey zone.

A third possible rewriting of the exchange terms was then derived, using the representation of an indicator function as a (product of) step functions. When the step function is on a flow variable — for instance the vertical velocity, or the buoyancy flux — the fluid fraction exchanges can be written in terms of the Lagrangian evolution equation for that flow variable. We recommend this new insight as a possible route to directly linking closures for the multi-fluid equations to mathematically-founded physical insight, rather than the fairly ad-hoc way in which closures have so far been suggested.

We then presented an in-depth discussion of all the terms requiring closure in the viscous Boussinesq multi-fluid equations, using exact results for the derivatives of the indicator function to provide geometric representations of the terms. A key result showed that, because the divergence of the velocity within a fluid partition is not generally zero (due to subfilter fluid relabelling), there is an extra contribution to the viscous terms which has been missed in previous studies where diffusion has been added post-hoc. We then showed that, if the within-partition stress tensors are modelled directly, choosing them to be Newtonian introduces an additional bulk viscous stress. As the resolved divergence is the difference between the resolved motion of fluid across the partition interface and the resolved advection of the resolved fluid fraction, the interpretation of bulk viscous stress is that the resolved *pressure* within a fluid partition must generally increase when fluid is relabelled into that partition (at fixed fluid fraction). Therefore the bulk viscous stress is suggested as a parametrization for (part of) the pressure difference between fluid partitions. This pressure difference is purely a consequence of the fluid relabelling.

Finally, the utility of the results for the exchange terms was shown by explicitly conditionally filtering the first normal mode of Rayleigh-Bénard convection.

In Chapter 4 we constructed and tested a two-fluid single-column model of Rayleigh-Bénard convection, intended as a proof-of-principle for multi-fluid modelling of turbulent convection. This began by choosing what the partitions represent[1]: a simple split into rising and falling fluids was chosen in order to capture the leading-order overturning circulation. No further representation of subfilter variability was included beyond the partition into two fluids except in the exchange

[1]This "partition-first" approach is fundamentally different to the approach taken by others working on mass-flux convection parametrization and its extensions (e.g. Arakawa et al. 2011; Tan et al. 2018; Yano 2014), where an explicit partition is rarely made. This leads to a disconnect between the theory behind the parametrizations, and the evaluation of the parametrizations against models and observations, which requires a choice of partition.

terms, consistent with the "top-hat" approximation usually employed in mass-flux parametrization (Gu et al. 2020).

Simple closures for all terms were provided based on the analysis of Chapter 3 and previous work on multi-fluid convection modelling. Fluid fraction transfers were taken to be proportional to convergence within a partition, while the transferred vertical velocity was forced to be zero due to the fluid definitions. The transferred buoyancy was chosen to be equal to the mean buoyancy within a partition, plus or minus a constant times the magnitude of the mean, as a crude first approximation of the subfilter buoyancy distribution. The pressure differences between the partitions were modelled as a bulk viscous stress, as suggested in Chapter 3. A scaling argument for the variation of the bulk viscosity with the Rayleigh number was presented, reducing the parametrization to the specification of two $\mathcal{O}(1)$ constants: C for the transferred buoyancy, and $\hat{\gamma}_0$ for the perturbation pressure. It is worth noting that, although single-column, the model is fully prognostic and has no limits on the fluid fraction beyond the constraints imposed by the initialization.

We then evaluated the single-column two-fluid parametrization by comparing the results of the single-column model to conditionally horizontally filtered DNS results. We showed that $\mathcal{O}(1)$ values of the two closure constants gave good agreement between the modelled profiles of pressure, buoyancy, and vertical velocity, and those of the DNS. The key result of this chapter is that, after fixing the magnitude of $\hat{\gamma}_0$ by measuring the value which gave the correct Nusselt number at one Rayleigh number, the correct scaling of both the Nusselt and Reynolds numbers with Ra was observed over six decades of Ra. In addition, approximately the correct transitional behaviour was observed in the vicinity of the critical Rayleigh number, and the two-fluid model shows similar initial transient behaviour to the horizontally-averaged DNS while spinning up to the equilibrium state across all Rayleigh numbers.

Some deficiencies of the model were noted; for instance, although the scaling of both Nu and Re was correct, the model could not simultaneously predict the correct magnitudes of both. The correct magnitude of Nu corresponded to the most accurate buoyancy profiles and the right magnitude of the pressure perturbation close to the boundaries, while the correct magnitude of Re corresponded to the most accurate mean pressure profile (as well as, trivially, the most accurate vertical velocity profiles). Neither could correctly capture the pressure differences between the fluids in the centre of the domain. This suggests that the scaling argument for the bulk viscosity is most applicable in the transitional and boundary regions, and that a model with a height-varying bulk viscosity may be able to correctly reproduce the magnitudes of Nu and Re as well as their scaling with Ra.

A bigger deficiency of the two-fluid single-column model is the divergence-based fluid fraction transfer. While this has good stability properties, and is correct for the

first normal mode of RBC, it fails to reproduce the variation of fluid fraction with height, especially once areas of recirculation develop in the plume separation regions ($\mathrm{Ra} \gtrsim 10^7$). The recirculation regions change the sign of the vertical gradient of fluid fraction close to the boundaries compared with the prediction of the single-column model, as well as introducing kinks in the profiles of within-fluid buoyancy, vertical velocity, and pressure.

Despite this, the two-fluid single-column model performs excellently given its simplicity. This is the first time that a single multi-fluid parametrization has been tested over a wide range of convective forcings, and the first time a two-fluid model with fluids defined by the sign of vertical velocity has been used to model fully turbulent convection. That the correct profile shapes, and the correct scalings of the global heat and momentum transports, are produced by the model, as well as the correct transient behaviour, suggest that even a simple two-fluid model of convection can accurately reproduce the statistics of RBC by directly providing a low-order description of the dominant coherent overturning circulation.

Chapter 5 presented a preliminary exploration of multi-fluid modelling in the grey zone of RBC. To do this, we used the closures from the single-column model of RBC developed in Chapter 4 in 2D two-fluid simulations of RBC for a range of horizontal resolutions spanning the grey zone. The only additional closure required was for the transferred horizontal velocity, which we chose to be equal to the mean within-partition horizontal velocity for simplicity. Results were compared with the single-fluid grey zone simulations of Chapter 2.

The two-fluid model with single-column closures performed well over relatively short times (up to ~ 25 eddy turnover times, T_e, or ≈ 8 hours in the context of the CBL) when compared to the unparametrized single-fluid results. An especially promising result is that there was no change in the time to initiation of convection across all resolutions for the two-fluid model, whereas the single-fluid model showed a delay of $\approx 10\%$ by grid spacings $\gtrsim 0.4H$, and a delay of $\approx 100\%$ by grid spacings $\gtrsim 1.2H$. This is because the two-fluid model can "resolve" convection within each fluid at *any* resolution, so there is no delay associated with coarsening the resolution. The model also performs well in the soft grey zone in terms of reproducing the correct profiles and global mean heat and momentum transports; after $\approx 25T_\mathrm{e}$, for grid spacings $\gtrsim 4H$, the observed Nusselt and Reynolds numbers, as well as the horizontal-mean profiles of buoyancy, pressure, and vertical velocity, are identical to the single-column model. At a time of $\approx 250T_\mathrm{e}$, the same is true but only for grid spacings $\gtrsim 10H$; this is the fully parametrized regime.

For grid spacings $0.5H \lesssim \Delta x \lesssim 10H$, by $\approx 250T_\mathrm{e}$ an unrealistic resolved circulation was observed in the mean fluid at the grid scale, producing artificially enhanced heat and momentum transports, incorrect variation of fields in the horizontal, and

incorrect vertical profiles of flow variables. This is very similar to the behaviour observed in the single-fluid grey zone simulations: the convective instability projects onto the smallest available scale, which is the grid scale. Although the two-fluid model initially spins up to the correct horizontally-averaged profiles across all grey zone resolutions, this does not appear to systematically delay the unrealistic grid projection compared to the single-fluid simulations. Further, all grey zone two-fluid simulations eventually allowed both signs of vertical velocity within a single partitions, showing that the chosen exchange terms are incorrect for fluids defined by the sign of the vertical velocity.

In the high-resolution limit, the two-fluid model does not tend to the DNS results because the closures used for the exchange terms do not possess the correct high resolution limits. Potential modifications to the transfers of buoyancy, and to the bulk viscous pressure, which do possess the correct high resolution limits were suggested but not tested. Fluid fraction transfers based on divergence were shown to be fundamentally incompatible in the high resolution limit with fluid partitions based on the sign of the vertical velocity. This reinforces the conclusion of Chapter 4 that better representations of the fluid fraction transfers are essential in order to accurately represent the physics of convection with a multi-fluid model.

6.2 Conclusions, and questions for future research

6.2.1 The grey zone, and Rayleigh-Bénard convection as a simplified model of atmospheric convection

In Chapter 2 we showed that Rayleigh-Bénard convection exhibits strikingly similar grey zone behaviour to that observed in the dry CBL and in the sub-cloud layer of both shallow and deep moist convection. We also showed some qualitative similarities between the grey zone behaviour and observed NWP grey zone behaviour for moist convection. This led us to conclude that RBC is a useful simple testbed for exploring the convective grey zone, and one that has so far been under-utilized.

There are several obvious directions for future research. Firstly, the work of Chapter 2 suggests the question: how far can the analogy between RBC and atmospheric convection be taken? RBC is often dismissed as irrelevant to real world convection (e.g. Vallis et al. 2019, §1, p. 162; Thuburn and Efstathiou 2020, §1, p. 1536). But there is no good evidence that the *local* dynamics of dry or unsaturated convection should differ between RBC and more complex cases. In addition, 3D DNS of turbulent RBC qualitatively looks remarkably similar to 3D LES of the dry CBL (Mellado 2012; also Peter Clark and Georgios Efstathiou, pers. comm.). Do the dissipation rates in the plumes and the bulk scale in the same way in RBC

and in the dry CBL? Do the plumes, bulk, and boundary layers interact in the same manner? This latter question is of vital and direct importance to modelling of the exchange and pressure perturbation terms in multi-fluid modelling, and of modelling terms such as the pressure transport terms in multi-moment modelling. It would benefit the atmospheric convection modelling community to know the quantitative limits of these correspondences, especially in light of new results on extended RBC with rough boundaries, or with radiative forcing.

Secondly, further studies of the grey zone of RBC are required. The analysis of Chapter 2 almost entirely focused on global properties of the solutions, such as the Nusselt and Reynolds numbers, time to convection initiation, and horizontal profiles; only qualitative descriptions of local properties (such as grid projection and implied length scales) were provided. We also only considered first-order quantities, rather than higher-order statistics. Future work on the grey zone of RBC should analyse in detail the higher-order statistics of RBC for filter scales from fully resolved convection to fully-subfilter convection, comparing with numerical solutions at the same implied resolution. Analysis of spatial and temporal correlation functions should also be carried out, in order to determine the expected level of intermittency for a given resolution. Analysis of the budget equations for kinetic energy and scalar covariances at various filter scales will provide insight into how to model the subfilter processes at different filter scales throughout the grey zone. In particular, evidence has been found in RBC of regions of inverse scale energy transfer — i.e. transfer of energy from small scales to large scales — associated with the plume separation and impingement regions (Togni et al. 2015). This suggests that for some range of filter scales, the subfilter flow could provide a net energy source for the resolved vertical motion, associated with the formation of the coherent structures. Similar conjectures have been made for the existence of a "reverse cascade" in atmospheric convection (e.g. Zilitinkevich et al. 1998, 2021). Scale-by-scale analysis of turbulent RBC in both 2D and 3D is required to verify or falsify these conjectures.

Thirdly, it is important to establish how the stability criteria for convection depend on the grid, and how the correct implied length scales can be maintained throughout all resolutions. B. Zhou et al. (2014) showed that, for grid spacings $> \lambda_c/2$, convection must develop at the grid scale if the critical Rayleigh number is exceeded at the grid scale, based on the standard RBC linear stability analysis. How do subgrid models alter the stability analysis? Suppressing this instability at the grid scale by providing better representations of subfilter transport is essential to the representation of convection in the grey zone. This may hinge on correct understanding of the *nonlinear* stability criteria; for fully-resolved RBC, the linear and nonlinear stability criteria are identical. Do they decouple as the resolution decreases? If so, this would potentially allow grid-scale circulations to develop even

when the flow is linearly stable to convection. This is of even greater relevance to extensions to moist convection, where the linear and nonlinear stability criteria are not the same, although unfortunately the general stability criteria for moist convection are not known. A starting point would be to derive nonlinear stability criteria for some of the simple moist extensions of RBC, for instance the precipitating model of Vallis et al. (2019) or the non-precipitating model of Pauluis and Schumacher (2010).

6.2.2 Multi-fluid modelling of convection

In Chapter 4, we showed that a simple two-fluid single-column model can accurately reproduce global heat and momentum transports in RBC across 6 orders of magnitude of buoyancy forcing, as well as reproducing qualitatively correct profiles of buoyancy, pressure, and vertical velocity. In Chapter 5, we used the same closures to simulate RBC in two dimensions at horizontal resolutions spanning from the fully-parametrized to fully-resolved limits. The closures were found to work well in the fully-parametrized limit, and were partially successful in the soft grey zone for times up to ≈ 25 eddy turnover times, as well as initiating convection at the correct time across all resolutions. However, the same grid projection was observed as in the case of unparametrized single-fluid simulations, showing that much further work is needed to create scale-aware multi-fluid parametrizations.

Some of the required work involves numerical considerations; for this, the concluding chapter of McIntyre (2020) provides an excellent overview. We therefore focus on the physical modelling issues.

We identified the principal weakness in the two-fluid model of Chapters 4-5 to be the closures for the fluid fraction transfers, which are incompatible with the chosen fluid definitions at high resolution. This raises two obvious avenues for investigation: the first is to find fluid fraction transfers which correspond to the chosen fluid definitions. The results of Chapter 3 will prove vital for this, both for diagnosing transfers (including those of buoyancy and momentum) from data, as well as providing exact integral expressions for the transfers which should be amenable to asymptotic analysis.

The second suggested line of inquiry is to find fluid definitions which better pick out the coherent structures of convection. Within the atmospheric convection literature the coherent structures of convection are often diagnosed via threshhold methods, for instance classifying as "updrafts" all regions with vertical velocities above some chosen threshold. Other techniques include partitioning based on concentrations of auxiliary tracer fields, either by threshold or by an optimization procedure (Efstathiou et al. 2020). For Rayleigh-Bénard convection, on the other hand, coher-

ent structures are often diagnosed by the heat flux or the thermal dissipation, since exact results and scaling theories for these quantities can be used to provide thresholds. Partitions based on, for instance, local heat flux criteria, should be compared to the nonlocal optimization-based partition of Efstathiou et al. (2020), as well as auxiliary tracer-based partitions, to see how well the different definitions correspond. The advantage of local methods such as those used for RBC is that the material derivative of the indicator function can be rewritten in terms of an integral over the partition interface of the evolution equation for a flow variable (Chapter 3). The resulting integral expressions could then be approximated using asymptotic methods to provide analytically-based expressions for closures for the multi-fluid exchange terms, as well as all other terms requiring closure in a multi-fluid model.

Expanding to other potential fluid definitions immediately suggests the question: is the optimal fluid partition for dry convection the same as the optimal partition for moist convection? And do the optimal partitions for shallow and deep convection differ? If so, what *local* partitions are implied by different nonlocal optimal partitions? And how should a multi-fluid model handle the transition between different implied partitions?

In order to develop a multi-fluid model which works well in the grey zone of convection, it will be necessary to draw on the previously suggested grey zone RBC research. Especially relevant will be the scale-by-scale budgets at different filter scales; since the multi-fluid method attempts to directly model the coherent structures of convection, correctly capturing the energy transferred to the coherent structures at different filter scales is vital for success. Analysis of multi-fluid second-moment equations will also be important, to understand how best to model the subfilter variability within partitions. The so-called top hat approximation is known to be poor within traditional mass flux schemes; in a multi-fluid scheme, is the inclusion of subfilter variability within the exchange terms enough, or is other accounting of subfilter variability required (e.g. within-partition Reynolds stress and subfilter buoyancy flux)? If representation of other subfilter variability is required, we must ask whether the assumptions underlying traditional multi-moment modelling (for instance, the Mellor-Yamada hierarchy introduced in Mellor and Yamada 1974) are valid within individual partitions. Even at first-order closure level, one might not expect isotropic closures to hold within-partition: buoyant plumes vary significantly faster across-plume than along plume.

A more practical question is: what is the best trade-off between moments and fluids? Both in terms of: how many fluid partitions is the optimal number, as well as: do multi-fluid schemes perform better than multi-moment schemes for a similar computational cost? In order to answer those questions, more work must be done to understand the correspondence between multi-fluid and multi-moment modelling.

Various authors have derived links between mass-flux closures and traditional turbulence modelling (e.g. Grant 2006a), and complete second-order equations have been derived within the multi-fluid framework (both by this author, and by John Thuburn — pers. comm.). However no work to date has been done analytically linking the standard spatially-filtered second-order equations to the multi-fluid equations. How might this be useful? Well, given a (potentially complex) multi-fluid model of turbulent convection, what are the implied closures for, for instance, the transport of turbulent kinetic energy by pressure, one of the least well-understood terms in the second-order turbulence equations? Even if a multi-fluid scheme proves computationally expensive, or too hard to integrate into a dynamical core, the insights from multi-fluid modelling — which *directly* models the coherent structures of convection — can be used to provide insight into how to better model higher moments in flows where coherent structures are dynamically important. In this regard, the multi-fluid framework should be seen as a useful research tool for the convection community in the years ahead.

6.3 Concluding remarks

This thesis has presented multi-fluid modelling not as a radically new approach to modelling convection, but rather as a natural outcome of viewing the traditional mass flux approach as an attempt to recognize the importance of coherent structures in convective turbulence. A conditionally-filtered representation makes perfect sense as a way of providing a low-order description of a turbulent flow with coherent structures. The natural consequence of this broader view is extending to time-dependent, 3D flows, with non-small fluid fractions. We show that the time dependent extension of mass flux with non-vanishing area produces interesting and promising results even in 1D: applying the simplest version of this framework — a two fluid model with no sub-filter variability — to horizontally-averaged Rayleigh-Bénard convection correctly captures the global equilibrium features of convection, providing proof-of-principle for the method. Even more promising is the fact that the same model also captures approximately correct spin-up behaviour.

We have also shown that the grey zone is a significant challenge even in the simplest convection problem, advocating the use of RBC as an arena for understanding the grey zone without the confounding complexities of real-world convection. Simulating RBC in the grey zone with a simple two-fluid model had limited success, due to the lack of understanding of how to parametrize the exchange terms. However, this thesis also provided theoretical results which we hope will serve as the basis for systematically improving understanding of the terms requiring closure in a

multi-fluid model.

Finally, we remark that while multi-fluid modelling of convection is promising and exciting in its own right, there is also ample opportunity for cross-fertilization between the traditional convection modelling, multi-moment modelling, and multi-fluid modelling communities. Such cooperation has the potential to significantly advance the understanding of convection and its representation in weather and climate models.

Appendices

Appendix A

Derivations of standard results in Rayleigh-Bénard convection

A.1 Exact integral results

In this section we collect several exact results for the Nusselt number, Nu. We begin by restating the Boussinesq equations from Chapter 2:

$$\frac{\mathrm{D}\mathbf{u}}{\mathrm{D}t} = b\mathbf{k} - \boldsymbol{\nabla} P + \nu \boldsymbol{\nabla}^2 \mathbf{u}, \tag{2.4}$$

$$\frac{\mathrm{D}b}{\mathrm{D}t} = \kappa \boldsymbol{\nabla}^2 b, \tag{2.5}$$

$$\boldsymbol{\nabla} \cdot \mathbf{u} = 0. \tag{2.6}$$

These equations are solved on a domain $D \subset \mathbb{R}^d$ possessing two non-intersecting boundaries (labelled "top" and "bottom") with normal vectors parallel to $\mathbf{k}$, a fixed distance H apart. The lateral boundaries satisfy $\mathbf{dS} \cdot \mathbf{k} = 0$, where $\mathbf{dS} = \hat{\mathbf{n}}\,\mathrm{d}S$ is the boundary surface element, and we choose the convention that the boundary normal $\hat{\mathbf{n}}$ always points into the domain D. We work with the dimensional equations to facilitate later comparison between different nondimensionalization choices; see Section A.2 for a discussion of the common nondimensionalizations.

Conditions on the velocity at the top and bottom boundaries are no normal flow,

$$\mathbf{u}_\perp \coloneqq (\mathbf{u} \cdot \hat{\mathbf{n}})\hat{\mathbf{n}} = \mathbf{0}; \tag{A.1}$$

along with either no slip,

$$\mathbf{u}_\parallel \coloneqq \mathbf{u} - \mathbf{u}_\perp = \mathbf{0}, \tag{A.2}$$

or free-slip,

$$\hat{\mathbf{n}} \cdot \boldsymbol{\nabla} \mathbf{u}_\parallel = \mathbf{0}. \tag{A.3}$$

Here $\mathbf{u}_\perp$ is the velocity normal to the boundary, while $\mathbf{u}_\parallel$ is the velocity tangential

to the boundary.

Conditions on the buoyancy are either constant buoyancy,

$$b(z=0) = b_B, \quad b(z=H) = b_T, \tag{A.4}$$

or constant buoyancy flux,

$$\hat{\mathbf{n}} \cdot \boldsymbol{\nabla} b\big|_{z=0,H} = -\beta. \tag{A.5}$$

Conditions at the lateral boundaries are either a) free-slip or no slip velocity, with adiabatic buoyancy conditions ($\boldsymbol{\nabla} b \cdot \hat{\mathbf{n}} = 0$); or b) periodic in all fields.

We define the Nusselt number most generally as the ratio of the volume- and time-averaged vertical buoyancy flux to the volume- and time-averaged purely diffusive vertical buoyancy flux. From (2.5) above, the full buoyancy flux is $\mathbf{j} \coloneqq \mathbf{u}b - \kappa\boldsymbol{\nabla} b$; the convective part is $\mathbf{j}_\mathrm{c} \coloneqq \mathbf{u}b$, and the diffusive part is $\mathbf{j}_\mathrm{d} \coloneqq -\kappa\boldsymbol{\nabla} b$. Thus the Nusselt number is defined as:

$$\begin{aligned}
\mathrm{Nu} &\coloneqq \frac{\langle \mathbf{j}\cdot\mathbf{k}\rangle_{V,T}}{\langle \mathbf{j}_\mathrm{d}\cdot\mathbf{k}\rangle_{V,T}} && \text{(A.6)}\\
&= \frac{\left\langle wb - \kappa\frac{\partial b}{\partial z}\right\rangle_{V,T}}{\left\langle -\kappa\frac{\partial b}{\partial z}\right\rangle_{V,T}} && \text{(A.7)}\\
&= 1 + \frac{\langle wb\rangle_{V,T}}{\left\langle -\kappa\frac{\partial b}{\partial z}\right\rangle_{V,T}} && \text{(A.8)}\\
&= 1 + \frac{\langle wb\rangle_{V,T}}{-\kappa\left((1/H)\left\langle b(z=z_\mathrm{T})\right\rangle_{A,T} - (1/H)\left\langle b(z=z_\mathrm{B})\right\rangle_{A,T}\right)} && \text{(A.9)}\\
&= 1 + \frac{\langle wb\rangle_{V,T}}{\kappa\Delta B/H} && \text{(A.10)}
\end{aligned}$$

In going from the third-last to the second-last line, we have used that $\int_{z_\mathrm{B}}^{z_\mathrm{T}} \hat{\mathbf{z}}\cdot\boldsymbol{\nabla} b\,\mathrm{d}z = b(z_\mathrm{T}) - b(z_\mathrm{B})$ (true even if x, y, z are not Cartesian coordinates). Perhaps interestingly, the volume-integrated diffusive buoyancy flux is always precisely equal to what it would be if the velocity field was uniformly zero.

To find our exact integral relations, first we volume-average the buoyancy equation (2.5):

$$\begin{aligned}
&\left\langle \frac{\partial b}{\partial t}\right\rangle_V + \left\langle \boldsymbol{\nabla}\cdot(\mathbf{u}b - \kappa\boldsymbol{\nabla} b)\right\rangle_V = 0 && \text{(A.11)}\\
\implies &\frac{\mathrm{d}}{\mathrm{d}t}\langle b\rangle_V + \frac{1}{H}\langle \mathbf{u}b - \kappa\boldsymbol{\nabla} b\rangle_{\partial V} = 0 \quad \text{(divergence theorem).} && \text{(A.12)}
\end{aligned}$$

We can split the integral over the boundary into the integral over the lateral boundaries plus the integral over the top and bottom boundaries. Over the lateral bound-

aries, $\int_S (\mathbf{u}b - \kappa\boldsymbol{\nabla}b)\cdot\mathbf{dS}$ is clearly zero for either periodic boundaries or a domain with infinite horizontal extent. For rigid insulating boundaries, $\mathbf{u}\cdot\mathbf{dS} = 0$ and $\boldsymbol{\nabla}b\cdot\mathbf{dS} = 0$. Therefore for all of the usual RBC lateral boundary conditions, $\langle\boldsymbol{\nabla}\cdot(\mathbf{u}b - \kappa\boldsymbol{\nabla}b)\rangle_V = (1/H)\langle(\mathbf{u}b - \kappa\boldsymbol{\nabla}b)\cdot\hat{\mathbf{n}}_\mathrm{T}\rangle_{A;z=z_\mathrm{T}} + (1/H)\langle(\mathbf{u}b - \kappa\boldsymbol{\nabla}b)\cdot\hat{\mathbf{n}}_\mathrm{B}\rangle_{A;z=z_\mathrm{B}}$. For both no-slip and free-slip boundaries, $\mathbf{u}\cdot\hat{\mathbf{n}} = 0$; we also have $\hat{\mathbf{n}}_\mathrm{T} = -\hat{\mathbf{n}}_\mathrm{B} = \mathbf{k}$. Collecting these results, we have:

$$\frac{\mathrm{d}}{\mathrm{d}t}\langle b\rangle_V - \langle\kappa\boldsymbol{\nabla}b\cdot\mathbf{k}\rangle_{A;z=z_\mathrm{T}} + \langle\kappa\boldsymbol{\nabla}b\cdot\mathbf{k}\rangle_{A;z=z_\mathrm{B}} = 0. \tag{A.13}$$

Performing a time-average, the first term drops out (because b is uniformly bounded in time), giving:

$$\langle\kappa\boldsymbol{\nabla}b\cdot\mathbf{k}\rangle_{A,T;z=z_\mathrm{T}} = \langle\kappa\boldsymbol{\nabla}b\cdot\mathbf{k}\rangle_{A,T;z=z_\mathrm{B}}\,, \tag{A.14}$$

i.e. the vertical buoyancy fluxes averaged over the top and bottom boundaries are equal to each other.

Next, we need to relate the buoyancy fluxes at the top and bottom boundaries to the Nusselt number. In Cartesian geometry, this follows easily by noting that

$$\begin{aligned}
\langle\boldsymbol{\nabla}\cdot(\mathbf{u}b - \kappa\boldsymbol{\nabla}b)\rangle_A &= \frac{1}{A}\int\boldsymbol{\nabla}\cdot(\mathbf{u}b - \kappa\boldsymbol{\nabla}b)\,\mathrm{d}A \\
&= \frac{1}{A}\int_A\boldsymbol{\nabla}_\mathrm{H}\cdot(\mathbf{u}b - \kappa\boldsymbol{\nabla}b)\,\mathrm{d}A \\
&\quad + \frac{1}{A}\int_A\frac{\partial}{\partial z}(\mathbf{u}b - \kappa\boldsymbol{\nabla}b)\cdot\mathbf{k}\,\mathrm{d}A \\
&= \frac{1}{A}\int_{\partial A}\hat{\mathbf{n}}_{\partial A}\cdot(\mathbf{u}b - \kappa\boldsymbol{\nabla}b)\,\mathrm{d}(\partial A) \\
&\quad + \frac{\partial}{\partial z}\frac{1}{A}\int_A(\mathbf{u}b - \kappa\boldsymbol{\nabla}b)\cdot\mathbf{k}\,\mathrm{d}A \\
\implies \langle\boldsymbol{\nabla}\cdot(\mathbf{u}b - \kappa\boldsymbol{\nabla}b)\rangle_A &= \frac{\partial}{\partial z}\langle(\mathbf{u}b - \kappa\boldsymbol{\nabla}b)\cdot\mathbf{k}\rangle_A\,.
\end{aligned} \tag{A.15}$$

In going from the penultimate to the final line, we have used that the integral over the horizontal boundary is zero for any combination of RBC boundary conditions. For periodic conditions, this is trivial. For either no-slip or free-slip boundary conditions, $\hat{\mathbf{n}}_{\partial A}\cdot\mathbf{u} = 0$ on the boundary, so the first term in the integrand is zero. For insulating lateral boundary conditions, $\hat{\mathbf{n}}_{\partial A}\cdot\boldsymbol{\nabla}b = 0$. Therefore $\langle\mathbf{u}b - \kappa\boldsymbol{\nabla}b\rangle_{A,T}/(\kappa\Delta B/H) = \mathrm{Nu}$ is independent of height z, allowing us to write:

$$\begin{aligned}
-\frac{1}{\Delta B/H}\langle\boldsymbol{\nabla}b\cdot\mathbf{k}\rangle_{A,T;z=z_\mathrm{B}} = \frac{\langle(\mathbf{u}b - \kappa\boldsymbol{\nabla}b)\cdot\mathbf{k}\rangle_{A,T}}{\kappa\Delta B/H} &= \mathrm{Nu} = 1 + \frac{\langle wb\rangle_{V,T}}{\kappa\Delta B/H} \\
\implies -\frac{1}{\Delta B/H}\langle\boldsymbol{\nabla}b\cdot\mathbf{k}\rangle_{A,T;z=z_\mathrm{B}} &= 1 + \frac{\langle wb\rangle_{V,T}}{\kappa\Delta B/H}.
\end{aligned} \tag{A.16}$$

The setup is complete; now we can calculate the thermal and kinetic dissipation rates. First we derive the buoyancy variance equation by multiplying equation 2.5 by the buoyancy:

$$\frac{\partial}{\partial t}\frac{1}{2}b^2 + \boldsymbol{\nabla}\cdot\left(\frac{1}{2}b^2\mathbf{u}\right) = \kappa\boldsymbol{\nabla}\cdot(b\boldsymbol{\nabla}b) - \kappa|\boldsymbol{\nabla}b|^2. \tag{A.17}$$

Applying a volume average yields:

$$\frac{\mathrm{d}}{\mathrm{d}t}\left\langle\frac{1}{2}b^2\right\rangle_V + \frac{1}{H}\left\langle\frac{1}{2}b^2\mathbf{u}\cdot\hat{\mathbf{n}}_{\partial_V}\right\rangle_{\partial V} = \kappa\frac{1}{H}\left\langle b\boldsymbol{\nabla}b\cdot\hat{\mathbf{n}}_{\partial_V}\right\rangle_{\partial V} - \kappa\left\langle|\boldsymbol{\nabla}b|^2\right\rangle_V. \tag{A.18}$$

Splitting $\left\langle\frac{1}{2}b^2\mathbf{u}\cdot\hat{\mathbf{n}}_{\partial_V}\right\rangle_{\partial V}$ up into contributions from the lateral boundaries and the vertical boundaries, we see that it must be zero. Clearly the contribution from the lateral boundaries is zero if the conditions there are periodic. At both vertical boundaries, as well as for rigid lateral boundaries, $\mathbf{u}\cdot\hat{\mathbf{n}}_{\partial_V} = 0$.

Splitting $\left\langle b\boldsymbol{\nabla}b\cdot\hat{\mathbf{n}}_{\partial_V}\right\rangle_{\partial V}$ similarly into its contributions from lateral and from vertical boundaries, we see that the contribution from lateral boundaries is zero. This is obvious for periodic conditions, and follows from $\hat{\mathbf{n}}_{\partial A}\cdot\boldsymbol{\nabla}b = 0$ for rigid insulating boundaries. The contribution from the vertical boundaries is however nonzero:

$$\left\langle b\boldsymbol{\nabla}b\cdot\hat{\mathbf{n}}_{\partial_V}\right\rangle_{\partial V} = \left\langle b\frac{\partial b}{\partial z}\right\rangle_{\partial V;z=H} - \left\langle b\frac{\partial b}{\partial z}\right\rangle_{\partial V;z=0}. \tag{A.19}$$

For fixed buoyancy boundary conditions, we can insert the boundary conditions, factor out the constant $\Delta B/2$, and use $\left\langle\kappa\boldsymbol{\nabla}b\cdot\mathbf{k}\right\rangle_{A,T;z=z_\mathrm{T}} = \left\langle\kappa\boldsymbol{\nabla}b\cdot\mathbf{k}\right\rangle_{A,T;z=z_\mathrm{B}}$, to give:

$$\left\langle b\boldsymbol{\nabla}b\cdot\hat{\mathbf{n}}_{\partial_V}\right\rangle_{\partial V} = -\Delta B\left\langle\frac{\partial b}{\partial z}\right\rangle_{\partial V;z=0}. \tag{A.20}$$

If instead the boundary conditions are fixed buoyancy gradient, we can factor out the constant $\partial b/\partial z\,|_{z=0} = \partial b/\partial z\,|_{z=H}$, and use $\Delta B := \langle b\rangle_{\partial V;z=0} - \langle b\rangle_{\partial V;z=H}$, to arrive at the same expression.

Inserting this back into the expression for the buoyancy variance and taking a time average finally gives the desired exact integral result for the thermal dissipation:

$$\kappa\left\langle|\boldsymbol{\nabla}b|^2\right\rangle_{V,T} = \kappa\frac{(\Delta B)^2}{H^2}\,\mathrm{Nu}\,. \tag{A.21}$$

For the kinetic dissipation, we follow essentially the same procedure. First we take the inner product of $\mathbf{u}$ with the momentum equation 2.4 to derive an equation

for the kinetic energy:

$$\frac{\partial}{\partial t}\frac{1}{2}|\mathbf{u}|^2 + \boldsymbol{\nabla}\cdot\left(\frac{1}{2}|\mathbf{u}|^2\mathbf{u}\right) = b\mathbf{u}\cdot\mathbf{k} - \boldsymbol{\nabla}\cdot(P\mathbf{u}) + \nu\boldsymbol{\nabla}\cdot\left(\mathbf{u}\cdot(\boldsymbol{\nabla}\mathbf{u})^{\mathsf{T}}\right) - \nu|\boldsymbol{\nabla}\mathbf{u}|^2. \tag{A.22}$$

Performing a volume average turns the three transport terms into surface integrals over the boundary via the divergence theorem:

$$\begin{aligned}\frac{\mathrm{d}}{\mathrm{d}t}\left\langle\frac{1}{2}|\mathbf{u}|^2\right\rangle_V + \frac{1}{H}\left\langle\frac{1}{2}|\mathbf{u}|^2\mathbf{u}\cdot\hat{\mathbf{n}}_{\partial V}\right\rangle_{\partial V} \\ = \langle b\mathbf{u}\cdot\mathbf{k}\rangle_V - \frac{1}{H}\langle P\mathbf{u}\cdot\hat{\mathbf{n}}_{\partial V}\rangle_{\partial V} + \frac{\nu}{H}\left\langle\mathbf{u}\cdot(\boldsymbol{\nabla}\mathbf{u})^{\mathsf{T}}\cdot\hat{\mathbf{n}}_{\partial V}\right\rangle_{\partial V} - \nu\left\langle|\boldsymbol{\nabla}\mathbf{u}|^2\right\rangle_V.\end{aligned} \tag{A.23}$$

Clearly $\left\langle\frac{1}{2}|\mathbf{u}|^2\mathbf{u}\cdot\hat{\mathbf{n}}_{\partial V}\right\rangle_{\partial V} = 0$ and $\frac{1}{H}\langle P\mathbf{u}\cdot\hat{\mathbf{n}}_{\partial V}\rangle_{\partial V} = 0$ for any choice of velocity boundary conditions; $\left\langle\mathbf{u}\cdot(\boldsymbol{\nabla}\mathbf{u})^{\mathsf{T}}\cdot\hat{\mathbf{n}}_{\partial V}\right\rangle_{\partial V}$ is less obvious. To parse it, note $\mathbf{u}\cdot(\boldsymbol{\nabla}\mathbf{u})^{\mathsf{T}}\cdot\hat{\mathbf{n}}_{\partial V} = \mathbf{u}\cdot\partial\mathbf{u}/\partial n = \mathbf{u}_\parallel\cdot\partial\mathbf{u}_\parallel/\partial n$, since $\mathbf{u}_\perp = \mathbf{0}$ at any impermeable boundary. Via the mass continuity relation, the normal stress must also be zero at a free-slip boundary. Therefore the whole term is zero regardless of the velocity boundary conditions.

We then take a time average; since the velocity magnitude is also uniformly bounded in time, the tendency again vanishes, leaving a balance between the buoyant production of kinetic energy and the dissipation:

$$\langle b\mathbf{u}\cdot\mathbf{k}\rangle_V = \nu\left\langle|\boldsymbol{\nabla}\mathbf{u}|^2\right\rangle_V. \tag{A.24}$$

The left hand side is equal to $(\kappa\Delta B/H)(\mathrm{Nu}-1)$, yielding the desired exact integral relation for the kinetic dissipation:

$$\nu\left\langle|\boldsymbol{\nabla}\mathbf{u}|^2\right\rangle_{V,T} = \frac{\kappa\Delta B}{H}(\mathrm{Nu}-1). \tag{A.25}$$

See Table A.1 for the form of the kinetic dissipation relation under different choices of nondimensionalization (the thermal dissipation relation always retains the same form).

A.2 Nondimensionalizations of the Boussinesq equations for RBC

In this section we collect several commonly-used nondimensionalizations of the governing Boussinesq equations for applications to RBC. As well as presenting the

different forms of the equations, we note how they are derived, what regimes they are applicable to, and how the form of the exact integral results differs between different nondimensionalizations. This should facilitate comparison of results in this thesis with other work on RBC.

The governing Boussinesq equations are (repeated from Chapter 2):

$$\frac{\mathrm{D}\mathbf{u}}{\mathrm{D}t} = b\mathbf{k} - \boldsymbol{\nabla} P + \nu \boldsymbol{\nabla}^2 \mathbf{u}, \tag{2.4}$$

$$\frac{\mathrm{D}b}{\mathrm{D}t} = \kappa \boldsymbol{\nabla}^2 b, \tag{2.5}$$

$$\boldsymbol{\nabla} \cdot \mathbf{u} = 0. \tag{2.6}$$

For all of these nondimensionalizations it is assumed that the fluid is confined between two smooth, impermeable parallel boundaries held a fixed distance H apart, that the thickness of the layer is small compared to the radius of curvature of the boundaries, and that the horizontal extent of the layer is much greater than its vertical extent.

All standard bulk nondimensionalizations begin by performing an isotropic rescaling of the variables $\{\mathbf{x}, \mathbf{u}, t, P, b\} \to \left\{X\hat{\mathbf{x}}, T\hat{t}, U\hat{\mathbf{u}}, P\hat{P}, B\hat{b}\right\}$. All of the nondimensionalizations also scale time advectively, i.e. the velocity scale is $U = X/T$ (which is equivalent to assuming that the advective part of the time dependence is at least as important as the Eulerian part).

The dimensional parameters entering the problem are then ν, κ, X, and B, allowing the construction of two independent dimensionless parameters. These are traditionally taken to be the Rayleigh and Prandtl numbers:

$$\mathrm{Ra} \coloneqq \frac{BX^3}{\nu\kappa}; \tag{A.26}$$

$$\mathrm{Pr} \coloneqq \frac{\nu}{\kappa}. \tag{A.27}$$

The characteristic buoyancy is set by the boundary conditions, $B = \Delta B$, and the characteristic length by the depth of the domain, $X = H$.

Thus the only differences arise in the choices for scaling the pressure, and for scaling the time (or equivalently the velocity, since they determine each other). The possible options are:

$$T = T_\kappa \coloneqq \frac{H^2}{\kappa} \tag{A.28}$$

$$T = T_\nu \coloneqq \frac{H^2}{\nu} \tag{A.29}$$

$$T = T_B \coloneqq \sqrt{\frac{H}{\Delta B}} \tag{A.30}$$

$$P = U^2 \tag{A.31}$$

$$P = \frac{U\nu}{H}. \tag{A.32}$$

For $\mathrm{Pr} = \mathcal{O}(1)$, either the diffusive or viscous scalings, with either dynamic or viscous scaling of the pressure, make sense; all the different choices do is alter where factors of Pr appear. However, for large or small Pr, the choices state something fundamental about the physics involved in scaling each term.

As well as affecting the form of the governing equations, the chosen nondimensionalization also affects the form of the exact expressions for the dissipation rates. These different expressions are collected in Table A.1.

A.2.1 Infinite and infinitesimal Pr

For fluids where $\mathrm{Pr} \to \infty$ (such as the Earth's mantle), it is appropriate to keep both terms in the buoyancy equation, yet the viscosity must dominate inertia in the momentum equation. Therefore the appropriate scalings are $T = T_\kappa, P = (U\nu)/H$, yielding

$$\frac{1}{\mathrm{Pr}}\frac{\mathrm{D}\hat{\mathbf{u}}}{\mathrm{D}\hat{t}} = \mathrm{Ra}\,\hat{b}\mathbf{k} - \hat{\boldsymbol{\nabla}}\hat{P} + \hat{\boldsymbol{\nabla}}^2\hat{\mathbf{u}}, \tag{A.33}$$

$$\frac{\mathrm{D}\hat{b}}{\mathrm{D}\hat{t}} = \hat{\boldsymbol{\nabla}}^2\hat{b}, \tag{A.34}$$

$$\hat{\boldsymbol{\nabla}}\cdot\hat{\mathbf{u}} = 0. \tag{A.35}$$

The viscous term must remain in the momentum equation, since we are assuming viscosity is important; likewise we cannot neglect the the buoyancy term, since the Prandtl number is independent of the buoyancy forcing. The pressure in this case *must* scale viscously rather than dynamically (which makes sense for the desired limit) in order to fulfil its role in satisfying the divergence constraint. This is effectively scaling the momentum equation with a *fast* time-scale $= T_\kappa/\,\mathrm{Pr}$, such that the momentum field adjusts very quickly to changed in the buoyancy. In the limit $\mathrm{Pr} \to \infty$, the velocity becomes entirely diagnostic.

The opposite limit, $\mathrm{Pr} \to 0$, is not necessarily compatible with the Boussinesq approximation, but is sometimes used in studies of the convection in stars. The appropriate asymptotic limit of the equations is arrived at by scaling time viscously, $T = T_\nu$, which makes both pressure scaling choices identical. This yields the equations:

$$\frac{\mathrm{D}\hat{\mathbf{u}}}{\mathrm{D}\hat{t}} = \frac{\mathrm{Ra}}{\mathrm{Pr}}\hat{b}\mathbf{k} - \hat{\boldsymbol{\nabla}}\hat{P} + \hat{\boldsymbol{\nabla}}^2\hat{\mathbf{u}}, \tag{A.36}$$

T	P	$\mathbf{u}$ equation	b equation	Kinetic dissipation	Limit
T_κ	$U \cdot \nu / H$	$\frac{1}{\mathrm{Pr}} \frac{\mathrm{D}\hat{\mathbf{u}}}{\mathrm{D}t} = \mathrm{Ra}\, \hat{b}\mathbf{k} - \hat{\boldsymbol{\nabla}} \hat{P} + \widehat{\boldsymbol{\nabla}}^2 \hat{\mathbf{u}}$	$\frac{\mathrm{D}\hat{b}}{\mathrm{D}t} = \widehat{\boldsymbol{\nabla}}^2 \hat{b}$	$\left\langle \left\lvert \hat{\boldsymbol{\nabla}} \hat{\mathbf{u}} \right\rvert^2 \right\rangle_{V,T} = \mathrm{Ra}\,(\mathrm{Nu} - 1)$	$\mathrm{Pr} \to \infty$
T_κ	U^2	$\frac{\mathrm{D}\hat{\mathbf{u}}}{\mathrm{D}t} = -\hat{\boldsymbol{\nabla}} \hat{P}\, \mathrm{Pr} \left(\mathrm{Ra}\, \hat{b}\mathbf{k} + \widehat{\boldsymbol{\nabla}}^2 \hat{\mathbf{u}} \right)$	$\frac{\mathrm{D}\hat{b}}{\mathrm{D}t} = \widehat{\boldsymbol{\nabla}}^2 \hat{b}$	$\left\langle \left\lvert \hat{\boldsymbol{\nabla}} \hat{\mathbf{u}} \right\rvert^2 \right\rangle_{V,T} = \mathrm{Ra}\,(\mathrm{Nu} - 1)$	None implied
T_ν	$U^2 = U \cdot \nu / H$	$\frac{\mathrm{D}\hat{\mathbf{u}}}{\mathrm{D}t} = \frac{\mathrm{Ra}}{\mathrm{Pr}} \hat{b}\mathbf{k} - \hat{\boldsymbol{\nabla}} \hat{P} + \widehat{\boldsymbol{\nabla}}^2 \hat{\mathbf{u}}$	$\mathrm{Pr}\, \frac{\mathrm{D}\hat{b}}{\mathrm{D}t} = \widehat{\boldsymbol{\nabla}}^2 \hat{b}$	$\left\langle \left\lvert \hat{\boldsymbol{\nabla}} \hat{\mathbf{u}} \right\rvert^2 \right\rangle_{V,T} = \frac{\mathrm{Ra}}{\mathrm{Pr}^2} (\mathrm{Nu} - 1)$	$\mathrm{Pr} \to 0$ (after rescaling buoyancy; see Section A.2.1)
T_B	$U \cdot \nu / H$	$\frac{1}{\mathrm{Pr}} \frac{\mathrm{D}\hat{\mathbf{u}}}{\mathrm{D}t} = \hat{b}\mathbf{k} - \hat{\boldsymbol{\nabla}} \hat{P} + \sqrt{\frac{\mathrm{Pr}}{\mathrm{Ra}}} \widehat{\boldsymbol{\nabla}}^2 \hat{\mathbf{u}}$	$\frac{\mathrm{D}\hat{b}}{\mathrm{D}t} = \frac{1}{\sqrt{\mathrm{Ra}\,\mathrm{Pr}}} \widehat{\boldsymbol{\nabla}}^2 \hat{b}$	$\left\langle \left\lvert \hat{\boldsymbol{\nabla}} \hat{\mathbf{u}} \right\rvert^2 \right\rangle_{V,T} = \frac{1}{\mathrm{Pr}} (\mathrm{Nu} - 1)$	$\mathrm{Ra} \to \infty$ (for finite Pr)

Table A.1: Comparison of different nondimensionalizations of the Boussinesq equations for RBC. The buoyancy is always nondimensionalized by ΔB, and the spatial dimensions are always nondimensionalized by H. The thermal dissipation rate is not included, since it always takes the same form: $\left\langle \left\lvert \hat{\boldsymbol{\nabla}} \hat{b} \right\rvert^2 \right\rangle_{V,T} = \mathrm{Nu}$.

$$\mathrm{Pr}\,\frac{\mathrm{D}\hat{b}}{\mathrm{D}\hat{t}} = \widehat{\boldsymbol{\nabla}}^2\hat{b}, \tag{A.37}$$

$$\hat{\boldsymbol{\nabla}}\cdot\hat{\mathbf{u}} = 0. \tag{A.38}$$

To consistently take the limit $\mathrm{Pr}\to 0$, we must transform variables to $b' \coloneqq b - (\Delta B/2H)(H-2z)$ (subtracting the associated hydrostatically balanced pressure gradient from the momentum equation). The appropriate scaling for this new variable includes a further factor of Pr, $\hat{b}' = b/(\mathrm{Pr}\,\Delta B)$, since deviations from the pure conductive buoyancy profile are suppressed at high Prandtl number; this removes the final factor of Pr from the momentum equation:

$$\frac{\mathrm{D}\hat{\mathbf{u}}}{\mathrm{D}\hat{t}} = \mathrm{Ra}\,\hat{b}'\mathbf{k} - \hat{\boldsymbol{\nabla}}\hat{P} + \widehat{\boldsymbol{\nabla}}^2\hat{\mathbf{u}}. \tag{A.39}$$

The buoyancy equation in terms of $\hat{b}'$ then includes an extra forcing from the vertical velocity:

$$\mathrm{Pr}\,\frac{\mathrm{D}\hat{b}'}{\mathrm{D}\hat{t}} = \hat{w} + \widehat{\boldsymbol{\nabla}}^2\hat{b}'. \tag{A.40}$$

Therefore in the limit $\mathrm{Pr}\to 0$ the buoyancy is given entirely diagnostically (and nonlocally) by the inverse Laplacian of the vertical velocity. This equation set may be derived rigorously as the low-Pr limit of the Boussinesq equations.

A.2.2 Fixed value vs. fixed flux buoyancy boundary conditions

With constant buoyancy flux boundary conditions (relevant whenever the finite conductivity of the boundaries is small compared to the effective conductivity of the potentially turbulent fluid), the control parameter is the buoyancy flux at the boundaries, rather than the buoyancy itself. We replace the fixed buoyancy boundary conditions with fixed flux conditions of the form:

$$\frac{\partial b}{\partial z}\Big|_{z=0,H} = -\beta. \tag{A.41}$$

This alters the nondimensionalization of the buoyancy to $b = \beta H\hat{b}$, and the (average) buoyancy difference between the boundaries then becomes a measurable response of the system,

$$\Delta B = \langle b(z=0)\rangle_{A,t} - \langle b(z=H)\rangle_{A,t}\,. \tag{A.42}$$

However, with the replacement $\Delta B \to \beta H$, all of the previous nondimensionalizations retain the same form upon the introduction of the flux Rayleigh number,

$$\mathrm{Ra}^* \coloneqq \frac{\beta H^4}{\nu\kappa}. \tag{A.43}$$

The flux Rayleigh number Ra^* may be related to the standard Rayleigh number Ra by noting that $\langle(\mathbf{u}b - \kappa\boldsymbol{\nabla}b)\cdot\mathbf{k}\rangle_{(A,T;z=0)} = \kappa\beta$, and $\langle -\kappa\mathbf{k}\cdot\boldsymbol{\nabla}b\rangle_{(A,T;z=0)} = (\kappa/H)\Big(\langle b(z=0)\rangle_{A,T} - \langle b(z=H)\rangle_{A,T}\Big)$. Therefore

$$\begin{aligned}
\mathrm{Nu} &\coloneqq \frac{\langle(\mathbf{u}b - \kappa\boldsymbol{\nabla}b)\cdot\mathbf{k}\rangle_{V,T}}{\langle(-\kappa\boldsymbol{\nabla}b)\cdot\mathbf{k}\rangle_{V,T}} && \text{(A.44)}\\
&= \frac{\langle(-\kappa\boldsymbol{\nabla}b)\cdot\mathbf{k}\rangle_{A,T;z=0}}{(\kappa/H)\left\langle -\int_0^H(\partial b/\partial z)\,\mathrm{d}z\right\rangle_{A,T}} && \text{(A.45)}\\
&= \frac{\kappa\,\langle -\partial b/\partial z\rangle_{(A,T;z=0)}}{(\kappa/H)\Big(\langle b(z=0)\rangle_{A,T} - \langle b(z=H)\rangle_{A,T}\Big)} && \text{(A.46)}\\
&= \frac{\beta H}{\Delta B} = \frac{\mathrm{Ra}^*}{\mathrm{Ra}} && \text{(A.47)}\\
\implies \mathrm{Ra}^* &\equiv \mathrm{Nu}\,\mathrm{Ra}\,. && \text{(A.48)}
\end{aligned}$$

This provides a recipe for converting between expressions written in terms of the natural variables for the fixed flux and fixed-value buoyancy boundary conditions, including the governing equations.

Appendix B

Additional results regarding the theory of the multi-fluid equations

B.1 Modelling of continuous media via conditional filtering

First let us make some general statements about multi-fluid modelling, which will actually be applicable to the conditional filtering of any continuous medium. The reason for beginning with this generality is to make clear that much of the development in Chapter 3 and later in this Appendix in the context of Boussinesq flows is actually applicable to far more general equation sets.

Consider a set of physical fields $\{\varphi\}$ defined over a region $\Omega \subseteq \mathbb{R}^d$, and over a time interval $[0, T]$; φ could be a scalar, vector, or tensor field, such as density ρ, material velocity $\mathbf{u}$, or stress $\boldsymbol{\tau}$. The evolution of these fields is described by generalized continuity equations of the form:

$$\frac{\partial \varphi}{\partial t} + \boldsymbol{\nabla} \cdot \mathbf{j} = \Sigma_\varphi, \tag{B.1}$$

where $\mathbf{j}_\varphi$ is the flux of φ and Σ_φ are sources/sinks of φ (i.e. anything which cannot be placed inside a divergence). All of the equations of continuum mechanics and, specifically, fluid dynamics can be cast into this form, including the averaged or filtered equations arising in turbulence research.

As in the main text of Chapter 3, we wish to conditionally filter these equations. Indicator functions are introduced exactly as in Section 3.3; however an extra term arises when filtering the left hand side of (3.36) due to the nonzero divergence of the velocity field:

$$\left(\frac{\mathrm{D}I_i}{\mathrm{D}t}\right)^{\mathrm{r}} = \left(\frac{\partial I_i}{\partial t}\right)^{\mathrm{r}} + (\mathbf{u} \cdot \boldsymbol{\nabla} I_i)^{\mathrm{r}} \tag{B.2}$$

$$= \left(\frac{\partial I_i}{\partial t}\right)^{\mathrm{r}} + (\boldsymbol{\nabla}\cdot(I_i\mathbf{u}))^{\mathrm{r}} - (I_i\boldsymbol{\nabla}\cdot\mathbf{u})^{\mathrm{r}}. \tag{B.3}$$

Equating with the right hand side of equation (3.36), and assuming the filtering operation commutes with space and time partial derivatives, yields the form of the "fluid" fraction conservation equation suitable for a general continuous medium in which a material velocity field $\mathbf{u}$ can be defined:

$$\frac{\partial \sigma_i}{\partial t} + \boldsymbol{\nabla}\cdot\sigma_i\mathbf{u}_i^{\mathrm{r}} = \langle(\mathbf{u}-\mathbf{V}_{\partial D_i})\cdot\boldsymbol{\nabla}I_i\rangle_g + \sigma_i(\boldsymbol{\nabla}\cdot\mathbf{u})_i^{\mathrm{r}}. \tag{B.4}$$

The presence of $\boldsymbol{\nabla}\cdot\mathbf{u}$ in one of the terms on the right-hand side suggests that, if the medium is compressible, we must directly consider the conditionally-filtered mass continuity equation in order to close the fluid fraction conservation equation. This is similar to the source term which appears when using non-Favre filtered definitions for resolved variables in standard filtering approaches to compressible turbulence.

In practice, it turns out to be easier to combine the continuity equation with the indicator function evolution equation, and then filter, which removes the direct appearance of the resolved divergence. Let us therefore conditionally filter the general continuity equation (B.1), again assuming uniform filter width and absent boundaries:

$$\begin{aligned}\left\langle I_i\left(\frac{\partial\varphi}{\partial t}+\boldsymbol{\nabla}\cdot\mathbf{j}-\Sigma_\varphi\right)+\varphi\left(\frac{\partial I_i}{\partial t}+\mathbf{u}\cdot\boldsymbol{\nabla}I_i-\frac{\mathrm{D}I_i}{\mathrm{D}t}\right)\right\rangle_g &= 0\\ \implies \left\langle\frac{\partial I_i\varphi}{\partial t}+\boldsymbol{\nabla}\cdot(I_i\mathbf{j})+(\varphi\mathbf{u}-\mathbf{j})\cdot\boldsymbol{\nabla}I_i\right\rangle_g &= \left\langle I_i\Sigma_\varphi+\varphi\frac{\mathrm{D}I_i}{\mathrm{D}t}\right\rangle_g.\end{aligned} \tag{B.5}$$

Using $\langle\varphi\,\mathrm{D}I_i/\mathrm{D}t\rangle_g = \langle\varphi(\mathbf{u}-\mathbf{V}_{\partial D_i})\cdot\boldsymbol{\nabla}I_i\rangle_g$ gives:

$$\frac{\partial\langle I_i\varphi\rangle_g}{\partial t}+\boldsymbol{\nabla}\cdot\langle I_i\mathbf{j}\rangle_g = \langle(\mathbf{j}-\varphi\mathbf{u})\cdot\boldsymbol{\nabla}I_i\rangle_g+\langle I_i\Sigma_\varphi\rangle_g+\langle\varphi(\mathbf{u}-\mathbf{V}_{\partial D_i})\cdot\boldsymbol{\nabla}I_i\rangle_g. \tag{B.6}$$

For $\varphi=\rho$, the flux $\mathbf{j}=\rho\mathbf{u}$ and the source term $\Sigma_\varphi=0$, simplifying the above expression to:

$$\frac{\partial\langle I_i\rho\rangle_g}{\partial t}+\boldsymbol{\nabla}\cdot\langle I_i\rho\mathbf{u}\rangle_g = \langle(\rho\mathbf{u}-\rho\mathbf{V}_{\partial D_i})\cdot\boldsymbol{\nabla}I_i\rangle_g. \tag{B.7}$$

The (relative) simplicity of this expression suggests that, for a compressible medium, the conditionally filtered mass continuity equation should be used in place of the filtered indicator function evolution equation. This also motivates defining some "resolved" variables to be density-weighted if the flow is compressible, similarly to considerations of compressible vs. incompressible flows when filtering *un*conditionally.

We therefore make the following definitions:

Definition 11 ("Resolved" variables: compressible case)**.** For a variable φ, density ρ, and filtering operation $\langle \dots \rangle_g$, we define the ***(Favre-)resolved part of*** φ by:

$$\widetilde{\varphi}^{\mathrm{r}} \coloneqq \frac{\langle \rho\varphi \rangle_g}{\rho^{\mathrm{r}}}. \tag{B.8}$$

Given an indicator function I_i, we also define the ***(Favre-)resolved part of*** φ ***in partition*** i by:

$$\widetilde{\varphi}_i^{\mathrm{r}} \coloneqq \frac{\langle I_i \rho\varphi \rangle_g}{\sigma_i \rho_i^{\mathrm{r}}}. \tag{B.9}$$

Note that this means $\widetilde{\varphi}_i^{\mathrm{r}}$ is undefined wherever $\sigma_i = 0$.

An immediate consequence is $\sum_i \sigma_i \rho_i^{\mathrm{r}} \widetilde{\varphi}_i^{\mathrm{r}} = \rho^{\mathrm{r}} \varphi^{\mathrm{r}}$.

Comments on compressible vs. incompressible flows

With these definitions, the conditionally-filtered mass continuity equation takes on the same form as the fluid fraction evolution equation for an *in*compressible fluid (repeated here for clarity):

$$\frac{\partial \sigma_i}{\partial t} + \boldsymbol{\nabla} \cdot \sigma_i \mathbf{u}_i^{\mathrm{r}} = [(\mathbf{u} - \mathbf{V}_{\partial D_i}) \cdot \boldsymbol{\nabla} I_i]^{\mathrm{r}} + \sigma_i (\boldsymbol{\nabla} \cdot \mathbf{u})_i^{\mathrm{r}} \tag{B.10}$$

$$\frac{\partial \sigma_i \rho_i^{\mathrm{r}}}{\partial t} + \boldsymbol{\nabla} \cdot \sigma_i \rho_i^{\mathrm{r}} \widetilde{\mathbf{u}}_i^{\mathrm{r}} = [\rho(\mathbf{u} - \mathbf{V}_{\partial D_i}) \cdot \boldsymbol{\nabla} I_i]^{\mathrm{r}}. \tag{B.11}$$

The first equation states that changes in resolved fluid fraction are due to the resolved movement of the interface relative to fluid parcels, plus a contribution from the compression or expansion of the underlying fluid. In the incompressible case, $\boldsymbol{\nabla} \cdot \mathbf{u} = 0$ and so the resolved fluid parcel-relative movement of the interface is the *only* contribution to changes in fluid fraction. The second equation states that changes in fluid fraction-weighted resolved density at a point are entirely due to the resolved *density-weighted* movement of the interface relative to fluid parcels at that point. (This can be seen as associating a momentum density, $\rho \mathbf{v}_{\partial D_i}$, to the fluid parcel-relative velocity of the interface.) Thus we name $(\mathbf{u} - \mathbf{V}_{\partial D_i}) \cdot \boldsymbol{\nabla} I_i$ and $\rho(\mathbf{u} - \mathbf{V}_{\partial D_i}) \cdot \boldsymbol{\nabla} I_i$ "relabelling" terms, as they serve to relabel material parcels from one partition to another.

Back to the relabeling terms. Something interesting emerges when we recast the fluid fraction conservation equation in advective form. First we need to define the material derivative operator in partition i:

Definition 12 (Material derivative in partition i)**.** Given a resolved velocity field in partition i, $\mathbf{u}_i^{\mathrm{r}}$, we define the ***material derivative operator in partition*** i to

be the total derivative operator following the path of the resolved velocity field in partition i:

$$\frac{\mathrm{D}_i}{\mathrm{D}t} \coloneqq \left(\frac{\partial}{\partial t} + \mathbf{u}_i^{\mathrm{r}} \cdot \boldsymbol{\nabla}\right). \tag{B.12}$$

Now we can write the advective form of the fluid fraction conservation equation concisely:

$$\frac{\mathrm{D}_i \sigma_i}{\mathrm{D}t} = [(\mathbf{u} - \mathbf{V}_{\partial D_i}) \cdot \boldsymbol{\nabla} I_i]^{\mathrm{r}} + \sigma_i (\boldsymbol{\nabla} \cdot \mathbf{u})_i^{\mathrm{r}} - \sigma_i \boldsymbol{\nabla} \cdot \mathbf{u}_i^{\mathrm{r}}. \tag{B.13}$$

Therefore the changes of fluid fraction following a *resolved* fluid parcel include contributions both from the resolved divergence in partition i, and from the divergence of the resolved velocity in partition i. This highlights an important point — the relabelling of fluid contributes to the divergence of the resolved velocity in partition i:

$$\boldsymbol{\nabla} \cdot \sigma_i \mathbf{u}_i^{\mathrm{r}} = \boldsymbol{\nabla} \cdot \langle I_i \mathbf{u} \rangle_g \tag{B.14}$$

$$= \langle (I_i \boldsymbol{\nabla} \cdot \mathbf{u} + \mathbf{u} \cdot \boldsymbol{\nabla} I_i) \rangle_g \tag{B.15}$$

$$\implies \sigma_i \boldsymbol{\nabla} \cdot \mathbf{u}_i^{\mathrm{r}} = \sigma_i (\boldsymbol{\nabla} \cdot \mathbf{u})_i^{\mathrm{r}} + (\mathbf{u} \cdot \boldsymbol{\nabla} I_i)^{\mathrm{r}} - \mathbf{u}_i^{\mathrm{r}} \cdot \boldsymbol{\nabla} \sigma_i. \tag{B.16}$$

Here the middle term, $(\mathbf{u} \cdot \boldsymbol{\nabla} I_i)^{\mathrm{r}}$, is due to motion of fluid across the interface ∂D_i. For small filter scales, we must have $\mathbf{u}_i^{\mathrm{r}} \cdot \boldsymbol{\nabla} \sigma_i \to (\mathbf{u} \cdot \boldsymbol{\nabla} I_i)^{\mathrm{r}}$, but there is no reason to expect those terms to be similar at larger filter scales. Thus even when the underlying fluid is incompressible, *the resolved velocity in each partition is* not *divergence-free*. This will turn out to have consequences later, especially for modelling conditionally-filtered stress tensors.

B.2 "Relabelling" and "exchange" terms

We turn now to exploring the relabelling terms, $\mathcal{S}_i$, in more detail. Since the fluid fraction-weighted mass conservation equation (B.11) is identical in form to the fluid fraction conservation equation (B.10) in the case of an incompressible underlying fluid, it suffices to consider only the latter in what follows.

Consider the explicit integral forms of the relabelling terms from Chapter 3, equations (3.31) and (3.32):

$$S_i \coloneqq -\int_{\mathbb{R}^d} g(\mathbf{V}_{\partial D_i} - \mathbf{u}) f \cdot \boldsymbol{\nabla} I_i \,\mathrm{d}V = \langle \mathbf{u} - \mathbf{V}_{\partial D_i} \cdot \boldsymbol{\nabla} I_i \rangle_g \tag{B.17}$$

$$= \oint_{\partial D_i} g(\mathbf{V}_{\partial D_i} - \mathbf{u}) f \cdot \hat{\mathbf{n}}_{\partial D_i} \,\mathrm{d}(\partial D_i). \tag{B.18}$$

As currently written, the terms are easy to make sense of conceptually but would

be of little practical use. Further, their relation to entrainment and detrainment terms in traditional convection modelling, or the conditional filtering framework of Thuburn et al. (2018), is currently not obvious.

Recall that the second expression results when using the surface delta function to transform the volume integral to one over the boundary of the indicated domain D_i. This is more useful both for computations, and for splitting the contributions to S_i into sources and sinks. To split into sources and sinks, note that if g is positive semidefinite, the integrand gives a positive contribution to the integral wherever $\mathbf{v}_{\partial D_i} \cdot \hat{\mathbf{n}}_{\partial D_i} > 0$, and a negative contribution wherever $\mathbf{v}_{\partial D_i} \cdot \hat{\mathbf{n}}_{\partial D_i} < 0$. This suggests the identifications

$$\begin{aligned} S_i^+ &\coloneqq \oint_{\partial D_i} g\ \mathcal{H}(\mathbf{v}_{\partial D_i} \cdot \hat{\mathbf{n}}_{\partial D_i}) \mathbf{v}_{\partial D_i} \cdot \hat{\mathbf{n}}_{\partial D_i}\, \mathrm{d}(\partial D_i), \\ S_i^- &\coloneqq \oint_{\partial D_i} g\ \mathcal{H}(-\mathbf{v}_{\partial D_i} \cdot \hat{\mathbf{n}}_{\partial D_i})\, (-\mathbf{v}_{\partial D_i} \cdot \hat{\mathbf{n}}_{\partial D_i})\, \mathrm{d}(\partial D_i), \end{aligned} \tag{B.19}$$

where $\mathcal{H}(x)$ denotes the Heaviside step function and $S_i^\pm \in \mathbb{R}_{\geq 0}$ are respectively sources and sinks of the resolved fluid fraction. We will call terms like this "fluid fraction transfer terms", or "transfer terms" for brevity. The expression "relabelling terms" will be reserved for discussions of the *un*filtered sources and sinks to the indicator function. That is, $\mathcal{H}(-\mathbf{v}_{\partial D_i} \cdot \hat{\mathbf{n}}_{\partial D_i}) \delta(\mathbf{x} \in \partial D_i)$ is a *relabelling term* for the indicator function; $\langle \mathcal{H}(-\mathbf{v}_{\partial D_i} \cdot \hat{\mathbf{n}}_{\partial D_i}) \delta(\mathbf{x} \in \partial D_i) \rangle_g = S_i^+$ is the corresponding *fluid fraction transfer term*.

These sources and sinks may be further decomposed into contributions from the boundary with each other partition, j. Assuming that there are $n \in \mathbb{N}_{>0}$ partitions, we have that the boundary of domain D_i may be written as the sum of the boundaries with each other domain D_j. We define ∂D_{ij} to be the subset of boundary ∂D_i which is in contact with domain D_j, and *only* domain D_j. We define ∂D_{ijk} to be the subset of boundary ∂D_i which is contact with both domain D_j and D_k, and *only* those two domains. For n fluid partitions we thus define $\partial D_{ia^1 \ldots a^p}$ to be the subset of the boundary ∂D_i which is in contact with subdomains $D_{a^1}, \ldots, D_{a^p}$ with $p \in \{0, n-2\}$; all such subsets are mutually disjoint. The entire boundary is the union of all these subsets, $\partial D_i = \bigcup_{a^1} \partial D_{ia^1} (\bigcup_{a^2} \partial D_{ia^1 a^2} (\bigcup_{a^3} \ldots (\bigcup_{a^p} \partial D_{ia^1 \ldots a^p}) \ldots))$. We can then decompose the integral over the entire boundary into the sum of the integrals over all subsets of the boundary,

$$\begin{aligned} &\oint_{\partial D_i} g\ \mathcal{H}(\mathbf{v}_{\partial D_i} \cdot \hat{\mathbf{n}}_{\partial D_i}) \mathbf{v}_{\partial D_i} \cdot \hat{\mathbf{n}}_{\partial D_i}\, \mathrm{d}(\partial D_i) \\ &\quad = \sum_{a^1 \neq i} \left(\int_{\partial D_{ia^1}} g\ \mathcal{H}(\mathbf{v}_{\partial D_i} \cdot \hat{\mathbf{n}}_{\partial D_i}) \mathbf{v}_{\partial D_i} \cdot \hat{\mathbf{n}}_{\partial D_i}\, \mathrm{d}(\partial D_i) \right) \end{aligned}$$

$$+\sum_{a^1\neq i}\sum_{a^2\neq i}\left(\int_{\partial D_{ia^1a^2}} g\ \mathcal{H}(\mathbf{v}_{\partial D_i}\cdot\hat{\mathbf{n}}_{\partial D_i})\mathbf{v}_{\partial D_i}\cdot\hat{\mathbf{n}}_{\partial D_i}\,\mathrm{d}(\partial D_i)\right)$$
$$+\ldots \tag{B.20}$$

Here the first sum is over all two-partition interactions; the second over all three-partition interactions; and so on, up to interactions of all n partitions. However, usually interactions between only two partitions are assumed; we certainly expect two-partition interactions to dominate, since $\bigcup_{a^1}\partial D_{ia^1}$ is almost the entire boundary[1]. Thus we specialize to two-partition interactions, leaving only the first sum, which suggests the definitions:

$$\sigma_i S_{ij} \coloneqq \int_{\partial D_{ij}} g\ \mathcal{H}(-\mathbf{v}_{\partial D_{ij}}\cdot\hat{\mathbf{n}}_{\partial D_{ij}})\left(-\mathbf{v}_{\partial D_{ij}}\cdot\hat{\mathbf{n}}_{\partial D_{ij}}\right)\mathrm{d}(\partial D_i) \tag{B.21}$$
$$= \int_{\partial D_{ji}} g\ \mathcal{H}(\mathbf{v}_{\partial D_{ji}}\cdot\hat{\mathbf{n}}_{\partial D_{ji}})\left(\mathbf{v}_{\partial D_{ji}}\cdot\hat{\mathbf{n}}_{\partial D_{ji}}\right)\mathrm{d}(\partial D_j), \tag{B.22}$$
$$\sigma_j S_{ji} \coloneqq \int_{\partial D_{ji}} g\ \mathcal{H}(-\mathbf{v}_{\partial D_{ji}}\cdot\hat{\mathbf{n}}_{\partial D_{ji}})\left(-\mathbf{v}_{\partial D_{ji}}\cdot\hat{\mathbf{n}}_{\partial D_{ji}}\right)\mathrm{d}(\partial D_j) \tag{B.23}$$
$$= \int_{\partial D_{ij}} g\ \mathcal{H}(\mathbf{v}_{\partial D_{ij}}\cdot\hat{\mathbf{n}}_{\partial D_{ij}})\left(\mathbf{v}_{\partial D_{ij}}\cdot\hat{\mathbf{n}}_{\partial D_{ij}}\right)\mathrm{d}(\partial D_i), \tag{B.24}$$

with $\sum_j \sigma_i S_{ij} = S_i^-, \sum_j \sigma_j S_{ji} = S_i^+$ (within the two-partition interaction approximation). Here $S_{ij} \in \mathbb{R}_{\geq 0}$ is the rate of fluid fraction transfer from partition i to j, while $S_{ji} \in \mathbb{R}_{\geq 0}$ is the rate of fluid fraction transfer from partition j to i. We choose to define the transfer terms as weighted by volume fraction to match the convention in earlier papers on multi-fluid modelling of convection (Thuburn et al. 2018; Weller and McIntyre 2019; Weller et al. 2020).

Since density is positive definite, exactly the same decomposition could have been performed for density-weighted relabelling terms to define mass transfer terms:

$$\sigma_i M_{ij} \coloneqq \int_{\partial D_{ij}} g\ \mathcal{H}(-\mathbf{v}_{\partial D_{ij}}\cdot\hat{\mathbf{n}}_{\partial D_{ij}})\rho\left(-\mathbf{v}_{\partial D_{ij}}\cdot\hat{\mathbf{n}}_{\partial D_{ij}}\right)\mathrm{d}(\partial D_i) \tag{B.25}$$
$$= \int_{\partial D_{ji}} g\ \mathcal{H}(\mathbf{v}_{\partial D_{ji}}\cdot\hat{\mathbf{n}}_{\partial D_{ji}})\rho\left(\mathbf{v}_{\partial D_{ji}}\cdot\hat{\mathbf{n}}_{\partial D_{ji}}\right)\mathrm{d}(\partial D_j), \tag{B.26}$$
$$\sigma_j M_{ji} \coloneqq \int_{\partial D_{ji}} g\ \mathcal{H}(-\mathbf{v}_{\partial D_{ji}}\cdot\hat{\mathbf{n}}_{\partial D_{ji}})\rho\left(-\mathbf{v}_{\partial D_{ji}}\cdot\hat{\mathbf{n}}_{\partial D_{ji}}\right)\mathrm{d}(\partial D_j) \tag{B.27}$$
$$= \int_{\partial D_{ij}} g\ \mathcal{H}(\mathbf{v}_{\partial D_{ij}}\cdot\hat{\mathbf{n}}_{\partial D_{ij}})\rho\left(\mathbf{v}_{\partial D_{ij}}\cdot\hat{\mathbf{n}}_{\partial D_{ij}}\right)\mathrm{d}(\partial D_i), \tag{B.28}$$

where the interpretation is the same as for the S_{ij}, except now for transfers of mass.

[1] To see this, note that in d dimensions, the interface between two measurable sets D_1 and D_2 with the property $D_1 \cap D_2 = \emptyset$, $\partial D_1 \cap \partial D_2 \neq \emptyset$ is $d-1$-dimensional, whereas the interface between more than two such sets is at most $d-2$-dimensional.

Substituting these expressions for the fluid fraction and mass transfer terms back into the conservation equations gives:

$$\frac{\partial \sigma_i}{\partial t} + \boldsymbol{\nabla} \cdot \sigma_i \mathbf{u}_i^{\mathrm{r}} = \sum_{j \neq i} \left(\sigma_j S_{ji} - \sigma_i S_{ij} \right) + \sigma_i (\boldsymbol{\nabla} \cdot \mathbf{u})_i^{\mathrm{r}}, \tag{B.29}$$

$$\frac{\partial \sigma_i \rho_i^{\mathrm{r}}}{\partial t} + \boldsymbol{\nabla} \cdot \sigma_i \rho_i^{\mathrm{r}} \widetilde{\mathbf{u}}_i^{\mathrm{r}} = \sum_{j \neq i} \left(\sigma_j M_{ji} - \sigma_i M_{ij} \right). \tag{B.30}$$

This completes the derivation of equations (3.44) and (3.48).

B.3 Proof of subfilter flux decomposition for arbitrarily many partitions

In Chapter 1 we introduced and proved a relation between the subfilter flux $s(a, b)$ and the within-partition values $a_i^{\mathrm{r}}, b_i^{\mathrm{r}}$ and the within-partition fluxes $s_i(a, b)$ for the special case of two partitions:

$$s(a, b) = \sigma_1 s_1(a, b) + \sigma_2 s_2(a, b) + \sigma_1 \sigma_2 \left(a_1^{\mathrm{r}} - a_2^{\mathrm{r}} \right) \left(b_1^{\mathrm{r}} - b_2^{\mathrm{r}} \right). \tag{1.35}$$

This leads us to conjecture the following relation for an arbitrary number of partitions:

$$s(a, b) = \sum_i \sigma_i s_i(a, b) + \frac{1}{2} \sum_{i,j} \sigma_i \sigma_j \left(a_i^{\mathrm{r}} - a_j^{\mathrm{r}} \right) \left(b_i^{\mathrm{r}} - b_j^{\mathrm{r}} \right), \tag{B.31}$$

which is used liberally from Chapter 3 onwards.

To prove (B.31), we begin with $\sum_i \sigma_i s_i(a, b)$ and work backwards:

$$\begin{aligned}
\sum_i \sigma_i s_i(a, b) &= \sum_i \sigma_i (ab)_i^{\mathrm{r}} - \sum_i \sigma_i a_i^{\mathrm{r}} b_i^{\mathrm{r}} \\
&= (ab)^{\mathrm{r}} - a^{\mathrm{r}} b^{\mathrm{r}} + \left(\sum_i \sigma_i a_i^{\mathrm{r}} \right) \left(\sum_j \sigma_j b_j^{\mathrm{r}} \right) - \sum_i \sigma_i \left(\sum_j \sigma_j \right) a_i^{\mathrm{r}} b_i^{\mathrm{r}} \\
&= s(a, b) + \sum_{i,j} \sigma_i \sigma_j a_i^{\mathrm{r}} b_j^{\mathrm{r}} - \sum_{i,j} \sigma_i \sigma_j a_i^{\mathrm{r}} b_i^{\mathrm{r}} \\
&= s(a, b) - \left(\sum_{i,j} \sigma_i \sigma_j a_i^{\mathrm{r}} b_i^{\mathrm{r}} - \sum_{i,j} \sigma_i \sigma_j a_i^{\mathrm{r}} b_j^{\mathrm{r}} \right) \\
&= s(a, b) - \frac{1}{2} \left(\sum_{i,j} \sigma_i \sigma_j a_i^{\mathrm{r}} b_i^{\mathrm{r}} - \sum_{i,j} \sigma_i \sigma_j a_i^{\mathrm{r}} b_j^{\mathrm{r}} + \sum_{i,j} \sigma_i \sigma_j a_i^{\mathrm{r}} b_i^{\mathrm{r}} - \sum_{i,j} \sigma_i \sigma_j a_i^{\mathrm{r}} b_j^{\mathrm{r}} \right)
\end{aligned} \tag{B.32}$$

$$= s(a,b) - \frac{1}{2}\left(\sum_{i,j}\sigma_i\sigma_j a_i^{\mathrm{r}} b_i^{\mathrm{r}} - \sum_{i,j}\sigma_i\sigma_j a_i^{\mathrm{r}} b_j^{\mathrm{r}} + \sum_{j,i}\sigma_j\sigma_i a_j^{\mathrm{r}} b_j^{\mathrm{r}} - \sum_{j,i}\sigma_j\sigma_i a_j^{\mathrm{r}} b_i^{\mathrm{r}}\right) \tag{B.33}$$

$$= s(a,b) - \frac{1}{2}\left(\sum_{i,j}\sigma_i\sigma_j a_i^{\mathrm{r}} b_i^{\mathrm{r}} - \sum_{i,j}\sigma_i\sigma_j a_i^{\mathrm{r}} b_j^{\mathrm{r}} + \sum_{i,j}\sigma_j\sigma_i a_j^{\mathrm{r}} b_j^{\mathrm{r}} - \sum_{i,j}\sigma_j\sigma_i a_j^{\mathrm{r}} b_i^{\mathrm{r}}\right) \tag{B.34}$$

$$= s(a,b) - \frac{1}{2}\sum_{i,j}\sigma_i\sigma_j\left(a_i^{\mathrm{r}} b_i^{\mathrm{r}} - a_i^{\mathrm{r}} b_j^{\mathrm{r}} - a_j^{\mathrm{r}} b_i^{\mathrm{r}} + a_j^{\mathrm{r}} b_j^{\mathrm{r}}\right)$$

$$\implies s(a,b) = \sum_i \sigma_i s_i(a,b) + \frac{1}{2}\sum_{i,j}\sigma_i\sigma_j\left(a_i^{\mathrm{r}} - a_j^{\mathrm{r}}\right)\left(b_i^{\mathrm{r}} - b_j^{\mathrm{r}}\right), \tag{B.35}$$

completing the proof of equation (B.31).

For clarity, in going from Equation (B.32) to Equation (B.33), we have relabelled the dummy indices in the second and fourth terms inside the parentheses, and in going from Equation (B.33) to Equation (B.34), we have swapped the summation order in the second and fourth terms inside the parentheses[2]. Therefore the split of fluxes/covariances into "organized turbulence" and "internal variability" carries through to a general filtering operation, and to any countable number of partitions.

Note that equation (1.35) is often written in the alternative form (for instance in Efstathiou et al. 2020):

$$s(a,b) = \sigma_1 s_1(a,b) + \sigma_2 s_2(a,b) + \sigma_1\left(a_1^{\mathrm{r}} - a^{\mathrm{r}}\right)\left(b_1^{\mathrm{r}} - b^{\mathrm{r}}\right) + \sigma_2\left(a_2^{\mathrm{r}} - a^{\mathrm{r}}\right)\left(b_2^{\mathrm{r}} - b^{\mathrm{r}}\right). \tag{B.36}$$

This form is obtained from equation (1.35) by noting $\sigma_2(a_1^{\mathrm{r}} - a_2^{\mathrm{r}}) = (a_1^{\mathrm{r}} - a^{\mathrm{r}})$ exactly, then adding and subtracting $b^{\mathrm{r}} = \sigma_1 b_1^{\mathrm{r}} + \sigma_2 b_2^{\mathrm{r}}$ inside the parentheses. We can also

[2]The order of summation can always be swapped if the number of partitions is finite. If the number of partitions is countably infinite, we note that $\sum_i \sum_j a_{ij} \sum_j \sum_i a_{ij}$ if and only if $\sum_i \sum_j |a_i j|$ exists (this is a special case of Fubini's theorem for infinite series).

generalize this result to countably many partitions:

$$\begin{aligned}
&\frac{1}{2}\sum_{i,j}\sigma_i\sigma_j\left(a_i^{\mathrm{r}}-a_j^{\mathrm{r}}\right)\left(b_i^{\mathrm{r}}-b_j^{\mathrm{r}}\right)\\
&\qquad=\frac{1}{2}\left\{\sum_{i,j}\sigma_i\sigma_j\left(a_i^{\mathrm{r}}-a_j^{\mathrm{r}}\right)\left(b_i^{\mathrm{r}}-b^{\mathrm{r}}\right)+\sum_{i,j}\sigma_i\sigma_j\left(a_i^{\mathrm{r}}-a_j^{\mathrm{r}}\right)\left(b^{\mathrm{r}}-b_j^{\mathrm{r}}\right)\right\}\\
&\qquad=\frac{1}{2}\left\{\sum_{i,j}\sigma_i\sigma_j\left(a_i^{\mathrm{r}}-a_j^{\mathrm{r}}\right)\left(b_i^{\mathrm{r}}-b^{\mathrm{r}}\right)+\sum_{j,i}\sigma_j\sigma_i\left(a_j^{\mathrm{r}}-a_i^{\mathrm{r}}\right)\left(b^{\mathrm{r}}-b_i^{\mathrm{r}}\right)\right\}\\
&\qquad=\frac{1}{2}\left\{\sum_{i,j}\sigma_i\sigma_j\left(a_i^{\mathrm{r}}-a_j^{\mathrm{r}}\right)\left(b_i^{\mathrm{r}}-b^{\mathrm{r}}\right)+\sum_{i,j}\sigma_i\sigma_j\left(a_i^{\mathrm{r}}-a_j^{\mathrm{r}}\right)\left(b_i^{\mathrm{r}}-b^{\mathrm{r}}\right)\right\}\\
&\qquad=\sum_{i,j}\sigma_i\sigma_j\left(a_i^{\mathrm{r}}-a_j^{\mathrm{r}}\right)\left(b_i^{\mathrm{r}}-b^{\mathrm{r}}\right)\\
&\qquad=\sum_{i}\sigma_i\left(b_i^{\mathrm{r}}-b^{\mathrm{r}}\right)\left(\left[\sum_j\sigma_j\right]a_i^{\mathrm{r}}-\left[\sum_j\sigma_j a_j^{\mathrm{r}}\right]\right)\\
&\qquad=\sum_{i}\sigma_i\left(b_i^{\mathrm{r}}-b^{\mathrm{r}}\right)\left(a_i^{\mathrm{r}}-a^{\mathrm{r}}\right).
\end{aligned}$$

In the first line we added $0=\sigma_i\sigma_j(a_i^{\mathrm{r}}-a_j^{\mathrm{r}})(b^{\mathrm{r}}-b^{\mathrm{r}})$ inside the summation; in going from the first line to the second, we re-labelled the dummy indices in the second term inside the curly braces; and in going from the second line to the third, we swapped the order of the summation in the second term inside the curly braces. Therefore we have proved an alternative form of equation (B.31):

$$s(a,b)=\sum_i\sigma_i s_i(a,b)+\sum_i\sigma_i\left(a_i^{\mathrm{r}}-a^{\mathrm{r}}\right)\left(b_i^{\mathrm{r}}-b^{\mathrm{r}}\right). \tag{B.37}$$

It is worth making a few remarks on the generality of the above derivation. Note that the only conditions the derivation makes use of are $\sum_i\sigma_i=1, \sum_i\sigma_i a_i^{\mathrm{r}}=a^{\mathrm{r}}$, as well as the formal definitions $s(a,b)\coloneqq ab^{\mathrm{r}}-a^{\mathrm{r}}b^{\mathrm{r}}$, $s_i(a,b)\coloneqq(ab)_i^{\mathrm{r}}-a_i^{\mathrm{r}}b_i^{\mathrm{r}}$. Therefore the results (B.31) and (B.37) are *not* restricted to conditional filtering using an integral spatiotemporal filter and a discontinuous indicator function. The filtering operation may be any linear filtering operation, which includes various ensemble averages. Additionally, the indicator function used for the conditioning could well be a "fuzzy" indicator.

It is also quite easily possible to extend to continuous partitioning, i.e. for some continuous conditions indexed by λ, a conditionally filtered field in an infinitesimal neighbourhood of λ would be given by $\sigma_\lambda\varphi_\lambda^{\mathrm{r}}$. Then the continuous analogues of the conditions $\sum_i\sigma_i=1$ and $\sum_i\sigma_i\varphi_i^{\mathrm{r}}=\varphi^{\mathrm{r}}$ become $\int_\lambda\sigma_\lambda\,\mathrm{d}\lambda=1$, $\int_\lambda\sigma_\lambda\varphi_\lambda^{\mathrm{r}}\,\mathrm{d}\lambda=\varphi^{\mathrm{r}}$, and the derivations proceed in much the same way as for the case of countable series

above, resulting in:

$$s(a,b) = \int_\lambda \sigma_\lambda s_\lambda(a,b) + \frac{1}{2}\int_{\lambda,\kappa} \sigma_\lambda \sigma_\kappa \left(a^{\mathrm{r}}_\lambda - a^{\mathrm{r}}_\kappa\right)\left(b^{\mathrm{r}}_\lambda - b^{\mathrm{r}}_\kappa\right) \mathrm{d}\lambda\, \mathrm{d}\kappa \tag{B.38}$$

$$= \int_\lambda \sigma_\lambda s_\lambda(a,b) + \int_\lambda \sigma_\lambda \left(a^{\mathrm{r}}_\lambda - a^{\mathrm{r}}\right)\left(b^{\mathrm{r}}_\lambda - b^{\mathrm{r}}\right) \mathrm{d}\lambda. \tag{B.39}$$

(The conditions allowing the order of the resulting integrals to be swapped are provided by Fubini's theorem.)

This extension to the case of continuously-indexed partitioning makes the sub-filter flux decomposition precise for the useful case of so-called "spectral" mass-flux schemes, including the original paper Arakawa and Schubert (1974).

Bibliography

Ahlers, Guenter, Siegfried Grossmann, and Detlef Lohse (2009). "Heat transfer and large scale dynamics in turbulent Rayleigh-Bénard convection". *Reviews of Modern Physics* 81 (2), pp. 503–537. DOI: 10.1103/RevModPhys.81.503 (cit. on pp. 3, 44, 47, 51, 56, 58, 61, 65, 128, 135).

Arakawa, Akio, J. H. Jung, and Chien-Ming Wu (2011). "Toward unification of the multiscale modelling of the atmosphere". *Atmospheric Chemistry and Physics* 11.8, pp. 3731–3742 (cit. on pp. 39, 180).

Arakawa, Akio and Wayne Howard Schubert (1974). "Interaction of a Cumulus Cloud Ensemble with the Large-Scale Environment, Part I". *Journal of the Atmospheric Sciences* 31, pp. 674–701 (cit. on pp. 1, 23, 24, 26, 28, 179, 210).

Arakawa, Akio and Chien-Ming Wu (2013). "A Unified Representation of Deep Moist Convection in Numerical Modeling of the Atmosphere. Part I". *Journal of the Atmospheric Sciences* 70.7, pp. 1977–1992. DOI: 10.1175/JAS-D-12-0330.1 (cit. on p. 34).

Baer, Melvin R. and Jace W. Nunziato (1986). "A two-phase mixture theory for the deflagration-to-detonation transition (DDT) in reactive granular materials". *International Journal of Multiphase Flow* 12.6, pp. 861–889. DOI: https://doi.org/10.1016/0301-9322(86)90033-9 (cit. on p. 87).

Bailon-Cuba, Jorge, Mohammad S. Emran, and Jörg Schumacher (2010). "Aspect ratio dependence of heat transfer and large-scale flow in turbulent convection". *Journal of Fluid Mechanics* 655, pp. 152–173. DOI: 10.1017/S0022112010000820 (cit. on p. 47).

Bakhuis, Dennis et al. (2018). "Mixed insulating and conducting thermal boundary conditions in Rayleigh–Bénard convection". *Journal of Fluid Mechanics* 835, pp. 491–511. DOI: 10.1017/jfm.2017.737 (cit. on p. 52).

Batchelor, G. K. (1967). *An Introduction to Fluid Dynamics*. Cambridge Mathematical Library. Cambridge University Press (cit. on pp. 5, 113, 114, 131).

— (1970). "The stress system in a suspension of force-free particles". *Journal of Fluid Mechanics* 41.3, pp. 545–570. DOI: 10.1017/S0022112070000745 (cit. on p. 111).

Beare, Robert J. (2014). "A Length Scale Defining Partially-Resolved Boundary-Layer Turbulence Simulations". *Boundary-Layer Meteorology* 151 (1), pp. 39–55. DOI: 10.1007/s10546-013-9881-3 (cit. on pp. 21, 77).

Beetham, S., R.O. Fox, and J. Capecelatro (2021). "Sparse identification of multiphase turbulence closures for coupled fluid–particle flows". *Journal of Fluid Mechanics* 914, A11-1–23. DOI: 10.1017/jfm.2021.53 (cit. on pp. 40, 176).

Behrens, Tim (2009). *OpenFOAM's basic solvers for linear systems of equations*. Report for course "CFD with Open Source software". Chalmers University of Technology (cit. on p. 61).

Bénard, Henri (1900). "Les Tourbillons cellulaires dans une nappe liquide". *Revue Général des Sciences Pures et Appliquées* 11, pp. 1261–1271, 1309–1328 (cit. on pp. 3, 43).

— (1901). "Les Tourbillons cellulaires dans une nappe liquide transportant de la chaleur par convection en régime permanent". *Annales de Chimie et de Physique* 23, pp. 62–144 (cit. on pp. 3, 43).

Berghout, Pieter, Woutijn J. Baars, and Dominik Krug (2021). "The large-scale footprint in small-scale Rayleigh–Bénard turbulence". *Journal of Fluid Mechanics* 911, A62-1–19. DOI: 10.1017/jfm.2020.1097 (cit. on p. 176).

Berner, Judith et al. (2017). "Stochastic Parameterization: Toward a New View of Weather and Climate Models". *Bulletin of the American Meteorological Society* 98.3, pp. 565–588. DOI: 10.1175/BAMS-D-15-00268.1 (cit. on p. 38).

Berselli, Luigi, Traian Iliescu, and William J. Layton (2006). *Mathematics of Large Eddy Simulation of Turbulent Flows*. Scientific Computation. Springer. DOI: 10.1007/b137408 (cit. on pp. 18, 20).

Betts, A. K. (1986). "A new convective adjustment scheme. Part 1: Observational and theoretical basis". *Quarterly Journal of the Royal Meteorological Society* 112, pp. 677–691. DOI: 10.1002/qj.49711247307 (cit. on p. 29).

Betts, A. K. and M. J. Miller (1986). "A new convective adjustment scheme. Part II: Single column tests using GATE wave, BOMEX, ATEX and arctic air-mass data sets". *Quarterly Journal of the Royal Meteorological Society* 112, pp. 693–709. DOI: https://doi.org/10.1002/qj.49711247308 (cit. on p. 29).

Blundell, Stephen J. and Katherine M. Blundell (2009). *Concepts in Thermal Physics*. 2nd ed. Oxford University Press (cit. on p. 9).

Bois, Pierre-Antoine (1991). "Asymptotic aspects of the Boussinesq approximation for gases and liquids". *Geophysical & Astrophysical Fluid Dynamics* 58.1-4, pp. 45–55. DOI: 10.1080/03091929108227330 (cit. on p. 46).

Bopape, Mary-Jane M., Robert S. Plant, and Omduth Coceal (2020). "Resolution Dependence of Turbulent Structures in Convective Boundary Layer Simulations". *Atmosphere* 11.9. DOI: 10.3390/atmos11090986 (cit. on p. 69).

Brennen, Christopher Earls (2005). *Fundamentals of multiphase flow*. Cambridge University Press (cit. on pp. 3, 85).

Bretherton, Christopher S. (1987). "A Theory for Nonprecipitating Moist Convection between Two Parallel Plates. Part I: Thermodynamics and "Linear" Solutions". *Journal of the Atmospheric Sciences* 44.14, pp. 1809–1827. DOI: 10.1175/1520-0469(1987)044<1809:ATFNMC>2.0.CO;2 (cit. on pp. 9, 44).

— (1988). "A Theory for Nonprecipitating Convection between Two Parallel Plates. Part II: Nonlinear Theory and Cloud Field Organization". *Journal of the Atmospheric Sci-*

ences 45.17, pp. 2391–2415. DOI: 10.1175/1520-0469(1988)045<2391:ATFNCB>2.0.CO;2 (cit. on pp. 9, 44).

Bryan, George H. and J. Michael Fritsch (2002). "A Benchmark Simulation for Moist Nonhydrostatic Numerical Models". *Monthly Weather Review* 130.12, pp. 2917–2928. DOI: 10.1175/1520-0493(2002)130<2917:ABSFMN>2.0.CO;2 (cit. on pp. 44, 87).

Buckingham, Edgar (1914). "On Physically Similar Systems; Illustrations of the Use of Dimensional Equations". *Physical Review* 4 (4), pp. 345–376. DOI: 10.1103/PhysRev.4.345 (cit. on p. 46).

Callen, Herbert B. (1985). *Thermodynamics and an Introduction to Thermostatistics*. 2nd ed. Wiley (cit. on p. 9).

Castaing, Bernard et al. (1989). "Scaling of hard thermal turbulence in Rayleigh-Bénard convection". *Journal of Fluid Mechanics* 204, pp. 1–30. DOI: 10.1017/S0022112089001643 (cit. on pp. 50, 58).

Chandrasekhar, Subrahmanyan (1961). *Hydrodynamic and Hydromagnetic Stability*. International Series of Monographs on Physics. Oxford University Press (cit. on pp. 44, 48, 49, 55, 76, 121, 128).

Charney, Jule G. and Arnt Eliassen (1964). "On the Growth of the Hurricane Depression". *Journal of Atmospheric Sciences* 21.1, pp. 68–75. DOI: 10.1175/1520-0469(1964)021<0068:OTGOTH>2.0.CO;2 (cit. on p. 22).

Cheinet, Sylvain (2003). "A Multiple Mass-Flux Parameterization for the Surface-Generated Convection. Part I: Dry Plumes". *Journal of the Atmospheric Sciences* 60.18, pp. 2313–2327. DOI: 10.1175/1520-0469(2003)060<2313:AMMPFT>2.0.CO;2 (cit. on p. 86).

Chillà, F and J Schumacher (2012). "New perspectives in turbulent Rayleigh-Bénard convection". *The European Physical Journal E* 35.7 (cit. on pp. 3, 44, 51, 56, 65, 85, 128).

Clark, Peter et al. (2016). "Convection-permitting models: a step-change in rainfall forecasting". *Meteorological Applications* 23.2, pp. 165–181. DOI: 10.1002/met.1538 (cit. on pp. 33, 157).

Cohen, Yair et al. (2020). "Unified Entrainment and Detrainment Closures for Extended Eddy-Diffusivity Mass-Flux Schemes". *Journal of Advances in Modeling Earth Systems* 12.9. DOI: https://doi.org/10.1029/2020MS002162 (cit. on pp. 36, 127).

Cullen, M. J. P. and A. R. Brown (2009). "Large Eddy Simulation of the Atmosphere on Various Scales". *Philosophical Transactions: Mathematical, Physical and Engineering Sciences* 367.1899, pp. 2947–2956 (cit. on pp. 13, 19, 21).

Curtis, W.D., J.David Logan, and W.A. Parker (1982). "Dimensional analysis and the pi theorem". *Linear Algebra and its Applications* 47, pp. 117–126. DOI: https://doi.org/10.1016/0024-3795(82)90229-4 (cit. on p. 46).

Davidson, Paul (2009). *Turbulence: An Introduction for Scientists and Engineers*. 2nd ed. Oxford University Press (cit. on pp. 13, 54, 57).

Davies, Terry et al. (2003). "Validity of anelastic and other equation sets as inferred from normal-mode analysis". *Quarterly Journal of the Royal Meteorological Society* 129.593, pp. 2761–2775. DOI: 10.1256/qj.02.1951 (cit. on p. 51).

de Rooy, Wim C. et al. (2013). "Entrainment and detrainment in cumulus convection: an overview". *Quarterly Journal of the Royal Meteorological Society* 139.670, pp. 1–19. DOI: 10.1002/qj.1959 (cit. on pp. 99, 101, 103, 127).

Deardorff, J. W. (1966). "The Counter-Gradient Heat Flux in the Lower Atmosphere and in the Laboratory". *Journal of Atmospheric Sciences* 23.5, pp. 503–506. DOI: 10.1175/1520-0469(1966)023<0503:TCGHFI>2.0.CO;2 (cit. on p. 35).

Deardorff, J. W. and G. E. Willis (1965). "The effect of two-dimensionality on the suppression of thermal turbulence". *Journal of Fluid Mechanics* 23.2, pp. 337–353. DOI: 10.1017/S0022112065001404 (cit. on p. 56).

DeLuca, E. E. et al. (1990). "Numerical simulations of soft and hard turbulence: Preliminary results for two-dimensional convection". *Physical Review Letters* 64 (20), pp. 2370–2373. DOI: 10.1103/PhysRevLett.64.2370 (cit. on p. 56).

Deng, Aijun and David R. Stauffer (2006). "On Improving 4-km Mesoscale Model Simulations". *Journal of Applied Meteorology and Climatology* 45.3, pp. 361–381. DOI: 10.1175/JAM2341.1 (cit. on pp. 32, 76).

Ding, Zijing and Baole Wen (2020). "A note on upper bound for heat transport in two-dimensional Rayleigh-Bénard convection". *International Communications in Heat and Mass Transfer* 117, p. 104785. DOI: https://doi.org/10.1016/j.icheatmasstransfer.2020.104785 (cit. on p. 50).

Doering, Charles R. (2019). "Thermal forcing and 'classical' and 'ultimate' regimes of Rayleigh–Bénard convection". *Journal of Fluid Mechanics* 868, pp. 1–4. DOI: 10.1017/jfm.2019.118 (cit. on p. 52).

— (2020). "Absence of Evidence for the Ultimate State of Turbulent Rayleigh-Bénard Convection". *Physical Review Letters* 124 (22), p. 229401. DOI: 10.1103/PhysRevLett.124.229401 (cit. on p. 51).

— (2021). "Confounding Complexities in Rayleigh-Bénard Convection". talk in the Mathematical Problems in Fluid Dynamics Program for the Mathematical Sciences Research Institute (cit. on p. 5).

Doering, Charles R. and J. D. Gibbon (1995). *Applied Analysis of the Navier-Stokes Equations*. Cambridge Texts in Applied Mathematics. Cambridge University Press. DOI: 10.1017/CBO9780511608803 (cit. on pp. 9, 10, 50).

Doering, Charles R., S. Toppaladoddi, and J. S. Wettlaufer (2019). "Absence of Evidence for the Ultimate Regime in Two-Dimensional Rayleigh-Bénard Convection". *Physical Review Letters* 123 (25), p. 259401. DOI: 10.1103/PhysRevLett.123.259401 (cit. on p. 51).

Dopazo, C. (1977). "On conditioned averages for intermittent turbulent flows". *Journal of Fluid Mechanics* 81, pp. 433–438. DOI: 10.1017/S0022112077002158 (cit. on pp. 3, 85, 86, 96, 111, 112, 125, 179).

Efstathiou, Georgios A., John Thuburn, and Robert J. Beare (2020). "Diagnosing coherent structures in the convective boundary layer by optimizing their vertical turbulent scalar transfer". *Boundary-Layer Meteorology* 174.1, pp. 119–144 (cit. on pp. 94, 185, 186, 208).

Efstathiou, Georgios A. et al. (2016). "Grey zone simulations of the morning convective boundary layer development". *Journal of Geophysical Research: Atmospheres* 121.9, pp. 4769–4782. DOI: https://doi.org/10.1002/2016JD024860 (cit. on p. 167).

Emanuel, Kerry A. (1994). *Atmospheric Convection*. Oxford University Press (cit. on pp. 4, 5, 8, 9, 26, 29, 30, 44).

Emran, Mohammad S. and Jörg Schumacher (2015). "Large-scale mean patterns in turbulent convection". *Journal of Fluid Mechanics* 776, pp. 96–108. DOI: 10.1017/jfm.2015.316 (cit. on p. 55).

Fantuzzi, Giovanni (2018). "Bounds for Rayleigh–Bénard convection between free-slip boundaries with an imposed heat flux". *Journal of Fluid Mechanics* 837, R5. DOI: 10.1017/jfm.2017.907 (cit. on p. 50).

Fitch, A. C. (2019). "An Improved Double-Gaussian Closure for the Subgrid Vertical Velocity Probability Distribution Function". *"Journal of the Atmospheric Sciences* 76.1, pp. 285–304. DOI: 10.1175/JAS-D-18-0149.1 (cit. on p. 86).

Fleming, James Rodger (2020). *First Woman: Joanne Simpson and the Tropical Atmosphere*. Oxford Unviersity Press. DOI: DOI:10.1093/oso/9780198862734.001.0001 (cit. on pp. 49, 50).

Frisch, Uriel (1995). *Turbulence: the legacy of A. N. Kolmogorov*. Cambridge University Press (cit. on pp. 11–13).

Fritsch, J. M. and C. F. Chappell (1980). "Numerical Prediction of Convectively Driven Mesoscale Pressure Systems. Part I: Convective Parameterization". *Journal of the Atmospheric Sciences* 37.8, pp. 1722–1733. DOI: 10.1175/1520-0469(1980)037<1722:NPOCDM>2.0.CO;2 (cit. on p. 29).

Fureby, C and G Tabor (1997). "Mathematical and physical constraints on large-eddy simulations". *Theoretical and Computational Fluid Dynamics* 9.2, pp. 85–102 (cit. on pp. 90, 95, 96, 120).

Garratt, J. R. (1994). *The Atmospheric Boundary Layer*. Cambridge University Press, pp316 (cit. on pp. 18, 47).

Gentine, P. et al. (2018). "Could Machine Learning Break the Convection Parameterization Deadlock?" *Geophysical Research Letters* 45.11, pp. 5742–5751. DOI: https://doi.org/10.1029/2018GL078202 (cit. on p. 39).

Gerard, Luc and J-F Geleyn (2005). "Evolution of a subgrid deep convection parametrization in a limited-area model with increasing resolution". *Quarterly Journal of the Royal Meteorological Society* 131.610, pp. 2293–2312 (cit. on p. 34).

Germano, Massimo (1992). "Turbulence: the filtering approach". *Journal of Fluid Mechanics* 238, pp. 325–336. DOI: 10.1017/S0022112092001733 (cit. on pp. 14, 15, 24, 99, 129).

Germano, Massimo et al. (1991). "A dynamic subgrid-scale eddy viscosity model". *Physics of Fluids A: Fluid Dynamics* 3.7, pp. 1760–1765. DOI: 10.1063/1.857955 (cit. on p. 20).

Gidaspow, D et al. (1973). "Characteristics of Unsteady One-Dimensional Two-phase Flow". In: *Transactions of the American Nuclear Society 1973 Winter Meeting* (Nov. 11–15, 1973). Vol. 17. San Francisco, California, pp. 249–250 (cit. on p. 87).

Gilbert, Andrew D., Xavier Riedinger, and John Thuburn (2014). "On the form of the viscous term for two dimensional Navier–Stokes flows". *The Quarterly Journal of Mechanics and Applied Mathematics* 67.2, pp. 205–228. DOI: 10.1093/qjmam/hbu004 (cit. on p. 108).

Grant, Alan L. M. (2006a). "The cumulus-capped boundary layer. I: Modelling transports in the cloud layer". *Quarterly Journal of the Royal Meteorological Society* 132.618, pp. 1385–1403 (cit. on pp. 37, 187).

— (2006b). "The cumulus-capped boundary layer. II: Interface fluxes". *Quarterly Journal of the Royal Meteorological Society* 132.618, pp. 1405–1422 (cit. on p. 37).

Grant, Alan L. M. and A. P. Lock (2004). "The turbulent kinetic energy budget for shallow cumulus convection". *Quarterly Journal of the Royal Meteorological Society* 130.597, pp. 401–422 (cit. on p. 37).

Gregory, David (2001). "Estimation of entrainment rate in simple models of convective clouds". *Quarterly Journal of the Royal Meteorological Society* 127.571, pp. 53–72. DOI: https://doi.org/10.1002/qj.49712757104 (cit. on p. 87).

Gregory, David and P. R. Rowntree (1990). "A Mass Flux Convection Scheme with Representation of Cloud Ensemble Characteristics and Stability-Dependent Closure". *Monthly Weather Review* 118.7, pp. 1483–1506. DOI: 10.1175/1520-0493(1990)118<1483:AMFCSW>2.0.CO;2 (cit. on p. 28).

Grossmann, Siegfried and Detlef Lohse (2000). "Scaling in thermal convection: a unifying theory". *Journal of Fluid Mechanics* 407, pp. 27–56 (cit. on pp. 50, 51, 56, 135).

— (2001). "Thermal Convection for Large Prandtl Numbers". *Physical Review Letters* 86 (15), pp. 3316–3319 (cit. on p. 50).

— (2002). "Prandtl and Rayleigh number dependence of the Reynolds number in turbulent thermal convection". *Physical Review E* 66 (1), p. 016305. DOI: 10.1103/PhysRevE.66.016305 (cit. on p. 50).

— (2003). "On geometry effects in Rayleigh-Bénard convection". *Journal of Fluid Mechanics* 486, pp. 105–114. DOI: 10.1017/S0022112003004270 (cit. on p. 50).

— (2004). "Fluctuations in turbulent Rayleigh–Bénard convection: The role of plumes". *Physics of Fluids* 16.12, pp. 4462–4472. DOI: 10.1063/1.1807751 (cit. on p. 50).

Grötzbach, Günther (1983). "Spatial resolution requirements for direct numerical simulation of the Rayleigh-Bénard convection". *Journal of Computational Physics* 49.2, pp. 241–264. DOI: https://doi.org/10.1016/0021-9991(83)90125-0 (cit. on pp. 57, 71).

Gu, Jian-Feng et al. (2020). "Evaluation of the Bulk Mass Flux Formulation Using Large-Eddy Simulations". *Journal of the Atmospheric Sciences* 77.6, pp. 2115–2137. DOI: 10.1175/JAS-D-19-0224.1 (cit. on pp. 30, 31, 181).

Han, Jongil et al. (2017). "Updates in the NCEP GFS Cumulus Convection Schemes with Scale and Aerosol Awareness". *Weather and Forecasting* 32.5, pp. 2005–2017. DOI: 10.1175/WAF-D-17-0046.1 (cit. on p. 34).

Hanley, Kirsty et al. (2019). "Modifications to the representation of subgrid mixing in kilometre-scale versions of the Unified Model". *Quarterly Journal of the Royal Meteorological Society* 145.725, pp. 3361–3375. DOI: https://doi.org/10.1002/qj.3624 (cit. on p. 33).

Hayes, Alexander G., Ralph D. Lorenz, and Jonathan I. Lunine (2018). "A post-Cassini view of Titan's methane-based hydrologic cycle". *Nature Geoscience* 11 (5), pp. 306–313. DOI: 10.1038/s41561-018-0103-y (cit. on p. 9).

He, Jia et al. (2020). "An Improved Perturbation Pressure Closure for Eddy-Diffusivity Mass-Flux Schemes". *Earth and Space Science Open Archive*, p. 28. DOI: 10.1002/essoar.10505084.1 (cit. on pp. 36, 128).

He, Xiaozhou, Eberhard Bodenschatz, and Guenter Ahlers (2020). "Aspect ratio dependence of the ultimate-state transition in turbulent thermal convection". *Proceedings of the National Academy of Sciences* 117.48, pp. 30022–30023. DOI: 10.1073/pnas.2007399117 (cit. on p. 51).

He, Xiaozhou et al. (2012). "Transition to the Ultimate State of Turbulent Rayleigh-Bénard Convection". *Physical Review Letters* 108 (2), p. 024502. DOI: 10.1103/PhysRevLett.108.024502 (cit. on p. 51).

Heslot, F., B. Castaing, and A. Libchaber (1987). "Transitions to turbulence in helium gas". *Physical Review A* 36 (12), pp. 5870–5873. DOI: 10.1103/PhysRevA.36.5870 (cit. on p. 50).

Holloway, Christopher E., Steven J. Woolnough, and Grenville M. S. Lister (2013). "The Effects of Explicit versus Parameterized Convection on the MJO in a Large-Domain High-Resolution Tropical Case Study. Part I: Characterization of Large-Scale Organization and Propagation". *Journal of the Atmospheric Sciences* 70.5, pp. 1342–1369. DOI: 10.1175/JAS-D-12-0227.1 (cit. on pp. 1, 32).

Holloway, Christopher E. et al. (2014). "Understanding and representing atmospheric convection across scales: recommendations from the meeting held at Dartington Hall, Devon, UK, 28–30 January 2013". *Atmospheric Science Letters* 15.4, pp. 348–353. DOI: 10.1002/asl2.508 (cit. on p. 177).

Holm, Darryl D. and Boris A. Kupershmidt (1984). "Multipressure regularization for multiphase flow". *Physics Letters A* 106, pp. 165–168. DOI: 10.1016/0375-9601(84)90309-8 (cit. on p. 97).

Honnert, Rachel, Valéry Masson, and Fleur Couvreux (2011). "A Diagnostic for Evaluating the Representation of Turbulence in Atmospheric Models at the Kilometric Scale". *Journal of the Atmospheric Sciences* 68.12, pp. 3112–3131 (cit. on p. 2).

Hörmander, Lars (2003). *The Analysis of Linear Partial Differential Operators I. Distribution Theory and Fourier Analysis*. 2nd ed. Classics in Mathematics. Springer-Verlag Berlin Heidelberg (cit. on p. 95).

Houghton, Henry G. and Harrison E. Cramer (1951). "A theory of entrainment in convective currents". *Journal of Atmospheric Sciences* 8.2, pp. 95–102. DOI: 10.1175/1520-0469(1951)008<0095:ATOEIC>2.0.CO;2 (cit. on p. 132).

Houze, Robert A. (2010). "Joanne Simpson (1923–2010)". *Nature* 464 (7289), p. 696. DOI: 10.1038/464696a (cit. on p. 50).

Howard, Louis N. (1963). "Heat transport by turbulent convection". *Journal of Fluid Mechanics* 17.3, pp. 405–432. DOI: 10.1017/S0022112063001427 (cit. on p. 50).

— (1964). "Convection at high Rayleigh number". In: *Applied Mechanics*. Ed. by Henry Görtler. Berlin, Heidelberg: Springer Berlin Heidelberg, pp. 1109–1115 (cit. on p. 49).

Hussain, A. K. M. Fazle (1983). "Coherent structures—reality and myth". *The Physics of Fluids* 26.10, pp. 2816–2850. DOI: 10.1063/1.864048 (cit. on pp. 31, 85, 179).

— (1986). "Coherent structures and turbulence". *Journal of Fluid Mechanics* 173, pp. 303–356. DOI: 10.1017/S0022112086001192 (cit. on pp. 11, 179).

"IFS Documentation CY47R3 - Part IV Physical processes" (2021). In: *IFS Documentation CY47R3*. IFS Documentation 4. ECMWF. DOI: 10.21957/eyrpir4vj (cit. on pp. 29, 35).

Iyer, Kartik P. et al. (2020). "Classical 1/3 scaling of convection holds up to Ra = 1015". *Proceedings of the National Academy of Sciences* 117.14, pp. 7594–7598. DOI: 10.1073/pnas.1922794117 (cit. on p. 51).

Jeffreys, Harold (1926). "LXXVI. The stability of a layer of fluid heated below". *The London, Edinburgh, and Dublin Philosophical Magazine and Journal of Science* 2.10, pp. 833–844. DOI: 10.1080/14786442608564114 (cit. on p. 43).

— (1928). "Some Cases of Instability in Fluid Motion". *Proceedings of the Royal Society of London Series A* 118, pp. 195–208. DOI: 10.1098/rspa.1928.0045 (cit. on p. 43).

Jeng, Jyh-horng and Brian Hassard (1999). "The critical wave number for the planar Bénard problem is unique". *International Journal of Non-Linear Mechanics* 34.2, pp. 221–229. DOI: https://doi.org/10.1016/S0020-7462(97)00078-4 (cit. on p. 48).

Johnston, Hans and Charles R. Doering (2009). "Comparison of Turbulent Thermal Convection between Conditions of Constant Temperature and Constant Flux". *Physical Review Letters* 102 (6), p. 064501. DOI: 10.1103/PhysRevLett.102.064501 (cit. on pp. 47, 52, 58, 64, 66, 151).

Joseph, Daniel D. (1966). "Nonlinear stability of the Boussinesq equations by the method of energy". *Archive for Rational Mechanics and Analysis* 22.3, pp. 163–184. DOI: 10.1007/BF00266474 (cit. on p. 48).

Kain, John S. (2004). "The Kain–Fritsch Convective Parameterization: An Update". *Journal of Applied Meteorology* 43.1, pp. 170–181. DOI: 10.1175/1520-0450(2004)043<0170:TKCPAU>2.0.CO;2 (cit. on p. 39).

Kain, John S. and J. Michael Fritsch (1990). "A One-Dimensional Entraining/Detraining Plume Model and Its Application in Convective Parameterization". *Journal of the Atmospheric Sciences* 47.23, pp. 2784–2802. DOI: 10.1175/1520-0469(1990)047<2784:AODEPM>2.0.CO;2 (cit. on p. 29).

— (1993). "Convective Parameterization for Mesoscale Models: The Kain-Fritsch Scheme". In: *The Representation of Cumulus Convection in Numerical Models*. Ed. by Kerry A. Emanuel and David J. Raymond. Boston, MA: American Meteorological Society, pp. 165–170. DOI: 10.1007/978-1-935704-13-3_16 (cit. on p. 29).

Karlin, Samuel (1983). "11th R. A. Fisher Memorial Lecture". Royal Society of London (cit. on p. xxv).

Kaye, N. B. (2008). "Turbulent plumes in stratified environments: A review of recent work". *Atmosphere-Ocean* 46.4, pp. 433–441. DOI: 10.3137/ao.460404 (cit. on p. 26).

Kerr, Robert M. (1985). "Higher-order derivative correlations and the alignment of small-scale structures in isotropic numerical turbulence". *Journal of Fluid Mechanics* 153, pp. 31–58. DOI: 10.1017/S0022112085001136 (cit. on p. 57).

— (1996). "Rayleigh number scaling in numerical convection". *Journal of Fluid Mechanics* 310, pp. 139–179. DOI: 10.1017/S0022112096001760 (cit. on pp. 50, 61, 62, 64, 68).

Kiš, P. and H. Herwig (2010). "A systematic derivation of a consistent set of "Boussinesq equations"". *Heat and Mass Transfer* 46.10, pp. 1111–1119. DOI: 10.1007/s00231-010-0680-9 (cit. on p. 46).

Klein, Rupert (2009). "Asymptotics, structure, and integration of sound-proof atmospheric flow equations". *Theoretical and Computational Fluid Dynamics* 23 (3), pp. 161–195. DOI: 10.1007/s00162-009-0104-y (cit. on p. 46).

Kolmogorov, A.N. (1941). "The Local Structure of Turbulence in Incompressible Viscous Fluid for Very Large Reynolds' Numbers". *Doklady Akademiia Nauk SSSR [Sov. Phys. Dokl.]* 30, pp. 301–305 (cit. on pp. 11, 19).

Kraichnan, Robert H. (1962). "Turbulent Thermal Convection at Arbitrary Prandtl Number". *The Physics of Fluids* 5.11, pp. 1374–1389. DOI: 10.1063/1.1706533 (cit. on p. 50).

— (1967). "Inertial Ranges in Two-Dimensional Turbulence". *The Physics of Fluids* 10.7, pp. 1417–1423. DOI: 10.1063/1.1762301 (cit. on p. 68).

Kuo, H. L. (1965). "On Formation and Intensification of Tropical Cyclones Through Latent Heat Release by Cumulus Convection". *Journal of the Atmospheric Sciences* 22.1, pp. 40–63. DOI: 10.1175/1520-0469(1965)022<0040:OFAIOT>2.0.CO;2 (cit. on pp. 22, 29).

Kurowski, Marcin J., Wojciech W. Grabowski, and Piotr K. Smolarkiewicz (2014). "Anelastic and Compressible Simulation of Moist Deep Convection". *Journal of the Atmospheric Sciences* 71.10, pp. 3767–3787. DOI: 10.1175/JAS-D-14-0017.1 (cit. on p. 51).

Landau, L. D. and E. M. Lifshitz (1987). *Fluid Mechanics*. 2nd ed. Vol. 6. Course of Theoretical Physics. Butterworth-Heinemann (cit. on pp. 5, 111, 113).

Lange, Rutger-Jan (2012). "Potential theory, path integrals and the Laplacian of the indicator". *Journal of High Energy Physics* 2012.11, pp. 1–46 (cit. on p. 96).

Lappen, Cara-Lyn and David A Randall (2001). "Toward a unified parameterization of the boundary layer and moist convection. Part I: A new type of mass-flux model". *Journal of the atmospheric sciences* 58.15, pp. 2021–2036 (cit. on p. 36).

Larson, Vincent E., Jean-Christophe Golaz, and William R. Cotton (2002). "Small-Scale and Mesoscale Variability in Cloudy Boundary Layers: Joint Probability Density Functions". *Journal of the Atmospheric Sciences* 59.24, pp. 3519–3539. DOI: 10.1175/1520-0469(2002)059<3519:SSAMVI>2.0.CO;2 (cit. on p. 86).

Larson, Vincent E. et al. (2012). "PDF Parameterization of Boundary Layer Clouds in Models with Horizontal Grid Spacings from 2 to 16 km". *Monthly Weather Review* 140.1, pp. 285–306. DOI: 10.1175/MWR-D-10-05059.1 (cit. on pp. 36, 86).

Lean, Humphrey W. et al. (2008). "Characteristics of High-Resolution Versions of the Met Office Unified Model for Forecasting Convection over the United Kingdom". *Monthly Weather Review* 136.9, pp. 3408–3424. DOI: 10.1175/2008MWR2332.1 (cit. on pp. 2, 32, 33, 77, 157, 162).

Leonard, A (1974). "Energy cascade in large-eddy simulations of turbulent fluid flows". In: *Turbulent Diffusion in Environmental Pollution*. Ed. by F. N. Frenkiel and R. E. Munn. Vol. 18A. Advances in Geophysics. International Union of Theoretical et al. Elsevier, pp. 237–248 (cit. on p. 16).

Lepot, Simon, Sébastien Aumaître, and Basile Gallet (2018). "Radiative heating achieves the ultimate regime of thermal convection". *Proceedings of the National Academy of Sciences* 115.36, pp. 8937–8941. DOI: 10.1073/pnas.1806823115 (cit. on p. 52).

Lesieur, Marcel (2008). *Turbulence in Fluids*. 4th ed. Vol. 84. Fluid Mechanics and Its Applications. Springer Netherlands (cit. on p. 10).

Libby, Paul A. (1976). "Prediction of the intermittent turbulent wake of a heated cylinder". *The Physics of Fluids* 19.4, pp. 494–501. DOI: 10.1063/1.861505 (cit. on p. 86).

Lilly, D. K. (1962). "On the numerical simulation of buoyant convection". *Tellus* 14.2, pp. 148–172. DOI: https://doi.org/10.1111/j.2153-3490.1962.tb00128.x (cit. on pp. 20, 54).

— (1966). "The Representation of Small-scale Turbulence in Numerical Simulation Experiments". In: NCAR Manuscripts 281 (cit. on p. 20).

Lindsay, K. A. and B. Straughan (1990). "Energy methods for nonlinear stability in convection problems primarily related to geophysics". *Continuum Mechanics and Thermodynamics* 2.4, pp. 245–277. DOI: 10.1007/BF01129121 (cit. on p. 48).

Lorenz, Edward N. (1963). "Deterministic Nonperiodic Flow." *Journal of the Atmospheric Sciences* 20, pp. 130–148. DOI: 10.1175/1520-0469(1963)020<0130:DNF>2.0.CO;2 (cit. on pp. 44, 80).

Lucarini, Valerio et al. (2014). "Mathematical and physical ideas for climate science". *Reviews of Geophysics* 52.4, pp. 809–859. DOI: https://doi.org/10.1002/2013RG000446 (cit. on p. 38).

Lundgren, Thomas S. (2003). "Kolmogorov turbulence by matched asymptotic expansions". *Physics of Fluids* 15.4, pp. 1074–1081. DOI: 10.1063/1.1558332 (cit. on p. 20).

Malardel, Sylvie and Peter Bechtold (2019). "The coupling of deep convection with the resolved flow via the divergence of mass flux in the IFS". *Quarterly Journal of the Royal Meteorological Society* 145.722, pp. 1832–1845. DOI: https://doi.org/10.1002/qj.3528 (cit. on p. 34).

Malkus, Willem V. R. (1954). "The heat transport and spectrum of thermal turbulence". *Proceedings of the Royal Society of London. Series A. Mathematical and Physical Sciences* 225.1161, pp. 196–212. DOI: 10.1098/rspa.1954.0197 (cit. on p. 49).

Manabe, Syukuro, Joseph Smagorinsky, and Robert F. Strickler (1965). "Simulated climatology of a general circulation model with a hydrologic cycle". *Monthly Weather Review* 93.12, pp. 769–798. DOI: 10.1175/1520-0493(1965)093<0769:SCOAGC>2.3.CO;2 (cit. on p. 22).

Mason, P. J. (1994). "Large-eddy simulation: A critical review of the technique". *Quarterly Journal of the Royal Meteorological Society* 120.515, pp. 1–26. DOI: 10.1002/qj.49712051503 (cit. on pp. 2, 19, 20, 53, 69).

Mason, P. J. and A. R. Brown (1994). "The sensitivity of large-eddy simulation of turbulent shear flow to subgrid models". *Boundary-Layer Meteorology* 70.1, pp. 133–150. DOI: 10.1007/BF00712526 (cit. on p. 20).

— (1999). "On Subgrid Models and Filter Operations in Large Eddy Simulations". *Journal of the Atmospheric Sciences* 56.13, pp. 2101–2114. DOI: 10.1175/1520-0469(1999)056<2101:OSMAFO>2.0.CO;2 (cit. on pp. 20, 57).

McComb, William David (1990). *The Physics of Fluid Turbulence*. Oxford Engineering Science Series 25. Oxford University Press (cit. on pp. 19, 85).

McIntyre, William A. (2020). "Multi-fluid modelling of dry convection". PhD thesis. University of Reading (cit. on pp. 87, 133, 185).

McIntyre, William A., Hilary Weller, and Christopher E. Holloway (2020). "Numerical methods for entrainment and detrainment in the multi-fluid Euler equations for convection". *Quarterly Journal of the Royal Meteorological Society* 146.728, pp. 1106–1120. DOI: 10.1002/qj.3728 (cit. on pp. 36, 132, 137).

Mellado, Juan Pedro (2012). "Direct numerical simulation of free convection over a heated plate". *Journal of Fluid Mechanics* 712, pp. 418–450. DOI: 10.1017/jfm.2012.428 (cit. on pp. 52, 183).

Mellado, Juan Pedro et al. (2018). "DNS and LES for Simulating Stratocumulus: Better Together". *Journal of Advances in Modeling Earth Systems* 10.7, pp. 1421–1438. DOI: https://doi.org/10.1029/2018MS001312 (cit. on pp. 53, 54).

Mellor, George L. and Tetsuji Yamada (1974). "A Hierarchy of Turbulence Closure Models for Planetary Boundary Layers". *Journal of the Atmospheric Sciences* 31.7, pp. 1791–1806. DOI: 10.1175/1520-0469(1974)031<1791:AHOTCM>2.0.CO;2 (cit. on p. 186).

Moin, Parviz and Krishnan Mahesh (1998). "Direct Numerical Simulation: A Tool in Turbulence Research". *Annual Review of Fluid Mechanics* 30.1, pp. 539–578. DOI: 10.1146/annurev.fluid.30.1.539 (cit. on p. 13).

Morton, B. R., Geoffrey Ingram Taylor, and John Stewart Turner (1956). "Turbulent gravitational convection from maintained and instantaneous sources". *Proceedings of the Royal Society of London. Series A. Mathematical and Physical Sciences* 234.1196, pp. 1–23. DOI: 10.1098/rspa.1956.0011 (cit. on p. 103).

Ooyama, Katsuyuki (1971). "A Theory on Parameterization of Cumulus Convection". *Journal of the Meteorological Society of Japan. Ser. II* 49A, pp. 744–756. DOI: 10.2151/jmsj1965.49A.0_744 (cit. on pp. 22, 24, 27).

The OpenFOAM Foundation (2019). *OpenFOAM v7 User Guide*. Available at https://cfd.direct/openfoam/user-guide-v7 (cit. on pp. 60, 136, 137).

Pan, Dzong-Ming and David A Randall (1998). "A cumulus parameterization with a prognostic closure". *Quarterly Journal of the Royal Meteorological Society* 124.547, pp. 949–981 (cit. on p. 34).

Papalexandris, Miltiadis V (2020). "On the applicability of Stokes' hypothesis to low-Mach-number flows". *Continuum Mechanics and Thermodynamics* 32.4, pp. 1245–1249 (cit. on p. 116).

Patterson, G. S. and Steven A. Orszag (1973). "Numerical Simulation of Turbulence". *Atmospheric Technology* 3, pp. 71–78 (cit. on p. 13).

Pauluis, Olivier M. and Jörg Schumacher (2010). "Idealized moist Rayleigh-Bénard convection with piecewise linear equation of state". *Communications in Mathematical Sciences* 8.1, pp. 295–319 (cit. on pp. 9, 44, 185).

Pearson, J. R. A. (1958). "On convection cells induced by surface tension". *Journal of Fluid Mechanics* 4.5, pp. 489–500. DOI: 10.1017/S0022112058000616 (cit. on p. 43).

Petch, J. C., A. R. Brown, and M. E. B. Gray (2002). "The impact of horizontal resolution on the simulations of convective development over land". *Quarterly Journal of the Royal Meteorological Society* 128.584, pp. 2031–2044. DOI: https://doi.org/10.1256/003590002320603511 (cit. on pp. 32, 75, 179).

Plant, R. S. and G. C. Craig (2008). "A Stochastic Parameterization for Deep Convection Based on Equilibrium Statistics". *Journal of the Atmospheric Sciences* 65.1, pp. 87–105. DOI: 10.1175/2007JAS2263.1 (cit. on p. 38).

Plant, Robert S. and Jun-Ichi Yano, eds. (2016a). *Parameterization of Atmospheric Convection. Theoretical Background and Formulation*. Vol. 1. Series on the Science of Climate Change 1. World Scientific (cit. on p. 1).

— eds. (2016b). *Parameterization of Atmospheric Convection. Current Issues and New Theories*. Vol. 2. Series on the Science of Climate Change 1. World Scientific (cit. on pp. 32, 37).

Pope, Stephen B. (2000). *Turbulent Flows*. Cambridge University Press. DOI: 10.1017/CBO9780511840531 (cit. on p. 54).

Prout, W (1834). *Chemistry, Meteorology, and the Function of Digestion, considered with reference to Natural Theology*. Ed. by W. Pickering. Bridgewater Treatises 8, p. 65 (cit. on p. 5).

Randall, David A. (2013). "Beyond deadlock". *Geophysical Research Letters* 40.22, pp. 5970–5976. DOI: 10.1002/2013GL057998 (cit. on p. 39).

Rasp, Stephan, Michael S. Pritchard, and Pierre Gentine (2018). "Deep learning to represent subgrid processes in climate models". *Proceedings of the National Academy of Sciences* 115.39, pp. 9684–9689. DOI: 10.1073/pnas.1810286115 (cit. on p. 39).

Ray, Durga (1965). "Cellular convection with nonisotropic eddys". *Tellus* 17.4, pp. 434–439. DOI: 10.3402/tellusa.v17i4.9167 (cit. on p. 77).

Lord Rayleigh (1916). "LIX. On convection currents in a horizontal layer of fluid, when the higher temperature is on the under side". *The London, Edinburgh, and Dublin Philosophical Magazine and Journal of Science* 32.192, pp. 529–546. DOI: 10.1080/14786441608635602 (cit. on pp. 3, 43).

Reynolds, Osborne (1895). "IV. On the dynamical theory of incompressible viscous fluids and the determination of the criterion". *Philosophical Transactions of the Royal Society of London (A)* 186, pp. 123–164. DOI: 10.1098/rsta.1895.0004 (cit. on pp. 16, 17).

Richardson, Lewis Fry (1922). *Weather Prediction by Numerical Process*. 1st ed. Cambridge University Press (cit. on p. 19).

Riehl, Herbert and Joanne S. Malkus (1958). "On the heat balance of the equatorial trough zone". *Geophysica* 6, pp. 503–538 (cit. on p. 49).

Rio, Catherine et al. (2010). "Resolved Versus Parametrized Boundary-Layer Plumes. Part II: Continuous Formulations of Mixing Rates for Mass-Flux Schemes". *Boundary-Layer Meteorology* 135 (3), pp. 469–483. DOI: 10.1007/s10546-010-9478-z (cit. on p. 87).

Roche, P-E et al. (2004). "Heat transfer in turbulent Rayleigh–Bénard convection below the ultimate regime". *Journal of low temperature physics* 134.5-6, pp. 1011–1042 (cit. on p. 151).

Rudy, Samuel H. et al. (2017). "Data-driven discovery of partial differential equations". *Science Advances* 3.4. DOI: 10.1126/sciadv.1602614 (cit. on p. 40).

Saad, Yousef (2003). *Iterative Methods for Sparse Linear Systems*. 2nd ed. Society for Industrial and Applied Mathematics (cit. on p. 61).

Sakradzija, M., A. Seifert, and T. Heus (2015). "Fluctuations in a quasi-stationary shallow cumulus cloud ensemble". *Nonlinear Processes in Geophysics* 22.1, pp. 65–85. DOI: 10.5194/npg-22-65-2015 (cit. on p. 39).

Salmon, Rick (1998). *Lectures on Geophysical Fluid Dynamics*. Oxford University Press (cit. on pp. 8, 10).

Satoh, Masaki et al. (2019). "Global Cloud-Resolving Models". *Current Climate Change Reports* 5 (3), pp. 172–184. DOI: 10.1007/s40641-019-00131-0 (cit. on p. 32).

Savre, Julien and Michael Herzog (2019). "A General Description of Entrainment in Buoyant Cloudy Plumes Including the Effects of Mixing-Induced Evaporation". *Journal of*

the Atmospheric Sciences 76.2, pp. 479–496. DOI: 10.1175/JAS-D-17-0326.1 (cit. on p. 104).

Schmalzl, J, M Breuer, and U Hansen (2004). "On the validity of two-dimensional numerical approaches to time-dependent thermal convection". *Europhysics Letters (EPL)* 67.3, pp. 390–396. DOI: 10.1209/epl/i2003-10298-4 (cit. on pp. 55, 56, 141).

Schumacher, Jörg and Olivier M. Pauluis (2010). "Buoyancy statistics in moist turbulent Rayleigh–Bénard convection". *Journal of Fluid Mechanics* 648, pp. 509–519. DOI: 10.1017/S0022112010000030 (cit. on p. 9).

Schwartz, Laurent (1951). *Théorie des distributions*. Hermann (cit. on p. 94).

Shaw, James et al. (2017). "Multidimensional method-of-lines transport for atmospheric flows over steep terrain using arbitrary meshes". *Journal of Computational Physics* 344, pp. 86–107. DOI: https://doi.org/10.1016/j.jcp.2017.04.061 (cit. on p. 136).

Sherwood, Steven C., Sandrine Bony, and Jean-Louis Dufresne (2014). "Spread in model climate sensitivity traced to atmospheric convective mixing". *Nature* 505, pp. 37–42 (cit. on p. 1).

Shipley, Daniel et al. (2022). "Two-fluid single-column modelling of Rayleigh-Bénard convection as a step towards multi-fluid modelling of atmospheric convection". *Quarterly Journal of the Royal Meteorological Society* 148.742, pp. 351–377. DOI: https://doi.org/10.1002/qj.4209 (cit. on pp. 36, 43, 127).

Shishkina, Olga et al. (2010). "Boundary layer structure in turbulent thermal convection and its consequences for the required numerical resolution". *New Journal of Physics* 12.7, p. 075022 (cit. on p. 57).

Shraiman, Boris I. and Eric D. Siggia (1990). "Heat transport in high-Rayleigh-number convection". *Physical Review A* 42 (6), pp. 3650–3653. DOI: 10.1103/PhysRevA.42.3650 (cit. on pp. 49, 50, 58).

Siebesma, A. P. (1998). "Shallow Cumulus Convection". In: *Buoyant Convection in Geophysical Flows*. Ed. by E. J. Plate et al. Dordrecht: Springer Netherlands, pp. 441–486. DOI: 10.1007/978-94-011-5058-3_19 (cit. on pp. 98, 99).

Siebesma, A. P. and J. W. M. Cuijpers (1995). "Evaluation of Parametric Assumptions for Shallow Cumulus Convection". *Journal of the Atmospheric Sciences* 52.6, pp. 650–666. DOI: 10.1175/1520-0469(1995)052<0650:EOPAFS>2.0.CO;2 (cit. on pp. 24, 30).

Siebesma, A. Pier, Pedro M. M. Soares, and João Teixeira (2007). "A Combined Eddy-Diffusivity Mass-Flux Approach for the Convective Boundary Layer". *Journal of the Atmospheric Sciences* 64.4, pp. 1230–1248. DOI: 10.1175/JAS3888.1 (cit. on pp. 35, 87).

Siebesma, A. Pier et al. (2003). "A Large Eddy Simulation Intercomparison Study of Shallow Cumulus Convection". *Journal of the Atmospheric Sciences* 60.10, pp. 1201–1219. DOI: 10.1175/1520-0469(2003)60<1201:ALESIS>2.0.CO;2 (cit. on p. 77).

Siggia, E. D. (1994). "High Rayleigh Number Convection". *Annual Review of Fluid Mechanics* 26.1, pp. 137–168. DOI: 10.1146/annurev.fl.26.010194.001033 (cit. on pp. 49, 56).

Simpson, Joanne S and Victor Wiggert (1969). "Models of precipitating cumulus towers". *Monthly Weather Review* 97.7, pp. 471–489. DOI: 10.1175/1520-0493(1969)097<0471:MOPCT>2.3.CO;2 (cit. on pp. 34, 50, 104).

Smagorinsky, J. (1963). "General circulation experiments with the primitive equations". *Monthly Weather Review* 91.3, pp. 99–164. DOI: 10.1175/1520-0493(1963)091<0099:GCEWTP>2.3.CO;2 (cit. on pp. 20, 53).

Soares, P. M. M. et al. (2004). "An eddy-diffusivity/mass-flux parametrization for dry and shallow cumulus convection". *Quarterly Journal of the Royal Meteorological Society* 130.604, pp. 3365–3383. DOI: 10.1256/qj.03.223 (cit. on p. 35).

Spiegel, Edward A. (1963). "A Generalization of the Mixing-Length Theory of Turbulent Convection." *The Astrophysical Journal* 138, p. 216. DOI: 10.1086/147628 (cit. on p. 50).

Städtke, H. (2007). *Gasdynamic Aspects of Two-Phase Flow*. John Wiley & Sons, Ltd, pp. 35–43. DOI: 10.1002/9783527610242.ch3 (cit. on pp. 3, 85, 127).

Stein, Thorwald H. M. et al. (2015). "The DYMECS Project: A Statistical Approach for the Evaluation of Convective Storms in High-Resolution NWP Models". *Bulletin of the American Meteorological Society* 96.6, pp. 939–951. DOI: 10.1175/BAMS-D-13-00279.1 (cit. on pp. 1, 2, 33, 157, 177).

Stephens, Graeme L. et al. (2010). "Dreary state of precipitation in global models". *Journal of Geophysical Research: Atmospheres* 115.D24. DOI: 10.1029/2010JD014532 (cit. on p. 1).

Stevens, Bjorn and Sandrine Bony (2013). "What Are Climate Models Missing?" *Science* 340.6136, pp. 1053–1054. DOI: 10.1126/science.1237554 (cit. on pp. 1, 177).

Stevens, Bjorn et al. (2005). "Evaluation of Large-Eddy Simulations via Observations of Nocturnal Marine Stratocumulus". *Monthly Weather Review* 133.6, pp. 1443–1462. DOI: 10.1175/MWR2930.1 (cit. on p. 53).

Straughan, Brian (2004). *The Energy Method, Stability, and Nonlinear Convection*. 2nd ed. Vol. 91. Applied Mathematical Sciences. Springer. DOI: 10.1007/978-0-387-21740-6 (cit. on p. 9).

Stull, Roland B. (1988). *An Introduction to Boundary Layer Meteorology*. Springer (cit. on p. 18).

Sullivan, Peter P. and Edward G. Patton (2011). "The effect of mesh resolution on convective boundary layer statistics and structures generated by large-eddy simulation". *Journal of the Atmospheric Sciences* 68.10, pp. 2395–2415. DOI: 10.1175/JAS-D-10-05010.1 (cit. on pp. 51, 54).

Tan, Zhihong et al. (2018). "An Extended Eddy-Diffusivity Mass-Flux Scheme for Unified Representation of Subgrid-Scale Turbulence and Convection". *Journal of Advances*

in Modeling Earth Systems 10.3, pp. 770–800. DOI: 10.1002/2017MS001162 (cit. on pp. 36, 87, 99, 117, 127, 128, 158, 175, 180).

Taylor, G. I. (1945). "Dynamics of a mass of hot gas rising in air". In: Los Alamos National Laboratory Report Library 236. Technical Information Division, Oak Ridge Operations, Oak Ridge, Tennessee: United States Atomic Energy Commission (cit. on p. 103).

Teixeira, João and A. P. Siebesma (2000). "An Advection-Diffusion scheme for the convective boundary layer: description and 1d-results". In: *Proc. 14th Symp. on Boundary Layers and Turbulence*, pp. 133–136 (cit. on p. 35).

Tennekes, Hendrik and John Leask Lumley (1972). *A First Course in Turbulence*. MIT Press (cit. on pp. xix, 10, 17).

Thuburn, John and Georgios A. Efstathiou (2020). "Marginal Stability of the Convective Boundary Layer". *Journal of the Atmospheric Sciences* 77.2, pp. 435–442. DOI: 10.1175/JAS-D-18-0222.1 (cit. on p. 183).

Thuburn, John, Georgios A. Efstathiou, and Robert J. Beare (2019). "A two-fluid single-column model of the dry, shear-free, convective boundary layer". *Quarterly Journal of the Royal Meteorological Society* 145.721, pp. 1535–1550. DOI: 10.1002/qj.3510 (cit. on pp. 9, 36, 43, 86, 87, 110, 117, 127, 128, 132, 133).

Thuburn, John and Geoffrey K. Vallis (2018). "Properties of conditionally filtered equations: Conservation, normal modes, and variational formulation". *Quarterly Journal of the Royal Meteorological Society* 144.714, pp. 1555–1571. DOI: 10.1002/qj.3307 (cit. on pp. 36, 117).

Thuburn, John et al. (2018). "A Framework for Convection and Boundary Layer Parameterization Derived from Conditional Filtering". *Journal of the Atmospheric Sciences* 75.3, pp. 965–981. DOI: 10.1175/JAS-D-17-0130.1 (cit. on pp. 2, 3, 31, 36, 86, 88–90, 95, 98, 106, 110, 125, 127, 130, 132, 179, 205, 206).

Tiedtke, M. (1989). "A Comprehensive Mass Flux Scheme for Cumulus Parameterization in Large-Scale Models". *Monthly Weather Review* 117.8, pp. 1779–1800. DOI: 10.1175/1520-0493(1989)117<1779:ACMFSF>2.0.CO;2 (cit. on p. 29).

Tipping, Michael E (2001). "Sparse Bayesian learning and the relevance vector machine". *Journal of Machine Learning Research* 1, pp. 211–244 (cit. on p. 39).

Togni, Riccardo, Andrea Cimarelli, and Elisabetta De Angelis (2015). "Physical and scale-by-scale analysis of Rayleigh–Bénard convection". *Journal of Fluid Mechanics* 782, pp. 380–404. DOI: 10.1017/jfm.2015.547 (cit. on pp. 69, 106, 176, 184).

The TOP500 Project (2022). *The 60th TOP500 List (November 2022)*. URL: https://www.top500.org/lists/top500/list/2022/11/ (visited on 03/09/2023) (cit. on p. 13).

Toppaladoddi, Srikanth et al. (2021). "Thermal convection over fractal surfaces". *Journal of Fluid Mechanics* 907, a12. DOI: 10.1017/jfm.2020.826 (cit. on p. 52).

Turner, J. S. (1962). "The 'starting plume' in neutral surroundings". *Journal of Fluid Mechanics* 13.3, pp. 356–368. DOI: 10.1017/S0022112062000762 (cit. on p. 104).

Vallis, Geoffrey K. (2017). *Atmospheric and Oceanic Fluid Dynamics*. 2nd. Cambridge University Press (cit. on pp. 7, 8, 10, 30, 46).

Vallis, Geoffrey K., Douglas J. Parker, and Steven M. Tobias (2019). "A simple system for moist convection: the Rainy–Bénard model". *Journal of Fluid Mechanics* 862, pp. 162–199. DOI: 10.1017/jfm.2018.954 (cit. on pp. 9, 44, 183, 185).

van der Poel, Erwin P, Richard J. A. M. Stevens, and Detlef Lohse (2013). "Comparison between two-and three-dimensional Rayleigh–Bénard convection". *Journal of Fluid Mechanics* 736, pp. 177–194 (cit. on p. 55).

Vaschy, A. (1892). "Sur les lois de similitude en physique". *Annales Télégraphiques* 19, pp. 25–28 (cit. on p. 46).

Verzicco, R. and K. R. Sreenivasan (2008). "A comparison of turbulent thermal convection between conditions of constant temperature and constant heat flux". *Journal of Fluid Mechanics* 595, pp. 203–219. DOI: 10.1017/S0022112007009135 (cit. on p. 52).

Wang, Shouping and Bjorn Stevens (2000). "Top-Hat Representation of Turbulence Statistics in Cloud-Topped Boundary Layers: A Large Eddy Simulation Study". *Journal of the Atmospheric Sciences* 57.3, pp. 423–441. DOI: 10.1175/1520-0469(2000)057<0423:THROTS>2.0.CO;2 (cit. on pp. 30, 31).

Weidauer, Thomas, Olivier M. Pauluis, and Jörg Schumacher (2010). "Cloud patterns and mixing properties in shallow moist Rayleigh–Bénard convection". *New Journal of Physics* 12.10, p. 105002 (cit. on p. 9).

Weidauer, Thomas and Jörg Schumacher (2012). "Moist turbulent Rayleigh-Bénard convection with Neumann and Dirichlet boundary conditions". *Physics of Fluids* 24.7, p. 076604 (cit. on pp. 9, 44).

Weller, Hilary and William A. McIntyre (2019). "Numerical solution of the conditionally averaged equations for representing net mass flux due to convection". *Quarterly Journal of the Royal Meteorological Society* 145.721, pp. 1337–1353. DOI: 10.1002/qj.3490 (cit. on pp. 36, 132, 206).

Weller, Hilary, William A. McIntyre, and Daniel Shipley (2020). "Multifluids for Representing Subgrid-Scale Convection". *Journal of Advances in Modeling Earth Systems* 12.8. DOI: https://doi.org/10.1029/2019MS001966 (cit. on pp. 36, 87, 89, 90, 98, 110, 117, 128, 131–133, 136, 137, 141, 152, 206).

Weller, Hilary and Ava Shahrokhi (2014). "Curl-Free Pressure Gradients over Orography in a Solution of the Fully Compressible Euler Equations with Implicit Treatment of Acoustic and Gravity Waves". *Monthly Weather Review* 142.12, pp. 4439–4457. DOI: 10.1175/MWR-D-14-00054.1 (cit. on pp. 60, 136).

Whitall, Michael (2017). "Some thoughts on convective "triggering", "closure" and "cloud model" ... and a new stochastic scale-aware scheme". Presentation at the ECMWF workshop "Shedding light on the greyzone", 13–16 November 2017 (cit. on p. 32).

Whitehead, Jared P. and Charles R. Doering (2011). "Ultimate State of Two-Dimensional Rayleigh-Bénard Convection between Free-Slip Fixed-Temperature Boundaries". *Phys-*

ical Review Letters 106 (24), p. 244501. DOI: 10.1103/PhysRevLett.106.244501 (cit. on p. 50).

Wyngaard, John C. (2004). "Toward Numerical Modeling in the "Terra Incognita"". *Journal of the Atmospheric Sciences* 61.14, pp. 1816–1826 (cit. on p. 21).

— (2010). *Turbulence in the Atmosphere*. Cambridge University Press (cit. on pp. 13, 17, 18).

Yano, Jun-Ichi (2014). "Formulation structure of the mass-flux convection parameterization". *Dynamics of Atmospheres and Oceans* 67, pp. 1–28. DOI: 10.1016/j.dynatmoce.2014.04.002 (cit. on pp. 24, 27, 31, 36, 86, 87, 99, 125, 127, 179, 180).

Yano, Jun-Ichi and Robert S. Plant (2012). "Convective quasi-equilibrium". *Reviews of Geophysics* 50.4 (cit. on pp. 24, 30).

Yano, Jun-Ichi et al. (2018). "Scientific Challenges of Convective-Scale Numerical Weather Prediction". *Bulletin of the American Meteorological Society* 99.4, pp. 699–710. DOI: 10.1175/BAMS-D-17-0125.1 (cit. on p. 1).

Young, George S. (1988). "Turbulence Structure of the Convective Boundary Layer. Part II. Phonenix 78 Aircraft Observations of Thermals and Their Environment". *Journal of the Atmospheric Sciences* 45.4, pp. 727–735. DOI: 10.1175/1520-0469(1988)045<0727:TSOTCB>2.0.CO;2 (cit. on p. 30).

Zadeh, Lotfi A. (1965). "Fuzzy sets". *Information and Control* 8.3, pp. 338–353. DOI: https://doi.org/10.1016/S0019-9958(65)90241-X (cit. on p. 104).

Zanna, Laure and Thomas Bolton (2020). "Data-Driven Equation Discovery of Ocean Mesoscale Closures". *Geophysical Research Letters* 47.17. DOI: https://doi.org/10.1029/2020GL088376 (cit. on pp. 40, 176).

Zhang, Sheng and Guang Lin (2018). "Robust data-driven discovery of governing physical laws with error bars". *Proceedings of the Royal Society A: Mathematical, Physical and Engineering Sciences* 474.2217, p. 20180305 (cit. on p. 40).

Zhou, Bowen, Jason S. Simon, and Fotini K. Chow (2014). "The Convective Boundary Layer in the Terra Incognita". *Journal of the Atmosheric Sciences* 71.7, pp. 2545–2563 (cit. on pp. 3, 21, 76, 77, 178, 184).

Zhou, Quan et al. (2012). "Aspect ratio dependence of heat transport by turbulent Rayleigh–Bénard convection in rectangular cells". *Journal of Fluid Mechanics* 710, pp. 260–276. DOI: 10.1017/jfm.2012.363 (cit. on p. 47).

Zhu, Ping and Paquita Zuidema (2009). "On the use of PDF schemes to parameterize sub-grid clouds". *Geophysical Research Letters* 36.5. DOI: https://doi.org/10.1029/2008GL036817 (cit. on p. 86).

Zhu, Xiaojue et al. (2018). "Transition to the Ultimate Regime in Two-Dimensional Rayleigh-Bénard Convection". *Physical Review Letters* 120 (14), p. 144502. DOI: 10.1103/PhysRevLett.120.144502 (cit. on p. 51).

Zhu, Xiaojue et al. (2019). "Scaling enabled by multiscale wall roughness in Rayleigh–Bénard turbulence". *Journal of Fluid Mechanics* 869, r4. DOI: 10.1017/jfm.2019.228 (cit. on p. 52).

Zilitinkevich, Sergej S. (1973). "Shear convection". *Boundary-Layer Meteorology* 3 (4), pp. 416–423. DOI: 10.1007/BF01034985 (cit. on p. 69).

Zilitinkevich, Sergej S., A. Grachev, and J. C. R. Hunt (1998). "Surface Frictional Processes and Non-Local Heat/Mass Transfer in the Shear-Free Convective Boundary Layer". In: *Buoyant Convection in Geophysical Flows*. Ed. by E. J. Plate et al. Dordrecht: Springer Netherlands, pp. 83–113. DOI: 10.1007/978-94-011-5058-3_4 (cit. on pp. 69, 184).

Zilitinkevich, Sergej S. et al. (2021). *Order out of chaos: Shifting paradigm of convective turbulence*. DOI: https://arxiv.org/abs/2005.07680 (cit. on pp. 69, 184).